$$W \to \ell \nu + n$$
 jets

 $\label{eq:Dale Stentz} \mbox{Dale Stentz}^1 \\ \mbox{Northwestern University, USA}$ 

#### Abstract

In this note we document the measurement of W + n jets. Outside the EWK properties the W, we examine jet kinematic variables in an effort to study pQCD predictions at high momentum transfer. We derive several differential cross-sections such as the inclusive jet multiplicity and the nth leading jet  $p_T$  for each inclusive n jet. In this analysis, we are using 2.8 fb<sup>-1</sup> of data and consider both the electron and muon lepton final states for the W decay.

<sup>&</sup>lt;sup>1</sup>dstentz@fnal.gov

# Contents

1	Dat	a and MC Samples	1
	1.1	Software and File Format	1
	1.2	Data	2
	1.3	Good Run List	2
	1.4	Joint Physics Scale Factors	3
	1.5	Monte Carlo (MC) Samples	3
	1.6	MC weighting to data	4
2	W s	selection	9
	2.1	Electron selection	9
	2.2	Anti-selected Electrons	10
	2.3	Muon selection	11
	2.4	Anti-selected Muons	13
	2.5	Z Veto	17
	2.6	Missing Energy Corrections (muons)	18
	2.7	W identification	19
3	Jet	definition and selection	22
	3.1	Jet definition	22
	3.2	Electron-Jet Reclustering/Removal	23
	3.3	Anti-selected Lepton-Jet removal	24
	3.4	Lepton/Jet separation	28
	3.5	$\Delta\phi(\ell,\wp)$ cut	28
	3.6	Jet Energy Scale Corrections	36
	3.7	Missing Energy Corrections (jets)	40
	3.8	Hadron Level Correction Procedure	45
	3.9	Hadron Level Correction (Unfolding) Results	57
4	Bac	kground Estimation	82

	4.1	Diboson + tt Background Estimation	82
	4.2	EWK Signal and Background Template	83
	4.3	QCD template	84
	4.4	Background Fitting Procedure and Results	90
	4.5	Background Estimation Results	91
	4.6	MC Vertex Reweighing (Promotion)	123
5	Acc	eptance and Efficiency	169
	5.1	Acceptance Procedure	169
	5.2	Exclusive and Inclusive Acceptance Definitions	171
	5.3	Electron and Muon Acceptance Results	174
	5.4	Reduced Acceptance Definition	177
	5.5	Reduced Acceptance Results	179
	5.6	Lepton Efficiencies	180
	5.7	Effective Luminosity $(LA\epsilon)$	181
6	Syst	tematics	186
6	<b>Syst</b> 6.1	tematics  Luminosity Measurement	
6	·		186
6	6.1	Luminosity Measurement	186 187
6	6.1 6.2	Luminosity Measurement	186 187 193
6	6.1 6.2 6.3	Luminosity Measurement	186 187 193 195
6	6.1 6.2 6.3 6.4 6.5	Luminosity Measurement	186 187 193 195 196
6	6.1 6.2 6.3 6.4 6.5	Luminosity Measurement	186 187 193 195 196 197
6	6.1 6.2 6.3 6.4 6.5 6.6		186 187 193 195 196 197
6	6.1 6.2 6.3 6.4 6.5 6.6 6.7	Luminosity Measurement  Parton Density Function (PDF) Acceptance  Final State Radiation (FSR)  Vertex Reweighting  Background Estimation Fitting  tt Background Estimation  Jet Energy Scale Corrections	186 187 193 195 196 197 199 200
6	6.1 6.2 6.3 6.4 6.5 6.6 6.7 6.8 6.9	Luminosity Measurement  Parton Density Function (PDF) Acceptance  Final State Radiation (FSR)  Vertex Reweighting  Background Estimation Fitting  tt Background Estimation  Jet Energy Scale Corrections  Hadron Level Unfolding Correction	186 187 193 195 196 197 199 200 200
6	6.1 6.2 6.3 6.4 6.5 6.6 6.7 6.8 6.9	Luminosity Measurement  Parton Density Function (PDF) Acceptance  Final State Radiation (FSR)  Vertex Reweighting  Background Estimation Fitting  tt Background Estimation  Jet Energy Scale Corrections  Hadron Level Unfolding Correction  Systematics Combination and Correlated Systematics Treatment  Relative Systematic Uncertainties	186 187 193 195 196 197 199 200 200
	6.1 6.2 6.3 6.4 6.5 6.6 6.7 6.8 6.9 6.10	Luminosity Measurement  Parton Density Function (PDF) Acceptance  Final State Radiation (FSR)  Vertex Reweighting  Background Estimation Fitting  tt Background Estimation  Jet Energy Scale Corrections  Hadron Level Unfolding Correction  Systematics Combination and Correlated Systematics Treatment  Relative Systematic Uncertainties	186 187 193 195 196 197 199 200 203 227

$\mathbf{A}$	$\operatorname{Cro}$	ss-section Tables	265
	7.9	$H_T$ Cross-sections	. 258
	7.8	$\eta^*$ Cross-sections	. 248
	7.7	$\Delta\eta$ Cross-sections	. 247
	7.6	Dijet Separation Cross-section	. 243
	7.5	Dijet Mass Cross-section	. 243
	7.4	$n^{\mathrm{th}}$ Leading Jet $p_T$ Differential Cross-section	. 232
	7.3	Jet Multiplicity Ratio, $\sigma_{n+1}/\sigma_n$	. 232

# 1 Data and MC Samples

This chapter deals with the basic description of the data and MC samples. We first describe several technical details with respect to the basic software analysis and data file format. In section 1.2 we discuss our data sample with respect to trigger requirements, run periods, and integrated luminosity. We note the use of the good run list (GRL) is section 1.3 which is used to skip runs where the detector was not optimal or consistent to be used in our analysis. Section 1.4 deals with the Joint Physics scale factor class and its use in our analysis. This is followed by two section on our Monte Carlo (MC) samples. The first (section 1.5) gives a description of each of the MC samples that is used while the last section deals with applying an event-by-event weight to the MC based on its generator or theoretical cross-section.

#### 1.1 Software and File Format

This analysis uses topNtuples in collaboration with the Top Group. The samples and basic details can be found on various Top Group pages [5]. MC samples as well as data samples are inclusive samples in the sense that they are not filtered by any selection criteria. The topNtuple uses an electron-jet reclustering algorithm which is explained in section 3.2. In addition, we used a modified "top tarball" [6] to rerun over the initially generated W MC samples in order to perform a hadron level correction to our final cross-sections the details of this procedure are given in section 3.8 starting on page 45).

From the topNtuple we derive a reduced ntuple version which has the relevant and largely self-explanatory branches: evt, lum, met, zvtxs, hepg, electron, muon, track, and jet. We never filter our W MC since we use these samples in their entirety for our acceptance calculation. However, if a data or background sample event fail a basic selection criteria we skip the event. For example there has to be at least one lepton with  $E_T$  ( $p_T$ ) > 20 GeV(/c) and that passes basic track and fiducial requirements. However, we do not simply look for tight central lepton as our QCD background requires us to allow several identification (ID) or lepton quality variables to fail. There are secondary concerns as well like accounting for stubless muons in our missing energy correction which are discussed in section 2.6.

Our simplified ntuple allows us to run our analysis code locally to produce the necessary histograms by loading the ntuples and making the necessary event-by-event cuts. Once the basic selection stage of the analysis is over we then run over our histograms with the goal producing a final cross-section. Necessarily the analysis involves several components that have to be run in parallel (acceptance calculation, pdf and  $t\bar{t}$  systematics) or separately (jet energy and hadron level systematics). Some components, most notably the reweighting of the MC via our vertex fitting (see section 4.6 on page 123) require rerunning the analysis as an iterative procedure and in conjunction with our background fitting procedure of section 4.4.

Our analysis code is produced via CDFsoft2 6.1.4(.m) and is run via complied ROOT code. The associated version of ROOT is 4.00/08 which is recognized as a relatively archaic version [7].

### 1.2 Data

In this analysis we concentrate on both the high  $p_T$  muon triggered data and also study corresponding trigger for the electrons. The electron trigger is via HIGH\_PT\_ELECTRON and the muon is via HIGH\_PT\_MUON.

We use data up to and including period 17 which are represented by 13 different run segments. Most of these segments directly correspond to a single run period or in the case of the first few segments a couple of periods taken together. These segments are defined in table 1 by the (inclusive) beginning and ending run numbers. Hereafter, we will refer to the integrated luminosity, L, as just the (total) luminosity. Technically this is just the summation of the individual luminosities ( $L_i$ ) of each (i<sup>th</sup>) segment:

$$L = \sum_{\forall i} L_i \tag{1}$$

where i represents the different run periods. The actual luminsoity is derived via the measurement of the instantaneous luminosity,  $\mathcal{L}$ , which can be symbolically written as

$$L = \int \mathcal{L} dt \tag{2}$$

In table 2 we breakdown each run segment with their respective integrated luminosities for both CEM electrons and CMUP muons as well as CMX (arch and miniskirt) muons.

Run Period	Beginning Run #	Ending Run #
0d	138425	186598
0h	190697	203799
5-7	203819	212133
8	217990	222426
9	222529	228596
10	228664	233111
11	233133	237795
12	237845	241664
13	241665	246231
14	252836	254683
15	254800	256824
16	256840	258787
17	258880	261005

Table 1: Beginning and ending run numbers (inclusive) for each defined run segment and the corresponding CDF run period(s).

#### 1.3 Good Run List

We are using good run list version 26 which includes runs up to and including period 17. We use the '(1, 0, 1, 1)' criteria which signifies the good detectors for CEM, CMUP, and CMX but

Run	CEM & CMUP	CMX-Arch & Mini
Period	Luminosity $(pb^{-1})$	Luminosity $(pb^{-1})$
0d	360.1	340.1
0h	399.4	395.9
5-7	269.0	269.0
8	172.7	172.7
9	167.2	162.5
10	257.5	257.8
11	242.5	237.2
12	165.1	157.3
13	305.6	290.5
14	35.1	33.3
15	163.6	157.6
16	103.7	102.6
17	184.4	183.8
Total	2826.	2760.

Table 2: Luminosity (L) for CEM/CMUP events and CMX-Arch/CMX-Mini events for each run segment/period. The total integrated luminosity is given at the bottom. We latter assign a 6% systematic uncertainty due to our knowledge of the CLC (see section 5.7).

no explicit SVX requirement [8].

### 1.4 Joint Physics Scale Factors

Details on the Joint Physics scale factor procedure are noted on the Joint Physics SF Spread-sheet/Class page [9]. The relevant results from which it is derived from are taken from the PerfIDia page [10]. Our discussion of the various lepton efficiencies that are needed for our cross-section measurements are described in section 5.6 on page 180. We apply the scale factor in part to address disagreement between MC (with full dector simulation) and data.

# 1.5 Monte Carlo (MC) Samples

Our analysis uses various *Monte Carlo* simulations (hereafter MC) to extract our background estimations and to compare with our expected signal. All of our main MC samples used in this analysis come from the Top Group's MC generation. With the exception of the special hadron level jet reconstruction samples described in section 3.8, we used the inclusive TopNtuples files [11]. Table 3 gives the CDF specific sample name and its corresponding process. The only special consideration of note in terms of specific parameters used in generations is for our  $t\bar{t}$  production (data set: ytkt72) where we use a top mass of 172.5 GeV/c<sup>2</sup>.

The Alpgen+Pythia MC references Alpgen (v2) with Pythia added to hadronize the W or Z + n parton generation. The Alpgen generator is described in [12]. Although n partons (via CDF and the top groups generation [13]) generally correlates to final state with n (exclusive) jets

this is not always the case. For example, Pythia can produce additional jets. This combined with jet detector acceptance allows for both promotion and demotion of the number of detector level jets relative to the number of generator level partons.

There is a real and potential concern for Alpgen with Pythia to "double count" events especially if one is interested in combining the various W+#p samples together as a description for  $W+\geq n$  jets. Indeed this was an issue with a previous version of Alpgen (v1.3) which did not fully account for the potential for the overlapping phase space if the samples were naively added together with respect to potential non-physical bias between generator level "jets" and hadron level jets. However, this is no longer an issue as the current version incorporates MLM matching [12] between both levels during generation and thus avoids the potential to over count. The end result is that n partons (np) is matched at generator level to n jets (or  $\geq 4$  jets for 4p).

# 1.6 MC weighting to data

As will be explain in greater detail in chapter 4 we want to avoid biasing our background estimation with predictions from the MC. In particular this is a concern for our overall background estimation method when we want to account for our QCD (e.g. multijet) background which we derive from data and for which MC estimation is particularly poorly suited. We formally tackle this concerns in chapter 4 but this section provides the baseline weighting of the MC for the analysis.

In order to get the relative cross-sections correct for W+jets and Z+jets production and in order to directly estimate the contributions for WW, WZ,  $W\gamma^*$ , and  $t\bar{t}$ , we scale the MC by weighting each event by w given by

$$w = \frac{L_{\text{data}}}{L_{\text{eff}}} \tag{3}$$

with  $L_{\rm eff}$  being the effective luminosity defined as

$$L_{\text{eff}} = \frac{N(\text{Generated})}{\sigma(\text{MC})} \tag{4}$$

where  $L_{\text{data}}$  is the total luminosity (2826. pb<sup>-1</sup>; see section 1.2), N(Generated) is the number of events generated in the MC sample, and  $\sigma(\text{MC})$  is the MC or theory based cross-section. Obviously, this procedure does not effect the data which is not weighted ( $w \equiv 1$ ). The theoretical cross-section values for WW, WZ, and  $W\gamma^*$  are taken from [14] while we derive the  $t\bar{t}$  cross-section from [15]. Section 4.1 (page 82) will elaborate on the details of our actual diboson and  $t\bar{t}$  background estimation.

As explained in the previous section, we do not have samples that directly correspond to  $\geq n$  jets for W+jets and Z+jets rather we have samples MLM matched for 0-4 partons at the generator level of Alpgen+Phythia. In this case, we present the a priori weighting based on equation 3 but the overall scale will be reweighted based off our template fitting method described in section 4.4. Thus only the relative cross-section for each parton sample will matter. The MC generator level cross-section for the W+#p and Z+#p partons comes from the top MC generation page [11].

Table 4 shows the event weight (w) for each MC sample along with the appropriate cross-section  $(\sigma(\text{MC}))$ , and number of events generated (N(Generated)). Note that the  $W\gamma^*$  cross-section is effectively doubled (from 19.3 pb) to account for both  $W \to e\nu$  and  $W \to \mu\nu$ . The number of events in each  $W\gamma^*$  sample is 661901 and 688901 for the electron and muon channels, respectively.

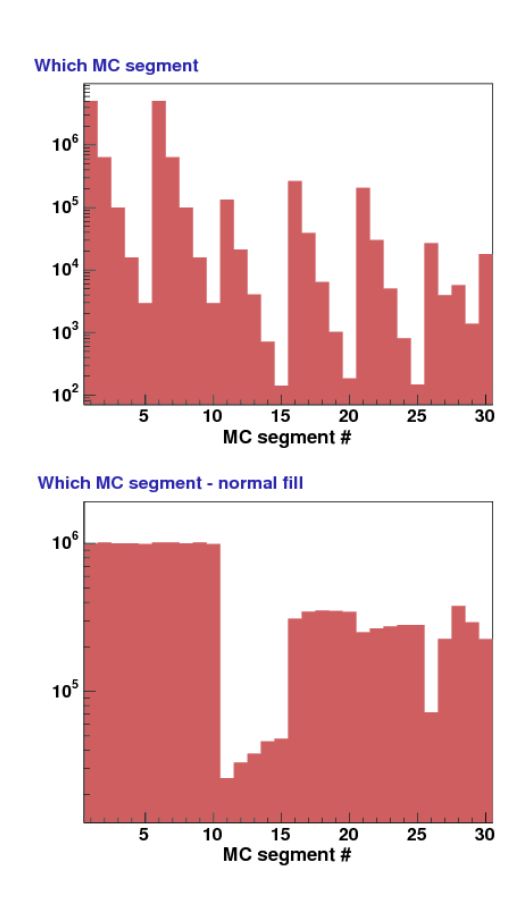


Figure 1: The bottom plot gives the number of events in each MC sample while the top gives the number of events relative to the luminosity via the weighting scheme given in equation 3. Note that for segments above 10 (non-signal MC) a simple filter has been applied to remove events that will clearly our selection (e.g. having a lepton with  $p_T > 10 \text{ GeV/c}$ . MC Segment # is given in table 4.

Dataset	MC Sample	Generator
ptop0w	$W \to e\nu + 0p$	Alpgen
ptop1w	$W \to e\nu + 1p$	Alpgen
ptop2w	$W \to e\nu + 2p$	Alpgen
ptop3w	$W \to e\nu + 3p$	Alpgen
ptop4w	$W \to e\nu + 4p$	Alpgen
ptop5w	$W \to \mu\nu + 0p$	Alpgen
ptop6w	$W \to \mu\nu + 1p$	Alpgen
ptop7w	$W \to \mu\nu + 2p$	Alpgen
ptop8w	$W \to \mu\nu + 3p$	Alpgen
ptop9w	$W \to \mu\nu + 4p$	Alpgen
utop0w	$W \to \tau \nu + 0 \mathrm{p}$	Alpgen
utop1w	$W \to \tau \nu + 1 \mathrm{p}$	Alpgen
utop2w	$W \to \tau \nu + 2p$	Alpgen
utop3w	$W \to \tau \nu + 3p$	Alpgen
utop4w	$W \to \tau \nu + 4p$	Alpgen
ztop0p	$Z \rightarrow ee + 0p$	Alpgen
ztop1p	$Z \rightarrow ee + 1p$	Alpgen
ztop2p	$Z \rightarrow ee + 2p$	Alpgen
ztop3p	$Z \rightarrow ee + 3p$	Alpgen
ztop4p	$Z \rightarrow ee + 4p$	Alpgen
ztop5p	$Z \to \mu\mu + 0p$	Alpgen
ztop6p	$Z \to \mu\mu + 1p$	Alpgen
ztop7p	$Z \to \mu\mu + 2p$	Alpgen
ztop8p	$Z \to \mu\mu + 3p$	Alpgen
ztop9p	$Z \to \mu\mu + 4p$	Alpgen
ztopt0	$Z \to \tau \tau + 0$ p	Alpgen
ytkt72	${ m t} { m ar t}$	Pythia
itopww	WW	Pythia
itopwz	WZ	Pythia
rewk28	$W(\to e\nu)\gamma^*$	Baur
rewk29	$W(\to \mu\nu)\gamma^*$	Baur

Table 3: The table gives the dataset name of MC samples used, their generator, and their corresponding physical processes. All samples are inclusive (no special filtering) and come from the Top MC page [11]. Standalone Pythia samples come from version 6.216 while Alpgen samples come from v2.10. In addition, the Alpgen generator also includes Pythia (v6.325) for showering and is often denoted by "Alpgen+Pythia". The number of events as well as the appropriate theoretical or MC generator based cross-section for weighting is given in table 4 and described in section 1.6. The ytkt72 ( $t\bar{t}$ ) sample was generated using a top mass of 172.5 GeV/ $c^2$ .

Segment #	MC Sample	$\sigma(MC/Theory)$ (pb)	N(Generated)	weight (w)
1	$W \to e\nu + 0p$	1800	997474	5.100
2	$W \to e \nu + 1 \mathrm{p}$	225	1013373	0.627
3	$W \to e \nu + 2 \mathrm{p}$	35.4	1003193	0.100
4	$W \to e \nu + 3 \mathrm{p}$	5.6	1003040	0.016
5	$W \to e \nu + 4 \mathrm{p}$	1.03	989607	0.003
6	$W \to \mu\nu + 0p$	1800	1013373	5.020
7	$W \to \mu \nu + 1 \mathrm{p}$	225	1013373	0.627
8	$W \to \mu \nu + 2p$	35.4	1002804	0.100
9	$W \to \mu \nu + 3p$	5.6	1013373	0.016
10	$W \to \mu \nu + 4 \mathrm{p}$	1.03	988545	0.003
11	$W \to \tau \nu + 0 \mathrm{p}$	1800	952876	5.338
12	$W \to \tau \nu + 1 \mathrm{p}$	225	965219	0.659
13	$W \to \tau \nu + 2p$	35.4	923989	0.108
14	$W \to \tau \nu + 3p$	5.6	1008221	0.016
15	$W \to \tau \nu + 4 \mathrm{p}$	1.03	986494	0.003
16	$Z \rightarrow ee + 0p$	158	513779	0.869
17	$Z \rightarrow ee{+1}{\rm p}$	21.6	536159	0.114
18	$Z \rightarrow ee{+}2\mathrm{p}$	3.47	536159	0.018
19	$Z \rightarrow ee{+}3\mathrm{p}$	0.55	528491	0.003
20	$Z \to ee{+4}{\rm p}$	0.0992	525065	0.001
21	$Z \to \mu\mu + 0p$	158	536159	0.833
22	$Z \to \mu \mu + 1 \mathrm{p}$	21.6	536159	0.114
23	$Z \to \mu \mu + 2p$	3.47	530843	0.018
24	$Z  o \mu \mu + 3 \mathrm{p}$	0.55	536159	0.003
25	$Z \to \mu \mu + 4 \mathrm{p}$	0.0992	536159	0.001
26	$Z \to \tau \tau + 0$ p	158	1170084	0.382
27	${ m t} \overline{ m t}$	7.5	1186128	0.018
28	WW	12.4	2284862	0.015
29	WZ	3.96	2340145	0.005
30	$W\gamma^*$	38.6	1350802	0.081

Table 4: Default MC weighting for each MC sample

# 2 W selection

The selection of the W boson candidate events is straight forward. We select high momentum electrons and muons which pass the standard "tight" central lepton cuts along with some additional analysis specific requirements. Using the transverse energy or momentum of the selected lepton (electron  $E_T$  and muon  $p_T$ , respectively) and the missing transverse energy ( $\not\!\!E_T$ ) of the event (representing the energy lost from the non-interacting neutrino), we reconstruct the W transverse mass  $(M_T)$  which we use as our final selection cut. In the next chapter, we define our jet selection and this will end up putting further constraints on our final W selection as will be explained in detail there.

The next section of this chapter deals with the electron selection while section 2.3 gives the selection criteria for the muons. Following each respective section we present the requirements of a sample that will be used to estimate our QCD background (from multi-jet fakes, etc.). This sample is defined by inverting certain selection cuts and will be denoted as our *anti-selected* lepton requirements. Sections 2.2 and 2.4 deal with our anti-selected electron and muon selection, respectively.

Our selection procedure produces events where we may have multiple candidates. Section 2.5 deals with event level veto on events with dileptons or otherwise characteristic of Z-like production. As a preamble to our W selection, we define our missing energy procedure in section 2.6. In the final section, we describe our W selection (for both electrons and muons) based off of our reconstructed W transverse mass.

#### 2.1 Electron selection

Electron candidate events are selected based on a high  $E_T$  requirement for central electromagnetic (CEM) object along with a series of quality and identification (ID) cuts in addition to basic fiducial and tracking constraints. In the CDF nomenclature these will be "tight electrons" [17] with a few additions mentioned below. Unlike the muons, there is only one equivalent (sub-)detector classification for electrons; namely the central calorimeter. We do not use more forward electrons (plug-electrons) in this analysis. We will simply refer to electron related quantities (for their acceptance, efficiencies, etc.) as CEM. Table 5 summaries our tight selection cuts.

The first non-standard lepton selection cut is our  $|\Delta z_{vtx}| < 2.0$  cm requirement. The motivation for this cut is to veto events where the lepton's vertex information was not well understood. The form the cut takes is similar to the  $|z_+ - z_-| < 4.0$  cm constraint on (opposite-sign) dileptons such as the  $Z \to \ell^+ \ell^-$  production. We define  $\Delta z_{vtx}$  as the separation between the leptons vertex position  $(z_0)$  and the closest (best) quality 12 vertex with  $\sum p_T^{vtx} > 10$  GeV/c or

$$\Delta z_{vtx} \equiv |z_0 - z_{vtx}| \tag{5}$$

Functionally, we loop over the zvtxs collection with the standard vertex quality check along with a sum vertex (track) momentum cut. At the level our implementation, this cut enforces our lower side # vertices  $\geq 1$  cut which is simply a check that the lepton vertex information

Selection Cut	Notes and Details
Fiducial CEM electron	
$ \eta  \le 1.1$	
$ z_0  \le 60. \text{ cm}$	
$ z_0 - z_{vtx}  \le 2.0 \text{ cm}$	$z_{vtx}$ closest vertex
$1 \le \# \text{ vertices} \le 3$	quality 12 vertices with $p_T > 10 \text{ GeV/c}$
Conversion Veto	not a conversion
$E_T \ge 20 \text{ GeV}$	calorimeter based $E_T$
$p_T \ge 10 \text{ GeV/c}$	track based $p_T$
$(E_{HAD}/E_{EM}) \le 0.055 + 0.00045E$	$E = E_{EM} + E_{HAD}$
$L_{\rm shr} \leq 0.2$	
$E/p \le 2.0 \text{ or } p_T \ge 50 \text{ GeV/c}$	
$-3.0 \le q\Delta x \le 1.5 \text{ cm}$	q = electron charge
$ \Delta z  \le 3.0 \text{ cm}$	
$\chi^2_{\rm strip} \le 10.$	
# COT Axial Segments $\geq 3$	with $\geq 5$ hits/segment
# COT Stereo Segments $\geq 2$	with $\geq 5$ hits/segment
(Relative) Isolation $\leq 0.1$	isolation with $R = 0.4$

Table 5: Electron selection requirements

matches to a good vertex. Section 4.6 on page 123 deals with our vertex definition and related particulars as it applies to our reweight of the number of vertices in the MC. We give the full motivation for our # vertices  $\leq 3$  cut there but the basic concept is to reduce the number of additional interactions in the event to control for promotion. As will be noted in full in our acceptance chapter, the acceptance is about 95% and does not show a dependence on jet multiplicity. In addition to using this  $\Delta z_{vtx}$  cut for electrons we apply it to muons as noted in section 2.3. We show the distribution (using the muon channel) in figure 2.

#### 2.2 Anti-selected Electrons

In this section we introduce a separate set of cut requirements that will allow us to build a sample that will be used to estimate our QCD/fake background. We call this sample our "anti-selected electrons" as they are comprised of events from our same high  $p_T$  trigger data sample that necessarily were not selected in the analysis but are informative of the behavior of non-W events. The sample will be composed of potential electron candidates which pass our basic kinematic/acceptance requirements but are likely fakes due to failing some of our identification requirements. This anti-selection electron sample becomes the bases for our QCD template explained in section 4.3 on page 84.

The previous version of this analysis was the vanguard of this procedure where the nomenclature of these candidates were called "anti-electrons" [1]. We note that several of our plots will make reference to this older and somewhat imprecise descriptor for convenience. This is more of an issue on our anti-selected muons (see section 2.4) where "anti-muon" could be confusing.

The selection criteria for our anti-selected electrons mirrors the selection requirements of the previous section. The difference is that several of the electron quality/identification cuts are allowed to be inverted. We require two or more of the cuts in table 6 to fail our normal selection cut. In other words, these anti-selected candidates must pass two (or more) of our inverted selection requirements. Consistent with finding of the previous analysis, we do not use the calorimeter based isolation requirement nor the E/p ratio to minimize potential bias in measuring our final jet kinematics.

Inverted Selection Cut	Notes and Details
$ z_0 - z_{vtx}  > 2.0 \text{ cm}$	$z_{vtx}$ closest vertex
$(E_{HAD}/E_{EM}) > 0.055 + 0.00045E$	$E = E_{EM} + E_{HAD}$
$L_{\rm shr} > 0.2$	
$\chi^2_{\rm strip} > 10.$	
$q\Delta x < -3.0 \text{ or } q\Delta x > 1.5 \text{ cm}$	CES $\Delta x$ , $q = \text{charge}$
$ \Delta z  > 3.0 \text{ cm}$	$CES \Delta z$

Table 6: Anti-selection electron candidates must pass two of the listed "inverted" cuts.

Events which pass our anti-selection cuts are subject to the same constraints as our normal W candidate events. As such, they undergo the same Z-veto procedure of section 2.5 as well as the transverse mass cutting scheme of section 2.7. They will also need to pass the same lepton-jet requirements but with several important caveats (e.g. section 3.3). We present the composition of our anti-selected sample ( $M_T > 20 \text{ GeV/c}^2$ ) in table 7. We have approximately 358k events in the total inclusive  $\geq 0$  jet bin and 600 in the inclusive  $\geq 4$  jet bin.

Inverted Cut	# of events	Relative
Variable	(in data)	Fraction (%)
HAD/EM	196582	54.9
CES $\Delta x$	100149	28.0
CES $\Delta z$	106938	29.9
$L_{ m shr}$	213848	59.7
$\chi^2_{ m strip}$	281185	78.5
$\Delta z_{vtx}$	16360	4.5
Total	358204	100.

Table 7: The composition of anti-selection electron candidates with  $M_T > 20 \text{ GeV/c}^2$ . Anti-selection electrons must fail two (or more) cuts of table 6 but pass the remaining lepton and W selection criteria modulo additional constraints due to jet selection. The relative fraction is the fraction of events that pass the inverted cut (i.e. fail the nominal lepton candidate selection cut).

#### 2.3 Muon selection

Our muon selection proceeds as follows. We select events by requiring a high transverse momentum track matched to a muon stub in the central muon detectors. These muon candidate

events then have to pass additional tracking requirements and have their own set of identification cuts. The latter are based on the amount of energy (absolute and relative) deposited in the calorimeter which is expected to be small for minimally ionizing particles (i.e. muons). Like our electron selection, our final muon selection is a "tight muon" [18] with a couple of additional constraints.

Whereas our candidate electrons are constructed via a universal selection of the central calorimeter (CEM), central muons are divided up into three sub-detectors which we will denote as CMUP, CMX-Arch, and CMX-Mini. A CMUP muon is formed using the stub information for both the CMU (Central MUon) and CMP (Central Muon uPgrade) detectors [19]. We do not use the exclusive CMU or CMP muon definitions in this analysis. However, some cuts (notably the stub minus tracking location in local x,  $\Delta x$ ) require specific detector. The detector coverage for CMU/CMP and therefore the range of our selected CMUP muons is approximately  $|\eta| < 0.6$  representing the central most selection of our muon sample.

The CMX (Central Muon eXtension) detector [19] is further sub-divided into the CMX arches, keystone, and miniskirts. The difference between the CMX divisions is primarily due to their coverage as well as historical details about their commissioning. A historical note giving details on using CMX muons is given in [20]. In our analysis CMX-Arch or simply Arches will represent the CMX arches and keystone while CMX-Mini will signify CMX miniskirt muons. In many cases, such as the selection cuts presented in this section, a CMX muon will represent the obvious union between CMX-Arch and CMX-Mini. True to its name, the CMX extends coverage out to approximately  $0.6 < |\eta| < 1.0$  although the azimuthal angle  $(\phi)$  coverage is not complete  $(300^{\circ}\text{east} \text{ and } 330^{\circ}\text{west})$ .

For our purposes here we note that for many considerations of the analysis we will have to deal with each sub-detector individually. For example, our acceptance and efficiencies calculations require this sub-dividing while our selected muon events from data and MC (after their respective detector dependent cuts) are simply pooled together as candidate muon events. Table 8 presents our selection requirements for CMUP and CMX muons. As needed, the type of muon cut required (CMUP and CMX) will be noted in the *Notes and Details* column.

The muon COT exit radius ( $\rho$ ) requirement is taken with the COT length ( $z_{\text{COT}}$ ) from the origin as 155 cm [21]. The formula for  $\rho$  is given by

$$\rho_{\eta \geq 0} \equiv \frac{\pm (z_{\text{COT}} \mp z_0)}{\tan\left(\frac{\pi}{2} - \theta\right)} \tag{6}$$

where  $\theta$  is the zenith angle of the muon in radians and the plus or minus signs correspond, respectively, for  $\eta \geq 0$ .

The  $\Delta z = |z_0 - z_{vtx}|$  requirement is the same as described in our electron section. We also apply the same vertex requirements as noted in the table. Its discrimination power in data for muons is a bit stronger due to the nature of potential fakes and is 98% efficient on signal with no significant correlation with jet multiplicity.

The  $\chi^2_{\text{COT}}$  is an additional lepton requirement for our muon selection beyond the normal tight muon cuts. It is a track based cut representing the reduced goodness of fit measure via the COT tracking information. This cut was suggested by colleagues and used in several analysises

Selection Cut	Notes and Details
Cosmic Veto	COT out of time veto
Muon Fiducial to CMU	for CMUP muons
Muon Fiducial to CMP	for CMUP muons
Muon Fiducial to CMX	for CMX muons
$\rho(\eta, z_0) \le 140 \text{ cm}$	COT exit radius cut for CMX muons
$ z_0  < 60.$ cm	
$ z_0 - z_{vtx}  < 2.0 \text{ cm}$	$z_{vtx}$ closest vertex
$1 \le \# \text{ vertices} \le 3$	quality 12 vertices with $p_T > 10 \text{ GeV/c}$
$p_T \ge 20 \text{ GeV/c}$	track based $p_T$
$ \Delta x_{CMU}  < 7.0 \text{ cm}$	CMU stub/track match
$ \Delta x_{CMP}  < 5.0 \text{ cm}$	CMP stub/track match
$ \Delta x_{CMX}  < 6.0 \text{ cm}$	CMX stub/track match
# COT Axial Segments $\geq 3$	with $\geq 5$ hits/segment
$\#$ COT Stereo Segments $\geq 2$	with $\geq 5$ hits/segment
$ d_0  \le 0.20$	no silicon hits
$ d_0  \le 0.02$	with silicon hits
$\chi^2_{\rm COT} < 2.75$	for run $\# \le 186598 \ (data \ only)$
$\chi^{2}_{\rm COT} < 2.30$	for run $\# > 186598 \ (data \ only)$
$E_{EM} \le \text{MAX}[2, 2+0.0115 \times (p - 100)]$	track based $p$
$E_{HAD} \le \text{MAX}[6, 6+0.0280 \times (p-100)]$	track based $p$
(Relative) Isolation $< 0.1$	isolation with $R = 0.4$

Table 8: CMUP and CMX Muon selection requirements

at CDF [22][23][24]. The discussion of this cut and its efficiency for intermediate (5 <  $p_T$  < 20 GeV/c) muons in [25] was also instructive. We note that the reduced COT  $\chi^2$  cut is run dependent and is applied only to the data consistent with [22][23]. Although this is likely an artifact of our tracking simulation and/or the details of the  $\chi^2_{\rm COT}$  calculation, the cut, if applied to our signal MC, would be fully efficient. The  $\chi^2_{\rm COT}$  distribution after the basic selection criteria given here but without our final W selection of section 2.7 is shown in figure 3.

# 2.4 Anti-selected Muons

As was the case with our electron sample we mirror our muon channel W selection with an anti-selected muon sample described here. The basic kinematic selection criteria is the same but we look for events that pass at least two of the inverted cuts as noted in table 9 with additional details to follow. The relative composition of our anti-selected muon pre-template is given in table 10.

It is instructive to divide the 6 quality/ID cuts into two classifications. First there are calorimeter/energy base cuts which include the isolation (ISO), EM, and HAD variables. These are the equivalent of the majority of the anti-selection electron quality/ID cuts and are characteristic of our multi-jet background as well as punch-throughs. The second triplet of cuts are

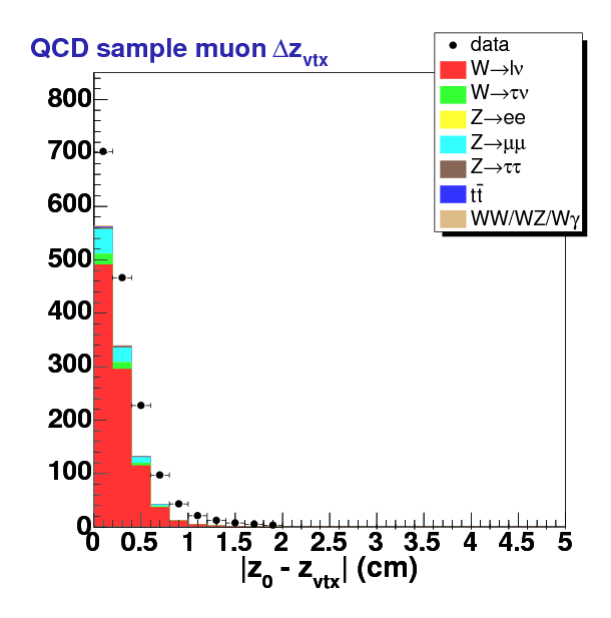


Figure 2:  $\Delta z_{vtx}$  (as defined in equation 5) used in our lepton selection (muon channel results shown). The cut at 2.0 cm is highly efficient with our signal MC and rejects potential fakes where  $\Delta z_{vtx}$  becomes flat in the data pass our cut.

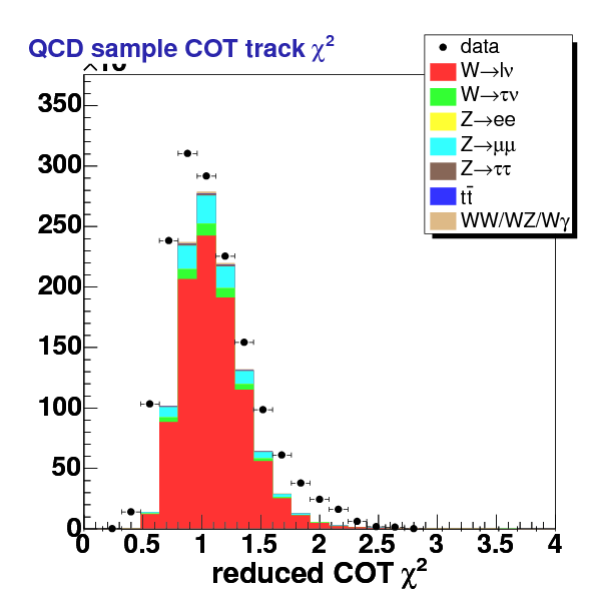


Figure 3:  $\chi^2_{\rm COT}$  is the per-degree-freedom  $\chi^2$  (COT) tracking quality of fit variable with our basic muon sample selection.

track/stub/vertex based using the  $\chi^2_{\text{COT}}$ ,  $\Delta z_{vtx}$ , and  $\Delta x$  variables. The latter set of inverted cuts is particularly descriptive of decays in flight as well as semi-leptonic decays. Note that the anti-selection muon candidates here form a single QCD template as noted in section 4.3. In other words, like our anti-selection electron sample we combine all the cuts together and do not try to separately account for different types of fakes.

Inverted Selection Cut	Notes and Details
$ z_0 - z_{vtx}  > 2.0 \text{ cm}$	$z_{vtx}$ closest vertex
$7.0 < \Delta x_{\rm CMU} < 14.0 \text{ cm}$	
$5.0 < \Delta x_{\rm CMP} < 13.0 \ {\rm cm}$	
$6.0 < \Delta x_{\rm CMX} < 12.0 \text{ cm}$	
$\chi^2_{ m COT} > 2.75$	for run $\# \le 186598$
$\chi^2_{\mathrm{COT}} > 2.30$	for run $\# > 186598$
$2 < E_{EM} < 20 \text{ GeV}$	
$6 < E_{HAD} < 60 \text{ GeV}$	
0.1 < Isolation < 0.67	isolation with $R = 0.4$

Table 9: Anti-selection muon candidates must pass two of the listed "inverted" cuts.

With our  $\Delta x$  cuts we decided to look at the shape of MC simulation and a sample of muon candidates without the stub-track cut in addition to our prospective anti-selection sample. We found these distributions (pass their respective nominal detector based  $\Delta x$  cut) were composed of a flat distribution that extended pass twice the normal cut and a tail consistent with our MC and quality data sample. Our upper bound anti-selection cut (as given in table 9) represent the cut off when the natural tail events where the stub and track were in all likely hood actually linked was dominated by the flat (random/uniform)  $\Delta x$  component.

The  $\Delta x$  cut for a CMUP muon counts as a single inverted cut. In our normal CMUP muon selection we require both the CMU and CMP  $\Delta x$  cuts to pass so when we invert it we only need one cut to fail the CMUP  $\Delta x$  criteria (i.e. we follow De Morgan's law). We originally had a much tighter CMU cut (3 cm verses 7 cm) but loosening the cut had no effect on the anti-selected muon sample size but effectively increased our signal acceptance and efficiency [26].

The energy based variables ( $E_{EM}$ ,  $E_{HAD}$ , and isolation) as well as our  $\Delta x$  have upper bounds on their inverted cuts. The former triplet is based on scaling the nominal (inverted) bound by a factor of 5. The basic feature of these observables is that they have long tails (see for example figures 4 and 5) for potential muon fakes. As one would expect cutting on isolation immediately limits the EM and HAD observables (they are efficient cuts given isolation).

Like our anti-selection electrons, events which pass our anti-selection muon cuts are subject to the same constraints as our normal W candidate events. As such, they undergo the same Z-veto procedure of section 2.5 as well as the transverse mass cutting scheme of section 2.7. They will also need to pass the same lepton-jet requirements but with several important caveats (e.g. section 3.3). We present the composition of our anti-selected sample ( $M_T > 20 \text{ GeV/c}^2$ ) in table 10. We have approximately 438k events in the total inclusive  $\geq 0$  jet bin and about 3200 in the inclusive  $\geq 4$  jet bin.

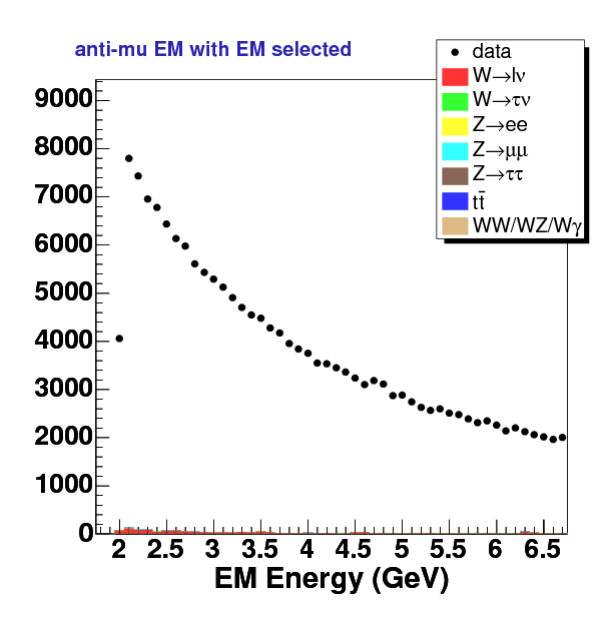


Figure 4: EM energy  $(E_{EM})$  associated with the linked calorimeter towers for an anti-selected muon sample with  $E_{EM} > 2.0 \text{ GeV}$ .

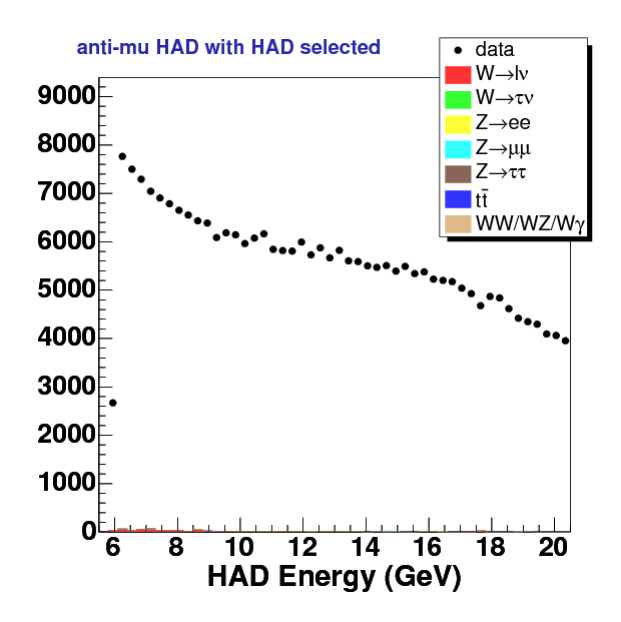


Figure 5: HAD energy  $(E_{HAD})$  associated with the linked calorimeter towers for an anti-selected muon sample with  $E_{HAD} > 6.0$  GeV.

Inverted Cut	# of events	Relative
Variable	(in data)	Fraction (%)
$\Delta x$	31318	7.2
$\Delta z_{vtx}$	64346	14.7
$\chi^2_{\rm COT}$	102289	23.3
$E_{EM}$	161756	37.0
$E_{HAD}$	259853	59.4
Isolation	397882	90.9
Total	437605	100.

Table 10: The composition of anti-selection muon candidates with  $M_T > 20 \text{ GeV/c}^2$ . Anti-selection muon must fail two (or more) cuts of table 9 but pass the remaining lepton and W selection criteria modulo additional constraints due to jet selection. The relative fraction is the fraction of events that pass the inverted cut (i.e. fail the nominal lepton candidate selection cut).

### **2.5** Z Veto

Events which have two or more selected leptons are vetoed as these are clearly not representative of our expected W signal. This is done regardless of the charge, dilepton mass, or electron/muon combination. The same procedure is carried out in our anti-selected lepton events with the equivalent motivation to produce representative W fakes. This procedure alone vetoes some 87k multi-lepton events most of which are likely Z decays as confirmed from our Z MC. The veto also removes obvious diboson candidates.

In addition, we look for Z production in the mass window of  $m_Z = 76\text{-}106 \text{ GeV/c}^2$  via two additional selection methods. First we look as lose lepton requirements as defined in table 11. The second method involves looking at the track collection and performing a similar simple selection as outlined in table 12. Once we have a selected (or anti-selected) lepton we loop through the other potential candidates in our lepton and track collections. If a opposite signed candidate spotted passing the prerequisite cuts and inside our mass window, we veto the event. There are over 123k events vetoed in this way with 80% coming from our additional lepton selection verses the 20% acquired via our track based veto method.

Electron	Muon	
$E_T > 10 \text{ GeV}$	$p_T > 10 \text{ GeV/c}$	
HAD/EM < 0.12	EM < 3  GeV	
·	HAD < 9  GeV	
Isolation $< 0.15$	Isolation $< 0.15$	

Table 11: Summary of lepton cuts use to veto potential Z and other non-single W decays. If an additional opposite signed lepton if found that passes the above cuts and has dilepton mass between 76 and 106  $\text{GeV/c}^2$  the event is vetoed.

Track Requirement	Notes and details	
# COT Axial Segments $\geq 3$	with $\geq 5$ hits/segment	
# COT Stereo Segments $\geq 2$	with $\geq 5$ hits/segment	
$p_T > 10 \text{ GeV/c}$	beam constrained track $p_T$	
$ z_0 - z_{\rm trk} $ ; 10 cm	lepton vs. track $z$	
Absolute Isolation $< 4 \text{ GeV}$	$p_T \times \text{Isolation}$	

Table 12: Summary of track based cuts use to veto potential Z and other non-single W decays. If an additional opposite signed track if found that passes the above cuts and has dilepton mass between 76 and 106 GeV/c<sup>2</sup> the event is vetoed.

# 2.6 Missing Energy Corrections (muons)

The procedure for calculating the missing transverse momentum  $(\not\!E_T)$  begins by calculating a vector sum over all calorimeter towers. Let  $\vec{E}_{\rm EM}^{\ \eta,\phi}$  and  $\vec{E}_{\rm HAD}^{\ \eta,\phi}$  be the respective transverse EM and HAD energy associated with a calorimeter tower denoted by its  $\eta$ - $\phi$  location. The equation for the raw missing energy  $(\vec{E}_{\rm TAW}^{\rm raw})$  is given by

$$\vec{E}_{T}^{\text{raw}} \equiv -\sum_{\forall \text{ towers}} \left( \vec{E}_{\text{EM}}^{\eta,\phi} + \vec{E}_{\text{HAD}}^{\eta,\phi} \right) \tag{7}$$

which is simply the sum negation of the EM and HAD vector sum. However, equation 7 does not account for the transverse energies associated with minimum ionizing particles that can have a high (track-based) transverse momentum that leave little energy in the calorimeter (e.g. muons). As a result, we need to correct for the effect of muons. The initial correction is just to subtract the vector transverse momentum of the muon  $(\vec{p}_T^{\ \mu})$ . This is correct but since muons do leave some energy in the calorimeter and this feature will need to be addressed. To this end, let  $\vec{E}_{\rm EM}$  and  $\vec{E}_{\rm HAD}^{\ \mu}$  be the transverse EM and HAD energy in the tower(s) associated with the muon's calorimeter flight path. We effectively need to add back in the calorimeter based energy associated with the muon. Thus the muon corrected  $\vec{E}_T$  is given by

$$\vec{E}_T = \vec{E}_T^{\text{raw}} - \left( \vec{p}_T^{\ \mu} - \vec{E}_{\text{EM}}^{\ \mu} - \vec{E}_{\text{HAD}}^{\ \mu} \right) \tag{8}$$

From equation 8 we have the  $\hat{\mathbf{x}}$  and  $\hat{\mathbf{y}}$  components of the missing energy. Trivially we can derive  $\not\!\!E_T = | \not\!\!E_T |$  and note the corresponding  $\phi$  variable. For convenience, the direction of the  $\not\!\!E_T$  can be noted by the neutrino symbol  $(\nu)$ . For example,  $\Delta\phi(\mu,\nu)$  is the difference in azimuthal angles for the muon and the missing energy.

There are a few additional details to this procedure. The  $E_T$  is corrected for all detector (fiducial) defined muons (e.g. CMUP, CMX, BMU, etc.) as well as stubless muons (CMIOs) [27]. No additional constraint is applied to detector muons; if they are in the collection they will contribute to the event's  $E_T$ . Stubless muons need to pass three cuts[28] in order to contribute to the corrected missing energy:

• 
$$p_T > 10 \text{ GeV/c}$$

- EM < 3 GeV
- HAD < 9 GeV

We can naturally extend equation 8 to multiple muons:

$$\vec{E}_T = \vec{E}_T^{\text{raw}} - \sum_{\forall \mu} \left( \vec{p}_T^{\mu} - \vec{E}_{\text{EM}}^{\mu} - \vec{E}_{\text{HAD}}^{\mu} \right) \tag{9}$$

Note that we will need to modify our missing transverse energy a final time when we account for our jet energy scale corrections (section 3.7).

### 2.7 W identification

Our final formal selection cut is to combine our selected lepton (electron/muon) with our missing energy (representative of the escaped neutrino) to form the mass of candidate W. With this we can require this to be large enough to reject a significant fraction of the background while accepting the signal. However, due to the limitations of measuring the missing energy we cannot fully reconstruct the mass and instead calculate the transverse mass,  $M_T$ , by effectively ignoring the z information in our momentum as well as our energy measurement. Via the equivalent "3-vector" calculation  $M_T$  is given by

$$M_T = 2\sqrt{\left(p_T^{\ell} \not\!\!E_T\right)} \sin\left(\frac{\Delta\phi(\ell,\nu)}{2}\right) \tag{10}$$

where  $\Delta\phi(\ell,\nu)$  is the difference in the respective azimuth angles of the charged lepton  $(\ell)$  and  $\not\!\!E_T$  ( $\nu$ ) and  $p_T^\ell$  is the  $E_T$  of the electron or the  $p_T$  of the muon. We note that both  $p_T^\ell$  and  $\not\!\!E_T$  peak around 39 GeV in signal  $W \to \ell \nu$  MC which suggests (for a back-to-back decay) a transverse mass around 76 GeV/ $c^2$ .

We have an additional goal and function for our transverse mass cut; we want to select a set of events with a loser requirement to aid in our background estimation. The full details of our background estimation will be dealt with in chapter 4. For now we note that this selection will be referred to as our pre-W sample. We will allow in larger fractions of Zs and QCD backgrounds at the lower values of  $M_T$  and then use this sample to fit for our (jet multiplicity dependent) backgrounds where we do not have an a priori cross-section knowledge.

For our pre-W sample we apply a  $M_T > 20 \text{ GeV/c}^2$  cut to both electron and muon samples. For clarity we will explicitly note this pre-final selection sample via " $W \to \ell \nu$  with  $M_T > 20 \text{ GeV/c}^2$ " when presenting results (i.e. tables and figures). Our final selection cut for our proper W candidate sample is  $M_T \ge 40 \text{ GeV/c}^2$  for the electron sample and  $M_T \ge 30 \text{ GeV/c}^2$  for the muon sample. The harder cut is required for the electrons due to the QCD background being larger whereas we gain a bit more acceptance with the cleaner muon sample. We present the  $M_T$  distribution for  $W \to \ell \nu + \ge 1$  jets with  $M_T > 20 \text{ GeV/c}^2$  in figures 6 (electrons) and 7 (muons). Both of these figures are presented without undergoing our formal background estimation procedure of section 4.4 (page 90) and as such do not have a formal QCD estimation nor are the W and Z MC modified away from our default weighting scheme of section 1.6.

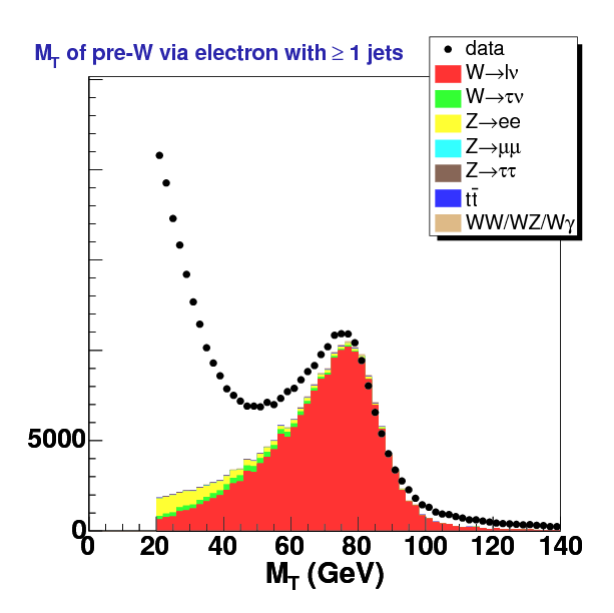


Figure 6: Transverse Mass  $(M_T)$  for  $W \to e\nu + \ge 1$  jets with  $M_T > 20$  GeV/c<sup>2</sup>. We are applying the raw MC weights for our  $W \to \ell\nu$  and  $Z \to \ell\ell$  MC and have not introduced our QCD estimation.

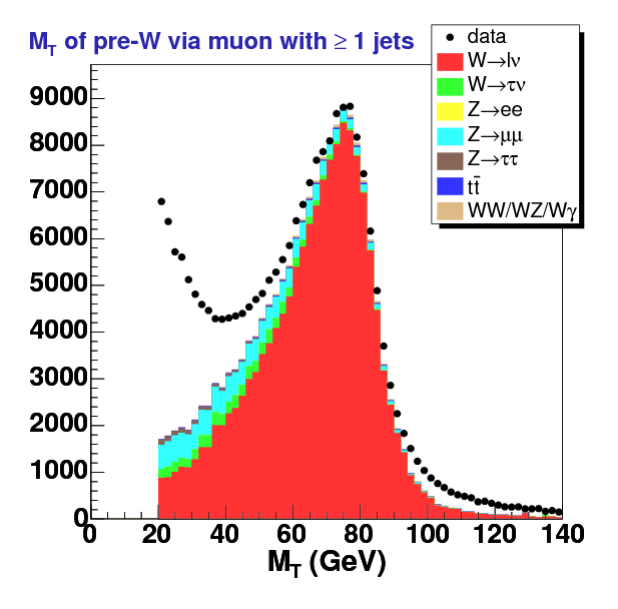


Figure 7: Transverse Mass  $(M_T)$  for  $W \to \mu\nu + \geq 1$  jets with  $M_T > 20 \text{ GeV/c}^2$ . We are applying the raw MC weights for our  $W \to \ell\nu$  and  $Z \to \ell\ell$  MC and have not introduced our QCD estimation.

The other lepton/W related selection cuts relate to our jet selection. Section 3.4 (page 28) deals with our separation veto which is enforced to remove potential bias for our final jet observables. In section 3.5 (page 28) we deal with an additional cut designed to reduce our QCD and improve overall background agreement. Formally in the analysis we assign these additional jet related requirements to our analysis before preceding to form our pre-W and final W samples via the final, respective,  $M_T$  selection cut.

# 3 Jet definition and selection

The previous chapter dealt with our W selection procedure but this is only gets us halfway to the various observables we wish to finally measure. Now that we have preferentially selected events with high momentum transfer, we discuss our classification, corrections, and concerns with respect to jets. We present our definition of jets in the next section. In section 3.2 we quickly note the electron-jet removal procedure which leads into our general prescription for identify and removing lepton-jets which is required for our anti-selected leptons. This procedure and its motivation are described in section 3.3. We then explain our lepton-jet separation veto in section 3.4. In the case of our electron sample, we also apply an additional cut based off of the  $\Delta \phi$  between the electron and the vector jet momentum sum as explained in section 3.5. Next we discuss our general detector level jet energy corrections in section 3.6. Finally we explain our correction procedure to unfold our cross-section to the hadron level from our detector level measurement via the MC in section 3.8 and give the our results of said procedure in the last section, 3.9.

This chapter makes heavy use of  $\Delta R(a,b)$  which is a separation variable in terms of pseudorapidity  $(\eta)$  and the azimuthal angle  $(\phi)$  between objects a and b. For convenience, this will sometimes be denoted as simply as  $R_{ab}$  for cases like the dijet separation variable  $(R_{jj})$  where there is an established meaning. More generally, R can be used the  $\eta$ - $\phi$  angular area such as describing the jet cone radius. For object a let  $\eta_a$  be its pseudo-rapidity and  $\phi_a$  be its azimuthal angle and likewise for object b then

$$\Delta R(a,b) \equiv \sqrt{(\phi_a - \phi_b)^2 + (\eta_a - \eta_b)^2} \tag{11}$$

or

$$\Delta R(a,b) = \sqrt{(\Delta \phi(a,b))^2 + (\Delta \eta(a,b))^2}$$

where  $\Delta \phi(a, b)$  is always taken to be in the  $[0, \pi)$  domain.

#### 3.1 Jet definition

Jets are selected using the cone-based Midpoint algorithm using an  $\eta$ - $\phi$  radius of 0.4 (R = 0.4) [29]. The Midpoint jet definition was preferred above the use of JetClu which is more typical in other CDF analyses (e.g. all major top analyses).

Both JetClu and Midpoint are seed based cone algorithms. As such, they are not infrared or collinear safe to all orders in p-QCD. However, Midpoint is thought as an improvement as it places additional seeds at the mid-point between tower seeds and the center of groups of seeds [29]. Thus, theoretical concerns like infrared radiation via soft gluon emission are better handled. Seedless jet algorithms are generally too CPU intensive while Midpoint only adds the addition of the midpoint seeds verses the relatively fast JetClu.

In the TopNtuple the jet collection from which we derive our data/MC samples is called: MyTop\_MIDPOINTO.4\_LJ\_ReclusterJetColl and was jet collection type 6 up to and included period 17. Note that it is no longer in the jet list for the topNtuple for periods above 17.

In the analysis jets are defined with two cuts:

- $p_T > 20 \text{ GeV/c}$
- $|\eta| < 2.0$

The pseudo-rapidity cut was chosen based on the understanding of the detector and the reliability of describing jet energy corrections at forward rapidity. The  $p_T$  cut was also similarly selected with the additional advantage being that a higher momentum jet definition selects against the effect of additional interactions (see our discussion in section 4.6 with respect to this potential "promotion" background). We note that the jet transverse momentum cut, in addition to the other jet observables we reference, is always on the corrected jet energy variable as detailed in section 3.6.

To get a scale of the numbers we load in over 30 million jets via our jet collection in our high lepton  $p_T$  data samples. We end up accepting (passing our base cuts) more than 18 million. Note that jet acceptance is not directly used in our acceptance calculation (section 5.2); rather, the jet multiplicity (i.e. the inclusive number of jets in an event) tautologically defines our acceptance for each jet multiplicity.

# 3.2 Electron-Jet Reclustering/Removal

Physics level objects such as electrons and jets overlap in their definitions with respect to being a calorimeter based measurement. As such it is possible for an electron to fake a jet and vice versa. There are several electron identification (ID) variables which does a relatively efficient job of removing jets faking electrons though these are still the source of much of our QCD background via multi-jets. There are also handles on distinguishing reconstructed jet objects that are electrons (such as the EM fraction shown in figure 8) but these are not directly used in our jet selection. We define an *electron-jet* as a jet object that matches a selected electron. Clearly, we must formally deal with electron-jets in order to get a proper measurement.

In the process of forming the jet (i.e. jet objects) and electron (i.e. electron objects) collections in the topNtuple an algorithm is used to remove and correct for cases where a jet is matched to a tight electron (as defined in section 2.1). The algorithm removes the energy associated with the electron and then allows for jets to be reconstructed normally via the desired cone algorithm [30]. We did not directly investigate the electron-jet algorithm as this is a standard analysis tool but did look at cases where there where we had a high  $E_T$  electron that passes most of our selection cuts. Unsurprisingly we find the algorithm highly effective. For example, figure 9 shows the  $\eta$ - $\phi$  separation (denoted as  $\Delta R(e,j)$ ) between the electron (which has passed most of the standard electron requirements including isolation less than 0.10) and the nearest jet. The bottom plot of the figure also shows the behavior for muons which (not being calorimeter based) has no equivalent tight muon-jet removal process. A follow up plot of the same  $\Delta R(e,j)$  variable in figure 10 shows the performance of a straightforward electron-jet removal algorithm. The muon version of this plot just shows our lepton-jet separation cut/veto which is dealt with in section 3.4.

The electron-jet removal process (as apposed to the jet reclustering/removal scheme automatically done at the level of topNtuple production) is not formally needed when running our

normal W selection analysis procedure on our data and MC samples. However, an additional procedure will be needed for a special sample comprised of potential electron as well as muon channel fakes. These anti-selected leptons that need to be removed from the jet collection are discussed in the next section (3.3). This lepton-jet removal procedure will also be applied when discussing our hadron level corrections in section 3.8.

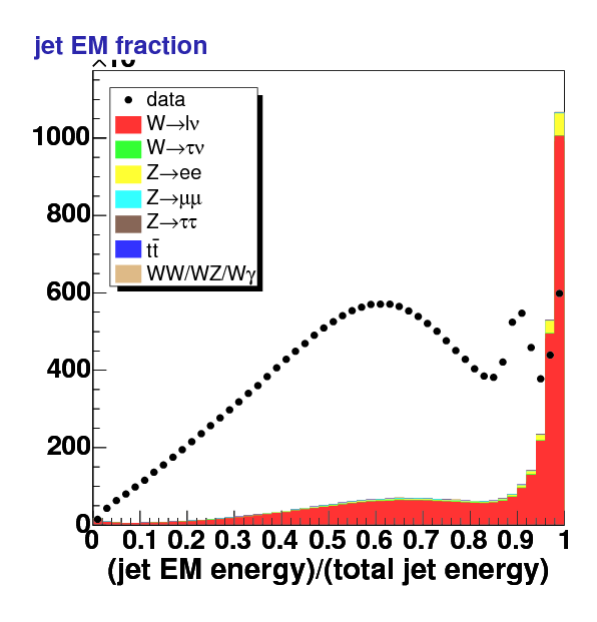


Figure 8: Jet EM fraction (defined as the fraction of EM calorimeter energy to the total energy) for all jets in all events. A component of the signal MC ( $W \to \ell \nu$ ) rapidly starts to peak starting at 0.9 with the maximum at the final bin. The vast majority of these "jets" are electrons that fail one or more of our tight electron cuts and are not de facto removed via the procedure of section 3.2.

# 3.3 Anti-selected Lepton-Jet removal

The previous section introduced the necessary complication in the electron channel that electrons and jets are expected to populate and potentially adversely effect each others collections. However, the tight electron removal and reclustering algorithm solves this problem. In this section, we turn to our anti-selected lepton samples which will serve as the basis for our QCD estimation as explained in chapter 4. We will need to manually remove the associated jets with our candidate electrons as well as the anti-selected muons. We begin by investigating cases where the anti-selected lepton is close to a jet before applying an additional lepton/jet separation veto which is the subject of the next section.

Figure 13 presents the  $\Delta R(\ell, j)$  between the anti-selected lepton and the nearest jet. It is analogous with the previous figure for candidate selected leptons (see figure 9) with the upper and lower plots representing the electron and muon channels, respectively. We given an additional pair of zoomed in plots of these distributions in figures 11 ( $\Delta R(e, j)$ ) and 12 ( $\Delta R(\mu, j)$ ) where

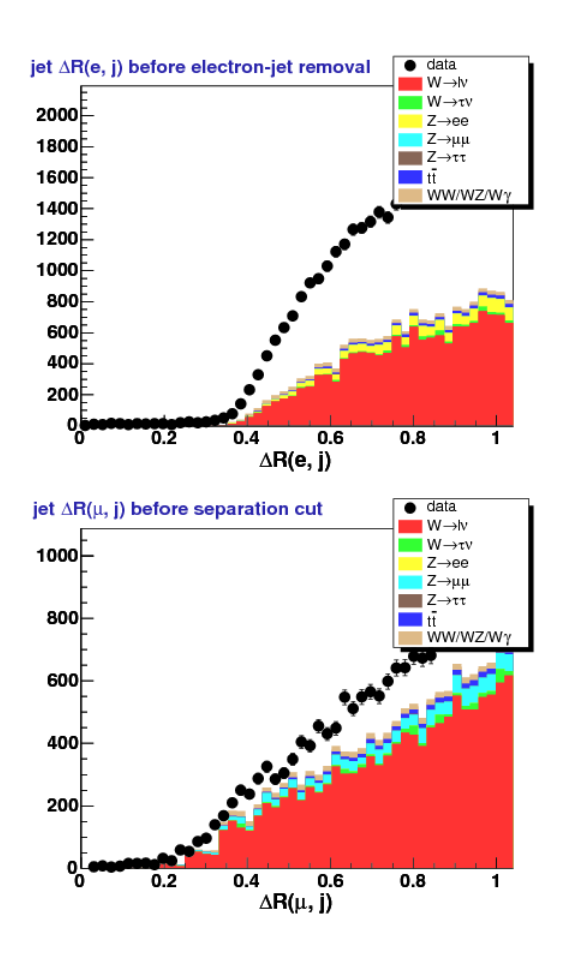


Figure 9:  $\eta$ - $\phi$  separation  $(\Delta R(\ell,j))$  between candidate lepton and closest jet. The top plot is for electrons while the bottom is reserved for muons. Leptons pass most of the standard W selection cuts and thus are negatively biased against colinear lepton/jet events. The electrons have the tight electron reculustering scheme applied which further reduces events within  $0.0 < \Delta R < 0.4$ . Muons have no such reclustering scheme.

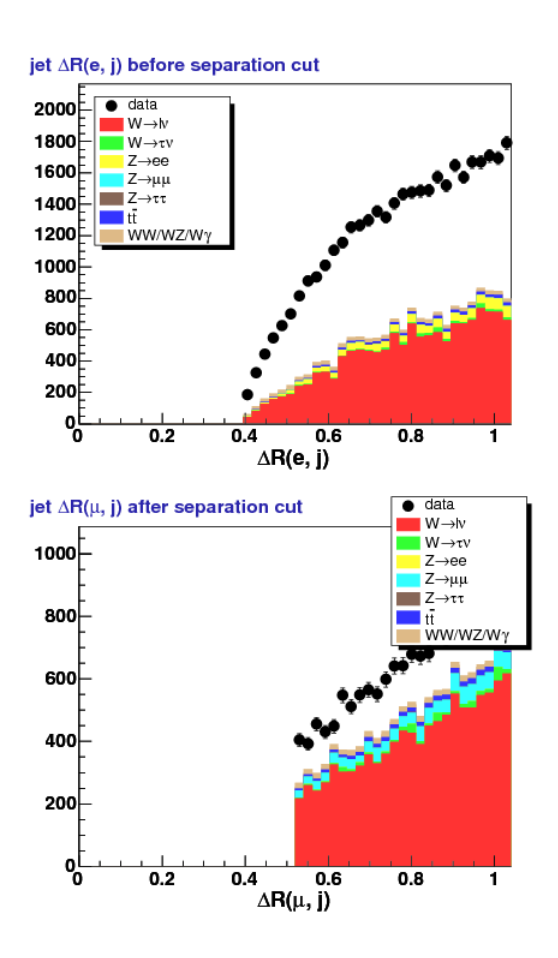


Figure 10:  $\eta$ - $\phi$  separation  $(\Delta R(\ell,j))$  between candidate lepton and closest jet. The top plot is for electrons while the bottom is reserved for muons. The lepton selection is the same as figure 9 but we skip jets that have been matched to the electron. The track based muons in the bottom plot simply have a  $\Delta R(\mu,j) < 0.52$  cut applied as per our discussion in section 3.4.

the range goes from  $\Delta R$ =0.00-0.24. Unlike in the previous section, the electron-jet is clearly not removed which is consistent with the electron necessarily failing at least two identification cuts (see section 2.2). Interestingly our anti-selected muon sample also shows the same tell-tale signature of a jet being very close to the muon object. Note that the events at low  $\Delta R$  (centered around 0.03) are completely dominated by events which pass our inverted energy (calorimeter variables) based cuts (see section 2.4). When we compare channels we notice that the muons tend to have a wider separation and tail in  $\Delta R(\ell, j)$  due to the nature of electron and muon reconstruction. The latter is track-stub based (calorimeter based ID variables are accounted for later) while the former is calorimeter based which is why we naturally expect jet objects to be in the electron collection and vice versa.

Originally our treatment for the (anti-selected) muons was to directly apply separation veto of the next section and this had the expected effect of eliminating many potential anti-selected candidates and actually producing a somewhat biased phase space for our W and jet related observables. However, the separation veto is designed to distance the effects of our defined jets with our lepton object. Given that our anti-selected muon sample allows and selects for the equivalent style multi-jet fakes in the electron channel due to its effective calorimeter dependence, we allow for this behavior and thus apply the same lepton-jet removal procedure for both anti-selected leptons samples.

The general procedure for removing a lepton-jet to search through the jet collection for the closest jet that satisfies  $\Delta R(\ell,j) < 0.40$ . While a tighter matching requirement (e.g.  $\Delta R(\ell,j) < 0.24$ ) is nearly fully efficient we take a full jet cone radius since this is the normative cutoff between reconstructing jets. Note that the separation veto (next section) is designed to separate the falling tail end of lepton-jets with the natural rise in reconstructing a near by jet. This is seen in the  $\Delta R(\ell,j)$  between 0.40-0.50 in figure 14 where we have followed through and removed our candidate anti-selection lepton-jets of figure 13. Figure 14 is analogous to figure 10 of the previous section.

Originally, when optimizing our electron-jet matching we opted for a jet EM fraction requirement in addition to a tighter separation. However, this additional requirement did not add anything when looking at high quality (i.e. tight) electrons where EM fraction greater than 0.8 (see figure 8) were nearly 100% by construction. Simply looking for the closest jet to the electron was enough. In the case of anti-selected electrons we are naturally looking for a fake in the electron collection that will necessarily fail a pair of ID cuts (e.g. HAD/EM) so this would not have been beneficial either. (For completeness, figures 15 and 16 show the jet EM fraction of anti-selected electron-jets and muon-jets, respectively.) In the case of our W selected muons there is are no observed muon-jets (as seen in data and MC) and thus geometrically matching anti-selected muons to the nearest jet is the natural procedure. Ultimately we find it unnecessary to add any additional requirements to our jet matching anti-selected lepton procedure. This has the benefit of keeping our jet selection and matching simple and consistent for both leptons yet fully efficient.

At the level of the analysis, matching and removing a lepton-jet literally means skipping said object in the jet collection as if it had failed our jet selection requirements. This is a natural procedure for the electrons but somewhat avant-garde for muons. As we will see in section 3.8, a similar procedure will be needed when reconstructing jets at the hadron level. It is also

worth noting that this removal scheme is consistent with our later treatment of our calorimeter (detector based) jets. All said jets go through jet energy scale corrections (section 3.6), but we do not correct the  $\mathbb{E}_T$  (section 3.7) with the removed lepton-jet.

# 3.4 Lepton/Jet separation

In our analysis we want to avoid potential lepton/jet overlap bias that comes from these objects being too close. Part of the motivation is to remove semi-leptonic decay events and other signatures were the charged lepton is colinear with a jet. Another issue is that our analysis does not directly account for out-of-cone effects where as applying an excluded buffer region between our leptons and the nearest selected jet removes this concern.

The approach for selected electrons effectively clears out a cone of R=0.4 due to the electron-jet removal/reclustering procedure and both electrons and muons enforce explicit isolation requirements such as isolation less than 0.1 (which itself is a R=0.4 cone base measurement). However, even when we switch to our anti-selected sample (potential QCD events from fakes and multijets) there is a motivation to keep the activity around the candidate anti-selected lepton separate from the normal jet activity outside of it cone of influence such that we can measure various jet observables independently.

In our analysis after having selected (or "anti-selected") a lepton passing our basic requirements we apply a  $\Delta R(\ell,j) < 0.52$  cut with j being the closest selected jet. The numerical value of 0.52 is based off (1) the historical use of this value as  $1.3 \times 0.4$  [1][61] and (2) our own analysis of the separation behavior in particular the previous section's description of anti-selected lepton-jets.

This is the second-to-last acceptance selection cut before our final acceptance selection cut (the subject of the next section). We give our full acceptance procedure description in section 5.1 (page 169) as well as our basic "raw" acceptance results via our signal MC there (see tables 30-33). Here we present these acceptance results for our  $\Delta R(\ell,j)$  cut in table 13 for each exclusive (= n) number of jets. We give the trivial exclusive 0 jet case for completeness and transparency. Our electron results (acceptance of  $\Delta R(e,j) < 0.52$ ) is given as CEM while we segment our muon results based on their fiducial sub-detector description. The muon results are internally consistent and the electron results show the obvious artifact of the efficient electron-jet removal/reclustering scheme. In the latter case, the acceptance is effectively lost in our basic electron geometric (detector fiducially requirement) and kinematic ( $E_T$  and  $p_T$  cuts) acceptance cuts.

# 3.5 $\Delta\phi(\ell,\wp)$ cut

As noted in the previous chapter there is an additional analysis wide cut we make as part of our final selection. The motivation was to find a variable that would help us understand our QCD backgrounds that could be correlated with a direct understand of our jet kinematics. Given that our expected background is made up a multi-jet where one jet fakes as a lepton to mask as our signal. One such handle, to consider dijet events specifically, would be to look at the  $\Delta \phi$  between lepton and a normally reconstructed jet. One would expect via conservation

n jets	CEM	CMUP	CMX-Arch	CMX-Mini
0	1.000	1.000	1.000	1.000
1	0.997	0.959	0.960	0.961
2	0.992	0.915	0.919	0.916
3	0.985	0.865	0.876	0.867
4	0.979	0.786	0.799	0.802

Table 13: Acceptance Results for  $\Delta R(\ell, j) < 0.52$  for electrons (CEM) and muons (CMUP, CMX-Arch, and CMX-Mini) for exclusive n jets. This partial acceptance result is calculated from events already passing our geometric and kinematic cuts of section 5.1.

of momentum that potential fakes be back-to-back while real leptons would ideally be flat in  $\Delta \phi$ . Realistically the latter situation where we select for tight lepton would be biased against colinear lepton/jets but would still have a linear dependence for signal while dijet fakes would exponentially favor high values of  $\Delta \phi$ .

As it turns out such a procedure has actually been used along with the relative isolation of the lepton to estimate the QCD background [31]. This was also cited as a possible improvement in estimating the QCD without resorting to the so called "iso vs. MET" method [32]. We investigated this early on in the analysis and made a obvious improvement. In cases where we record 2 or more jets (with the expected background coming from tri-jets, etc.) this procedure will not work as stated. The solution is to form a vector sum of jet energies and then compare this to lepton or rather compare their directions with  $\Delta \phi$ . We represent this vector jet quantity with the variable  $\wp$  and define it as follows,

$$\wp \equiv \sum_{\forall \text{ jets}} \left( E_x \hat{\mathbf{x}} + E_y \hat{\mathbf{y}} + E_z \hat{\mathbf{z}} \right) \tag{12}$$

with  $E_x$ , etc., the jet energy components.

Although we do not use  $\wp$  directly to select for a QCD rich sample it is instructive to show that its behavior is as advertised. We will then compare the behavior of  $\Delta \phi(\ell, \wp)$  between data, signal and background MC, and our preliminary QCD estimation. We begin with plots where we have found a lepton passing our basic selection but where we have not enforced a tight triggered lepton requirement nor made a W transverse mass cut. Figures 17 (for  $W \to e\nu + \ge 1$  jet) and 18 (for  $W \to \mu\nu + \ge 1$  jet) show the missing transverse energy  $(\not E_T)$  after partition events into two plots using  $\Delta \phi(\ell, \wp) \ge 120^\circ$ . These plots show that data for events in the highest 60°are dominated by an undescribed background which favors  $\not E_T$  unlike our signal. This same shape can be seen in the lower 120°but the signal and other backgrounds from the MC are relatively distinct.

For completeness we can flip around the nature of these plots and show  $\Delta\phi(\ell,\wp)$  where we partition with the missing energy. Figure 19 shows the  $\Delta\phi(e,\wp)$  with  $\not\!E_T \geqslant 30$  GeV for the electron channel while figure 20 showcases  $\Delta\phi(\mu,\wp)$  with  $\not\!E_T \geqslant 20$  GeV. Events in the low  $\not\!E_T$  region which are necessarily poorly populated by signal MC events, show a very strong turn on of  $\Delta\phi(\ell,\wp)$  in the data which is maximal where the lepton is approximately back-to-back to the sum vector jet energy. Meanwhile the higher  $\not\!E_T$  region we can clearly see the data being

made up of the behavior of lower region along with the behavior of our signal and background estimations from MC.

Consistent with our motivation to study the QCD by exploiting the behavior of multi-jet events, figures 17-20 suggest an obvious correlation with the undescribed QCD background and  $\Delta\phi(\ell,\wp)$ via our definition of  $\wp$ . We can then use this distribution as a good bench-mark and quality check for anti-selected leptons which forms our QCD estimation as explained in detail in the next chapter. We now plot  $\Delta\phi(\ell,\wp)$  for each inclusive jet multiplicity (1-4) after applying our formal background estimation procedure in figures 21  $(\Delta \phi(e,\wp))$  and 22  $(\Delta \phi(\mu,\wp))$ . Both of these plots represent our final W selection modulo the lower requirement of  $M_T > 20 \text{ GeV/c}^2$ rather than our final 40 (30) GeV/c<sup>2</sup> cut for  $W \to e\nu$  ( $W \to \mu\nu$ ). We note the basic good agreement and that the behavior of the backgrounds and the data are independent of jet multiplicity. In the electron channel (figure 21) we initially overestimate the QCD fraction of events with  $\Delta\phi(e,\wp) > 2.95$  in the data. We interpret this as our QCD shape being too multijet fake-like. In other words, candidate events in data contain events will less purity than our unmodified QCD estimation from our anti-selected electrons. In the case of the muon channel (figure 22) there is similar but smaller excess is seen for  $\Delta \phi(\mu, \wp) > 2.95$ . We also observe that the agreement is actually quite good for the higher jet multiplicities in comparison to the electrons.

From the  $\Delta\phi(\ell,\wp)$  results we will apply  $\Delta\phi(e,\wp) < 2.95$  cut in just the electron channel. We originally had the same  $\Delta\phi(\ell,\wp)$  cut on the muons as well but this hypothetical selection cut would drop the  $\geq 1$  jet acceptance but about 10% without improving the quality of any W or jet kinematic observable. As a result, we have eliminated this cut from our muon selection in favor of better acceptance. As noted later in our chapter of acceptance (chapter 5) this cut reduces our full acceptance for events with at least one jet by about 5% for electrons and 10% for muons. Updated version of these  $\Delta\phi(\ell,\wp)$  plots with our final W transverse mass selection cut are given in the next chapter as part of a general survey as to the quality of our background estimation. They can be seen in figures 129 (page 116) and 141 (page 122).

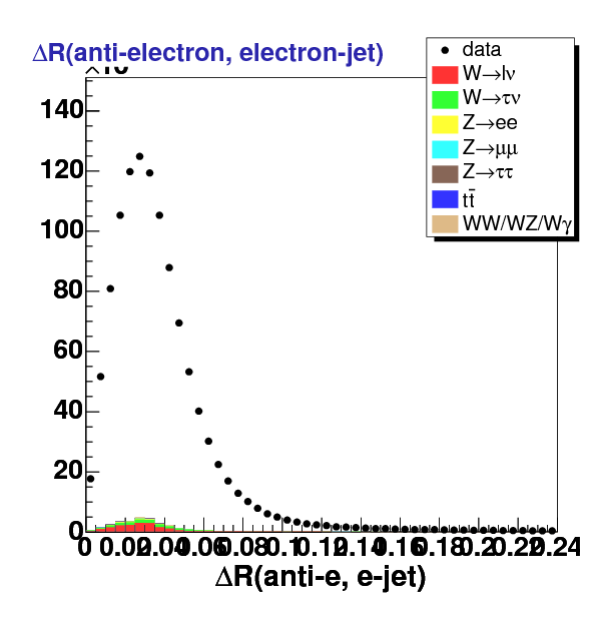


Figure 11: The  $\eta$ - $\phi$  separation ( $\Delta R(\text{anti-}e,\text{jet})$ ) for anti-selected muons and the closest jet. There is some signal contamination from the MC which is small and shows the same behavior. We identify the jet as the anti-selection electron-jet. This plot is effectively the zoomed in version of figure 13 with the range set from  $\Delta R$ =0.00 to 0.24.

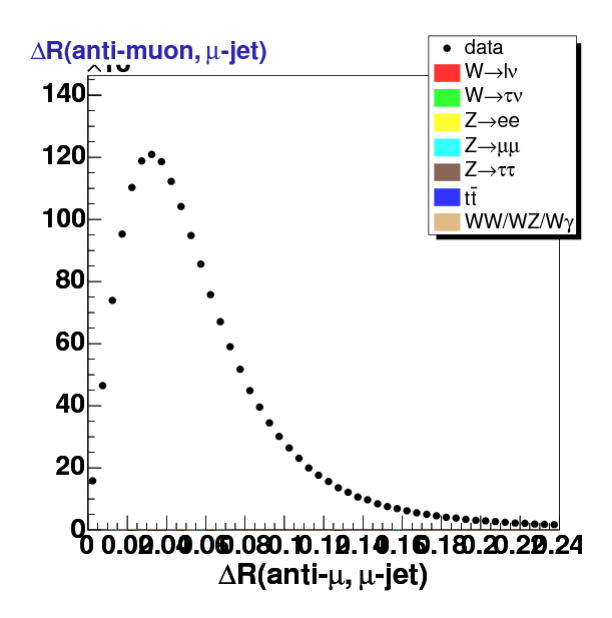


Figure 12: The  $\eta$ - $\phi$  separation ( $\Delta R(\text{anti-}\mu,\text{jet})$ ) for anti-selected muons and the closest jet. There is virtually no contamination from our MC signal or other backgrounds as these poorly fake our anti-selection requirements. We identify the jet as the anti-selection muon-jet. This plot is effectively the zoomed in version of figure 13 with the range set from  $\Delta R$ =0.00 to 0.24. Several of our inverted selection cuts are based off of the calorimeter with the result being a similar behavior as seen in the anti-selected electrons (see figure 11).

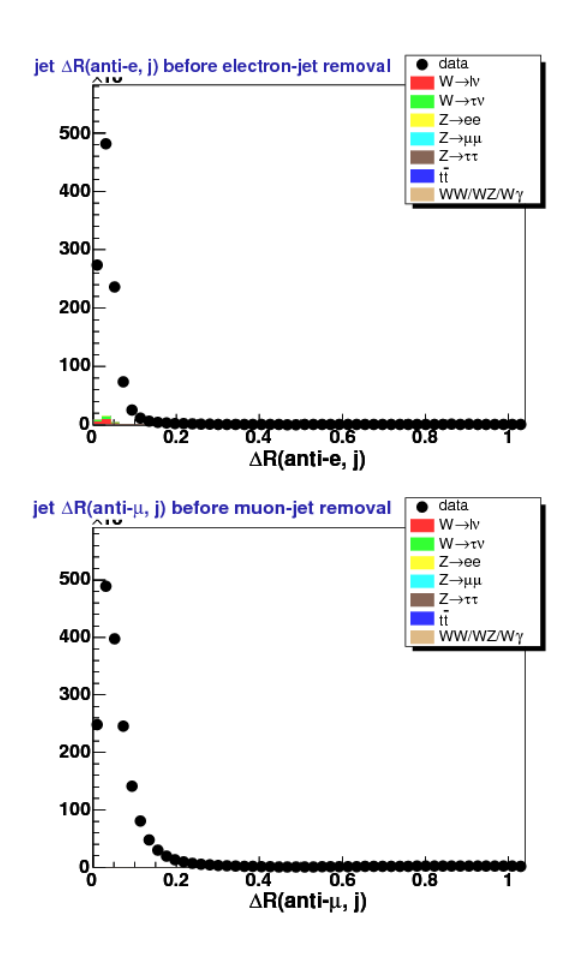


Figure 13:  $\eta$ - $\phi$  separation  $(\Delta R(\ell,j))$  between candidate anti-selected lepton and the closest jet. This is before our separation veto and before any lepton-jet removal procedure is applied. The top plot is for anti-selected electrons while the bottom is reserved for anti-selected muons. Unlike figure 9 there is no automatic removal for electrons and both leptons show the presence of overlapping jets. We identify these jets as the anti-selection lepton-jets. Figure 14 shows  $\Delta R(\ell,j)$  after these jets are removed.

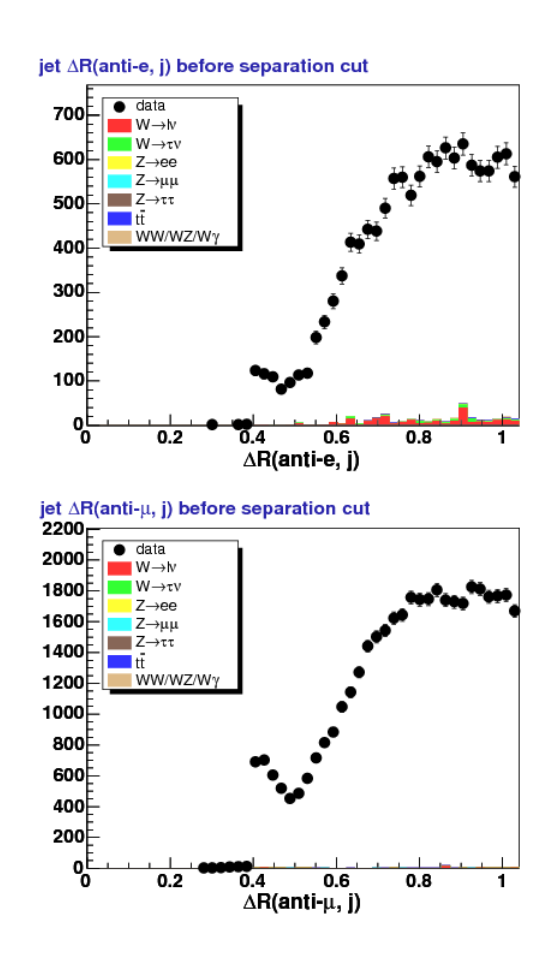


Figure 14:  $\eta$ - $\phi$  separation ( $\Delta R(\ell,j)$ ) between candidate anti-selected lepton and the closest jet. This is just before our separation veto but after we removed the (anti-selected) lepton-jet. There is a slight tail effect of candidate lepton-jets between  $\Delta R0.40$ -0.50 but The top plot is for anti-selected electrons while the bottom is reserved for anti-selected muons.

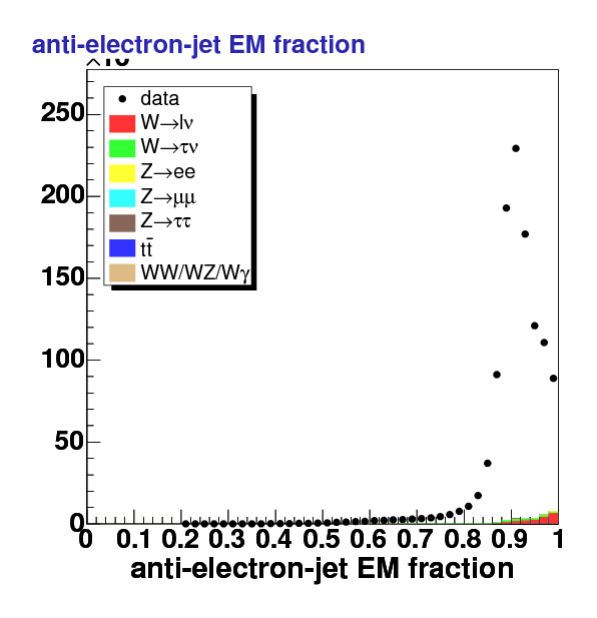


Figure 15: Jet EM fraction of jets matched to an anti-selected electron (anti-electron-jet).

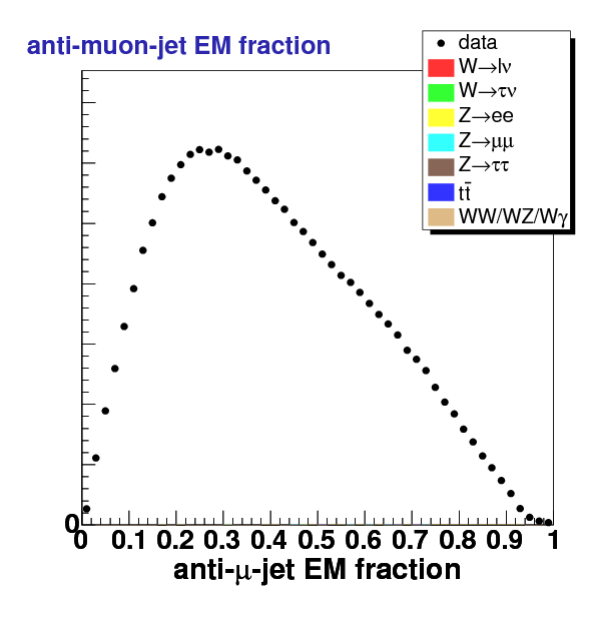


Figure 16: Jet EM fraction for all jets in events with an anti-selected muon (anti-muon-jet).

## 3.6 Jet Energy Scale Corrections

The details for the jet energy corrections are explained on the Jet Energy and Resolution Group page [33]. A full description of the procedure with and additional detector level and jet definition specific information is given elsewhere [34]. We use the corrections based up to our last run period/number (see table 1) which corresponds to jetCorr17. The correction is applied in a straightforward way via the instructions for generation 6 CDF code [35]. This amounts to loading corrections for each event based on the number of quality 12 vertices in addition to the run number and the types or level of jet corrections to apply. There is also the option to systematically vary the procedure by the derived uncertainties ( $\pm \sigma_{\rm JES}$ ) in order to obtain a systematic uncertainty. Our full discussion of the jet energy scale systematic on our cross-section is given in section 6.7.

In the CDF nomenclature we use a level 5 jet energy correction which is comprised of a relative, multiple interaction, and absolute corrections as described below. This is in addition to the CDF basic calibration of the calorimeter energy scale [36]. This baseline (level 0) detector-level correction is automatically applied in our reconstructed objects in our jet collection. For brevity, we will call these our "raw" or uncorrected jets which are corrected via the following procedures.

- Relative correction: This jet  $\eta$  dependent correction is designed to make the jet energy response uniform in  $\eta$  relative to the behavior of jets in the  $0.2 < |\eta| < 0.6$  region which is fiducial to our best understood part of our detector. This is accomplished by measuring dijet events where one expects the transverse energy for each jet to be equal and backto-back. The correction is applied to the raw jet energies as measured in the calorimeter. [38]
- Multiple interaction correction: This correction accounts for additional  $p\bar{p}$  interactions in the same bunch crossing producing additional energy that can fall inside a candidate jet cluster. Using minimum bias data, an averaged energy contribution is calculated along with the number of vertices in the event which is highly correlated with the effect of multiple interactions. The correction takes the form of a subtracted averaged contribution due to multiple interactions parameterized based on the number of vertices. [37]
- Absolute correction: The final type of correction deals with non-linearity in the calorimeter response as well as the effect of energy loss in the non-instrumented regions of the calorimeter. Here MC is added to better improve the description between simulation and data. The jet energy is corrected to the  $\sum p_T$  of the particles within a cone of R=0.4 centered on a generated parton (p) matched ( $\Delta R_{p,j} < 0.4$ ) to a calorimeter jet (j). [39].

The comparison of  $\gamma$ +jet events is instructive here as a cross-check as the photon can be well measured and compared back-to-back to the response of the jet [43]. We do not append additional (higher level) corrections like underlying event [40] or out-of-cone effects [41][42]. However, an additional global correction is made to correct the data to the hadron level to remove the (corrected) detector dependence, and this is the subject on the next section.

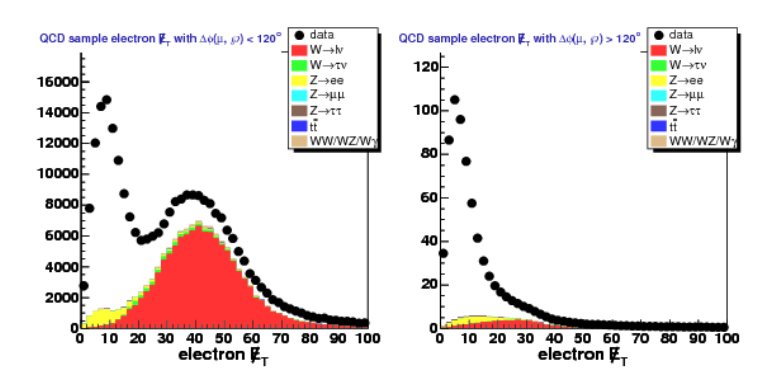


Figure 17: The  $\not\!E_T$  for  $W \to e\nu + \ge 1$  jet where the left plot represents events with  $\Delta\phi(e,\wp) < 120^\circ$ while the right plot shows  $\Delta\phi(e,\wp) > 120^\circ$ . The latter (right) plot is dominated by non-signal non-MC background events.

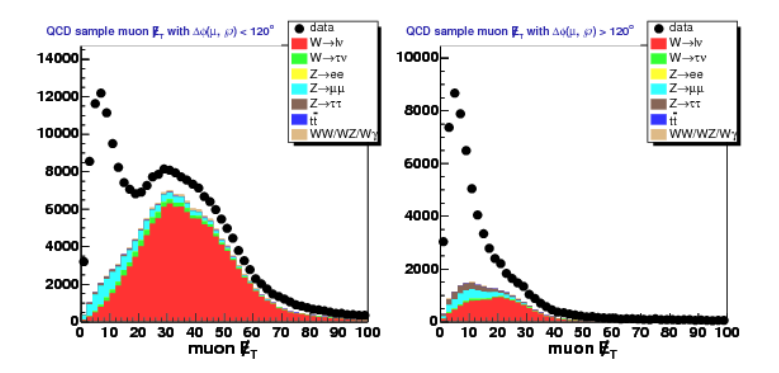


Figure 18: The  $\not\!\!E_T$  for  $W \to \mu\nu + \geq 1$  jet where the left plot represents events with  $\Delta\phi(\mu, \wp) < 120^{\circ}$ while the right plot shows  $\Delta\phi(\mu, \wp) > 120^{\circ}$ . The latter (right) plot is dominated by non-signal non-MC background events.

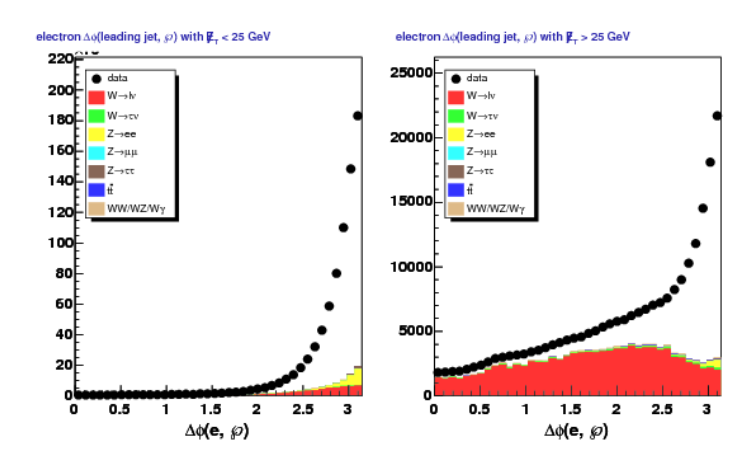


Figure 19: The  $\Delta\phi(e,\wp)$  for  $W\to e\nu+\geq 1$  jet where the left plot represents events with  $E_T>30$  GeV while the right plot shows  $E_T<30$  GeV. Note that the in-plot titles incorrectly imply that the  $E_T$  cut is at 25 GeV. The former (left) plot shows Jacobian turn on for back-to-back events with low  $E_T$ 

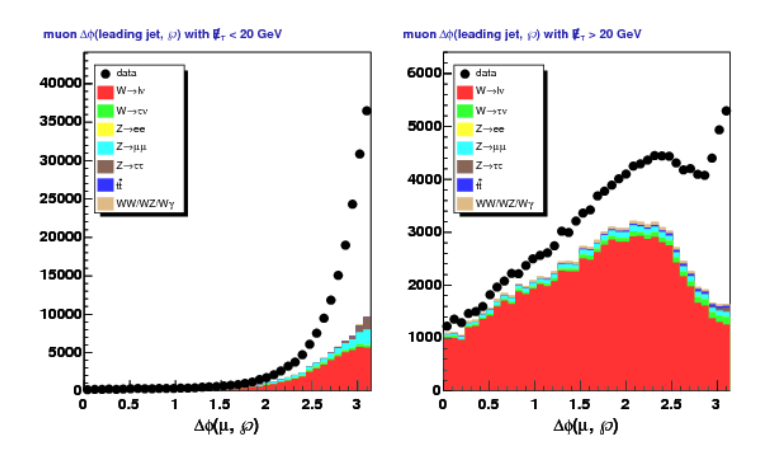


Figure 20: The  $\Delta\phi(\mu,\wp)$  for  $W\to\mu\nu+\geq 1$  jet where the left plot represents events with  $E_T>20$  GeV while the right plot shows  $E_T<20$  GeV. The former (left) plot shows Jacobian turn on for back-to-back events with low  $E_T$ .

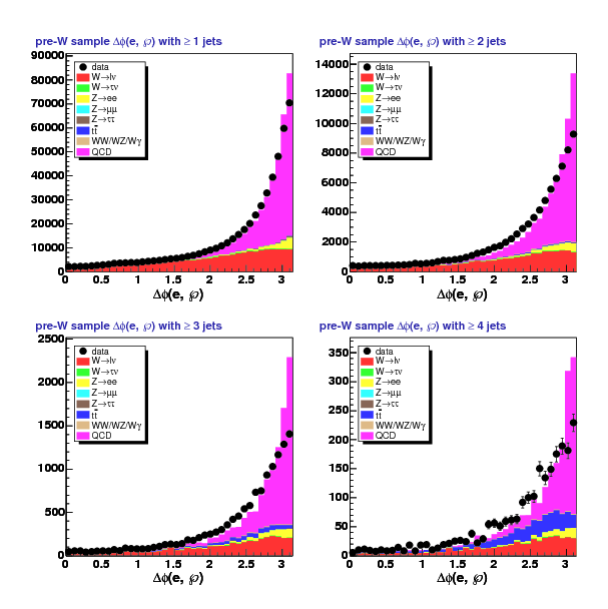


Figure 21: The  $\Delta \phi$  between the muon and the jet vector sum,  $\wp$  (see equation 12) for  $W \to e\nu + \geq n$  jets with  $M_T > 20$  GeV/c. (The full W selection requires  $M_T > 40$  GeV/c; see figure 129.) Upper-left plot is for  $\geq 1$  jets, upper-right for  $\geq 2$ , lower-left for  $\geq 3$ , and lower-right for  $\geq 4$ .

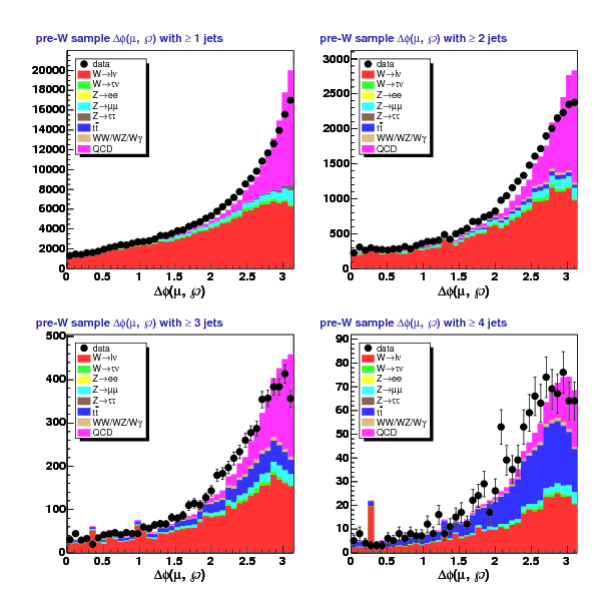


Figure 22: The  $\Delta \phi$  between the muon and the jet vector sum,  $\wp$  (see equation 12) for  $W \to \mu\nu + \geq n$  jets with  $M_T > 20$  GeV/c. (The full W selection requires  $M_T > 30$  GeV/c; see figure 141.) Upper-left plot is for  $\geq 1$  jets, upper-right for  $\geq 2$ , lower-left for  $\geq 3$ , and lower-right for  $\geq 4$ .

Once the jet corrections are setup, we loop through the jet collection and derive a jet energy scale factor based on the uncorrected  $p_T$ ,  $\eta$ , and EM fraction of the jet. Typically this correction is between 1.05-1.75. We then apply this scale factor  $(s_{\rm JES})$  as appropriate to our energy based jet observables. Equation 13 provides an obvious and important example of this correction in action for the raw (uncorrected) jet transverse momentum  $(p_T^{\rm corr})$  in becoming our nominal (corrected) jet transverse momentum  $(p_T^{\rm corr})$ .

$$p_T^{\text{corr}} = s_{\text{JES}} \left( p_T^{\text{raw}} \right) \tag{13}$$

We note that all jet variables referenced and used in this analysis are the corrected variables (e.g.  $p_T = p_T^{\text{corr}}$ ) unless explicitly stated otherwise.

As would be expected, jet corrections do "promote" jets that would have failed our jet  $p_T$  cut if left uncorrected. Of the 18.5 million passed jets some 3.8 million were promoted. We never observe the converse: a jet demoted by corrections that would have passed if left uncorrected. Figures 23-26 give the basic flavor of the jet energy scale factor  $(s_{\rm JES})$  dependence. The former pair (figures 23 and 24) is the dependence on jet  $p_T$  for electrons and muons, respectively, via a 2-dimensional plot. The latter pair (figures 25 and 26) likewise show the constructed dependence via jet  $\eta$ .

## 3.7 Missing Energy Corrections (jets)

Section 2.6 gave an overview of our  $\not E_T$  definition and how we handle additions due to our track based muons. In this section, we note an additional correction based on the jet energy corrections of the previous section. The procedure is straightforward: adjust the missing energy by the difference in the energy (specifically the vector transverse momentum) between corrected and uncorrected jets. Let the default (level 0) jet transverse momentum be given by  $\vec{p}_T^{\text{raw}}$  while  $\vec{p}_T^{\text{corr}}$  is the level 5 jet energy corrected variable consistent with our notation in equation 13. Via our  $\not E_T$  as defined in equation 8 (page 18) we derive our corrected missing energy ( $\not E_T^{\text{corr}}$ )

$$\vec{E}_{T}^{\text{corr}} = \vec{E}_{T} - \sum_{\forall \text{ jets}} \left( \vec{p}_{T}^{\text{ corr}} - \vec{p}_{T}^{\text{ base}} \right)$$
 (14)

The order of operations is important so to be clear:

- All raw candidate jets are corrected to level 5 (section 3.6)
- Candidates identified as (anti-)lepton-jets are skipped (section 3.3)
- Analysis level jets pass our selection/definition cuts (section 3.1)
- $E_T$  is corrected via equation 14 based off selected jets (this section)
- The corrected  $\not\!\!E_T$  is always used in our  $M_T$  cuts for our W selection (section 2.7)
- Events that fail our lepton-jet separation cut are vetoed (section 3.4)

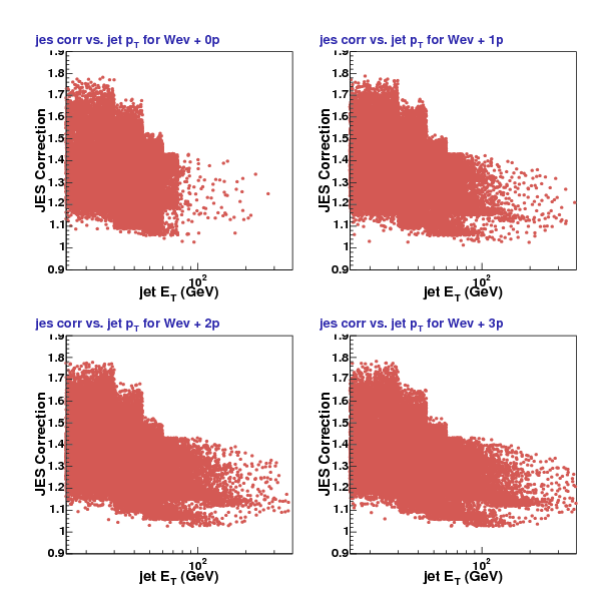


Figure 23: 2D histogram of the jet energy scale (JES) correction verses corrected jet  $p_T$  for all jets with  $|\eta| < 2.0$  and  $p_T > 20$ . GeV/c in Alpgen+Pythia  $W \to e\nu + n p$  MC. Each plot represents n patron sample with 4p omitted.

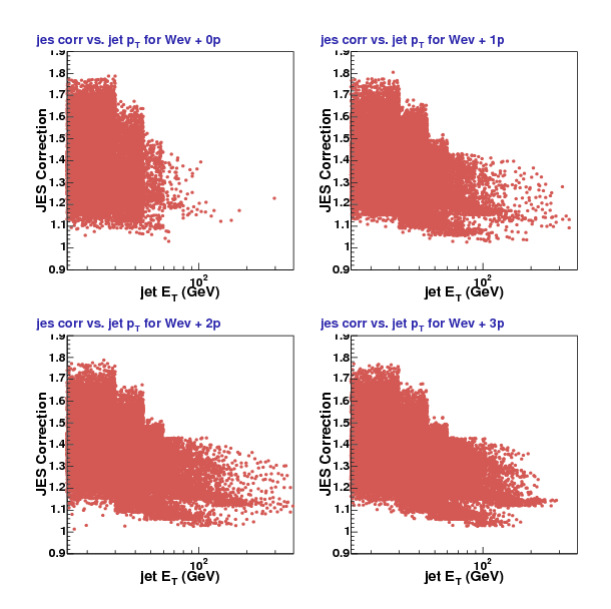


Figure 24: 2D histogram of the jet energy scale (JES) correction verses corrected jet  $p_T$  for all jets with  $|\eta| < 2.0$  and  $p_T > 20$ . GeV/c in Alpgen+Pythia  $W \to \mu\nu + n\mathrm{p}$  MC. Each plot represents n patron sample with 4p omitted.

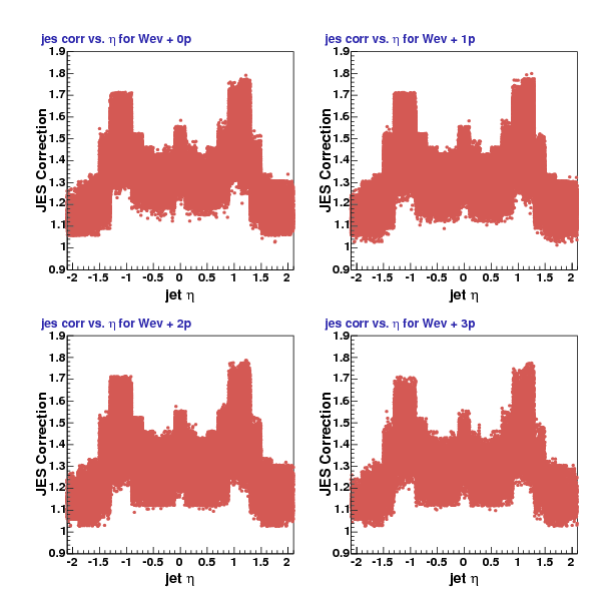


Figure 25: 2D histogram of the jet energy scale (JES) correction verses jet  $\eta$  for all jets with  $|\eta| < 2.0$  and  $p_T > 20$ . GeV/c in Alpgen+Pythia  $W \to e\nu + n p$  MC. Each plot represents n patron sample with 4p omitted.

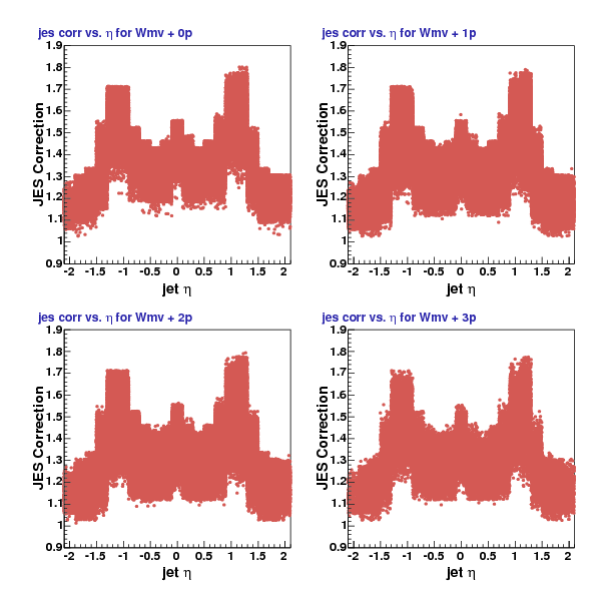


Figure 26: 2D histogram of the jet energy scale (JES) correction verses jet  $\eta$  for all jets with  $|\eta| < 2.0$  and  $p_T > 20$ . GeV/c in Alpgen+Pythia  $W \to \mu\nu + n\mathrm{p}$  MC. Each plot represents n patron sample with 4p omitted.

To get a sense of overall effect of our jet energy scale correction to the missing energy correction, we plot the ratio between the corrected and uncorrected  $\not\!\!E_T$  values. The former is unoriginally called "Corrected  $\not\!\!E_T$ " while the latter is noted as "Raw  $\not\!\!E_T$ " which is actually the  $|\vec{E}_T|$  of equation 14. Figure 27 is the  $W \to e\nu + \geq n$  jets version of  $|\vec{E}_T^{\text{corr}}|/|\vec{E}_T|$  while figure 28 is likewise the muon channel version. We plot n=1-4 as the total inclusive ( $\geq 0$  jets) case is completely dominated by the bin at unity.

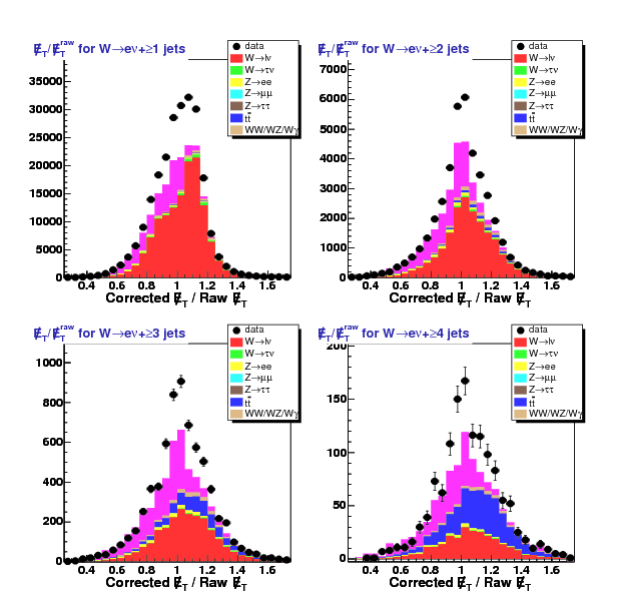


Figure 27: Ratio of the jet energy scale (JES) corrected  $\not\!E_T$  with the non-JES  $\not\!E_T$  as defined in equation 14 for  $W \to e\nu + \geq n$  jets. Upper-left plot is for  $\geq 1$  jets, upper-right for  $\geq 2$ , lower-left for  $\geq 3$ , and lower-right for  $\geq 4$ .

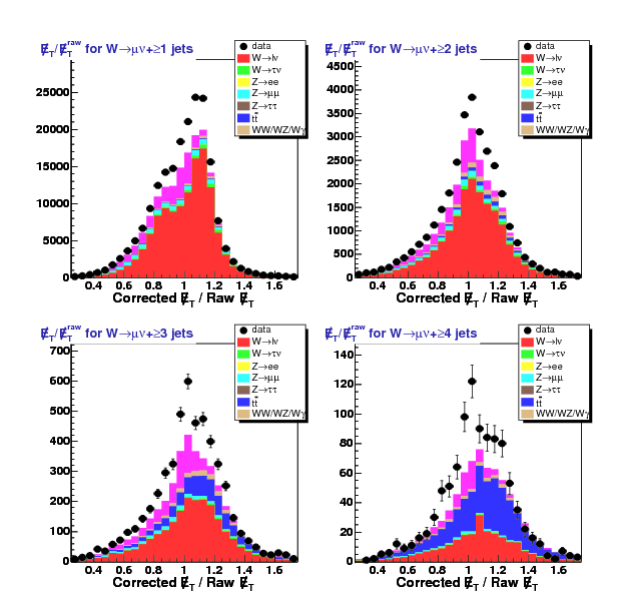


Figure 28: Ratio of the jet energy scale (JES) corrected  $\not\!\!E_T$  with the non-JES corrected  $\not\!\!E_T$  as defined in equation 14 for  $W \to \mu\nu + \geq n$  jets. In this plot, the Raw  $\not\!\!E_T$  refers to the already  $\mu$  correct  $\not\!\!E_T$  of equation 8 (18). Upper-left plot is for  $\geq 1$  jets, upper-right for  $\geq 2$ , lower-left for  $\geq 3$ , and lower-right for  $\geq 4$ .

## 3.8 Hadron Level Correction Procedure

Section 3.6 dealt with detector level jet corrections. However, for our final cross-section we wish to effectively apply an additional correction that maps our jet related observables to the hadron rather than the calorimeter level. We do this by studying the signal W MC and tracking its response to the default CDF detector simulated calorimeter jets and to jets reconstructed using the same midpoint (R=0.4) algorithm but applied to the (post-shower) pre-CDF simulation. For simplicity, we denote the normal CDF simulation level calorimeter jets, whether from signal MC or via the data, by CAL while the signal MC sample that has been run for hadron level jets will be referred by HAD. The final goal is to effectively measure the cross-section from each sample (HAD and CAL) and then correct the data, bin-by-bin as necessary, given the response. We describe this correction process as an unfolding of the data to the hadron level.

We construct a pseudo-cross-section with both MC samples by applying the same W selection criteria as described in chapter 2. In particular, we use the same (detector-simulation based) lepton and missing energy objects such that the acceptance is defined in a consistent way so that our final correction factor is a simple quotient of the number of weighted events. Section 5.2 deals with our acceptance definition and the results follow in section 5.3. For our purposes here, the acceptance is calculated with respect to the jet multiplicity (the number of inclusive jets in an event) for CAL jets to be consistent with what we measure in data. The motivation is not to have the hadron level correction linked to the W selection criteria but rather to focus on the unfolding the corrected CAL jets to the behavior of HAD jets by looking at the spectrum of jet kinematic observables. This procedure is therefore invariant with respect to our acceptance and systematics considerations. The acceptance differs between jet multiplicity bins by only a couple of percent maximum and we account for potential correlations in our systematics between acceptance and both jet corrections as well as between jet energy corrections and the hadron level corrections described in this section. Our systematic treatment for our unfolding will be addressed in section 6.8.

The default topNtuple does not have hadron level jets (midpoint or otherwise) in the default jet collection. Thus we reproduced the topNtuples for our W signal MC (the first 10 samples of table 3 on page 7) by running the hadron level midpoint (R=0.4) algorithm over raw CDF MC samples via a modified top tarball from tarball\_614\_1invfb.tar [6] which was commonly used in the MC samples used in this analysis. Like most things in CDF software (i.e. AC++), the needed modification was straightforward once one knew where to look [44]. Modification to the code included changing TopAlgorithms.cc such that it would recognize an additional jet algorithm label (jetAlgorithm="MPHAD"). After including JetMods/MidPointModule.hh to go along with the existing JetMods/JetCluModule.hh in TopFind.cc, we then modified topevent\_SAM.tcl to replace the last two jet collections (JetCluModule-cone0.4H1 and JetCluModule-cone0.7H1) via the "jetList add" command. The new jet list included MidPointModule-had-cone0.4 and JetCluModule-hadCone0.4. Per the instructions of Ben Kilminster, we also modified CollectionAndViewTypeFinder.hh such that the jet types were 10 and 11 for midpoint and jetclu, respectively.

While making the new topNtuples with the HAD jet modifications we discovered that some of the original MC files had been overwritten and thus some of the samples have fewer "generated" events. This is most dramatic in  $W \to e\nu + 4p$  sample which has 40% of number of events that are in the default topNtuples. Table 14 shows the number of events as well as the relative weight calculated via equation 3 assuming the CEM/CMUP luminosity of table 2. For brevity we do not include the separate weights for CMX muons as this follows from the cited procedure in section 1.6. As is the case in general in this analysis we do not assume the theoretical (MC generator) cross-section,  $\sigma(MC)$ , is absolutely correct but that it gets the relative weight between samples correct. The one advantage to this consistency is that we can cross check basic distributions (lepton  $p_T$ , missing energy,  $\phi$  and  $\eta$  coverage, etc.) between the nominal samples presented in section 1.5. Near total agreement is found with only minor differences due to sample composition.

MC Sample	N(GEN)	$\sigma(MC)$ (pb)	weight $(w)$
$W \to e\nu + 0p$	939749	1800	5.4129
$W \to e\nu + 1p$	1012254	225	0.6282
$W \to e\nu + 2p$	776802	35.4	0.1288
$W \to e\nu + 3p$	783415	5.6	0.0202
$W \to e\nu + 4p$	397543	1.03	0.0073
$W \to \mu\nu + 0p$	981752	1800	5.1813
$W \to \mu\nu + 1p$	962243	225	0.6608
$W \to \mu\nu + 2p$	867378	35.4	0.1153
$W \to \mu\nu + 3p$	817043	5.6	0.0194
$W \to \mu\nu + 4p$	906274	1.03	0.0032

Table 14: MC samples reconstructed using midpoint calorimeter and hadron level jets with the number of events and the event weight. The weight (w) is calculated via equation 3 using 2826.  $pb^{-1}$  for the total luminosity in the data.

This part of the analysis first selects for a W before applying any lepton/jet seperation veto. Then we consider the number of jets in the event and compute our desired set of observables (e.g.  $n^{\text{th}}$  leading jet  $p_T$ , etc.) independently in both samples and treat these as pseudo-cross-sections. Selecting HAD jets mirrors our CAL jets based cuts:

- $p_T > 20 \text{ GeV/c}$
- $|\eta| < 2.0$

We mirror the procedure and concern of section 3.4 by vetoing events where the electron or muon is too close to the nearest jet in  $\eta$ - $\phi$  such that we effectively require  $R_{\ell j} < 0.52$ .

The HAD jet collection does have some unique considerations that needed to be addressed. Normally for a tight electron, it is removed from the jet list and is reclustered (see section 3.2) but the HAD jet algorithm does not automatically do this. In addition, the muon as well as the respective neutrinos also make it into the jet collection. We call these objects lepton-HAD-jets. In once sense the problem is minimal as there are no towers to be reclustered, etc. and cases where the lepton would be near  $(R_{\ell j} < 0.52)$  the closest jet are vetoed anyway. However, we have to first find the leptons in our HAD jet collection and remove them from consideration.

This follows from our basic lepton-jet removal procedure explained in section 3.3 modulo some additional details that we have via working with the MC.

First we identify the leptons from the W decay via the hepg information bank. We loop through the jet collection (skipping jets that fail selection criteria) and match the leptons ( $\ell$  and then  $\nu$ ) to the closest jet within R < 0.40. The jet cone radius is chosen as our matching criteria to be consistent with our normal (detector based) lepton-jet removal procedure. Even more so than our anti-selected lepton-jets this is largely overkill but matching with R < 0.40 removes a potential overlap bias on the rising edge of  $R_{\ell j}$  after apply our separation veto. In cases where there are only 2 HAD jet objects and the hepg information on the leptons satisfies our equivalent kinematic and geometric jet level cuts, our matching algorithm is over 99.9% effective for R < 0.20. The efficiency drops to about 98% if the matching requirement is relaxed to R < 0.15.

As a graphical check of our matching lepton-HAD-jet algorithm and more generally of our hadron level objects via the midpoint algorithm definition from the MC, we present a fully "reconstructed" W mass plots using the equivalent 4-vector information from the HAD jet collection. No additional cuts besides our baseline jet selection are used. Figures 29 and 30 show the results for  $W \to e\nu + \geq n$  jets while figures 31 and 32 show the equivalent results for  $W \to \mu\nu + \geq n$  jets.

For completeness we checked some basic variables to compare the HAD and CAL results directly at the event-by-event level. In particular, we were interested in how often jets (whether by jet multiplicity, momentum, and rapidity) were matched in both collections. In general the agreement is good and we see the type of spread that one expects when effectively changing the jet definition from detector based to being independent of the calorimeter. Figures 33 and 34 show the even-by-event difference in the number of HAD and CAL jets for electrons and muon, respectively. Additionally, we made the same plot but looked at the events that failed our W selection cuts which can be seen in figures 35 and 36. The motivation for looking at non-accepted events will be discussed below but the basic idea for these was to confirm that there was no W acceptance dependence. For now, we observe that there is no obvious dependence on the number of exclusive jets with regard to the HAD and CAL jets.

Continuing our basic investigation of HAD to CAL jets, we looked at various ratio plots of basic jet kinematic variables. Our final goal will be to compare the overall distributions of HAD and CAL jets and this will intrinsically allow for a jet in one collection to have no corresponding jet in the others collection. This also allows for corresponding jets in both collections to shift their relative rank in jet  $p_T$  which we colloquially refer to as "jockeying for position". For example, the 1<sup>st</sup> leading CAL jet might occupy the same  $\eta$ - $\phi$  as the 2<sup>nd</sup> leading HAD jet. However, it is instructive to look at cases where we can match our default calorimeter based jets to our hadron level jets. Operationally we loop through the CAL jets and match them (independent of their energy or  $p_T$  rank) by a simple  $R_{jCAL_jHAD} < 0.4$  algorithm. We chose the jet cone size (R = 0.4) as this as the effective minimum separation between jets in both collections. For our investigation here, the jet transverse momentum rank (i.e.  $n^{\text{th}}$  leading jet) is always with respect to the CAL based jet. Obviously, this procedure does not allow for comparisons of unmatched jets in either collections.

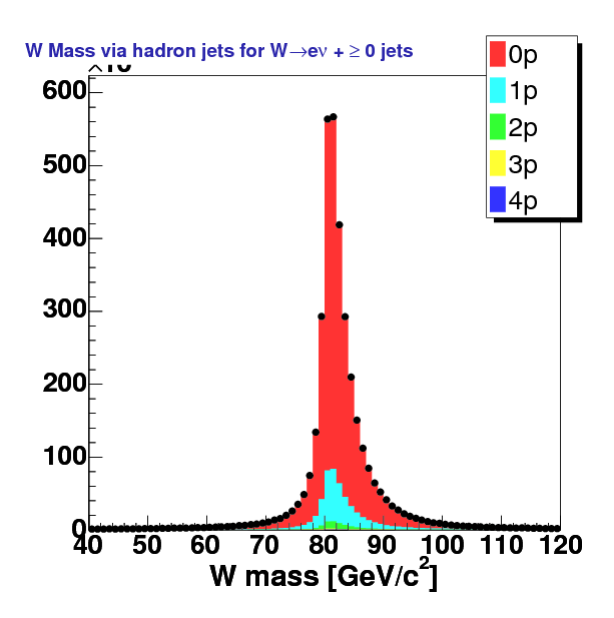


Figure 29: W mass constructed with hadron level jets for  $W \to e\nu + \ge 0$  jets in the post-shower/pre-cdf-detector-sim Alpgen+Pythia MC. The stacked histogram shows the contributions from each of the 5 parton samples ( $W \to e\nu + 0$ -4p).

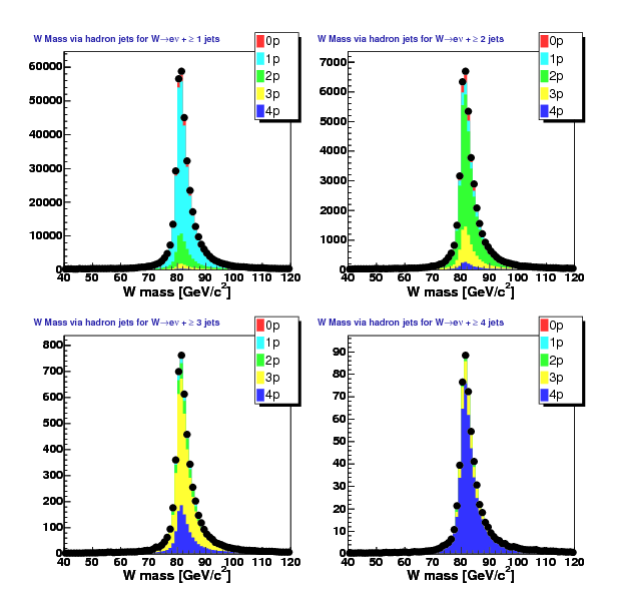


Figure 30: W mass constructed with hadron level jets for  $W \to e\nu + \ge 1$ -4 jets in the post-shower/pre-cdf-detector-sim Alpgen+Pythia MC. The stacked histogram shows the contributions from each of the 5 parton samples ( $W \to e\nu + 0$ -4p). The four plot represent each inclusive jet multiplicity:  $\ge 1$  for upper-left,  $\ge 2$  for upper-right,  $\ge 3$  for lower-left, and  $\ge 4$  for lower-right.

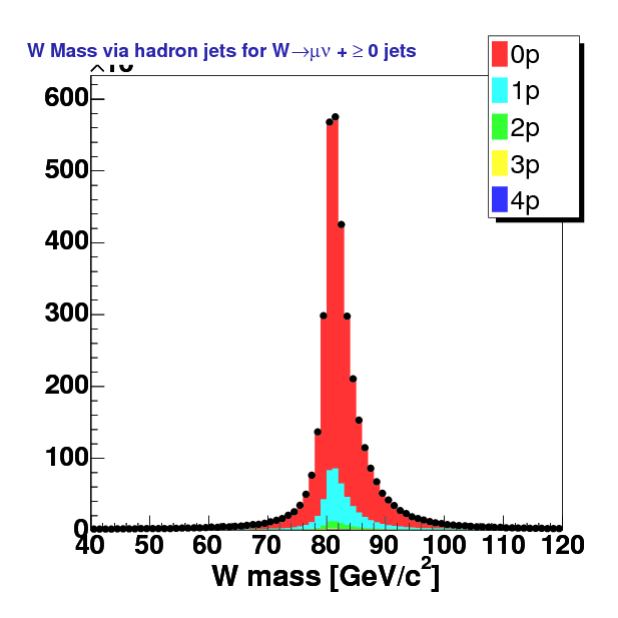


Figure 31: W mass constructed with hadron level jets for  $W \to \mu\nu + \ge 0$  jets in the post-shower/pre-cdf-detector-sim Alpgen+Pythia MC. The stacked histogram shows the contributions from each of the 5 parton samples ( $W \to \mu\nu + 0$ -4p).

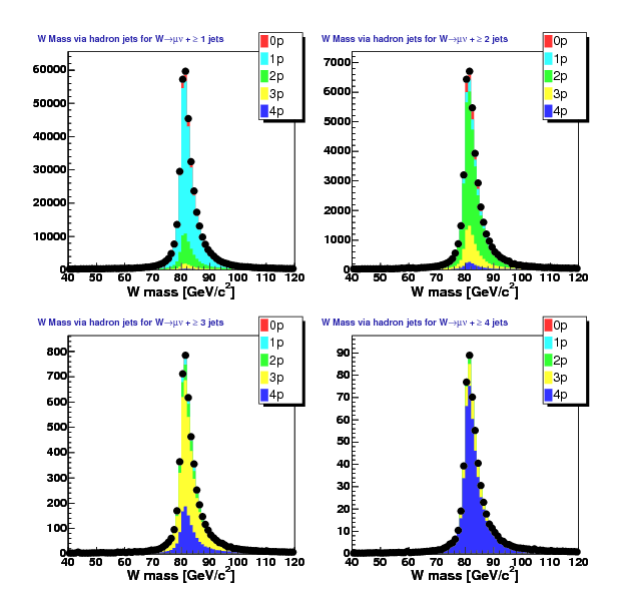


Figure 32: W mass constructed with hadron level jets for  $W \to \mu\nu + \geq 1$ -4 jets in the post-shower/pre-cdf-detector-sim Alpgen+Pythia MC. The stacked histogram shows the contributions from each of the 5 parton samples ( $W \to \mu\nu + 0$ -4p). The four plot represent each inclusive jet multiplicity:  $\geq 1$  for upper-left,  $\geq 2$  for upper-right,  $\geq 3$  for lower-left, and  $\geq 4$  for lower-right.

First we looked at the event-by-event ratio of the  $n^{\rm th}$  leading jet  $p_T$  ( $p_T^{HAD}/p_T^{CAL}$ ) as well as the corresponding jet  $\eta$  ratio ( $\eta^{HAD}/\eta^{CAL}$ ). The former is plotted in figures 37 and 38 for the electron and muon channel, respectively. Likewise the jet  $\eta$  ratio is shown in figures 39 and 40. In both sets of plots it is clear that jets often match up and favor a ratio around unity as would be expected. The jet pseudo-rapidity is considerably narrower relative to the jet transverse momentum and this is consistent in general with the relative spread in these variables with respect to jet energy correction and the general bias we introduced in our matching procedure. As a final check we looked at two dijet distributions:  $m_{jj}$  (jet-jet mass) and  $R_{jj}$  (the  $\eta$ - $\phi$  separation) between the leading two CAL jets and their matching corespondents in the HAD collection. The dijet mass HAD/CAL ratio is presented in figures 41 and 42 for the electron and muon channel, respectively. Similarly, the dijet separation plots are given in figures 43 and 44. These dijet plots mirror the basic features of the  $n^{\rm th}$  leading jet  $p_T$  and  $\eta$  plots with  $m_{jj}$  being relatively smeared while  $R_{jj}$  is very narrow.

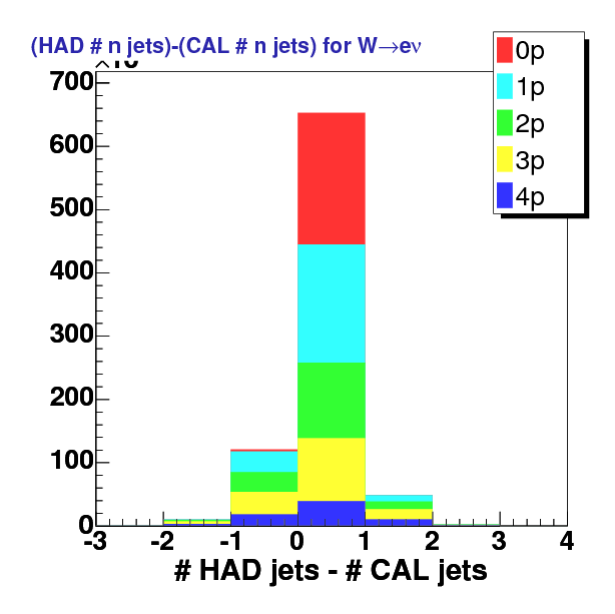


Figure 33: The difference in the number of exclusive HAD jets to CAL jets for  $W \to e\nu + \ge 0$  jets from Alpgen+Pythia MC. This is an event-by-event distribution that passes all our W selection cuts. The stacked histogram shows the contributions from each of the 5 parton samples  $(W \to e\nu + 0\text{-}4\text{p})$ .

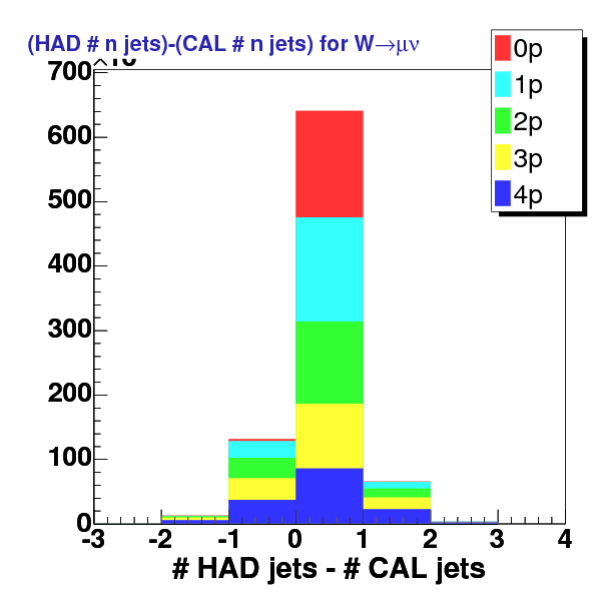


Figure 34: The difference in the number of exclusive HAD jets to CAL jets for  $W \to \mu\nu + \geq$  0 jets from Alpgen+Pythia MC. This is an event-by-event distribution that passes all our W selection cuts. The stacked histogram shows the contributions from each of the 5 parton samples  $(W \to \mu\nu + 0\text{-}4\text{p})$ .

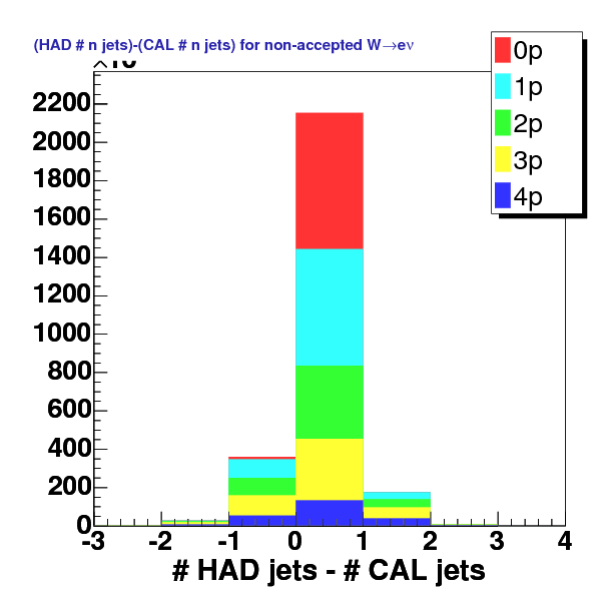


Figure 35: The difference in the number of exclusive HAD jets to CAL jets for non-accepted  $W \to e\nu + \geq 0$  jets from Alpgen+Pythia MC. This is an event-by-event distribution that *fails* our W selection criteria. The stacked histogram shows the contributions from each of the 5 parton samples  $(W \to e\nu + 0\text{-}4\text{p})$ .

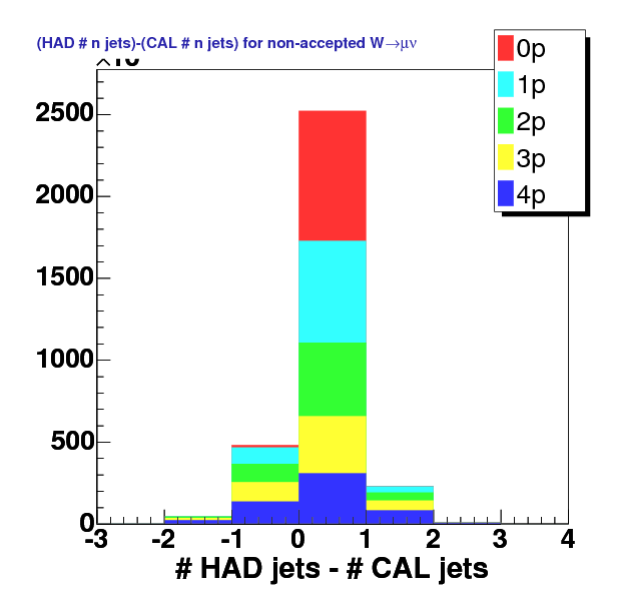


Figure 36: The difference in the number of exclusive HAD jets to CAL jets for non-accepted  $W \to \mu\nu + \geq 0$  jets from Alpgen+Pythia MC. This is an event-by-event distribution that *fails* our W selection criteria. The stacked histogram shows the contributions from each of the 5 parton samples ( $W \to \mu\nu + 0$ -4p).

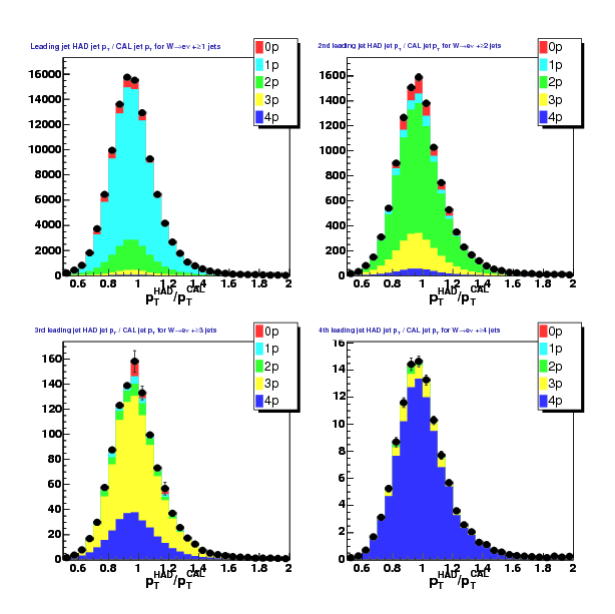


Figure 37: The  $n^{\rm th}$  leading jet  $p_T$  ratio between HAD and CAL jets for  $W \to e\nu + \geq n$  jets from Alpgen+Pythia MC. This is an event-by-event distribution of  $p_T^{HAD}/p_T^{CAL}$ . The stacked histogram shows the contributions from each of the 5 parton samples  $(W \to e\nu + 0\text{-}4\text{p})$ . The four plot represent each inclusive jet multiplicity:  $\geq 1$  for upper-left,  $\geq 2$  for upper-right,  $\geq 3$  for lower-left, and  $\geq 4$  for lower-right.

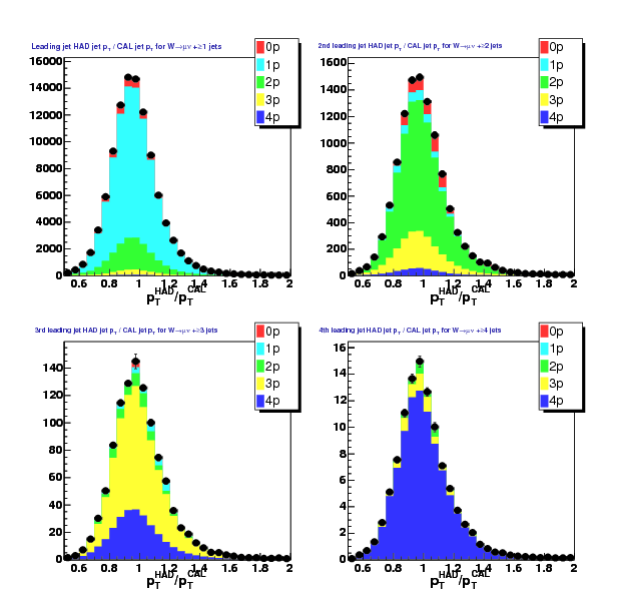


Figure 38: The  $n^{\rm th}$  leading jet  $p_T$  ratio between HAD and CAL jets for  $W \to \mu\nu + \geq n$  jets from Alpgen+Pythia MC. This is an event-by-event distribution of  $p_T^{HAD}/p_T^{CAL}$ . The stacked histogram shows the contributions from each of the 5 parton samples ( $W \to \mu\nu + 0$ -4p). The four plot represent each inclusive jet multiplicity:  $\geq 1$  for upper-left,  $\geq 2$  for upper-right,  $\geq 3$  for lower-left, and  $\geq 4$  for lower-right.

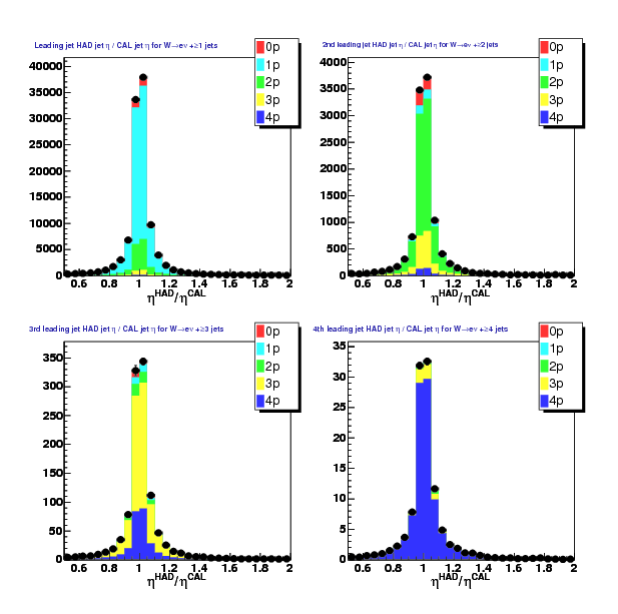


Figure 39: The  $n^{\rm th}$  leading jet  $\eta$  ratio between HAD and CAL jets for  $W \to e\nu + \geq n$  jets from Alpgen+Pythia MC. This is an event-by-event distribution of  $\eta^{HAD}/\eta^{CAL}$ . The stacked histogram shows the contributions from each of the 5 parton samples  $(W \to e\nu + 0\text{-}4\text{p})$ . The four plot represent each inclusive jet multiplicity:  $\geq 1$  for upper-left,  $\geq 2$  for upper-right,  $\geq 3$  for lower-left, and  $\geq 4$  for lower-right.

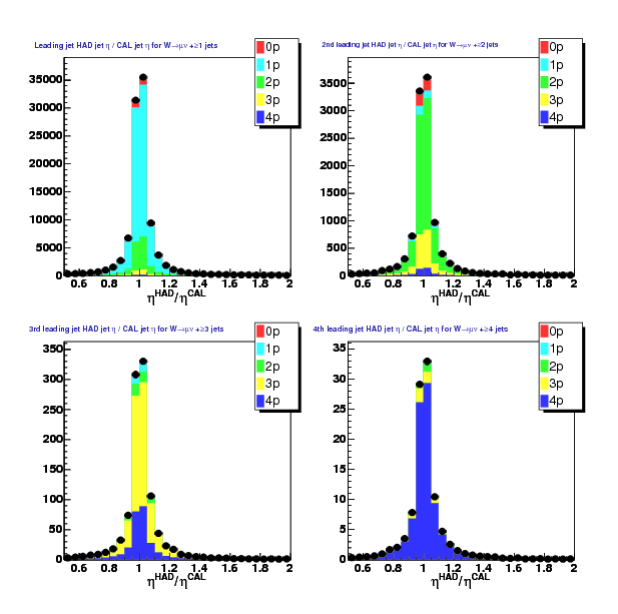


Figure 40: The  $n^{\rm th}$  leading jet  $\eta$  ratio between HAD and CAL jets for  $W \to \mu\nu + \geq n$  jets from Alpgen+Pythia MC. This is an event-by-event distribution of  $\eta^{HAD}/\eta^{CAL}$ . The stacked histogram shows the contributions from each of the 5 parton samples  $(W \to \mu\nu + 0\text{-}4p)$ . The four plot represent each inclusive jet multiplicity:  $\geq 1$  for upper-left,  $\geq 2$  for upper-right,  $\geq 3$  for lower-left, and  $\geq 4$  for lower-right.

At this stage, we have dealt with several potential pit falls such as dealing with lepton-HAD-jets and have a basic handle on understanding our hadron level jets with respect to our nominal detector derived calorimeter jets. Now we turn to the process of deriving an unfolding factor that will correct our calorimeter jet based cross-sections to a detector independent hadron level cross-section. We proceed by forming distributions using both HAD and CAL jets using our normal W selection criteria and also accounting for additional global analysis factors like our vertex reweighting (full details in section 4.6). The goal is to from a ratio between our HAD results and CAL results; this literally takes the form of dividing the HAD based distribution (histogram) by the CAL distribution. Since the relative weighting of events is completely consistent and acceptance/efficiency terms are by definition the same this ratio is identical to a full cross-section measurement.

Let  $\sigma_{CAL}({\rm data})$  be a CAL jet based cross-section (for example the  $n^{\rm th}$  leading jet differential cross-section,  ${\rm d}\sigma/{\rm d}p_T^{n^{\rm th}}$ ) based on the data minus background estimates divided by the product of luminosity, acceptance, and efficiency (see section 7.1 for details on our cross-section definition). Let  $\sigma_{HAD}({\rm MC})$  and  $\sigma_{CAL}({\rm MC})$  be W MC based distributions based, respectively, on the hadron level jet collection and the post-CDF simulation based calorimeter jets. We define our unfolding factor, u, as

$$u \equiv \left(\frac{\sigma_{HAD}(MC)}{\sigma_{CAL}(MC)}\right) \tag{15}$$

As we desire to correct the data to the hadron level with this unfolding factor, we have  $\sigma_{HAD}(\text{data}) = u(\sigma_{CAL}(\text{data}))$  or

$$\sigma_{HAD}(\text{data}) = \left(\frac{\sigma_{HAD}(\text{MC})}{\sigma_{CAL}(\text{MC})}\right) \sigma_{CAL}(\text{data})$$
 (16)

The uncertainty in u which we call  $\Delta u$  we take as the standard error propagation (equation 17) from quotient of the HAD and CAL statistical (Poisson) uncertainty;  $\Delta \sigma_{HAD}$  and  $\Delta \sigma_{CAL}$ , respectively. Note that we take these errors as uncorrelated as they represent two independent statements about our MC sample.

$$\Delta u = u \sqrt{\left(\frac{\Delta \sigma_{HAD}}{\sigma_{HAD}}\right)^2 + \left(\frac{\Delta \sigma_{CAL}}{\sigma_{CAL}}\right)^2}$$
 (17)

A full example of this procedure is given in the next section along with our full hadron level correction (unfolding) results. The use of this unfolding scale factor is later mentioned in our cross-section definition (equation 82) on page 228 in section 7.1. Our systematic treatment for the unfolding is given in section 6.8.

## 3.9 Hadron Level Correction (Unfolding) Results

As a general test of this procedure in action and to double check our basic HAD results we consider a trivial distribution that should be independent of jet collection/level. The example which follows involves an idealized case where the sample is artificially confined to have  $\geq n$  jets matched between HAD and CAL jets. This same sampling process was use to produce our

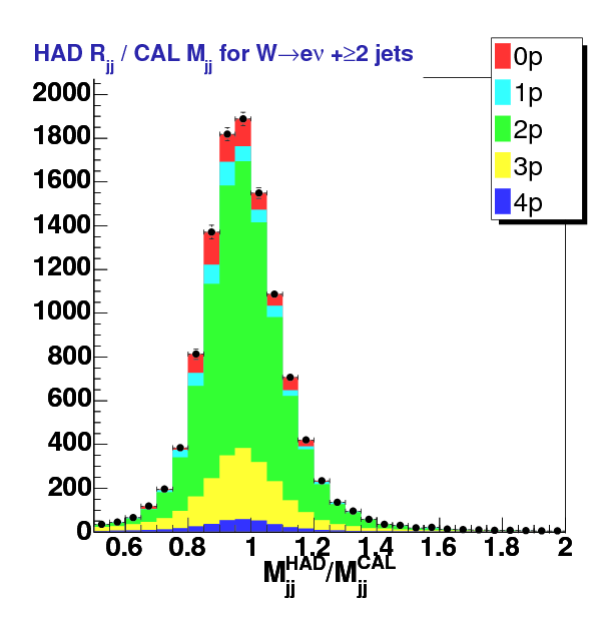


Figure 41: The dijet mass ratio for HAD and CAL jets for  $W \to e\nu + \geq 2$  jets from Alpgen+Pythia MC. This is an event-by-event distribution of  $M_{jj}^{HAD}/M_{jj}^{CAL}$ . The stacked histogram shows the contributions from each of the 5 parton samples  $(W \to e\nu + 0\text{-}4\text{p})$ .

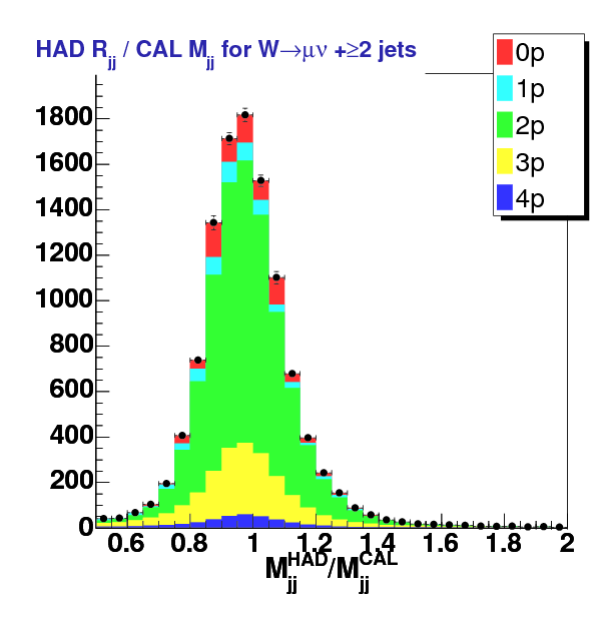


Figure 42: The dijet mass ratio for HAD and CAL jets for  $W \to \mu\nu + \geq 2$  jets from Alpgen+Pythia MC. This is an event-by-event distribution of  $M_{jj}^{HAD}/M_{jj}^{CAL}$ . The stacked histogram shows the contributions from each of the 5 parton samples  $(W \to \mu\nu + 0\text{-}4\text{p})$ .

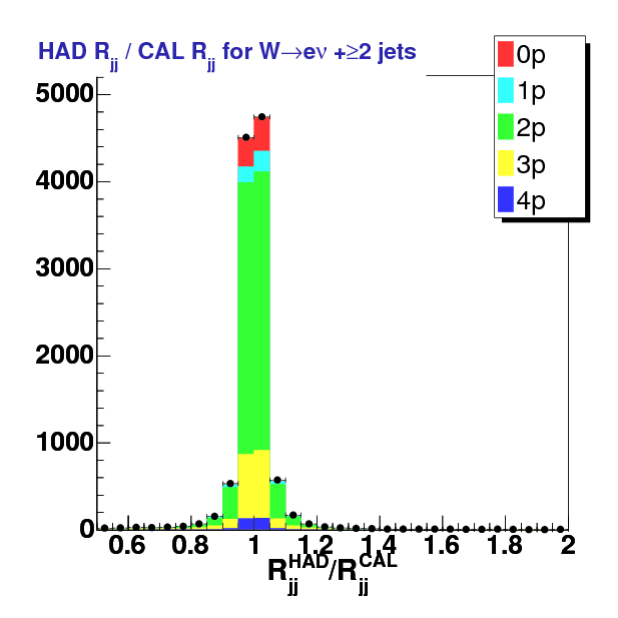


Figure 43: The dijet separation ratio for HAD and CAL jets for  $W \to e\nu + \geq 2$  jets from Alpgen+Pythia MC. This is an event-by-event distribution of  $R_{jj}^{HAD}/R_{jj}^{CAL}$ . The stacked histogram shows the contributions from each of the 5 parton samples  $(W \to e\nu + 0\text{-}4\text{p})$ .

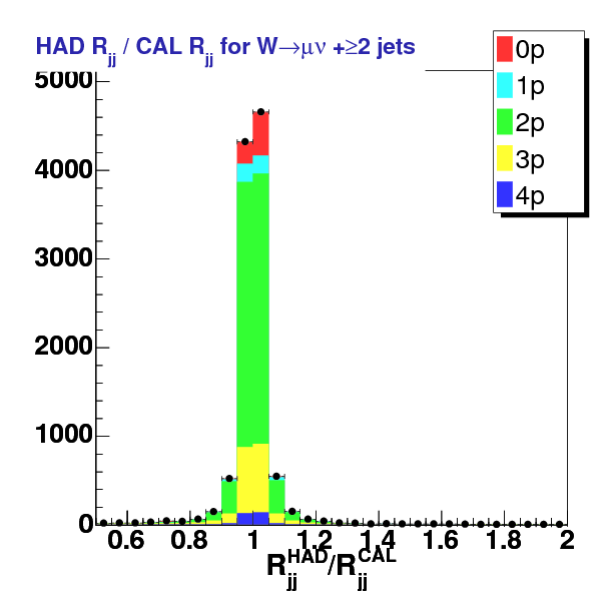


Figure 44: The dijet separation ratio for HAD and CAL jets for  $W \to \mu\nu + \geq 2$  jets from Alpgen+Pythia MC. This is an event-by-event distribution of  $R_{jj}^{HAD}/R_{jj}^{CAL}$ . The stacked histogram shows the contributions from each of the 5 parton samples  $(W \to \mu\nu + 0\text{-}4\text{p})$ .

HAD/CAL event-by-event ratios of figures 37-44. Let  $\Delta R_{\ell j}$  be the  $\eta$ - $\phi$  separation between the charged lepton ( $\ell=e$  or  $\mu$ ) and the  $n^{\rm th}$  leading jet (j). This distribution is expected to largely be independent of jet multiplicity as well as lepton channel and should not have an dependence HAD or CAL jets modulo the handling of jets very close to the lepton. Figures 45 and 46 shows the HAD and CAL results, respectively, for  $\Delta R_{ej}$ . In the same fashion, figures 47 and 48 gives the results for  $\Delta R_{\mu j}$ . Our bin-by-bin unfolding factors are given in figures 49 and 50 for  $\Delta R_{ej}$  and  $\Delta R_{\mu j}$ , respectively.

As advertised, there is broad agreement in the distributions across jet multiplicity, lepton channel, and between HAD and CAL jets. The unfolding factor distribution  $(\sigma_{HAD}/\sigma_{CAL})$  is consistent unity. Only the first bin which starts at  $\Delta R_{\ell j}$ =0.4 and only has content for  $\Delta R_{\ell j}$  > 0.52 deviates. Since the effect is seen in both electrons and muons (and the latter is indifferent to the response in the calorimeter) we take this as an indication that our lepton-jet veto is overly efficient. In any event, if we were constructing a cross-section based off of  $\Delta R_{\ell j}$  we would be able to correct to the hadron level by multiplying bin-by-bin by our unfolding factor. As already noted, in this case we could safely declare the unfolding factor as globally consistent with unity and derive an uncertainty based on the spread which would ultimately be negligible relative to the basic jet energy scale systematic.

As an additional test, we also looked at the unfolding of the  $n^{\rm th}$  leading jet  $\eta$  using the same matched sample as our  $\Delta R_{\ell j}$  example. This variable is of interest as we know our jet energy corrections have an obvious  $\eta$  dependence due to the composition of calorimeter (for example see figures 25 and 26). Looking at the response without the (simulated) detector via our hadron level jet  $\eta$  compared to the (corrected) detector response at the calorimeter level is useful as we expect our relative jet energy corrections combined with rigidity of the pseudo-rapidity variable for jets that are in both jet collections to produce a relatively flat unfolding. First we show the HAD results for the  $n^{\rm th}$  leading jet  $\eta$  in figures 51 (electrons) and 53 (muons). Likewise our CAL results are given in figures 52 and 54. We present the respective electron and muon unfolding in figures 55 and 56.

In cases where the unfolding is flat or where we want explicitly estimate the overall unfolding fraction for each inclusive jet multiplicity (as indeed we must for the jet multiplicity cross-section itself) we calculate the unfolding factor with its associated uncertainty directly using our jet multiplicity pseudo-cross-sections with our HAD and CAL jet collections. This procedure is straightforward as it follows for our prescription of equations 15 and 17 and is consistent with the bin-by-bin approach outlined in our previous two examples. Our original approach of averaging over each unfolding spectrum gave a consistent result but was overly complicated and potentially statistically problematic [45].

The jet multiplicity unfolding factor (u) for both lepton channels is given in table 15. Not surprisingly, distributions with  $\eta$  and  $\phi$  are more uniform and flat and thus an overall unfolding factor and its error can with the universal factor presented in the table. For example, we apply the  $\geq 2$  jet unfolding factor for our dijet separation  $(R_{jj})$  differential cross-section.

Our unfolding results for our jet kinematic variables follows is a straight forward way. The definition of most of these plots will be formally introduced in chapter 7. We will generally omit the individual HAD and CAL plots and go straight to their quotient represented on the

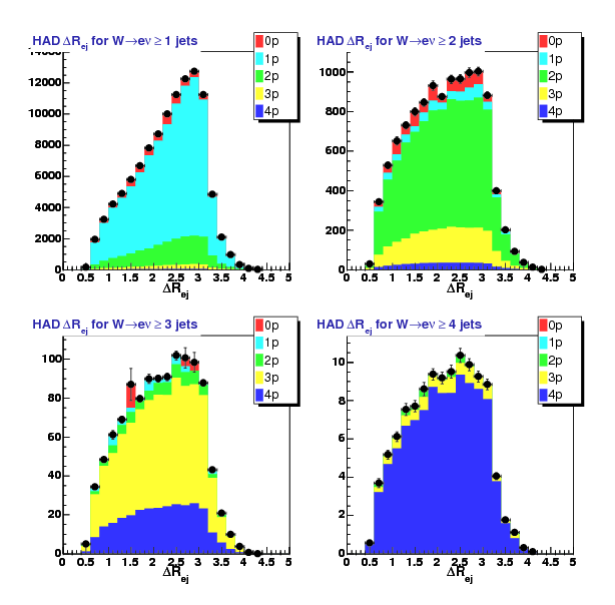


Figure 45: The electron and  $n^{\text{th}}$  leading jet separation  $(\Delta R_{ej})$  for hadron level jets for  $W \to e\nu + \geq n$  jets from Alpgen+Pythia MC. The stacked histogram shows the contributions from each of the 5 parton samples  $(W \to e\nu + 0\text{-}4\text{p})$ . The four plot represent each inclusive jet multiplicity:  $\geq 1$  for upper-left,  $\geq 2$  for upper-right,  $\geq 3$  for lower-left, and  $\geq 4$  for lower-right.

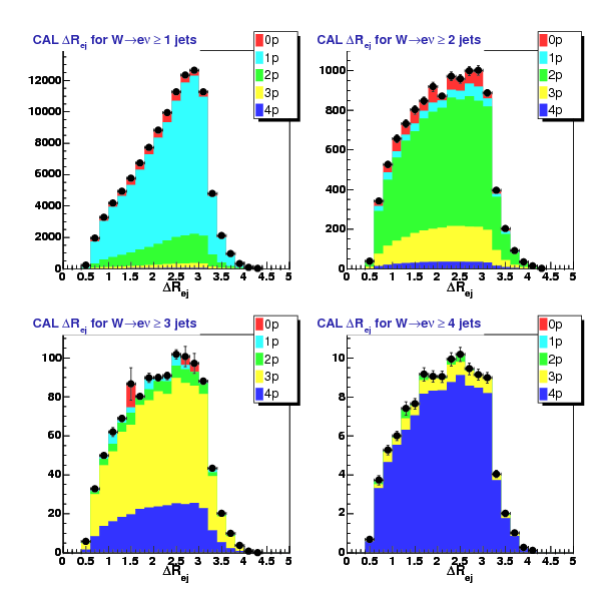


Figure 46: The electron and  $n^{\text{th}}$  leading jet separation ( $\Delta R_{ej}$ ) for calorimeter (detector simulation) level jets for  $W \to e\nu + \geq n$  jets from Alpgen+Pythia MC. The stacked histogram shows the contributions from each of the 5 parton samples ( $W \to e\nu + 0$ -4p). The four plot represent each inclusive jet multiplicity:  $\geq 1$  for upper-left,  $\geq 2$  for upper-right,  $\geq 3$  for lower-left, and  $\geq 4$  for lower-right.

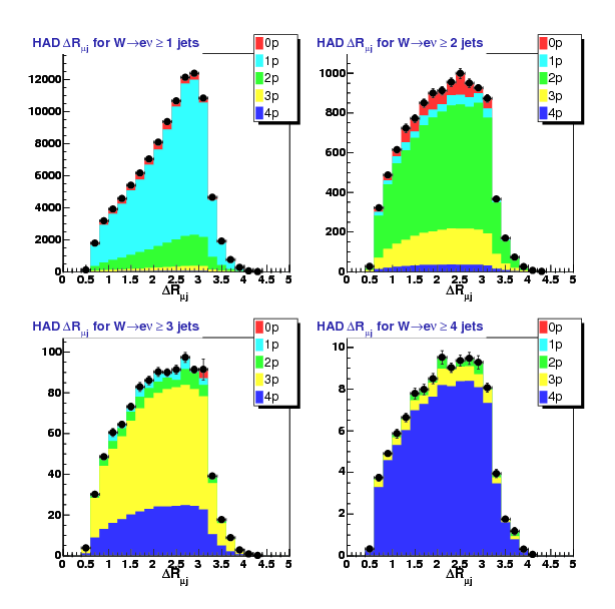


Figure 47: The muon and  $n^{\text{th}}$  leading jet separation  $(\Delta R_{\mu j})$  for hadron level jets for  $W \to \mu\nu + \geq n$  jets from Alpgen+Pythia MC. The stacked histogram shows the contributions from each of the 5 parton samples  $(W \to e\nu + 0\text{-}4\text{p})$ . The four plot represent each inclusive jet multiplicity:  $\geq 1$  for upper-left,  $\geq 2$  for upper-right,  $\geq 3$  for lower-left, and  $\geq 4$  for lower-right.

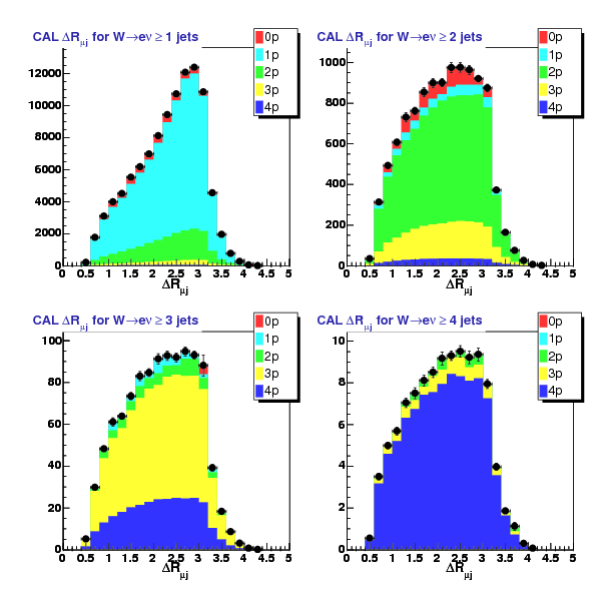


Figure 48: The muon and  $n^{\text{th}}$  leading jet separation ( $\Delta R_{\mu j}$ ) for calorimeter (detector simulation) level jets for  $W \to \mu \nu + \geq n$  jets from Alpgen+Pythia MC. The stacked histogram shows the contributions from each of the 5 parton samples ( $W \to \mu \nu + 0$ -4p). The four plot represent each inclusive jet multiplicity:  $\geq 1$  for upper-left,  $\geq 2$  for upper-right,  $\geq 3$  for lower-left, and  $\geq 4$  for lower-right.

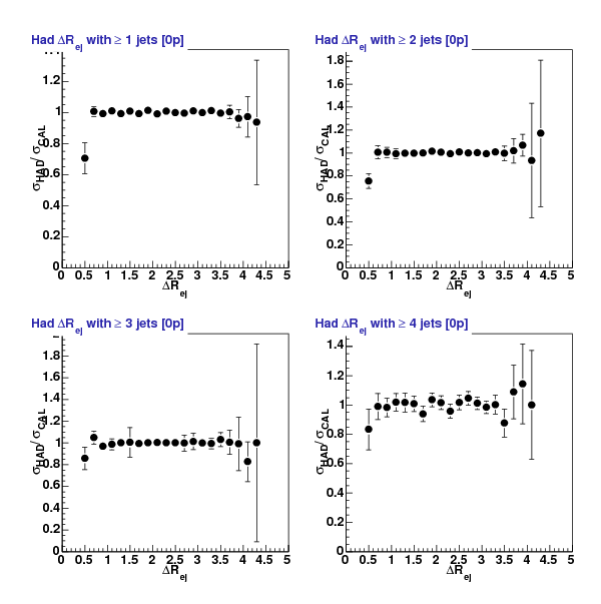


Figure 49: Unfolding factor  $(u = \sigma(HAD)/\sigma(CAL))$ , see equation 15 on page 57) for  $\Delta R_{ej}$  for  $W \to e\nu + \geq n$  jets from Alpgen+Pythia MC. The title for each plot should be ignored to avoid confusion with its content. The four plot represent each inclusive jet multiplicity:  $\geq 1$  for upper-left,  $\geq 2$  for upper-right,  $\geq 3$  for lower-left, and  $\geq 4$  for lower-right.

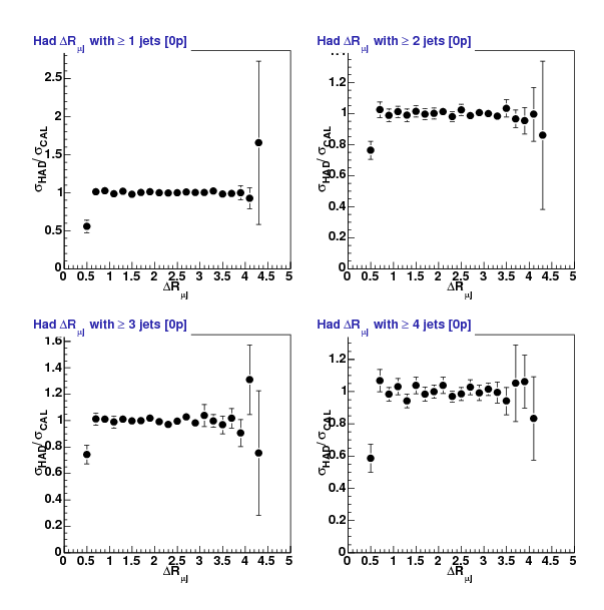


Figure 50: Unfolding factor  $(u = \sigma(HAD)/\sigma(CAL))$ , see equation 15 on page 57) for  $\Delta R_{\mu j}$  for  $W \to \mu \nu + \geq n$  jets from Alpgen+Pythia MC. The title for each plot should be ignored to avoid confusion with its content. The four plot represent each inclusive jet multiplicity:  $\geq 1$  for upper-left,  $\geq 2$  for upper-right,  $\geq 3$  for lower-left, and  $\geq 4$  for lower-right.

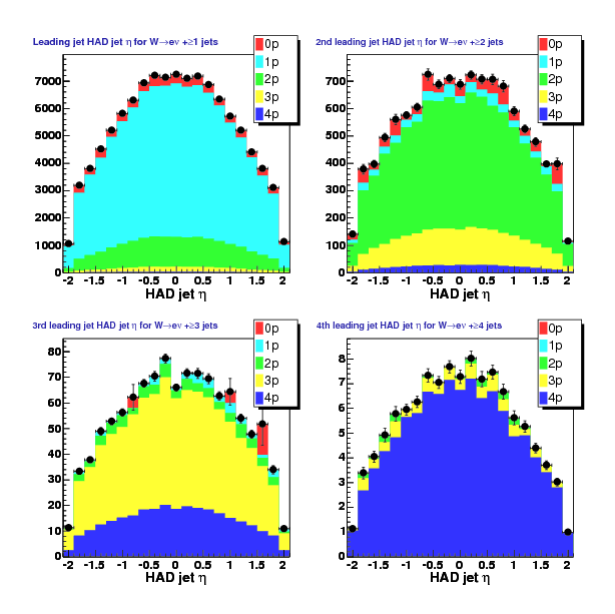


Figure 51:  $n^{\text{th}}$  leading jet  $\eta$  of hadron level jets for  $W \to e\nu + \geq n$  jets from Alpgen+Pythia MC. The stacked histogram shows the contributions from each of the 5 parton samples  $(W \to e\nu + 0-4p)$ . The four plot represent each inclusive jet multiplicity:  $\geq 1$  for upper-left,  $\geq 2$  for upper-right,  $\geq 3$  for lower-left, and  $\geq 4$  for lower-right.

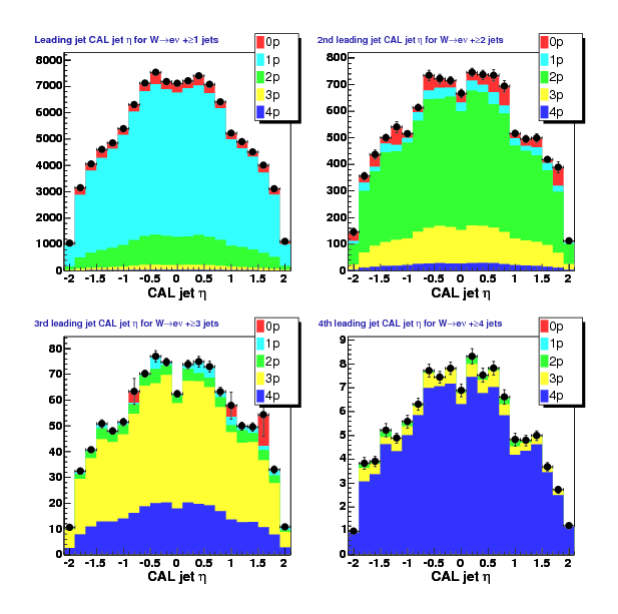


Figure 52:  $n^{\rm th}$  leading jet  $\eta$  of calorimeter (detector simulation) level jets for  $W \to e\nu + \geq n$  jets from Alpgen+Pythia MC. The stacked histogram shows the contributions from each of the 5 parton samples ( $W \to e\nu + 0$ -4p). The four plot represent each inclusive jet multiplicity:  $\geq 1$  for upper-left,  $\geq 2$  for upper-right,  $\geq 3$  for lower-left, and  $\geq 4$  for lower-right.

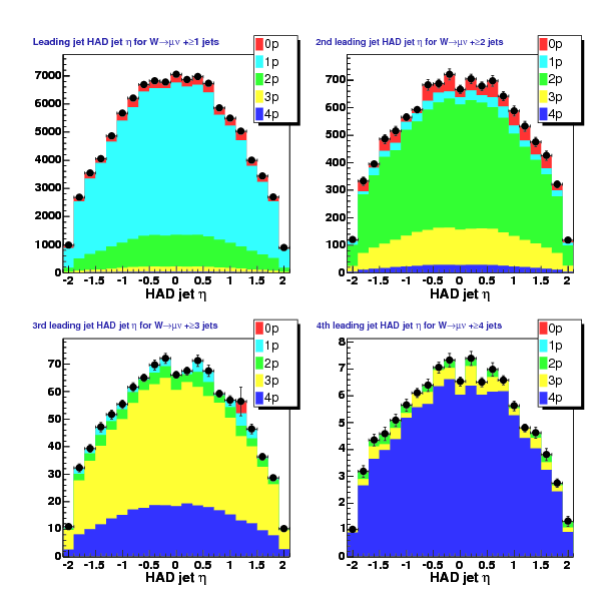


Figure 53:  $n^{\rm th}$  leading jet  $\eta$  of hadron level jets for  $W \to \mu\nu + \geq n$  jets from Alpgen+Pythia MC. The stacked histogram shows the contributions from each of the 5 parton samples ( $W \to \mu\nu + 0$ -4p). The four plot represent each inclusive jet multiplicity:  $\geq 1$  for upper-left,  $\geq 2$  for upper-right,  $\geq 3$  for lower-left, and  $\geq 4$  for lower-right.

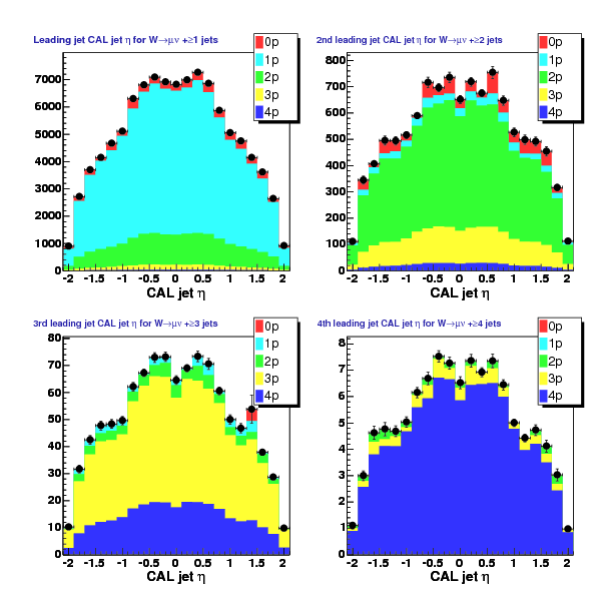


Figure 54:  $n^{\rm th}$  leading jet  $\eta$  of calorimeter (detector simulation) level jets for  $W \to \mu\nu + \geq n$  jets from Alpgen+Pythia MC. The stacked histogram shows the contributions from each of the 5 parton samples ( $W \to \mu\nu + 0$ -4p). The four plot represent each inclusive jet multiplicity:  $\geq 1$  for upper-left,  $\geq 2$  for upper-right,  $\geq 3$  for lower-left, and  $\geq 4$  for lower-right.

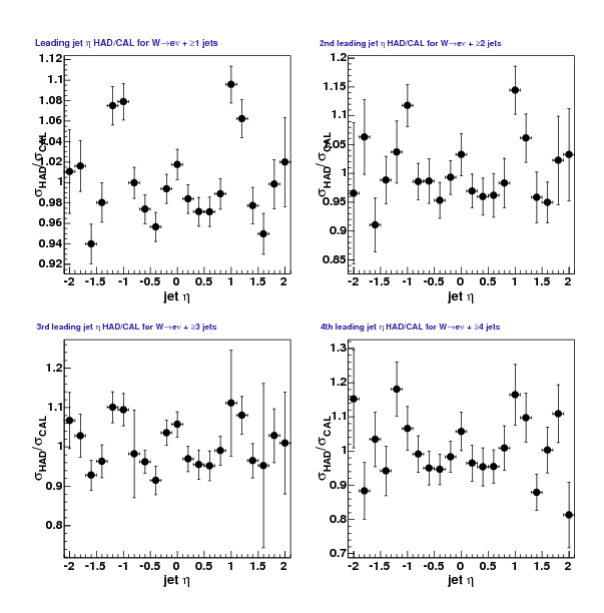


Figure 55: Unfolding factor  $(\sigma(HAD)/\sigma(CAL))$  of the  $n^{\text{th}}$  leading jet  $\eta$  for  $W \to e\nu + \geq n$  jets from Alpgen+Pythia MC. The four plot represent each inclusive jet multiplicity:  $\geq 1$  for upper-left,  $\geq 2$  for upper-right,  $\geq 3$  for lower-left, and  $\geq 4$  for lower-right.

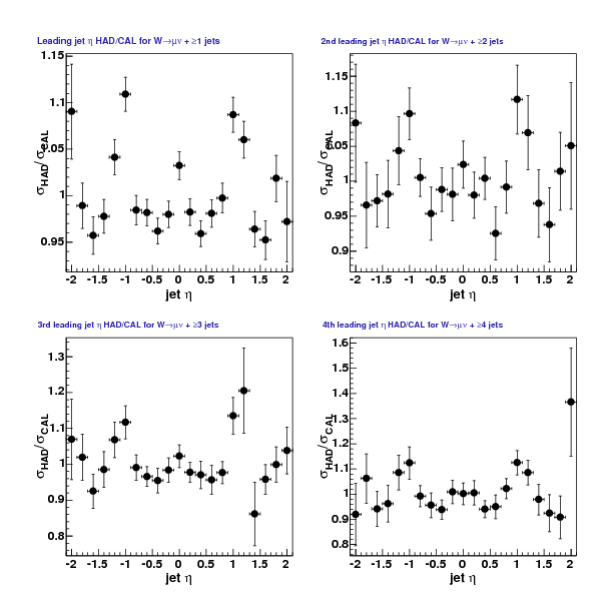


Figure 56: Unfolding factor  $(\sigma(HAD)/\sigma(CAL))$  of the  $n^{\text{th}}$  leading jet  $\eta$  for  $W \to \mu\nu + \geq n$  jets from Alpgen+Pythia MC. The four plot represent each inclusive jet multiplicity:  $\geq 1$  for upper-left,  $\geq 2$  for upper-right,  $\geq 3$  for lower-left, and  $\geq 4$  for lower-right.

	$W \rightarrow e\nu$	$W \rightarrow e\nu$	$W \rightarrow \mu\nu$	$W \rightarrow \mu\nu$
$\geq n$ jets	u	$\Delta u$	u	$\Delta u$
0	1.0000	0.0028	1.0000	0.0029
1	0.7557	0.0031	0.7793	0.0032
2	0.6445	0.0061	0.6771	0.0064
3	0.5759	0.0103	0.6069	0.0101
4	0.5410	0.0134	0.5822	0.0186

Table 15: Jet multiplicity unfolding factor and its associated error for  $W \to \ell \nu$  Alpgen MC. Calculated directly via equations 15 and 17. This unfolding factor can be applied to results where the bin-by-bin unfolding factor for a differential cross-section is flat and relatively uniform (e.g.  $R_{jj}$ ). The total inclusive unfolding factor is effectively unity by construction as the inclusive W acceptance is invariant to jet definition/algorithm.

y-axis as  $\sigma_{HAD}/\sigma_{CAL}$ . The error is statistical and follows via the naive error propagation of dividing the two histograms (see equation 17). Kinematic observables with momentum, mass, energy, etc. by in large have features that make bin-by-bin corrections a necessity and as such do not use the universal unfolding factor of table 15.

We begin by presenting the unfolding factor for the  $n^{\rm th}$  leading jet  $p_T$  for  $W \to \ell \nu + \geq n$  jets. Figure 57 presents the results for 1-4 jets in the electron channel; likewise the muon channel results are given in figure 58. The jet  $p_T$  is very much central to this analysis and is directly effected by this hadron level correction procedure. As a result, we also have several follow up plots that check various factors. For example, figure 59 shows the first and second jet  $p_T$  for inclusive 3 jets for both electron and muon channels. This was done to check the unfolding factor at higher jet multiplicities (the  $n^{\rm th}$  leading jet  $p_T$  is dominated by the exclusive n number of jets). We repeated this style of plot for the first, second, and third leading jet  $p_T$  for  $\geq 4$  jets. The electron channel is shown in figure 60 while the muon channel is given in figure 61.

Continuing with our additional set of unfolding plots for jet  $p_T$  we present results where we modified our procedure to directly match (event-by-event) hadron level jets to their calorimeter simulated counterparts. Figures 64 and 65 correspond to the electron and muon results, respectively, of figures 57 and 58. Although we do not use this results directly, they are useful as a check on our default (unmatched) scheme described previously. This "true matching" scheme is effectively the same make up sample wise with our ratio plots present in the previous section (e.g. figures 37-44 and our  $\Delta R_{\ell,j}$  example). The strict matching requirement requires each jet in the CAL sample to have a corresponding jet in the HAD sample and vise versa. Hadron level jets are allowed to jockey for position relative to being matched with the calorimeter jet ordering. The unfolding factor is still calculated as a proper quotient between pseudo cross-sections for HAD and CAL. The advantage to this procedure is that the acceptance is literally equal between both qualities (the jet multiplicity is identical for HAD and CAL event-by-event).

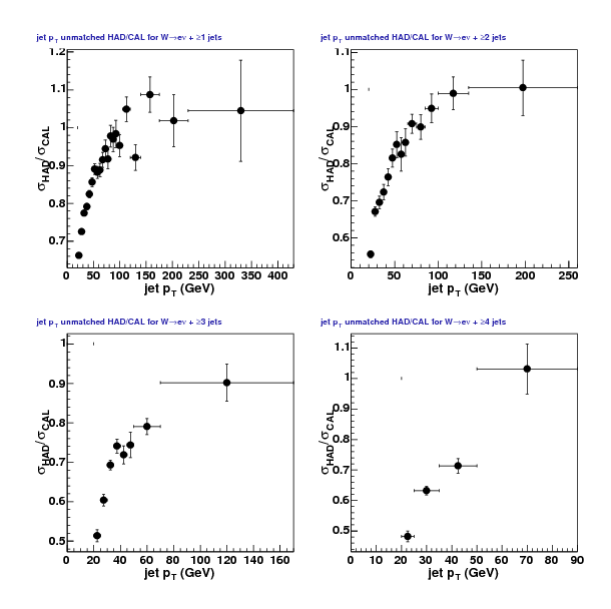


Figure 57: Unfolding factor  $(\sigma(HAD)/\sigma(CAL))$  of the  $n^{\rm th}$  leading jet  $p_T$  for  $W \to e\nu + \geq n$  jets from Alpgen+Pythia MC. The four plot represent each inclusive jet multiplicity:  $\geq 1$  for upper-left,  $\geq 2$  for upper-right,  $\geq 3$  for lower-left, and  $\geq 4$  for lower-right.

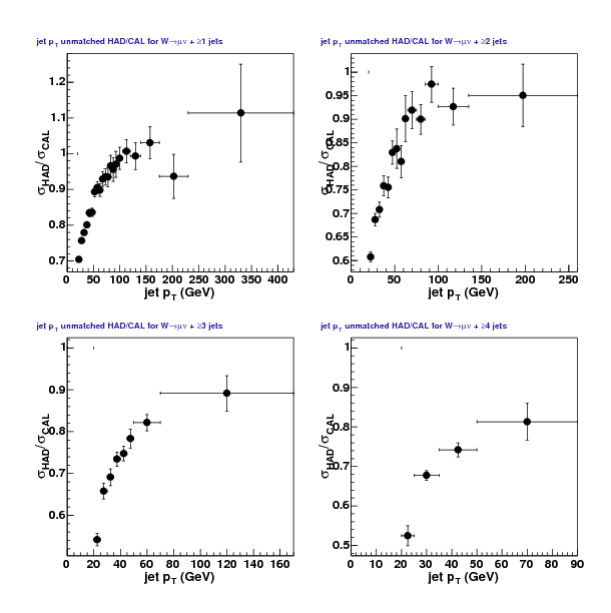


Figure 58: Unfolding factor  $(\sigma(HAD)/\sigma(CAL))$  of the  $n^{\text{th}}$  leading jet  $p_T$  for  $W \to \mu\nu + \geq n$  jets from Alpgen+Pythia MC. The four plot represent each inclusive jet multiplicity:  $\geq 1$  for upper-left,  $\geq 2$  for upper-right,  $\geq 3$  for lower-left, and  $\geq 4$  for lower-right.

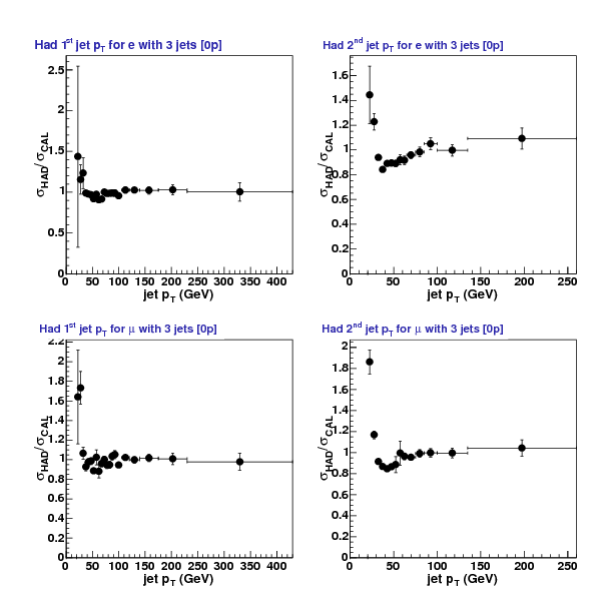


Figure 59: Unfolding factor  $(\sigma(HAD)/\sigma(CAL))$  of the first (left side) and second (right side) leading jet  $p_T$  for  $W \to \ell \nu + \geq 3$  jets from Alpgen+Pythia MC. The top plots are for the electron channel while the bottom ones are for the muon channel.

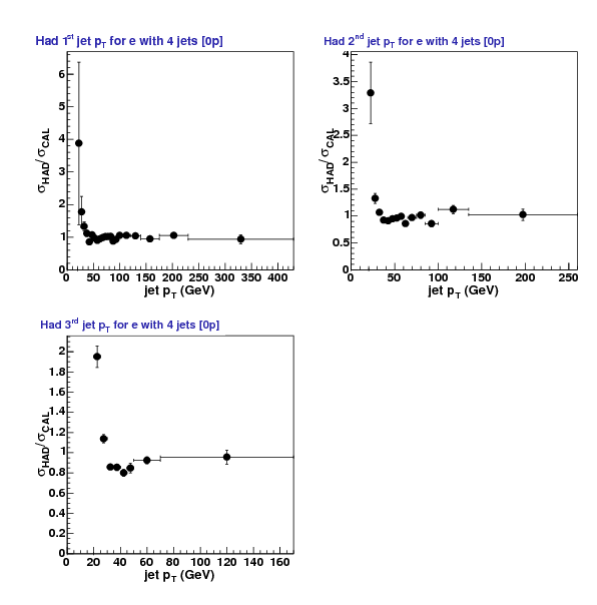


Figure 60: Unfolding factor  $(\sigma(HAD)/\sigma(CAL))$  of the first (upper-left side), second (upper-right side), and third leading jet (lower-left side) leading jet  $p_T$  for  $W \to e\nu + \geq 3$  jets from Alpgen+Pythia MC.

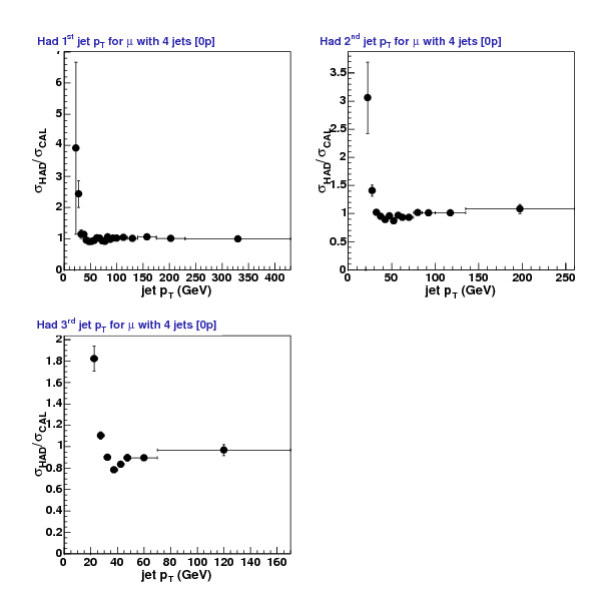


Figure 61: Unfolding factor  $(\sigma(HAD)/\sigma(CAL))$  of the first (upper-left side), second (upper-right side), and third leading jet (lower-left side) leading jet  $p_T$  for  $W \to \mu\nu + \geq 3$  jets from Alpgen+Pythia MC.

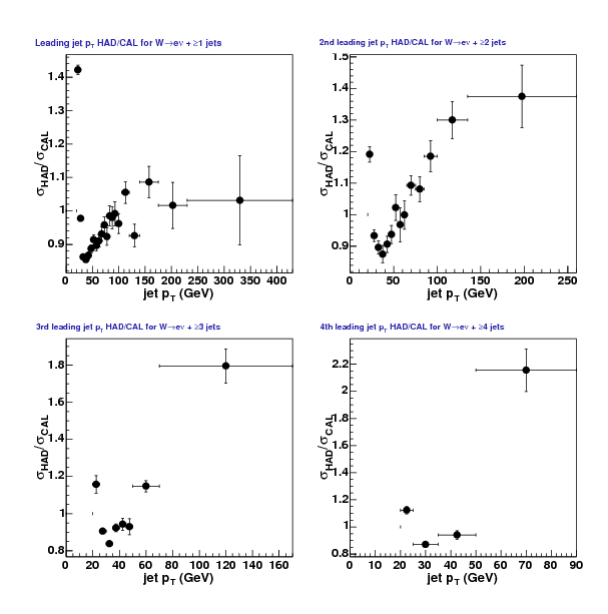


Figure 62: Unfolding factor  $(\sigma(HAD)/\sigma(CAL))$  of the  $n^{\text{th}}$  leading jet  $p_T$  for  $W \to e\nu + \geq n$  jets from Alpgen+Pythia MC. These results require that n jets be matched although the number and order are not required to be the same. The four plot represent each inclusive jet multiplicity:  $\geq 1$  for upper-left,  $\geq 2$  for upper-right,  $\geq 3$  for lower-left, and  $\geq 4$  for lower-right.

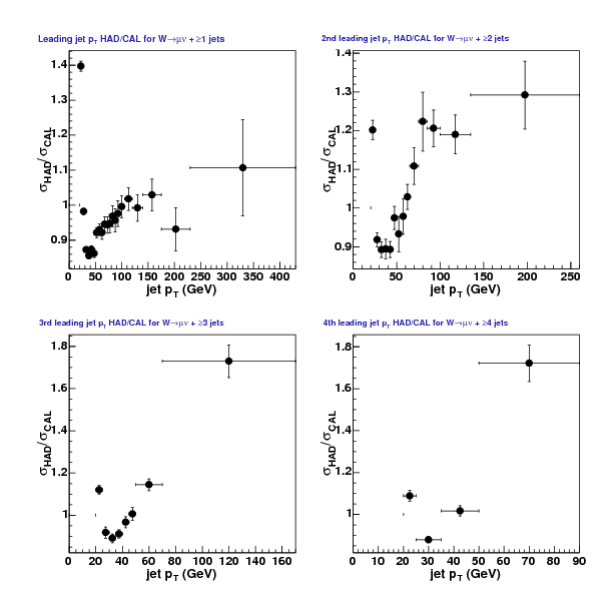


Figure 63: Unfolding factor  $(\sigma(HAD)/\sigma(CAL))$  of the  $n^{\text{th}}$  leading jet  $p_T$  for  $W \to \mu\nu + \geq n$  jets from Alpgen+Pythia MC. These results require that n jets be matched although the number and order are not required to be the same. The four plot represent each inclusive jet multiplicity:  $\geq 1$  for upper-left,  $\geq 2$  for upper-right,  $\geq 3$  for lower-left, and  $\geq 4$  for lower-right.

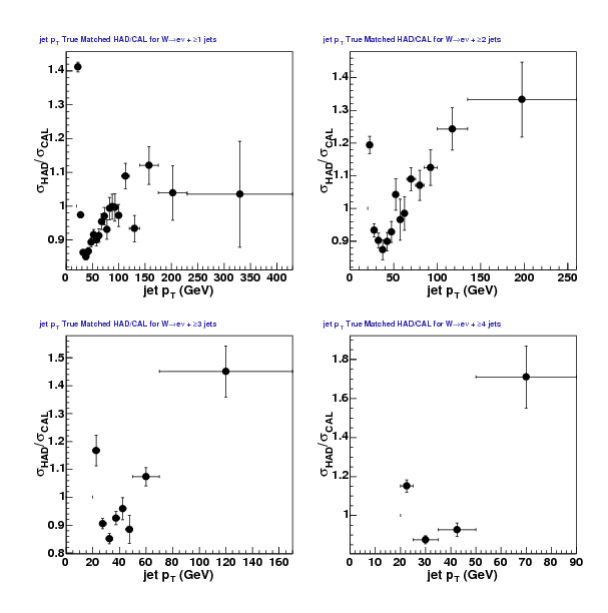


Figure 64: Unfolding factor  $(\sigma(HAD)/\sigma(CAL))$  of the  $n^{\text{th}}$  leading jet  $p_T$  for  $W \to e\nu + \geq n$  jets from Alpgen+Pythia MC where both pseudo-cross-sections have been constructed via a sample where every calorimeter jet is matched ("true matched") to its hadron level counterpart. While biased toward the calorimeter jet definition jet  $p_T$  ordering, it has the virtue of having explicitly equal number of events in both HAD and CAL samples. The four plot represent each inclusive jet multiplicity:  $\geq 1$  for upper-left,  $\geq 2$  for upper-right,  $\geq 3$  for lower-left, and  $\geq 4$  for lower-right.

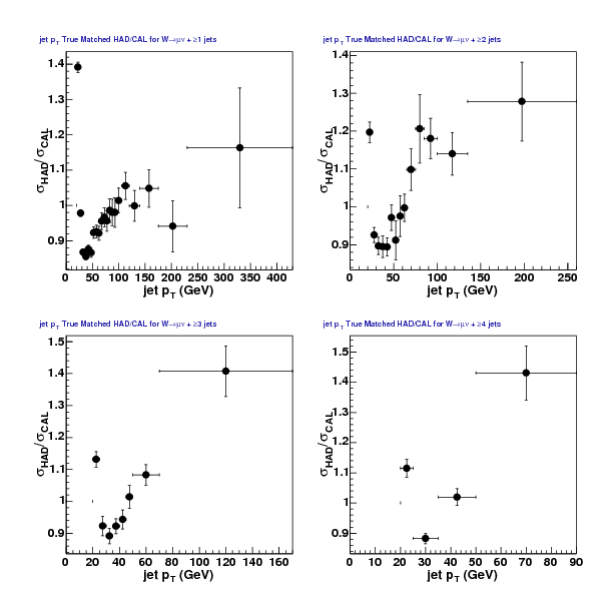


Figure 65: Unfolding factor  $(\sigma(HAD)/\sigma(CAL))$  of the  $n^{\text{th}}$  leading jet  $p_T$  for  $W \to \mu\nu + \geq n$  jets from Alpgen+Pythia MC where both pseudo-cross-sections have been constructed via a sample where every calorimeter jet is matched ("true matched") to its hadron level counterpart. While biased toward the calorimeter jet definition jet  $p_T$  ordering, it has the virtue of having explicitly equal number of events in both HAD and CAL samples. The four plot represent each inclusive jet multiplicity:  $\geq 1$  for upper-left,  $\geq 2$  for upper-right,  $\geq 3$  for lower-left, and  $\geq 4$  for lower-right.

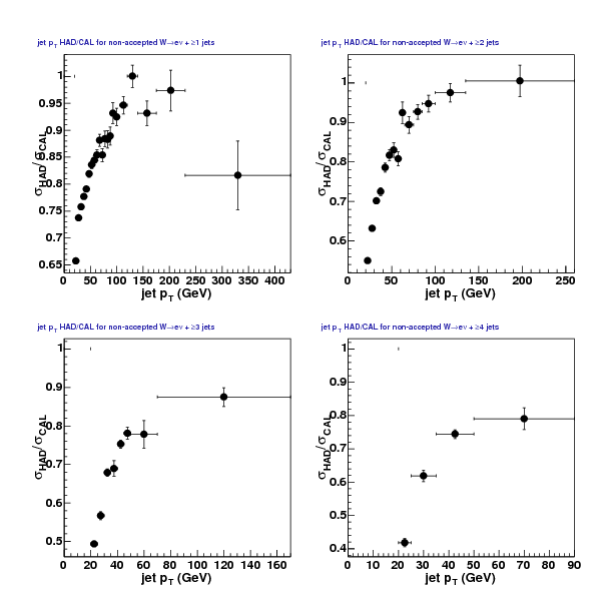


Figure 66: Unfolding factor  $(\sigma(HAD)/\sigma(CAL))$  of the  $n^{\text{th}}$  leading jet  $p_T$  for  $W \to e\nu + \geq n$  jets from Alpgen+Pythia MC for events where it failed W selection (i.e. was not accepted). The four plot represent each inclusive jet multiplicity:  $\geq 1$  for upper-left,  $\geq 2$  for upper-right,  $\geq 3$  for lower-left, and  $\geq 4$  for lower-right.

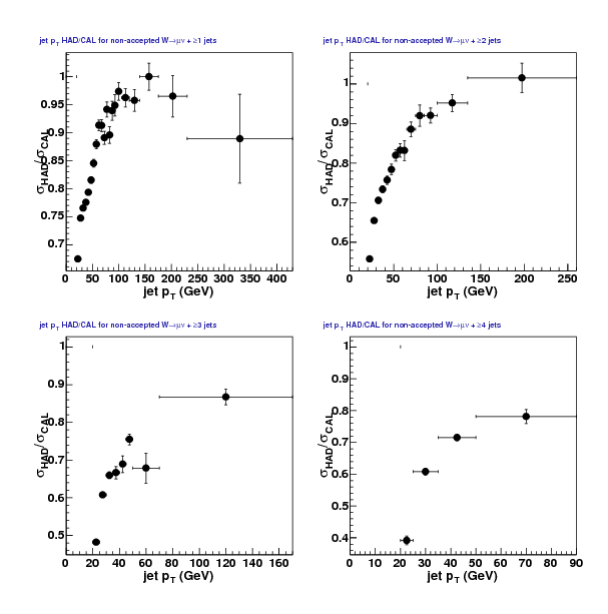


Figure 67: Unfolding factor  $(\sigma(HAD)/\sigma(CAL))$  of the  $n^{\text{th}}$  leading jet  $p_T$  for  $W \to \mu\nu + \geq n$  jets from Alpgen+Pythia MC for events where it failed W selection (i.e. was not accepted). The four plot represent each inclusive jet multiplicity:  $\geq 1$  for upper-left,  $\geq 2$  for upper-right,  $\geq 3$  for lower-left, and  $\geq 4$  for lower-right.

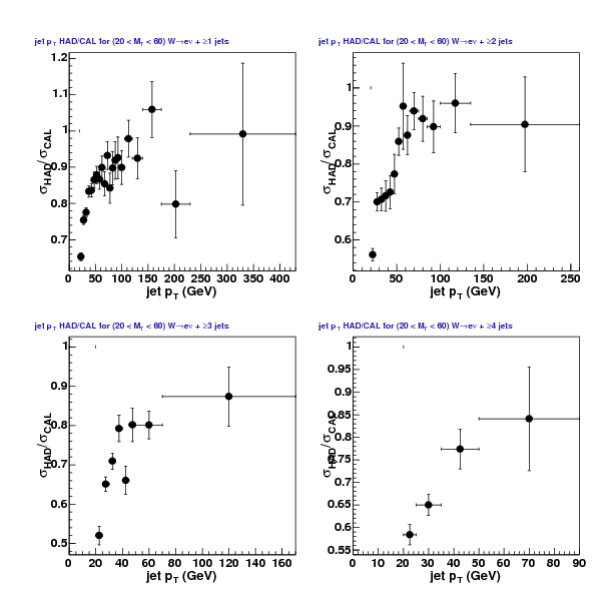


Figure 68: Unfolding factor  $(\sigma(HAD)/\sigma(CAL))$  of the  $n^{\text{th}}$  leading jet  $p_T$  for  $W \to e\nu + \geq n$  jets for events with the W transverse mass limited to  $20 < M_T < 60$  from Alpgen+Pythia MC. The four plot represent each inclusive jet multiplicity:  $\geq 1$  for upper-left,  $\geq 2$  for upper-right,  $\geq 3$  for lower-left, and  $\geq 4$  for lower-right.

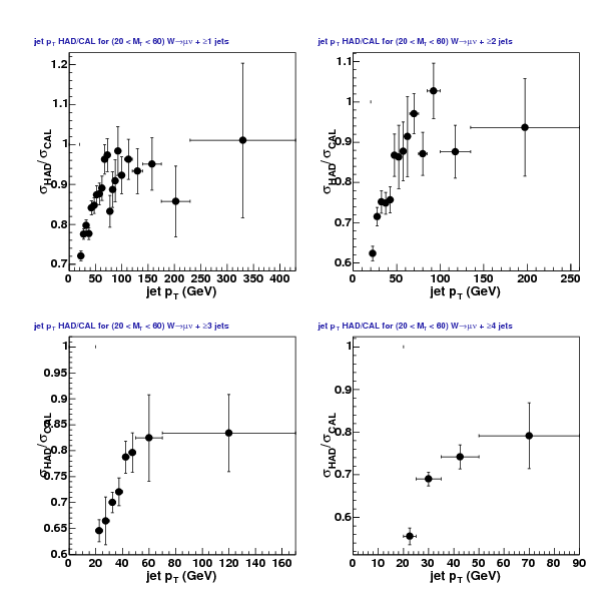


Figure 69: Unfolding factor  $(\sigma(HAD)/\sigma(CAL))$  of the  $n^{\text{th}}$  leading jet  $p_T$  for  $W \to \mu\nu + \geq n$  jets for events with the W transverse mass limited to  $20 < M_T < 60$  from Alpgen+Pythia MC. The four plot represent each inclusive jet multiplicity:  $\geq 1$  for upper-left,  $\geq 2$  for upper-right,  $\geq 3$  for lower-left, and  $\geq 4$  for lower-right.

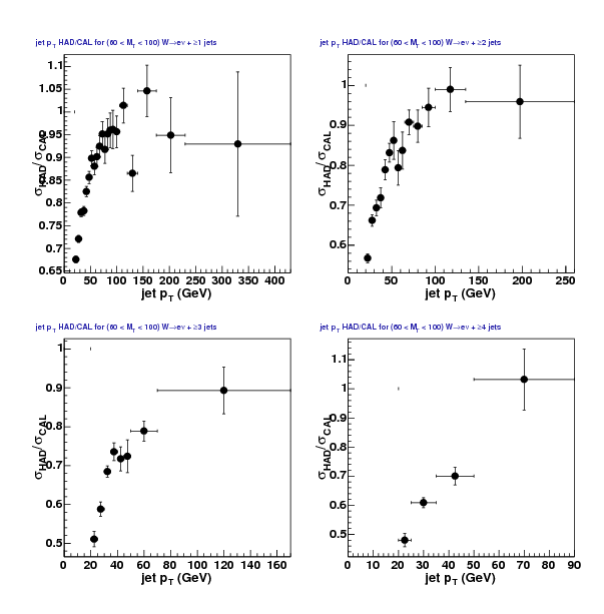


Figure 70: Unfolding factor  $(\sigma(HAD)/\sigma(CAL))$  of the  $n^{\text{th}}$  leading jet  $p_T$  for  $W \to e\nu + \geq n$  jets for events with the W transverse mass limited to  $60 < M_T < 100$  from Alpgen+Pythia MC. The four plot represent each inclusive jet multiplicity:  $\geq 1$  for upper-left,  $\geq 2$  for upper-right,  $\geq 3$  for lower-left, and  $\geq 4$  for lower-right.

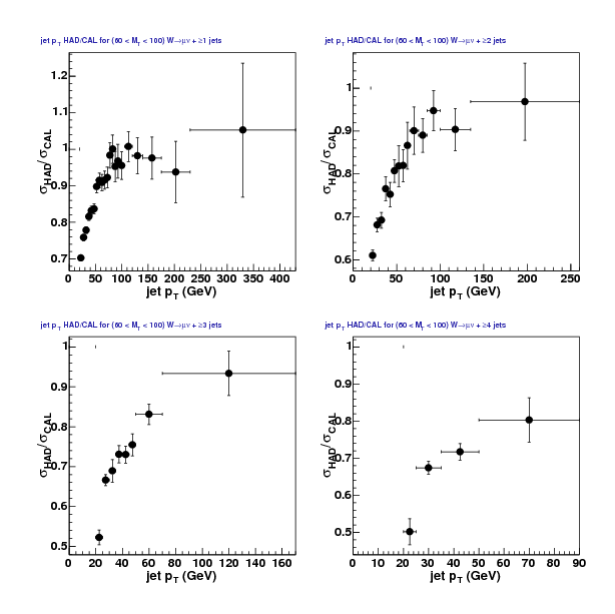


Figure 71: Unfolding factor  $(\sigma(HAD)/\sigma(CAL))$  of the  $n^{\text{th}}$  leading jet  $p_T$  for  $W \to \mu\nu + \geq n$  jets for events with the W transverse mass limited to  $60 < M_T < 100$  from Alpgen+Pythia MC. The four plot represent each inclusive jet multiplicity:  $\geq 1$  for upper-left,  $\geq 2$  for upper-right,  $\geq 3$  for lower-left, and  $\geq 4$  for lower-right.

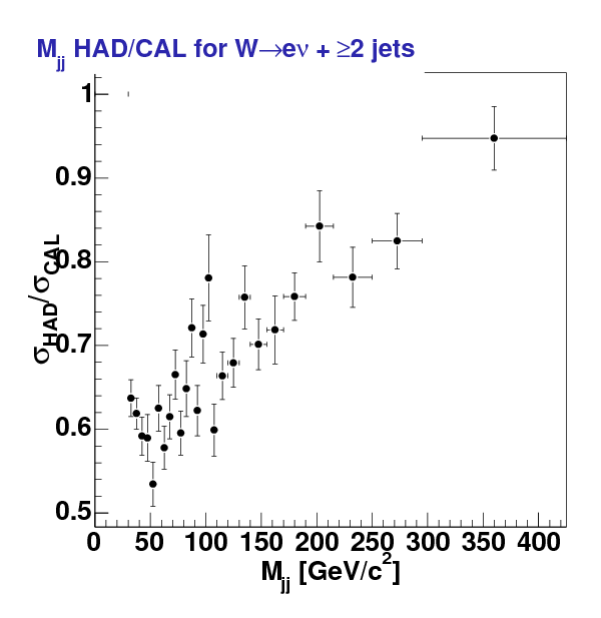


Figure 72: Unfolding factor  $(\sigma(HAD)/\sigma(CAL))$  of the dijet mass  $(m_{jj})$  as defined in section 7.5 (page 243) for  $W \to e\nu + \geq 2$  jets from Alpgen+Pythia MC.

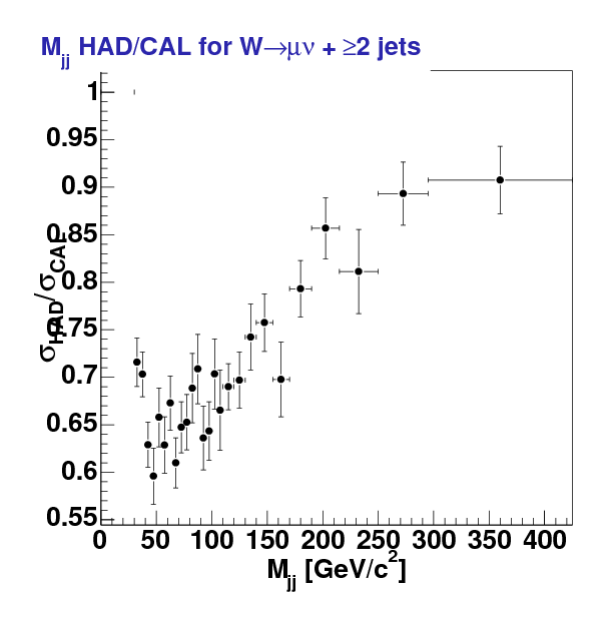


Figure 73: Unfolding factor  $(\sigma(HAD)/\sigma(CAL))$  of the dijet mass  $(m_{jj})$  as defined in section 7.5 (page 243) for  $W \to \mu\nu + \geq 2$  jets from Alpgen+Pythia MC.

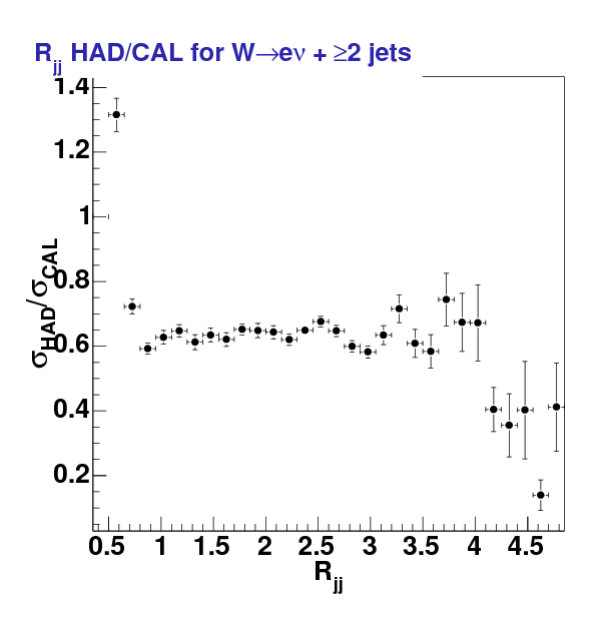


Figure 74: Unfolding factor  $(\sigma(HAD)/\sigma(CAL))$  of the dijet separation  $(R_{jj})$  as defined in section 7.6 (page 243) for  $W \to e\nu + \geq 2$  jets from Alpgen+Pythia MC.

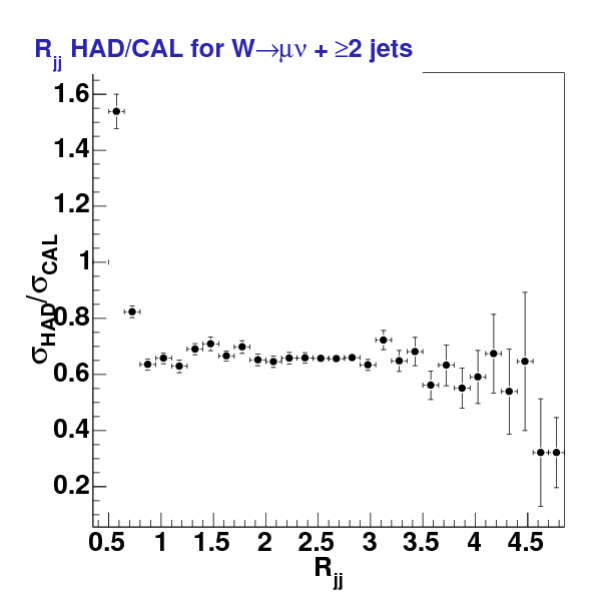


Figure 75: Unfolding factor  $(\sigma(HAD)/\sigma(CAL))$  of the dijet separation  $(R_{jj})$  as defined in section 7.6 (page 243) for  $W \to \mu\nu + \geq 2$  jets from Alpgen+Pythia MC.

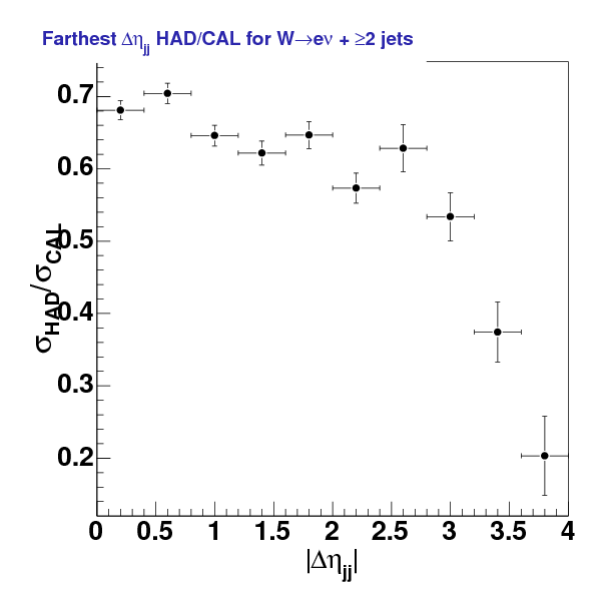


Figure 76: Unfolding factor  $(\sigma(HAD)/\sigma(CAL))$  for  $\Delta \eta_{jj}$  between the closest jet pair (defined in section 7.7 on page 247) for  $W \to e\nu + \geq 2$  jets from Alpgen+Pythia MC.

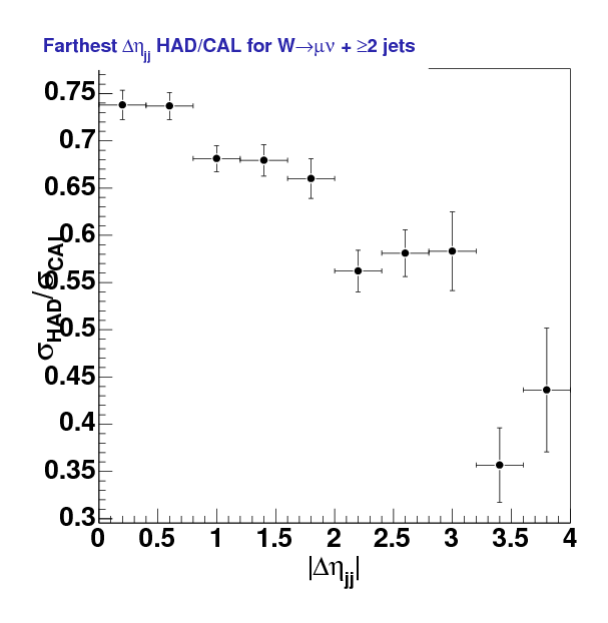


Figure 77: Unfolding factor  $(\sigma(HAD)/\sigma(CAL))$  for  $\Delta \eta_{jj}$  between the closest jet pair (defined in section 7.7 on page 247) for  $W \to \mu\nu + \geq 2$  jets from Alpgen+Pythia MC.

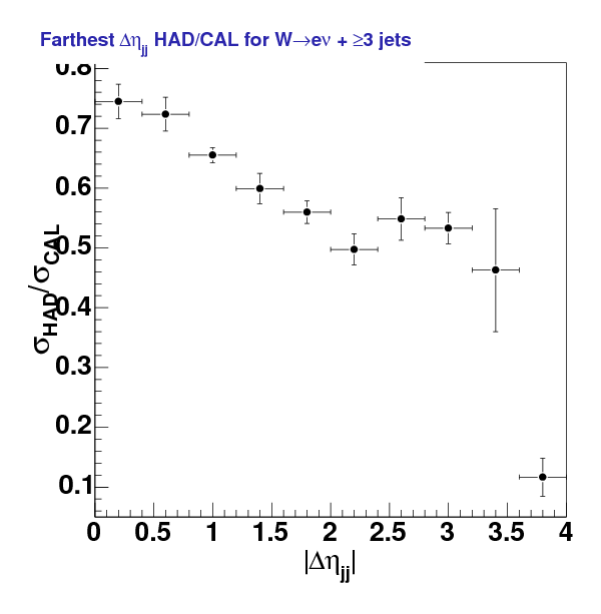


Figure 78: Unfolding factor  $(\sigma(HAD)/\sigma(CAL))$  for  $\Delta \eta_{jj}$  between the closest jet pair (defined in section 7.7 on page 247) for  $W \to e\nu + \geq 3$  jets from Alpgen+Pythia MC.

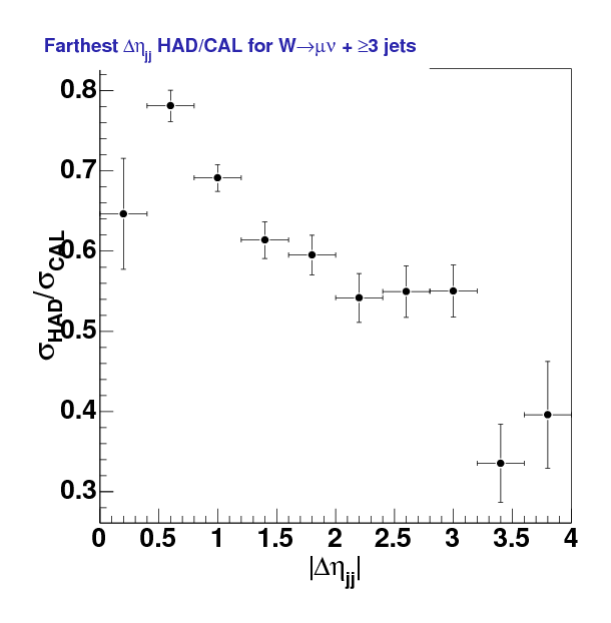


Figure 79: Unfolding factor  $(\sigma(HAD)/\sigma(CAL))$  for  $\Delta \eta_{jj}$  between the closest jet pair (defined in section 7.7 on page 247) for  $W \to \mu\nu + \geq 3$  jets from Alpgen+Pythia MC.

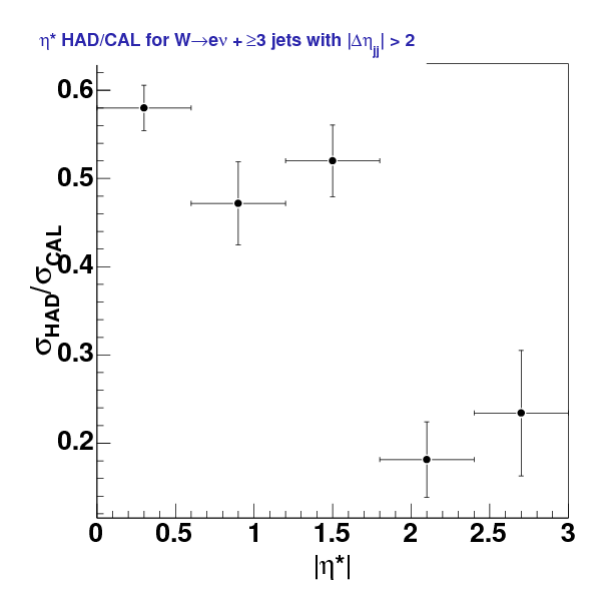


Figure 80: Unfolding factor  $(\sigma(HAD)/\sigma(CAL))$  for  $\eta^*$  as defined in section 7.7 (page 247) for  $W \to e\nu + \geq 3$  jets from Alpgen+Pythia MC.

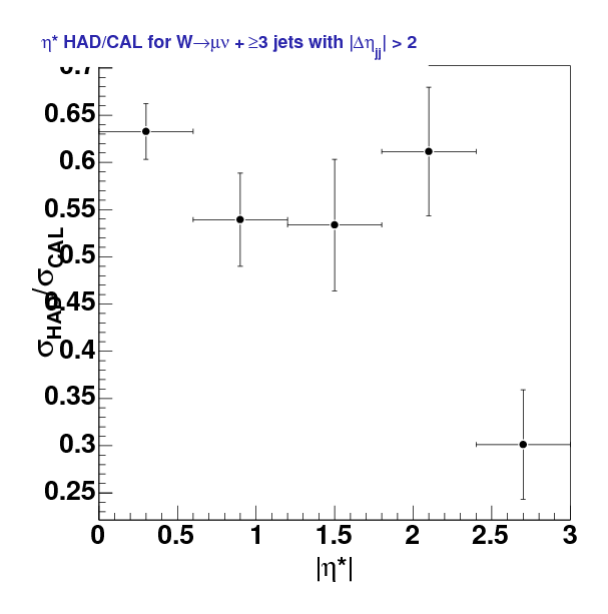


Figure 81: Unfolding factor  $(\sigma(HAD)/\sigma(CAL))$  for  $\eta^*$  as defined in section 7.7 (page 247) for  $W \to \mu\nu + \geq 3$  jets from Alpgen+Pythia MC.

# 4 Background Estimation

In order to measure various jet kinematic cross-sections for W+jets we must first understand the various backgrounds that either have the same final state or that can otherwise mimic or fake our signal. This chapter deals with our background estimation in addition to a basic goal of understanding our signal MC. We classify our backgrounds into three different categories: electro-weak (EWK) backgrounds from  $W \to \tau \nu+$ jets and  $Z \to \ell\ell+$ jets, quantum chromodynamics (QCD) background fakes from multi-jets and semi-leptonic decays as well as punch-throughs, and "fixed" contributions including diboson (defined here as WW, WZ, and  $W\gamma^*$ ) and  $t\bar{t}$  production. We describe the latter estimation of our fixed contributions in a straightforward manner in section 4.1.

In the case of our EWK background the goal is to get estimations that do not depend upon theoretical predictions for  $W \to \tau \nu$  and  $Z \to \ell \ell$  with n inclusive jets. Similarly, it is difficult to obtain an appropriate and inclusive fake rate for our non-W QCD background and to be able to comfortably apply a rate that is not jet multiplicity dependent. Our solution to these separate issues is to form two templates based on the shape of various lepton variables via our MC samples (EWK) and a special anti-selection lepton sample from the data (QCD). In particular, we look at the transverse mass shapes (before our final W selection cut via the transverse mass) for each template and fit this to the observed distribution in data minus our contributions from our previously mentioned dibosons and  $t\bar{t}$  estimation. Based on our fitted scalings we then apply this scale to each of template samples (with the final W selection cut on the transverse mass) to arrive at our final background estimation.

Our EWK template is explained in section 4.2. The construction and details of our QCD sample and template are given in 4.3 which follows from the modified selection criteria of sections 2.2 (anti-selected electrons) and 2.4 (anti-selected muons). The theory and formal procedure for fitting our templates to the data is described in section 4.4. This is followed by our fitting results from which we derive our final background estimations. Additionally section 4.5 showcases numerous quality check plots which demonstrate good agreement across a spectrum of W and lepton observables. Based on this agreement and understanding we can then subtract our background estimation across an array of jet kinematic observables which serves as the basses for the W+jets cross-sections we present in chapter 7.

# 4.1 Diboson + $t\bar{t}$ Background Estimation

We use the WW, WZ,  $W\gamma^*$ , and  $t\bar{t}$  MC samples outlined in section 1.5 and our normal W selection criteria (see chapter 2). Unlike in our estimation of the other processes where we wish to have a data-driven method that is independent of theoretical cross-section, we directly estimate the number of expected events via the theoretical cross-section, the number of events in each MC sample, and the luminosity of the data. We present the theoretical cross-sections used and their associated errors in table 16.

The diboson (defined here as WW, WZ, and  $W\gamma^*$ ) theoretical cross-sections are taken from [14]. Note that the  $W\gamma^*$  cross-section production is for a single lepton channel and we consider

Background	Cross-section	Error
Process	$\sigma(\text{theory}) \text{ (pb)}$	$\Delta \sigma(\text{theory}) \text{ (pb)}$
$t\bar{t}$	7.50	0.48
WW	12.4	0.8
WZ	3.96	0.3
$W\gamma^*$	19.3	1.4

Table 16: Experimental  $t\bar{t}$  cross-section and theoretical cross-sections for WW, WZ,  $W\gamma^*$ . See references cited in [14] (dibosons) and [15] ( $t\bar{t}$ ) for the theoretical cross-sections while the experimental (CDF)  $t\bar{t}$  cross-section comes from [16]. Tables 3 and 4 provide the MC sample and generator information as well as the # of events in each sample.

both the electron and muon channel but neglect the tau channel. For simplicity we will present the diboson contributions summed together as these never rise above 4% of the expected signal+background. We have investigated the background from ZZ production which is already negligible relative to the smallest included diboson contribution.

The largest "fixed" theoretical (actually experimental) cross-section background estimation contribution comes from  $t\bar{t}$  production [15]. This becomes a significant background for three or more jets. In addition, the jet kinematics for  $t\bar{t}$  (notably the jet  $p_T$  shape) are generally very different from the other backgrounds and the signal. The theoretical cross-section is  $7.27 \pm 0.87$  pb which is the extrapolated (Run II tevatron) cross-section for a top mass of  $172.5 \text{ GeV/c}^2$ . The actual cited and used value of  $7.5 \pm 0.48$  pb is the CDF experimental result assuming a top mass of  $172.5 \text{ GeV/c}^2$  [16].

### 4.2 EWK Signal and Background Template

In order to estimate the electro-weak backgrounds we combine both our signal and background W+jets and Z+jets MC into a common electro-weak (EWK) sample. Our W selection follows from our procedure in chapter 2. However, in order to derive a theory independent estimation of the electro-weak backgrounds we form a template with the W transverse mass ( $M_T$ ) shape with a relaxed  $M_T > 20 \text{ GeV/c}^2$  requirement. We normalize this template for each inclusive jet multiplicity (0-4) to the respective number of events in data (minus the "fixed" diboson and  $t\bar{t}$  backgrounds of the previous section) in the range of  $20 < M_T < 120 \text{ GeV/c}^2$ . We define  $n_{EWK}$  to be the multiplicative scale factor needed to normalize the unscaled EWK sample to the data via our relaxed transverse mass samples. We give the normalization scale factors in table 17. This normalization of the templates (we do this for the QCD template as well) is just an artifact of our fitting which gives us a percentage of each template best describes the data. This "fitting fraction" will eventually be combined with our normalization scale factor and applied to our final electron (muon) EWK background sample with  $M_T > 40$  (30) GeV/c² based on the fitting described in section 4.4.

The results of table 17 are relatively trivial to understand in relation to the dependence on the size and background composition of our W candidates in data. For example, the electrons universally have a higher normalization as we expect more QCD/fakes background events in our

$\geq n$ jets	$n_{EWK}$ for Electrons	$n_{EWK}$ for Muons
0	1.723	1.290
1	2.284	1.395
2	2.604	1.507
3	2.957	1.760
4	3.539	1.948

Table 17: EWK template normalization scale factors  $(n_{EWK})$  for each inclusive jet multiplicity (0-4). The electron results will be used for our  $W \to e\nu + \geq n$  jets EWK background while the muons will be used for  $W \to \mu\nu + \geq n$  jets.

data sample compared to the muons. Likewise, the inclusive  $(\geq)$  0 jet multiplicity bin which is dominated by exclusive (=) 0 jet by construction filters the potential QCD background present and results in a smaller normalization. In the case of our electron channel, this is exacerbated due to electrons and jets both sharing being reconstructed (in part, in the former case) by the calorimeter.

Note that unlike the case for the QCD template construction (see the following section) the sample construction is straightforward as we apply the same selection cuts as we do in the data. The samples we use are given in section 1.5 and include the various W (electron and muon for signal with tau as a background) and Z (all lepton channels) samples with 0-4 partons MLM matched and the relative weighting of the MC described in section 1.6. Although this is implicit in the handling of our Z background and W signal samples, we want to make it explicit that we are not applying a post hoc W/Z cross-section ratio to scale the background to the signal (or vice-versa). Rather we make the assumption that the underlining electroweak physics is correct and consistent for each 0-4 parton sample. We then observe that the ratio of the W and Z cross-sections ( $R_{W/Z} = \sigma_W/\sigma_Z$ ) using Alpgen MC is consistant with the CDF measurements in data [46]. We also trivially note that we observe lepton universality ( $\sigma(W \to e\nu) = \sigma(W \to \mu\nu)$ ) in the Alpgen MC as well.

Figures 82 (electron channel) and 83 (muon channel) show our EWK templates from  $\geq$  1-4 jets using the W transverse mass spectrum after it has after its normalization to the data. As expected, the signal W MC is the dominate contribution peaking just before a  $M_T$  of 80 GeV/ $c^2$ . The same figures also show QCD template which is the subject of the next section. Later in section 4.5 we will show the templates for the inclusive 1 jet as an example case and how a linear combination of the templates replicates the  $M_T$  distribution of the data.

## 4.3 QCD template

The final piece to our background puzzle is our non-W background that we cannot directly extract from any MC: QCD. We use QCD as a catch-all term that specifies actual quantum chromodynamics processes like dijet and multi-jet production as well as other potential fakes to our W signal such as punch throughs, decays-in-flights, semi-leptonic meson decay, etc. We have attempted to track some of these contributions separately (e.g. decays-in-flights for our muon sample) but find an inclusive approach (modulo refinements and additions to our default

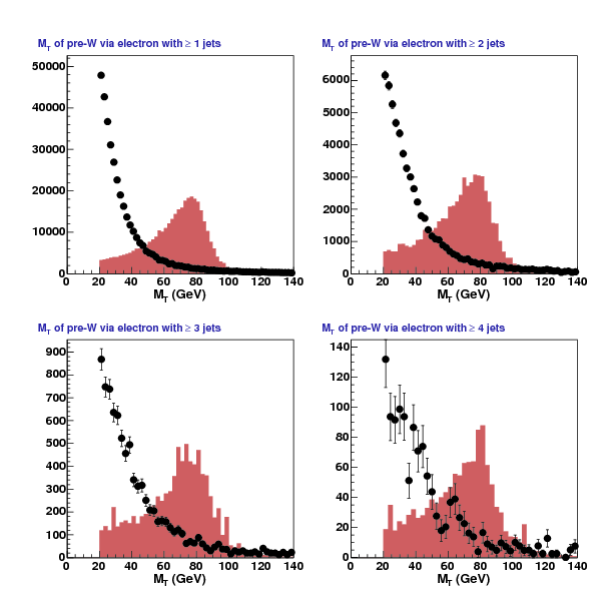


Figure 82: Transverse Mass  $(M_T)$  for the EWK (maroon histogram) and QCD (data points) templates for  $W \to e\nu + \geq n$  jets with  $M_T > 20$  GeV/c<sup>2</sup> for n = 1-4. Both templates have been normalized to the number of events in the same distribution in data after  $t\bar{t}$  and diboson estimation removal.

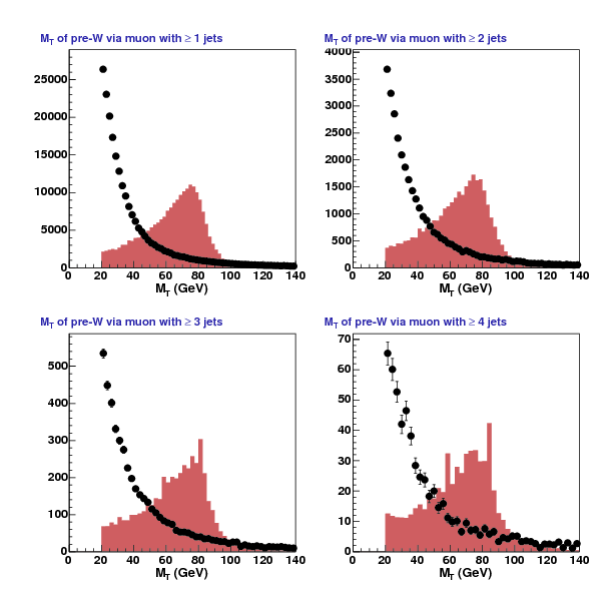


Figure 83: Transverse Mass  $(M_T)$  for the EWK (maroon histogram) and QCD (data points) templates for  $W \to \mu\nu + \geq n$  jets with  $M_T > 20$  GeV/c<sup>2</sup> for n = 1-4. Both templates have been normalized to the number of events in the same distribution in data after  $t\bar{t}$  and diboson estimation removal.

selection criteria) sufficient to explain this encompassing background.

The objective is to use a data based method to calculate this important background. This template is constructed in parallel to our normal W selection via our anti-selection lepton criteria as described in sections 2.2 and 2.4 for the electron and muon channels, respectively. Recall that these samples use the same basic kinematic and geometric requirements (including a mirrored W selection of section 2.7) but must fail two or more of our normal quality/identification cuts.

Like the EWK template of the previous section, we normalize these samples to the size of the data (minus the "fixed" diboson and  $t\bar{t}$  backgrounds of section 4.1) in the range of  $20 < M_T < 120~{\rm GeV/c^2}$ . We define  $n_{QCD}$  to be the multiplicative scale factor needed to normalize the unscaled QCD sample to the data via our relaxed transverse mass samples. We give the normalization scale factors in table 18. Like the basic behavior of our EWK normalization (table 17) the jet multiplicity and lepton differences are simply an artifact of our selection criteria on the composition of the data.

$\geq n$ jets	$n_{QCD}$ for Electrons	$n_{QCD}$ for Muons
0	7.671	3.338
1	3.468	0.8914
2	2.998	0.4959
3	2.685	0.3057
4	2.734	0.2011

Table 18: QCD template normalization scale factors  $(n_{QCD})$  for each inclusive jet multiplicity (0-4)

Unlike the EWK template, our QCD template has the additional complication of contamination from other backgrounds and even the signal that satisfy our anti-selection criteria. Clearly, we intend to use the data (detector based) sample to form a template but we first need to subtract the contributions from already accounted for by the other backgrounds. The contamination is roughly 5% in the electron channel and less than 0.5% in the muon. While contamination removal has virtually no effect on our muon channel results care is taken to make sure the contamination is properly removed from both the electron and muon channels.

Removing the diboson and  $t\bar{t}$  contributions is done by a literal subtraction. In the case of our EWK signal  $(W \to \ell \nu)$  and backgrounds  $(W \to \tau \nu + Z)$  we have to remove the contamination by using the fitting procedure and their results of the next two sections. We preform this iterative procedure until we reach a steady convergence. This is readily achieved after a single refitting due to the default weighting being relatively close to the data to begin with. Note that this background subtraction procedure is also carried out anytime we reevaluate our backgrounds/fittings. For example, we assign a systematic on our  $t\bar{t}$  background estimation (see section 6.6) and that separate background fitting procedure requires us to remove our EWK signal and background contamination to our QCD template.

Example plots of the QCD template (along with the EWK template of the previous section) normalized to the data for the  $M_T$  distribution were given in figures 82 and 83 for the electron and muon channel, respectively. The QCD template shows the expected exponential like decay of the W transverse mass spectrum which dominates the EWK spectrum for  $M_T < 50 \text{ GeV/c}^2$ .

# M<sub>T</sub> of pre-W via electron with ≥ 1 jets • QCD Template EWK Template 0 20 40 60 80 100 120 140 M<sub>T</sub> (GeV)

Figure 84: Transverse Mass  $(M_T)$  for the EWK (histogram) and QCD (data points) templates for  $W \to e\nu + \geq 1$  jets with  $M_T > 20 \text{ GeV/c}^2$ . Both templates have been normalized to the number of events in the same distribution in data after  $t\bar{t}$  and diboson estimation removal.

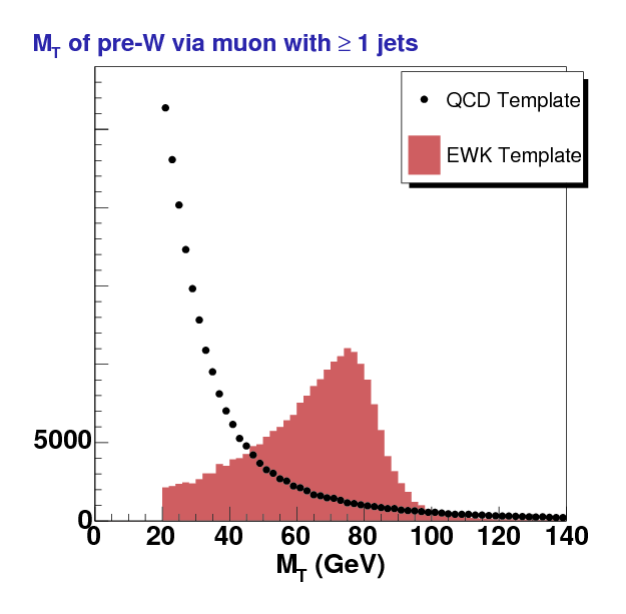


Figure 85: Transverse Mass  $(M_T)$  for the EWK (histogram) and QCD (data points) templates for  $W \to \mu\nu + \geq 1$  jets with  $M_T > 20 \text{ GeV/c}^2$ . Both templates have been normalized to the number of events in the same distribution in data after  $t\bar{t}$  and diboson estimation removal.

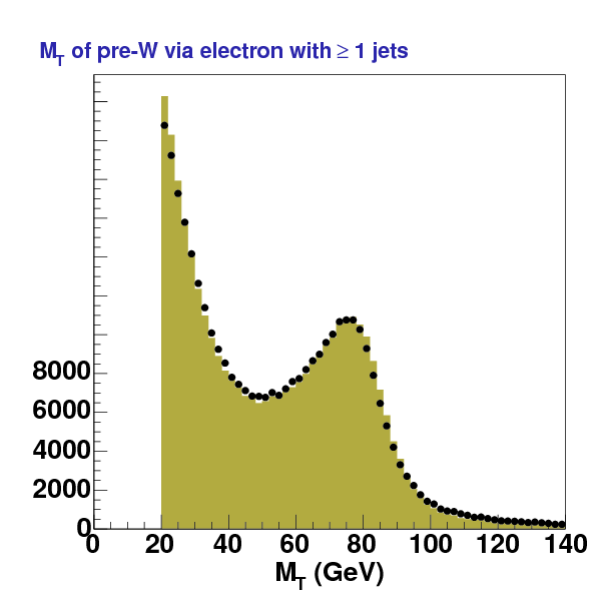


Figure 86: Transverse Mass  $(M_T)$  for the combined EWK+QCD templates fit (histogram) and data (data points) after  $t\bar{t}$  and diboson estimation removal for  $W \to e\nu + \ge 1$  jets with  $M_T > 20$  GeV/c<sup>2</sup>. The fitting is done using TFractionFitter [47]. To arrive at our final W background estimation and samples (across the scaled EWK+QCD templates and in the data) we take  $M_T > 40 \text{ GeV/c}^2$ .

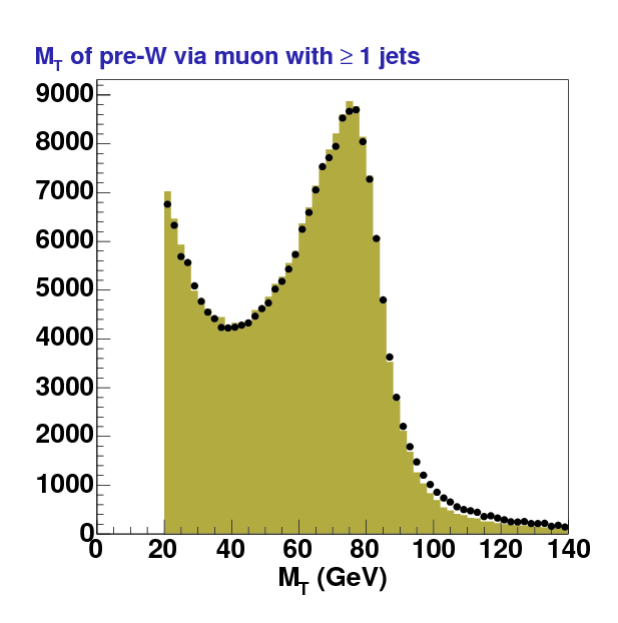


Figure 87: Transverse Mass  $(M_T)$  for the combined EWK+QCD templates fit (histogram) and data (data points) after  $t\bar{t}$  and diboson estimation removal for  $W \to \mu\nu + \geq 1$  jets with  $M_T > 20$  GeV/c<sup>2</sup>. The fitting is done using TFractionFitter [47]. To arrive at our final W background estimation and samples (across the scaled EWK+QCD templates and in the data) we take  $M_T > 30 \text{ GeV/c}^2$ .

# 4.4 Background Fitting Procedure and Results

The background fitting procedure is designed to circumvent the need for a direct jet multiplicity dependent theoretical cross-section for our  $W \to \tau \nu + Z$  backgrounds which come from the MC via our normal W selection process in addition to providing the relative scale for our QCD/fake estimation. The former is important since directly assigning a theoretical cross-section would be circular; we would be assuming the thing we wish to measure. The latter case with our catch-all QCD template via our anti-selection sample is even more problematic as the sample relies on the inefficiency of our quality/identification variables via our anti-selection sample and, in any event, there does not exist a single representative process from which to apply a jet dependent cross-section.

Our goal here is to take our EWK and QCD templates and fit them to shape of the W transverse mass distribution for each jet multiplicity and for both electron and muon channels. In this way, we can calculate the relative fraction of each template which will give us a linear combination that when taken together should provide a bin-by-bin background estimation of the data not only for distributions like  $M_T$  and  $E_T$  but for several important kinematic variables based on our lepton and jet selection. Unlike the previous version of this analysis [1], we use the transverse mass distribution instead of the missing transverse energy ( $E_T$ ) as is has slightly better separation power between our W signal and our non-W backgrounds. This was also the reason for using the  $M_T$  as our final kinematic variable (as noted in section 2.7) as it has better signal-to-background ratio for a given W acceptance. Note however that we do use the  $E_T$  shape as a cross-check to our method and as a potential systematic for our background estimation procedure. The fitting procedure for the  $E_T$  is the same as outlined here although we normalize over the entire range of the histogram (0-100 GeV). The results given as the relative difference in the electron channel were no more than 1.1% and within our given uncertainties. The same relative differences in  $M_T$  and  $E_T$  for the muon channel was as high as 2.6%.

Recall that in section 4.1 we applied our knowledge of the theoretical cross-sections for our diboson and  $t\bar{t}$  (via Pythia MC) background estimations. Therefore, for the purpose of our procedure here, we subtract these accounted for background estimates from our raw data shape in the  $M_T$  distribution. We use the number of events in this corrected data distribution between  $20 < M_T < 120 \text{ GeV/c}^2$  to normalize to our EWK and QCD templates as noted in the previous sections (see tables 17 and 18). We then setup TFractionFitter which is one of the general histogram tools in R00T [47]. The basic details of the original (Fortran) algorithm are described in [48]. The TFractionFitter method takes the templates and perform a likelihood fit to the modified data. The virtue of this fitting method

is that it takes into account both data and Monte Carlo statistical uncertainties. The way in which this is done is through a standard likelihood fit using Poisson statistics; however, the template (MC) predictions are also varied within statistics, leading to additional contributions to the overall likelihood. [47]

The fitting is done for each lepton channel and for each inclusive jet multiplicity. We set the fitting range over the same normalization range of  $20-120 \text{ GeV/c}^2$ . By default, the fitting fraction starts at 0.5 for both templates. The TFractionFitter method also allows for us to

directly output the combined likelihood fit histogram which we now give an example of along with our basic templates prior to fitting. Figures 84 and 85 show the QCD and EWK and templates normalized to the data (minus the fixed background components) for  $W \to \ell \nu + \geq 1$  jets for the electron and muon channel, respectively. The final "fitted" results are shown in figures 86 and 87 which shows the output via TFractionFitter with the data for the same jet multiplicity. The basic template behavior and fit results are typical for the higher jet multiplicities.

The output of the fit is the relative fitting fractions for each template ( $k_{EWK}$  for EWK and  $k_{QCD}$  for QCD) along with an uncertainty in the parameter ( $\Delta k_{EWK}$  and  $\Delta k_{QCD}$ , respectively). Note that due to the normalization of each template to the data there is actually only one degree of freedom:

$$k_{EWK} + k_{OCD} = 1 ag{18}$$

$$k_{QCD} = 1 - k_{EWK} \tag{19}$$

In order to apply these results to all of our distributions we need to account for the normalization factors  $(n_{EWK} \text{ and } n_{QCD})$  of the previous section. We then apply the product of these two factors  $(k_{EWK} \times n_{EWK} \text{ and } k_{QCD} \times n_{QCD})$  to our EWK and QCD histograms, respectively, finally giving us a full bin-by-bin background estimation for all distributions. Note that the histograms of interest to us include our final W transverse mass cut and thus the absolute number of background events need not be precisely equal to the number of W candidate events in the data. As a result, we expect the jet multiplicity in data to be close but not exactly equal to the number of events predicted in our signal+background estimation.

As noted in the previous section, the QCD template deals with contamination that comes from our MC based estimates also "passing" our inverted cut scheme for our anti-selection samples. Technically, this includes our diboson and  $t\bar{t}$  samples but these are simply subtracted from the data before hand and thus are not effected by the iterative method outlined here. We deal with this by scaling the EWK contamination by the result of the previous fit  $(k_{EWK})$  and then subtracting it as normal from the data (minus the diboson and  $t\bar{t}$  contribution) to form QCD template. We normalize to our pre-candidate W data sample as normal and refit. As suggested, the effect on the electron channel is small (0.5%). On a second pass the fit changes by only 1 part in 10,000. The effect is trivial in the muon channel where there was less contamination to begin with. As a result, the change in our fit fractions was only a few parts in 10,000 after the first iteration.

Finally, we present tables 19 and 20 which give fit values from TFractionFitter and their uncertainty. The fit fractions ( $k_{EWK}$  and  $k_{QCD}$ ) when combined with the normalization fractions (via tables 17 and 18) give us a scale factor (not presented) to apply to each template for each jet multiplicity.

### 4.5 Background Estimation Results

In order to highlight the effectiveness of our background fitting method and as an overview of our basic analysis results, we present an array of plots giving a breakdown of the various

$\geq n$ jets	$k_{EWK}$	$\Delta k_{EWK}$	$k_{QCD}$	$\Delta k_{QCD}$
0	0.7701	0.0008	0.2299	0.0004
1	0.5746	0.0020	0.4254	0.0017
2	0.5048	0.0048	0.4952	0.0048
3	0.4770	0.0134	0.5230	0.0138
4	0.5008	0.0355	0.4991	0.0353

Table 19: The EWK and QCD template fitting fractions  $(k_{EWK} \text{ and } k_{QCD})$  and their errors for  $W \rightarrow e\nu + \geq n$  jets

$\geq n$ jets	$k_{EWK}$	$\Delta k_{EWK}$	$k_{QCD}$	$\Delta k_{QCD}$
0	0.9010	0.0012	0.0990	0.0005
1	0.8404	0.0033	0.1596	0.0018
2	0.8090	0.0086	0.1910	0.0055
3	0.7823	0.0237	0.2177	0.0167
4	0.7581	0.0707	0.2419	0.0555

Table 20: The EWK and QCD template fitting fractions  $(k_{EWK} \text{ and } k_{QCD})$  and their errors for  $W \to \mu\nu + \geq n$  jets

background contributions of the expected number of events for different variables. Some will serve as a quality check of our final results, while others are the actual observables that we will use to form our final cross-sections. All of these plots unless otherwise noted come from our final W selection including the final transverse mass cut.

Before diving into these results we want to present a basic table with the number of candidate W events for each jet multiplicity as well as a breakdown into the fraction of events from each background process. Table 21 gives the electron channel results while table 22 shows the muon channel results. Keeping with section 4.1, the diboson contributions are taken together as a single column. The final column in these tables is our measured W fraction taken by summing all background processes and subtracting this from unity.

$\geq n$ jets	Data	$W \rightarrow \tau \nu$	$Z \rightarrow ee$	$Z \rightarrow \tau \tau$	$t\overline{t}$	Diboson	QCD	$W \rightarrow e\nu$
0	1849213	0.029	0.011	0.002	0.001	0.004	0.059	0.895
1	230222	0.019	0.021	0.001	0.004	0.012	0.178	0.765
2	39417	0.016	0.036	0.000	0.023	0.025	0.266	0.634
3	6662	0.011	0.041	0.000	0.103	0.029	0.292	0.524
4	1280	0.008	0.041	0.000	0.282	0.024	0.256	0.388

Table 21: Background estimation fraction for  $W \to e\nu + \geq n$  jets. Data represents the number of candidates events in data passing our W selection criteria while  $W \to e\nu$  is the measured W signal fraction via the total minus the background  $(N(\text{data}) - \sum N(\text{backgrounds}))$ . Diboson represents WW, WZ, and  $W\gamma^*$  production.

Figures 88 and 103 shows the jet multiplicity (0-4 inclusive number of jets) for the electron and muon channel, respectfully. The data are present as points with signal, QCD background estimation along with a combined EWK, diboson, and  $t\bar{t}$  background prediction given as a

$\geq n$ jets	Data	$W \rightarrow \tau \nu$	$Z \rightarrow \mu\mu$	$Z \rightarrow \tau \tau$	${ m t} \overline{ m t}$	Diboson	QCD	$W \rightarrow \mu\nu$
0	1309926	0.032	0.052	0.002	0.001	0.004	0.047	0.861
1	164843	0.028	0.054	0.001	0.005	0.014	0.083	0.816
2	26459	0.026	0.055	0.001	0.030	0.033	0.108	0.747
3	4383	0.020	0.049	0.000	0.143	0.038	0.117	0.633
4	857	0.013	0.032	0.000	0.380	0.030	0.102	0.442

Table 22: Background estimation fraction for  $W \to \mu\nu + \geq n$  jets. Data represents the number of candidates events in data passing our W selection criteria while  $W \to \mu\nu$  is the measured W signal fraction via the total minus the background  $(N(\text{data}) - \sum N(\text{backgrounds}))$ . Diboson represents WW, WZ, and  $W\gamma^*$  production.

stacked histogram. With respect to our fitting, each histogram bin represents a different set of fitting fractions as well as our pre-fit normalizations. As such, these figures serve a visual representation of our most basic W+jets result. We note that the total expectation is not guaranteed to be perfect with the data due to the different transverse mass range difference used in fitting and with our final result. However, the agreement is by the nature of the method quite good.

Next we present the flagship measurement of this analysis: the  $n^{\text{th}}$  leading jet  $p_T$  distribution for  $\geq n$  jets. The electron channel results (n=1-4) are shown in figures 99-102 while the muon channel results are likewise given in figures 114-117. For the purpose of comparison we normalize the background and signal prediction to the data in each plot. The take away point from these jet transverse momentum distributions is a basic consistency. Needless the say the fact that the W MC prediction appears slightly softer (more events at lower jet  $p_T$ ) is ultimately the type of quantitative observation we desire in our final result when we compare to theoretical predictions.

The remaining plots of this section highlight a variety of basic quality control distributions concerning our W signal as well as relational kinematic plots between our selected jets with respect to our W selection. The main motivation for looking at these observables is to insure that our background estimation method does not introduce any unexpected bias. We desire our QCD estimation (more precisely our anti-selected lepton samples used to form the QCD template) along with our MC signal and background contributions to be in broad agreement across the phase space of various W+jets variables. It is possible to have an optimal fit with respect to the W transverse mass spectrum but for other distributions to have tell-tale signs of bias that can effect our final jet observables. For example, if one does not remove the anti-selected muon-jet (see section 3.3 on page 24) in the jet collection, the resulting sample not only has a noticeable muon low  $p_T$  bias but also poorly describes the transverse jet momentum distributions for the first and second leading jet.

Figures 89-93 show the W transverse mass distribution for  $\geq$ 0-4 jets for the electron channel. Likewise, the muon channel version of  $M_T$  follows in figures 104-108. For comparison we also highlight the missing energy  $(\not\!E_T)$  distributions for each jet multiplicity as well in figures 94-98 (electrons) and 109-113 (muons).

For completeness we also present a breakdown of the lepton and missing energy information. In

the plots to be referenced in the remainder of this section, we actually break down the various background into their individual components rather than the "public relations" versions of figures 88-113. We start with the electron transverse energy  $(E_T)$  for each jet multiplicity which is shown in figures 118 (the total inclusive  $\geq 0$  jets sample) and 119 (inclusive jet multiplicities 1-4). Similarly we give the muon transverse momentum  $(p_T)$  in figures 130 and 131 for the total inclusive case and each jet inclusive multiplicity 1-4, respectively. We also measure the  $\Delta \phi$  between the lepton and the missing energy  $(\Delta \phi(\ell, \nu))$ . The electron channel results are shown in figures 122 and 123 for  $\geq 0$  jets and the  $\geq 1$ -4 jet multiplicities, respectively. The muon channel results are likewise presented in figures 134 and 135.

We reproduce the missing energy and transverse mass plots from before but this time with a full breakdown of individual background components and formatting as the previous referenced plots. The  $E_T$  for the electron channel is shown in figures 120 and 121 while the muon results are given in figures 132 and 133. The  $M_T$  results are presented in figures 124 (136) for the total inclusive jet multiplicity for the electron (muon) channel. Likewise, figures 125 and 137 give the results for the higher inclusive jet multiplicities (1-4) for the electron and muon channels, respectively.

Figures 126 and 138 give the  $n^{\rm th}$  leading jet  $\eta$  distributions for  $\geq n$  jets (1-4) with respect to the electron and muon results. Each plot also gives the  $\pm 1\sigma_{\rm JES}$  jet energy scale correction (see section 3.6 on page 36) applied to the data and represented by a black line for each variation.

Next we present three distributions which look at the relative spacing between the selected lepton and a jet observable. First we look at the  $\Delta R(\ell,j)$  (or simply  $R(\ell,j)$ ) which is the  $\eta$ - $\phi$  separation between the lepton and the closest jet (as measured via  $\Delta R(\ell,j)$ ). The electron channel results  $(\Delta R(e,j))$  are presented in figure 127 while the muon results  $(\Delta R(\mu,j))$  are shown in figure 139. We also look at just the separation in  $\phi$  between the same variables  $(\Delta \phi(\ell,j))$ . Figure 128 are the  $\Delta \phi(e,j)$  results for each jet multiplicity bin while figure 140 presents the  $\Delta \phi(\mu,j)$  results, likewise. The comparison in these plots is still between the closest jet as measured in  $\eta$ - $\phi$  via  $\Delta R$ . We observe the characteristic back-to-back bias in the data in the inclusive 1 jet case and the subsequent reduction to smaller values of  $\Delta R/\Delta \phi$  of the available lepton-jet phase space as the just multiplicity increases.

Finally we consider a variation in the previous  $\Delta \phi$  distributions where we look at the vector sum of jet energy and compare the resulting direction  $(\wp)$  with the lepton. We introduced this variable in the previous chapter (see section 3.5) and defined in via equation 12 on page 29. As noted, this  $\Delta \phi(\ell, \wp)$  variable has the advantage of producing a spectrum that is approximately the same for all jet multiplicities and thus useful for checking for consistency between the signal and electro-weak based backgrounds and our QCD estimation. Figure 129 gives the  $\Delta \phi(e, \wp)$  results while figure 141 shows the  $\Delta \phi(\mu, \wp)$  distribution for each inclusive jet multiplicity (1-4). Both of the cited plots have a  $\Delta \phi(\ell, \wp) < 2.95$  cut applied during selection.

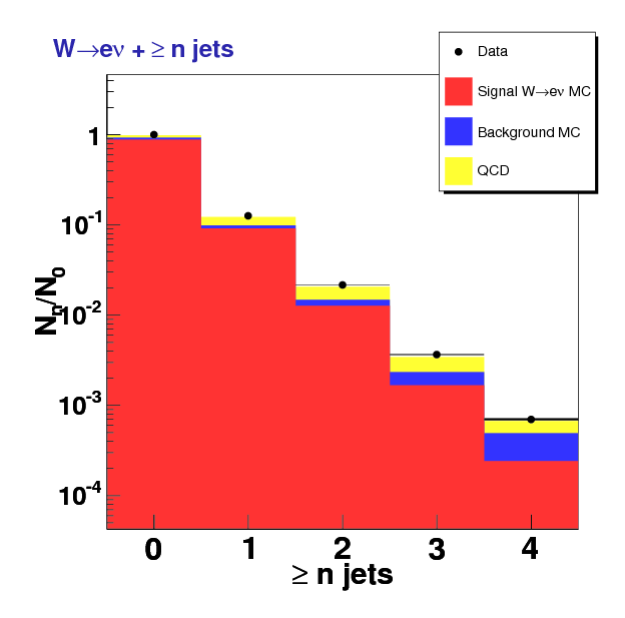


Figure 88: Inclusive jet multiplicity for  $W \to e\nu + \geq n$  jets. The plot has been normalized to the total number of events in the data. The black points are the data, the red histogram is the signal MC, the blue histogram is all other MC based backgrounds summed together, and the yellow histogram is the QCD estimation.

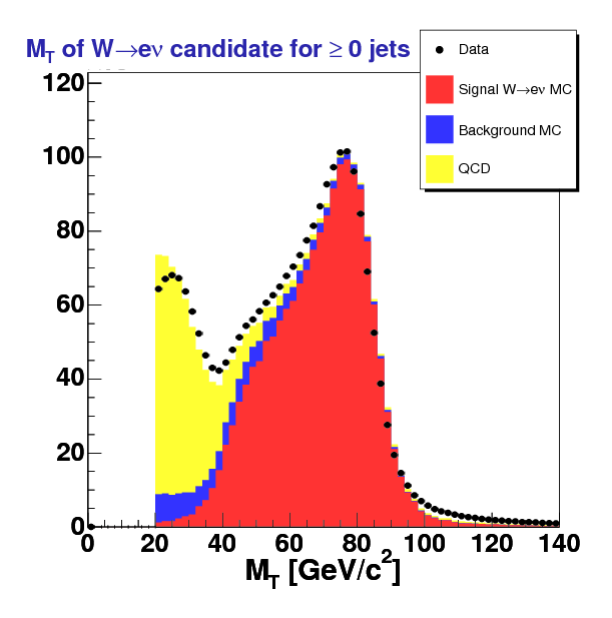


Figure 89: W transverse mass  $(M_T)$  for  $W \to e\nu + \ge 0$  jets. This is before the final W selection cut of  $M_T > 40 \text{ GeV/c}^2$ . The black points are the data, the red histogram is the signal MC, the blue histogram is all other MC based backgrounds summed together, and the yellow histogram is the QCD estimation.

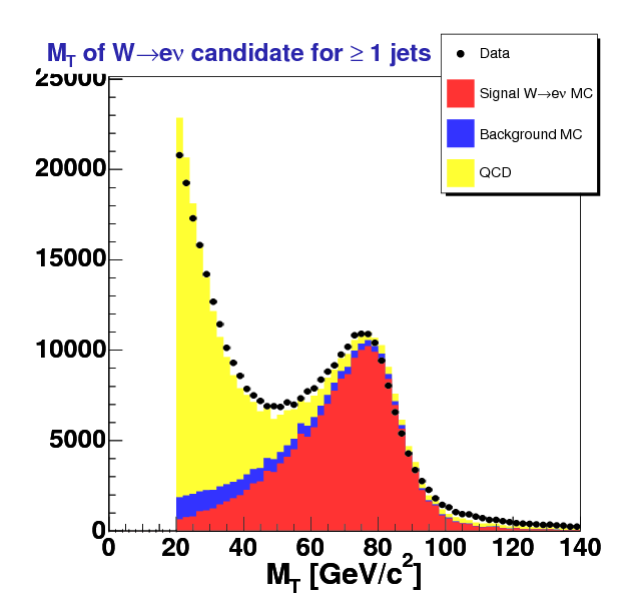


Figure 90: W transverse mass  $(M_T)$  for  $W \to e\nu + \ge 1$  jets. This is before the final W selection cut of  $M_T > 40 \text{ GeV/c}^2$ . The black points are the data, the red histogram is the signal MC, the blue histogram is all other MC based backgrounds summed together, and the yellow histogram is the QCD estimation.

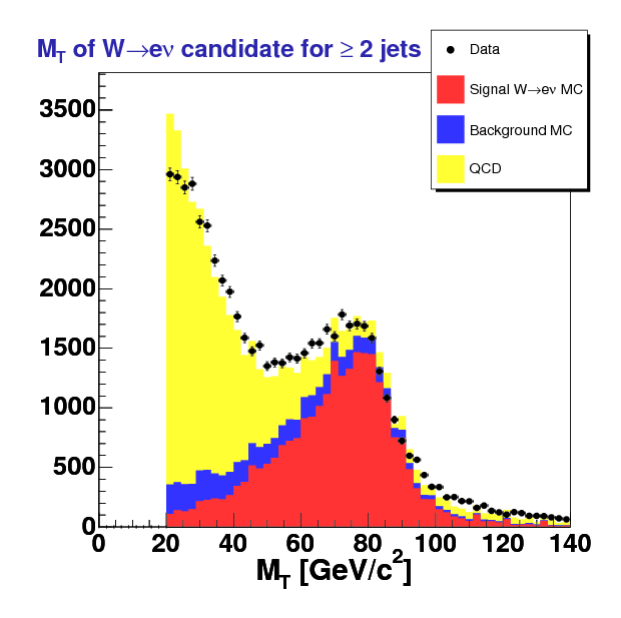


Figure 91: W transverse mass  $(M_T)$  for  $W \to e\nu + \geq 2$  jets. This is before the final W selection cut of  $M_T > 40 \text{ GeV/c}^2$ . The black points are the data, the red histogram is the signal MC, the blue histogram is all other MC based backgrounds summed together, and the yellow histogram is the QCD estimation.

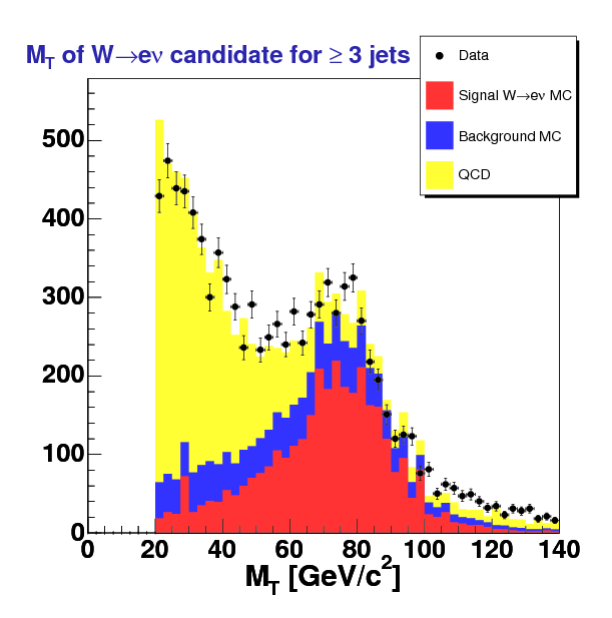


Figure 92: W transverse mass  $(M_T)$  for  $W \to e\nu + \geq 3$  jets. This is before the final W selection cut of  $M_T > 40 \text{ GeV/c}^2$ . The black points are the data, the red histogram is the signal MC, the blue histogram is all other MC based backgrounds summed together, and the yellow histogram is the QCD estimation.

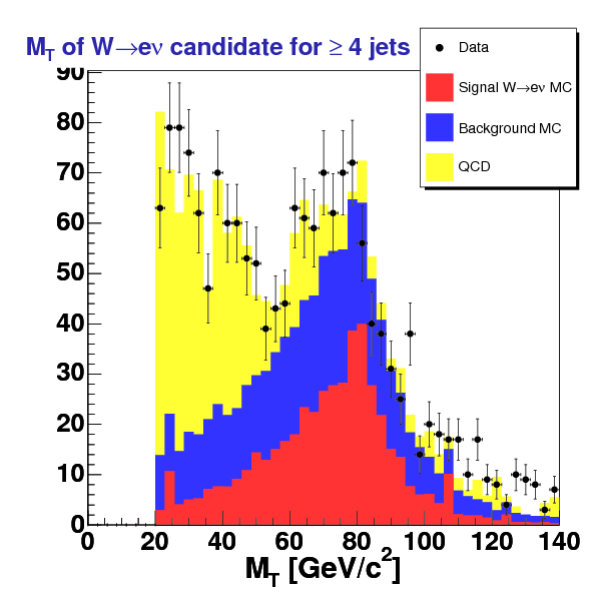


Figure 93: W transverse mass  $(M_T)$  for  $W \to e\nu + \ge 4$  jets. This is before the final W selection cut of  $M_T > 40 \text{ GeV/c}^2$ . The black points are the data, the red histogram is the signal MC, the blue histogram is all other MC based backgrounds summed together, and the yellow histogram is the QCD estimation.

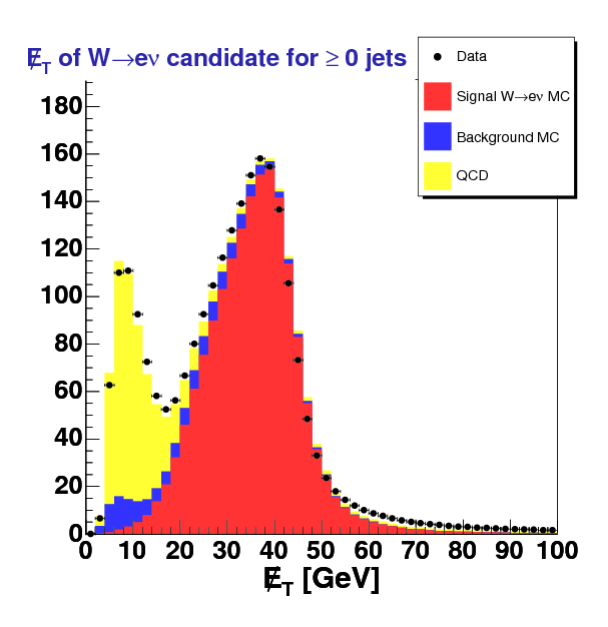


Figure 94: Missing transverse energy  $(\not\!E_T)$  for  $W \to e\nu + \ge 0$  jets. This is before the final W selection cut of  $M_T > 40 \text{ GeV/c}^2$ . The black points are the data, the red histogram is the signal MC, the blue histogram is all other MC based backgrounds summed together, and the yellow histogram is the QCD estimation.

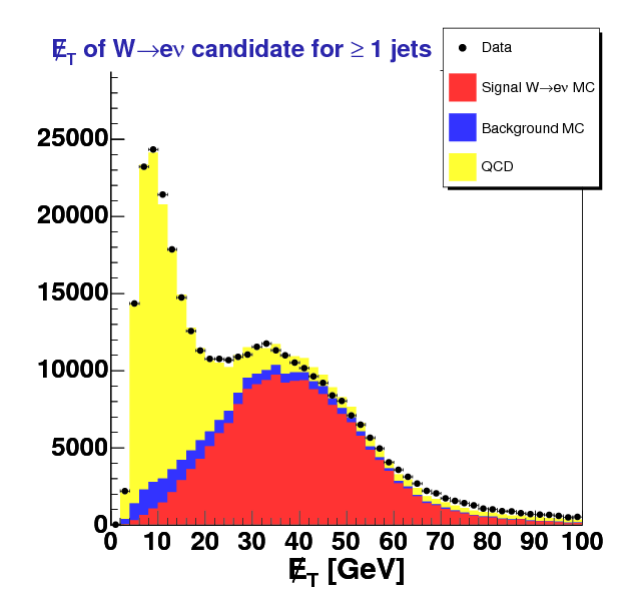


Figure 95: Missing transverse energy  $(\not\!E_T)$  for  $W \to e\nu + \ge 1$  jets. This is before the final W selection cut of  $M_T > 40~{\rm GeV/c^2}$ . The black points are the data, the red histogram is the signal MC, the blue histogram is all other MC based backgrounds summed together, and the yellow histogram is the QCD estimation.

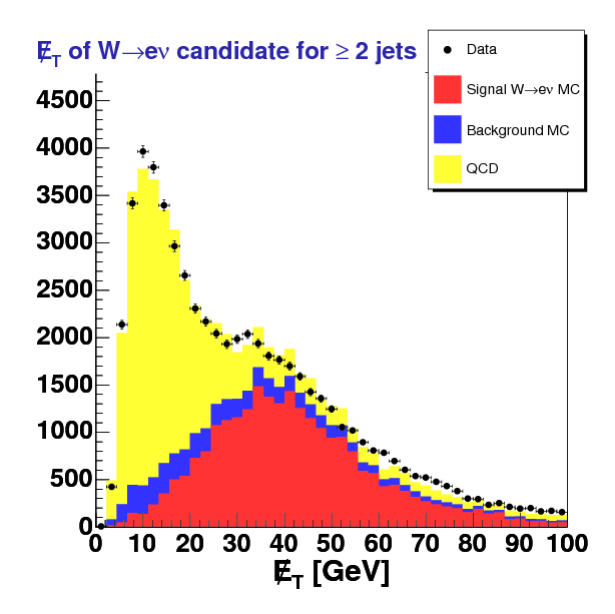


Figure 96: Missing transverse energy  $(\not\!E_T)$  for  $W \to e\nu + \geq 2$  jets. This is before the final W selection cut of  $M_T > 40 \text{ GeV/c}^2$ . The black points are the data, the red histogram is the signal MC, the blue histogram is all other MC based backgrounds summed together, and the yellow histogram is the QCD estimation.

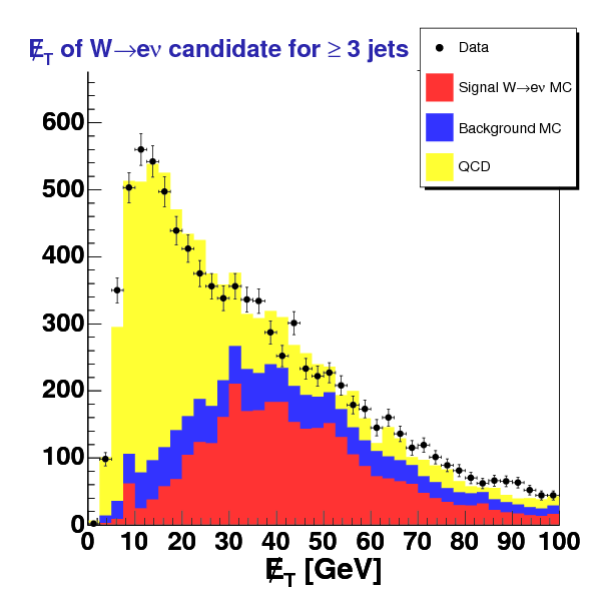


Figure 97: Missing transverse energy  $(\not\!E_T)$  for  $W \to e\nu + \ge 3$  jets. This is before the final W selection cut of  $M_T > 40~{\rm GeV/c^2}$ . The black points are the data, the red histogram is the signal MC, the blue histogram is all other MC based backgrounds summed together, and the yellow histogram is the QCD estimation.

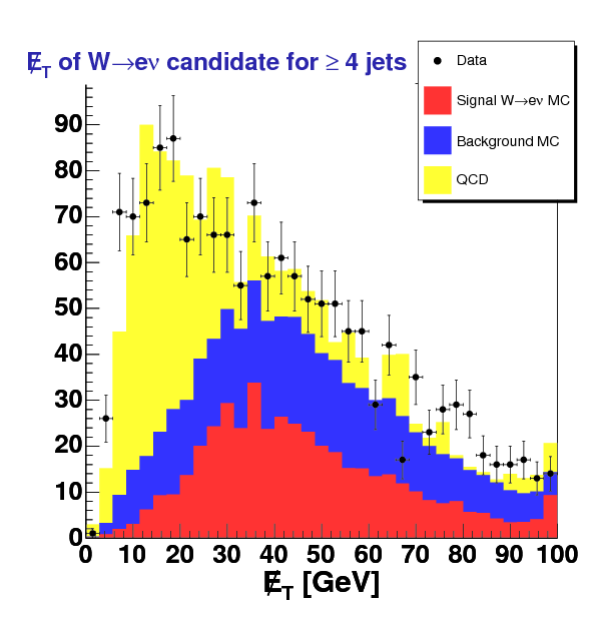


Figure 98: Missing transverse energy  $(\not\!E_T)$  for  $W \to e\nu + \ge 4$  jets. This is before the final W selection cut of  $M_T > 40~{\rm GeV/c^2}$ . The black points are the data, the red histogram is the signal MC, the blue histogram is all other MC based backgrounds summed together, and the yellow histogram is the QCD estimation.

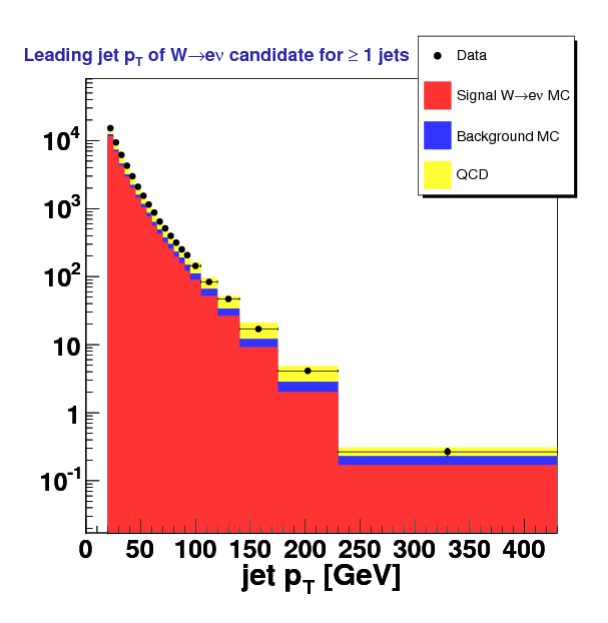


Figure 99: First leading jet transverse momentum  $(p_T)$  for  $W \to e\nu + \geq 1$  jets. The black points are the data, the red histogram is the signal MC, the blue histogram is all other MC based backgrounds summed together, and the yellow histogram is the QCD estimation.

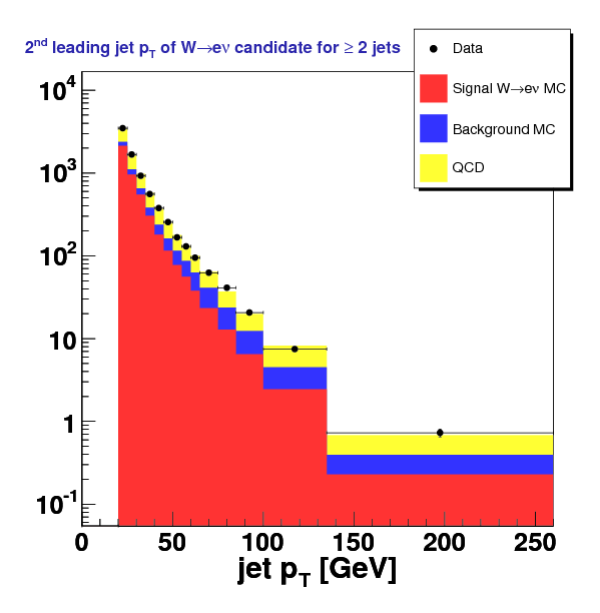


Figure 100: Second leading jet transverse momentum  $(p_T)$  for  $W \to e\nu + \geq 2$  jets. The black points are the data, the red histogram is the signal MC, the blue histogram is all other MC based backgrounds summed together, and the yellow histogram is the QCD estimation.

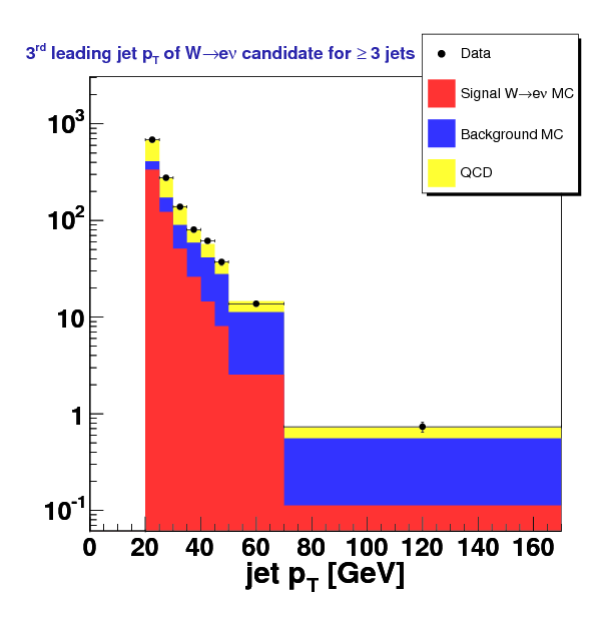


Figure 101: Third leading jet transverse momentum  $(p_T)$  for  $W \to e\nu + \ge 1$  jets. The black points are the data, the red histogram is the signal MC, the blue histogram is all other MC based backgrounds summed together, and the yellow histogram is the QCD estimation.

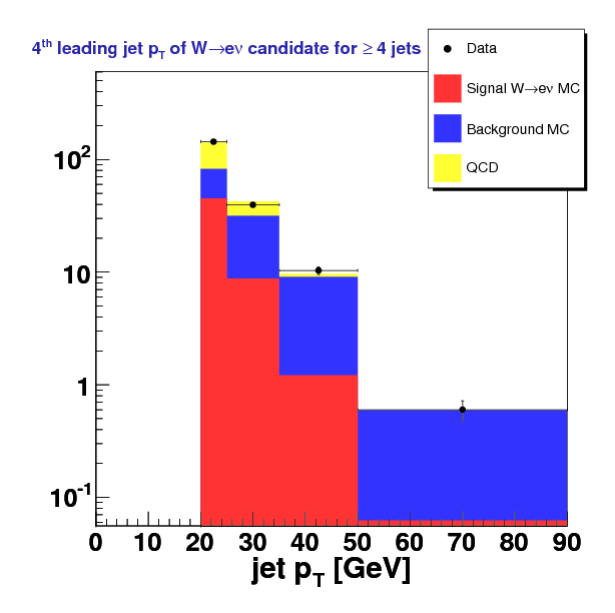


Figure 102: Forth leading jet transverse momentum  $(p_T)$  for  $W \to e\nu + \geq 2$  jets. The black points are the data, the red histogram is the signal MC, the blue histogram is all other MC based backgrounds summed together, and the yellow histogram is the QCD estimation.

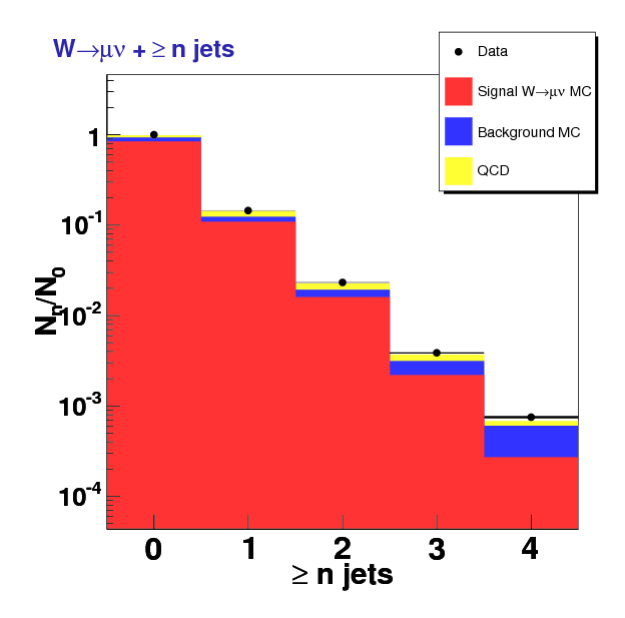


Figure 103: Inclusive jet multiplicity for  $W \to \mu\nu + \geq n$  jets. The plot has been normalized to the total number of events in the data. The black points are the data, the red histogram is the signal MC, the blue histogram is all other MC based backgrounds summed together, and the yellow histogram is the QCD estimation.

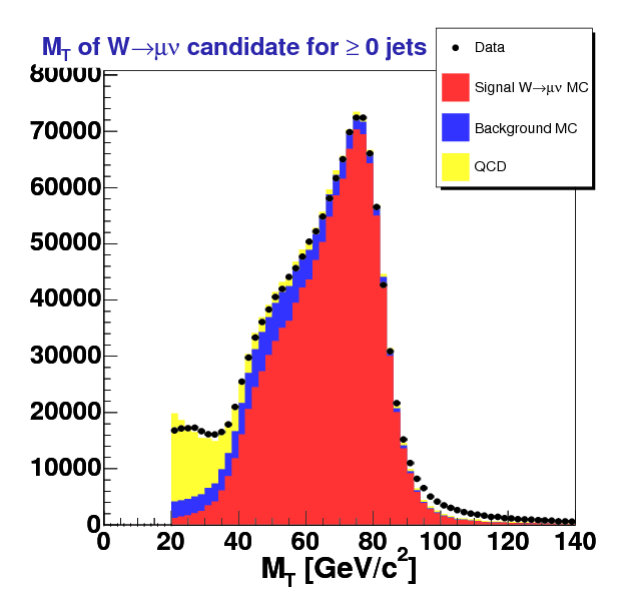


Figure 104: W transverse mass  $(M_T)$  for  $W \to \mu\nu + \geq 0$  jets. This is before the final W selection cut of  $M_T > 30 \text{ GeV/c}^2$ . The black points are the data, the red histogram is the signal MC, the blue histogram is all other MC based backgrounds summed together, and the yellow histogram is the QCD estimation.

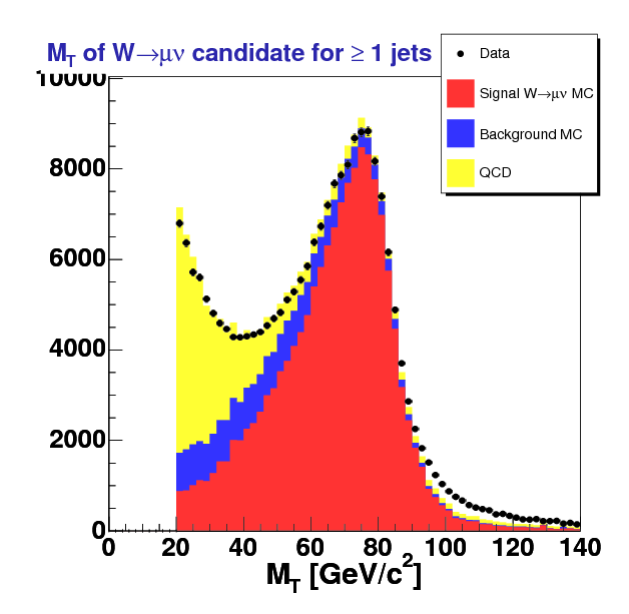


Figure 105: W transverse mass  $(M_T)$  for  $W \to \mu\nu + \geq 1$  jets. This is before the final W selection cut of  $M_T > 30 \text{ GeV/c}^2$ . The black points are the data, the red histogram is the signal MC, the blue histogram is all other MC based backgrounds summed together, and the yellow histogram is the QCD estimation.

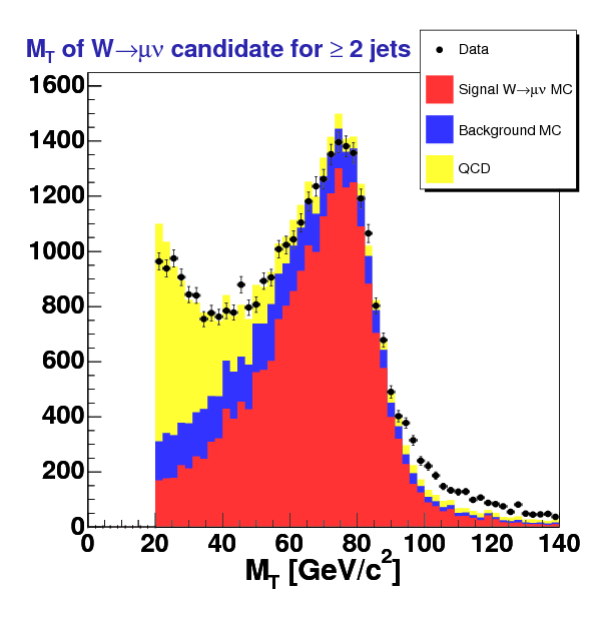


Figure 106: W transverse mass  $(M_T)$  for  $W \to \mu\nu + \geq 2$  jets. This is before the final W selection cut of  $M_T > 30 \text{ GeV/c}^2$ . The black points are the data, the red histogram is the signal MC, the blue histogram is all other MC based backgrounds summed together, and the yellow histogram is the QCD estimation.

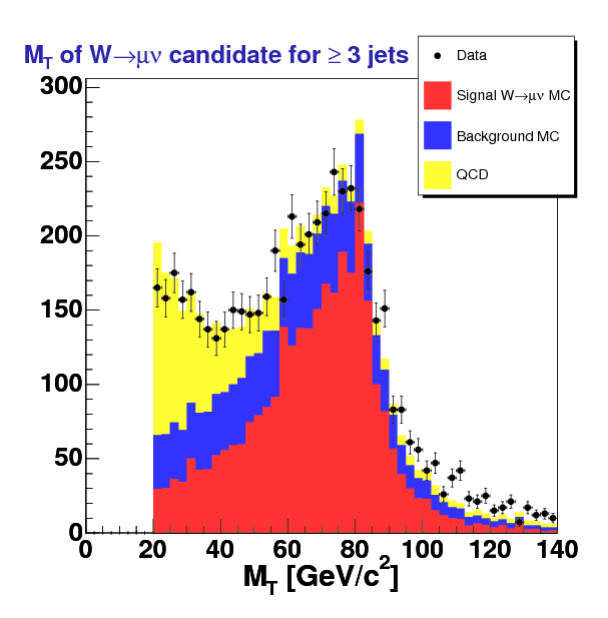


Figure 107: W transverse mass  $(M_T)$  for  $W \to \mu\nu + \geq 3$  jets. This is before the final W selection cut of  $M_T > 30 \text{ GeV/c}^2$ . The black points are the data, the red histogram is the signal MC, the blue histogram is all other MC based backgrounds summed together, and the yellow histogram is the QCD estimation.

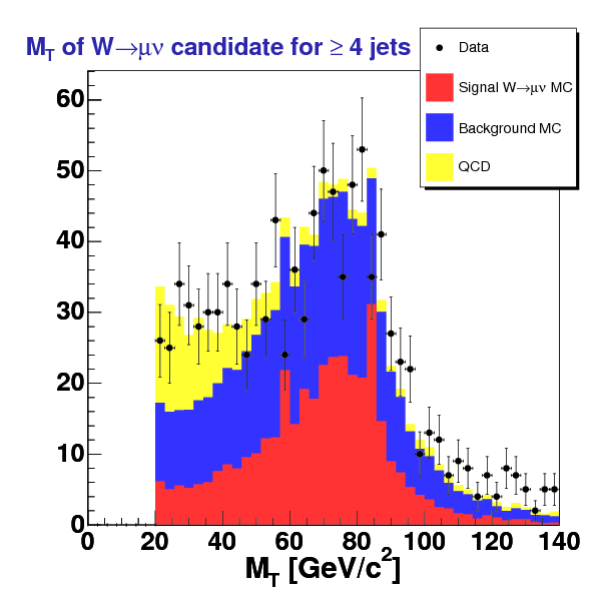


Figure 108: W transverse mass  $(M_T)$  for  $W \to \mu\nu + \geq 4$  jets. This is before the final W selection cut of  $M_T > 30 \text{ GeV/c}^2$ . The black points are the data, the red histogram is the signal MC, the blue histogram is all other MC based backgrounds summed together, and the yellow histogram is the QCD estimation.

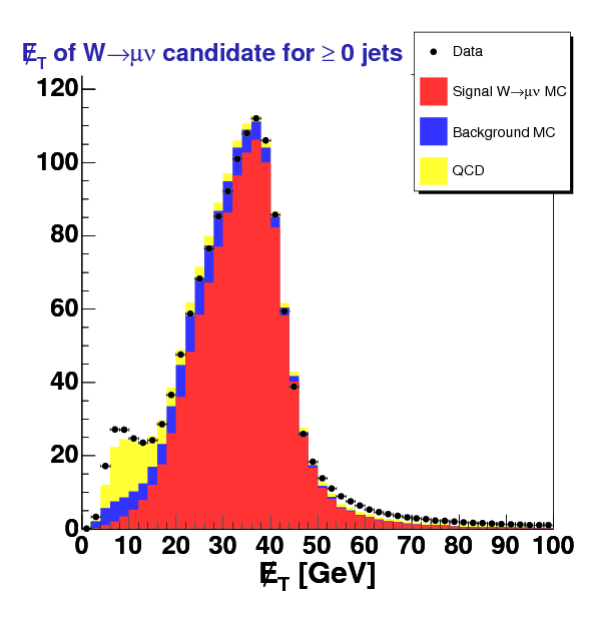


Figure 109: Missing transverse energy  $(\not E_T)$  for  $W \to \mu\nu + \geq 0$  jets. This is before the final W selection cut of  $M_T > 30 \text{ GeV/c}^2$ . The black points are the data, the red histogram is the signal MC, the blue histogram is all other MC based backgrounds summed together, and the yellow histogram is the QCD estimation.

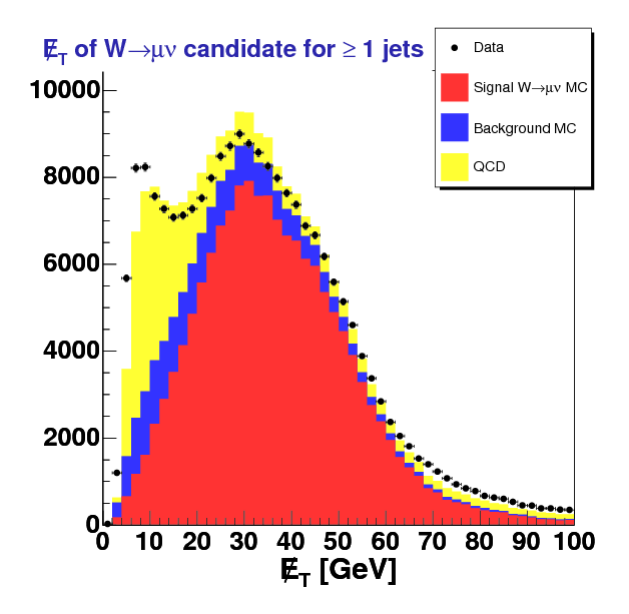


Figure 110: Missing transverse energy  $(\not E_T)$  for  $W \to \mu\nu + \ge 1$  jets. This is before the final W selection cut of  $M_T > 30 \text{ GeV/c}^2$ . The black points are the data, the red histogram is the signal MC, the blue histogram is all other MC based backgrounds summed together, and the yellow histogram is the QCD estimation.

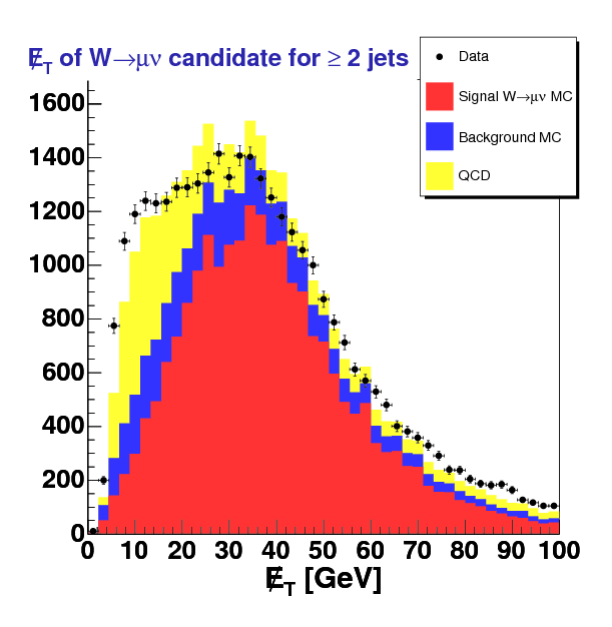


Figure 111: Missing transverse energy  $(\not E_T)$  for  $W \to \mu\nu + \geq 2$  jets. This is before the final W selection cut of  $M_T > 30 \text{ GeV/c}^2$ . The black points are the data, the red histogram is the signal MC, the blue histogram is all other MC based backgrounds summed together, and the yellow histogram is the QCD estimation.

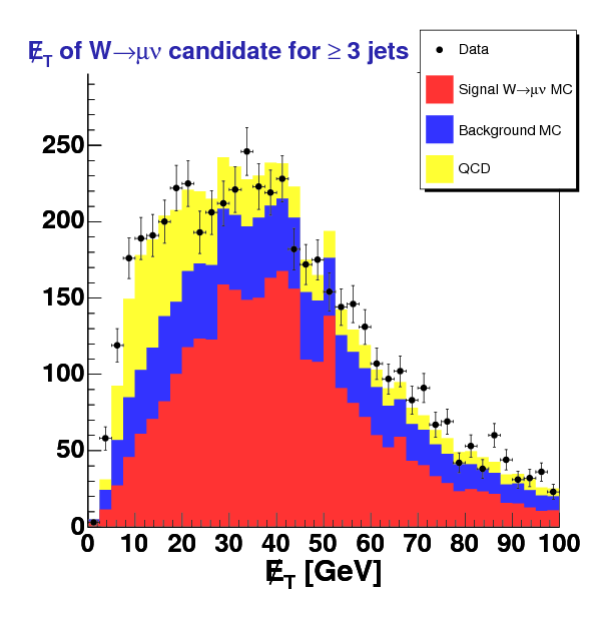


Figure 112: Missing transverse energy  $(\not E_T)$  for  $W \to \mu\nu + \geq 3$  jets. This is before the final W selection cut of  $M_T > 30 \text{ GeV/c}^2$ . The black points are the data, the red histogram is the signal MC, the blue histogram is all other MC based backgrounds summed together, and the yellow histogram is the QCD estimation.

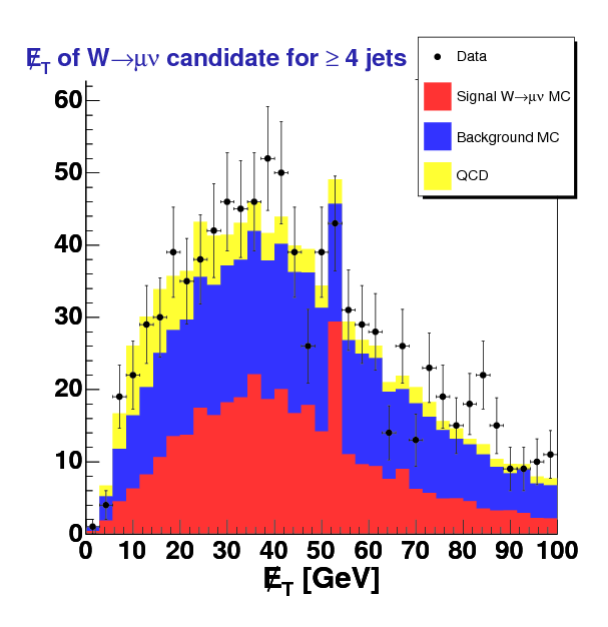


Figure 113: Missing transverse energy  $(\not\!E_T)$  for  $W \to \mu\nu + \ge 4$  jets. This is before the final W selection cut of  $M_T > 30~{\rm GeV/c^2}$ . The black points are the data, the red histogram is the signal MC, the blue histogram is all other MC based backgrounds summed together, and the yellow histogram is the QCD estimation.

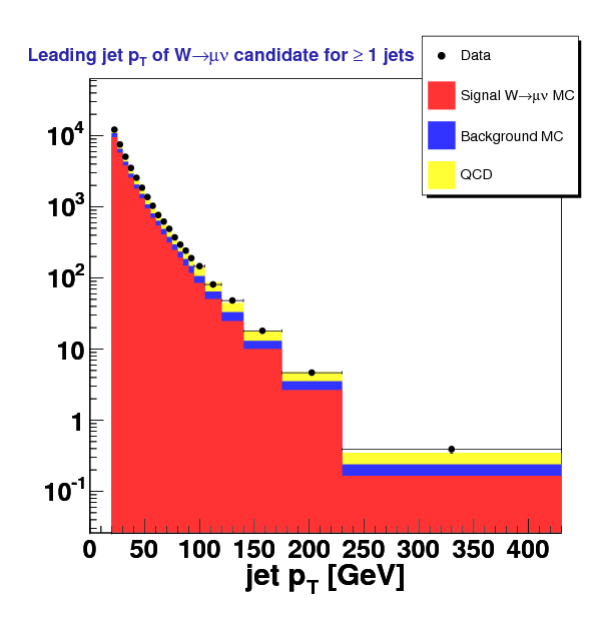


Figure 114: First leading jet transverse momentum  $(p_T)$  for  $W \to \mu\nu + \geq 1$  jets. The black points are the data, the red histogram is the signal MC, the blue histogram is all other MC based backgrounds summed together, and the yellow histogram is the QCD estimation.

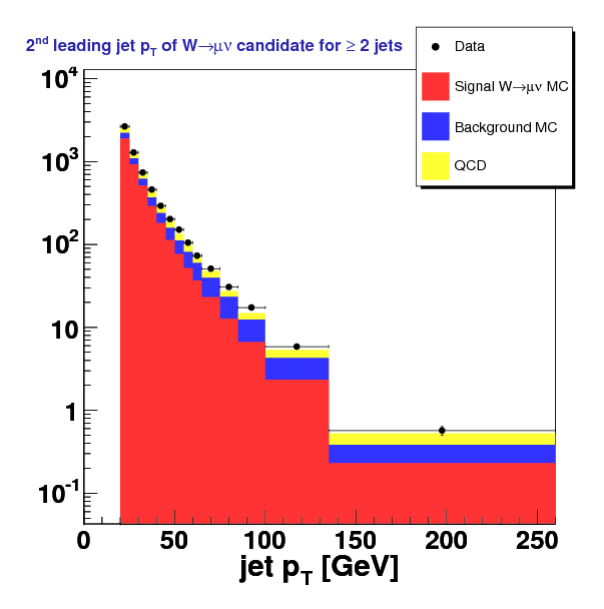


Figure 115: Second leading jet transverse momentum  $(p_T)$  for  $W \to \mu\nu + \geq 2$  jets. The black points are the data, the red histogram is the signal MC, the blue histogram is all other MC based backgrounds summed together, and the yellow histogram is the QCD estimation.

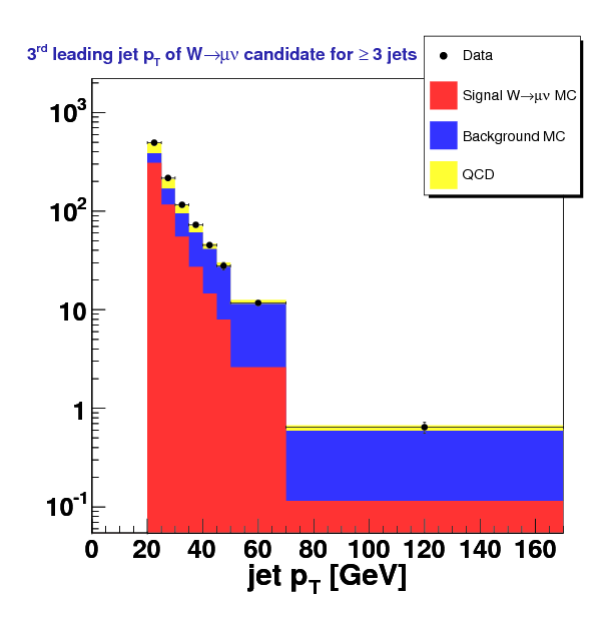


Figure 116: Third leading jet transverse momentum  $(p_T)$  for  $W \to \mu\nu + \geq 3$  jets. The black points are the data, the red histogram is the signal MC, the blue histogram is all other MC based backgrounds summed together, and the yellow histogram is the QCD estimation.

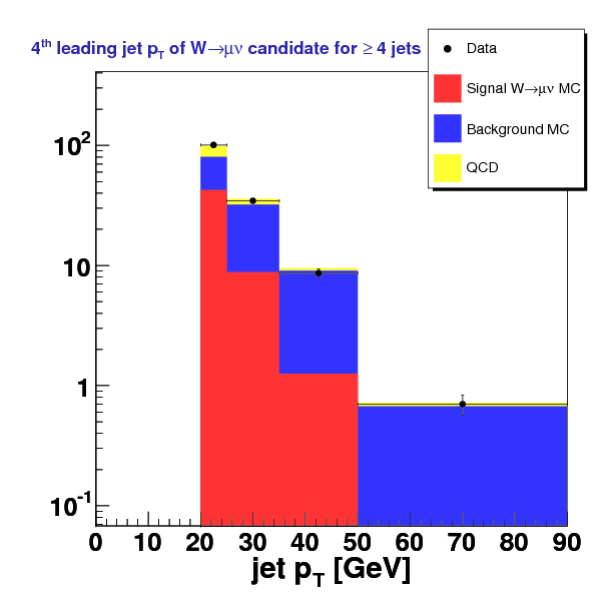


Figure 117: Forth leading jet transverse momentum  $(p_T)$  for  $W \to \mu\nu + \geq 4$  jets. The black points are the data, the red histogram is the signal MC, the blue histogram is all other MC based backgrounds summed together, and the yellow histogram is the QCD estimation.

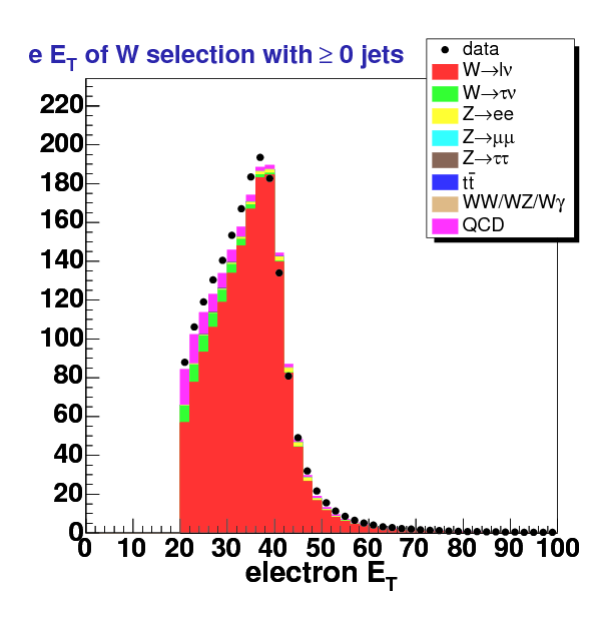


Figure 118: Electron transverse energy  $(E_T)$  for  $W \to e\nu + \ge 0$  jets.

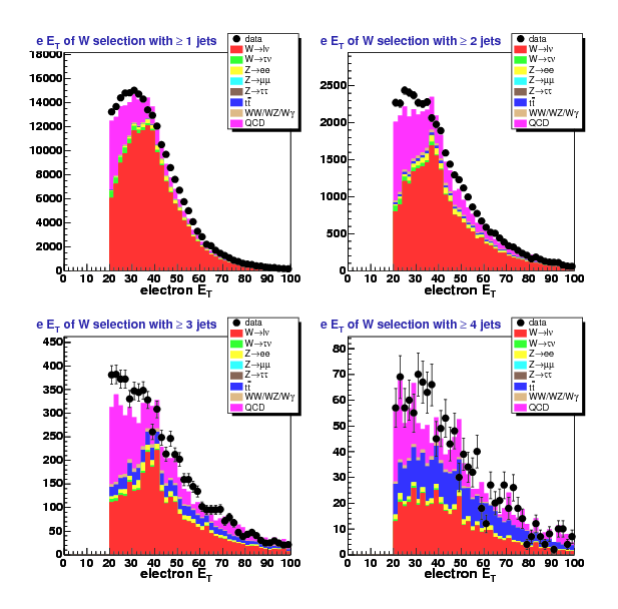


Figure 119: Electron transverse energy  $(E_T)$  for  $W \to e\nu + \ge n$  jets. Upper-left plot is for  $\ge 1$  jets, upper-right for  $\ge 2$ , lower-left for  $\ge 3$ , and lower-right for  $\ge 4$ .

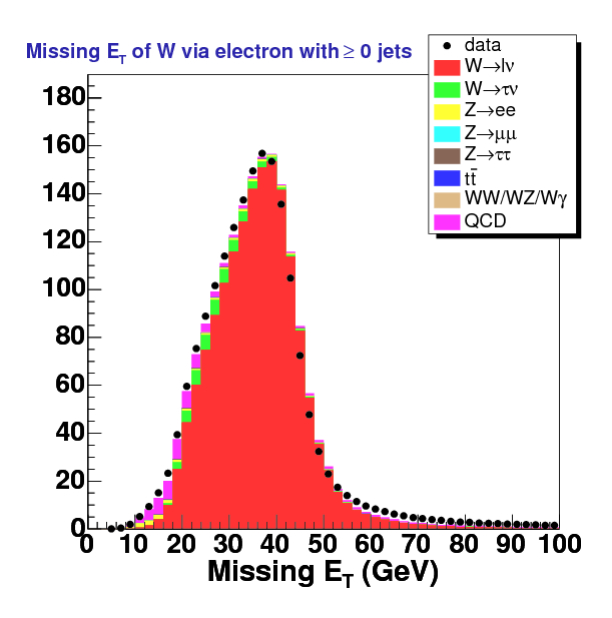


Figure 120: Missing transverse energy  $(\not\!\!E_T)$  for  $W \to e\nu + \ge 0$  jets.

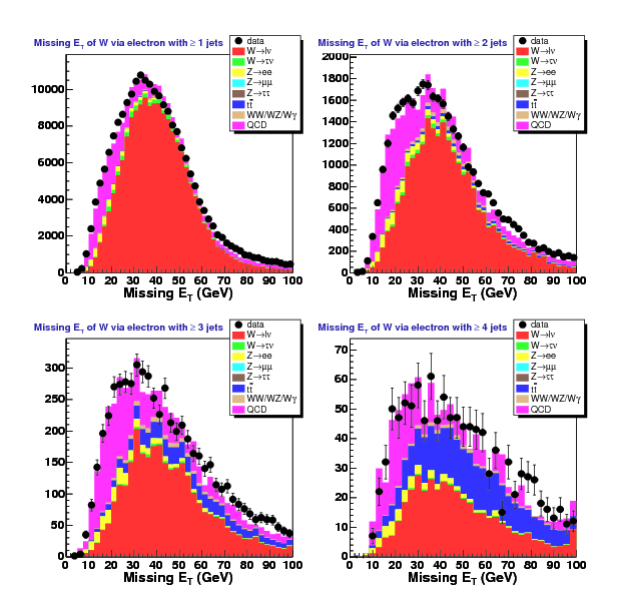


Figure 121: Missing transverse energy  $(\not\!E_T)$  for  $W \to e\nu + \geq n$  jets. Upper-left plot is for  $\geq 1$  jets, upper-right for  $\geq 2$ , lower-left for  $\geq 3$ , and lower-right for  $\geq 4$ .

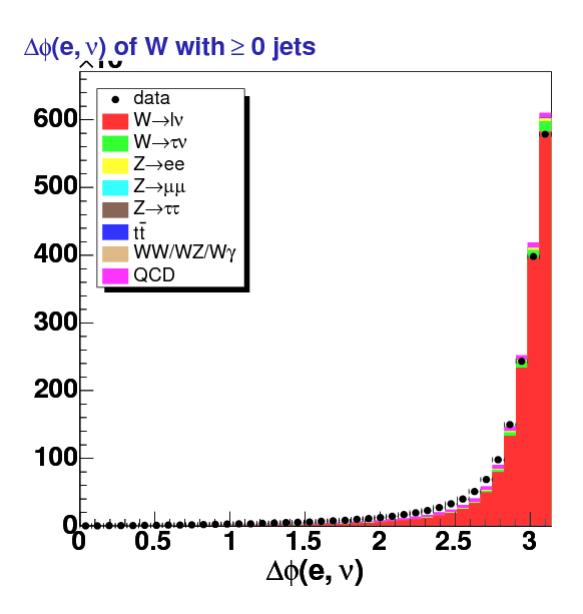


Figure 122:  $\Delta \phi$  between missing transverse energy and the electron  $(\Delta \phi(\mathbf{e}, \nu))$  for  $W \to e\nu + \geq 0$  jets.

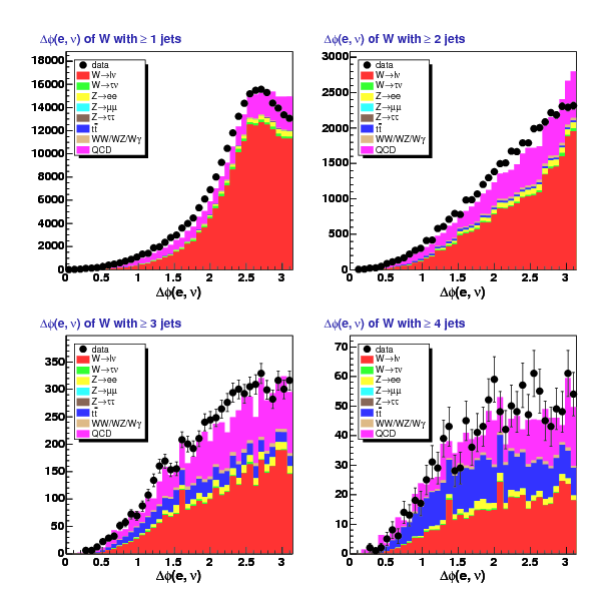


Figure 123:  $\Delta \phi$  between missing transverse energy and the electron  $(\Delta \phi(\mathbf{e}, \nu))$  for  $W \to e\nu + \geq n$  jets. Upper-left plot is for  $\geq 1$  jets, upper-right for  $\geq 2$ , lower-left for  $\geq 3$ , and lower-right for  $\geq 4$ .

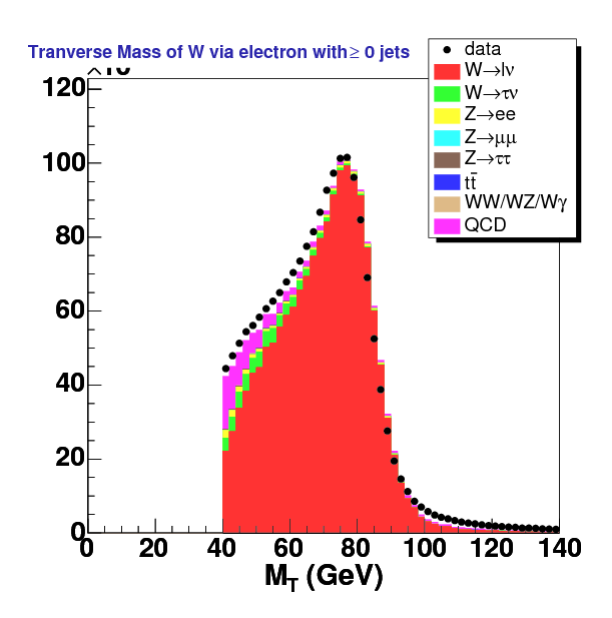


Figure 124: W transverse mass  $(M_T)$  for  $W \to e\nu + \ge 0$  jets.

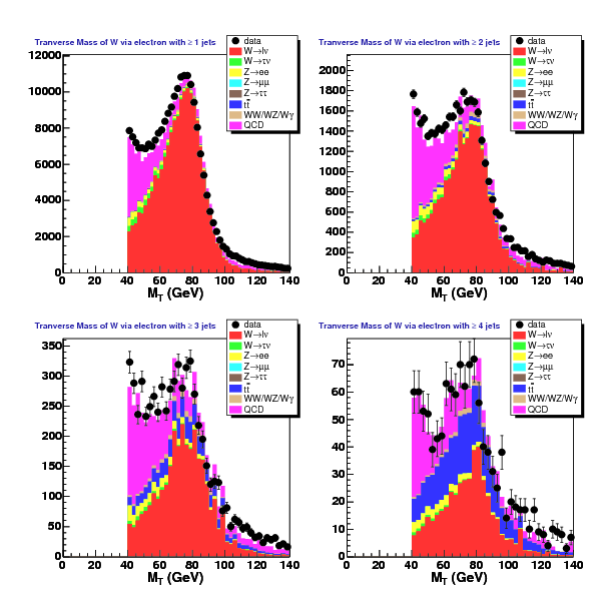


Figure 125: W transverse mass  $(M_T)$  for  $W \to e\nu + \geq n$  jets. Upper-left plot is for  $\geq 1$  jets, upper-right for  $\geq 2$ , lower-left for  $\geq 3$ , and lower-right for  $\geq 4$ .

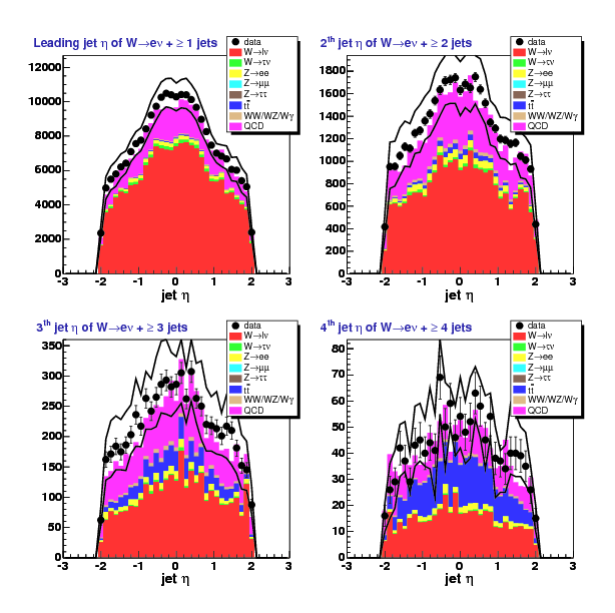


Figure 126:  $n^{\text{th}}$  leading jet  $\eta$  for  $W \to e\nu + \geq n$  jets. The black lines represent the systematic on the jet energy scale. Upper-left plot is for  $\geq 1$  jets, upper-right for  $\geq 2$ , lower-left for  $\geq 3$ , and lower-right for  $\geq 4$ .

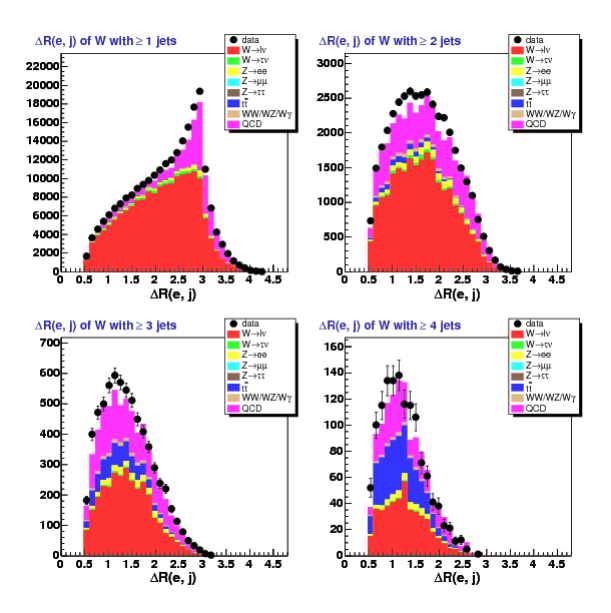


Figure 127: The  $\eta - \phi$  separation ( $\Delta R(e,j)$  with  $\Delta R_{a,b} = \sqrt{(\eta_a - \eta_b)^2 + (\phi_a - \phi_b)^2}$ ) for  $W \to e\nu + \geq n$  jets between the electron and the closest jet. Upper-left plot is for  $\geq 1$  jets, upper-right for  $\geq 2$ , lower-left for  $\geq 3$ , and lower-right for  $\geq 4$ .

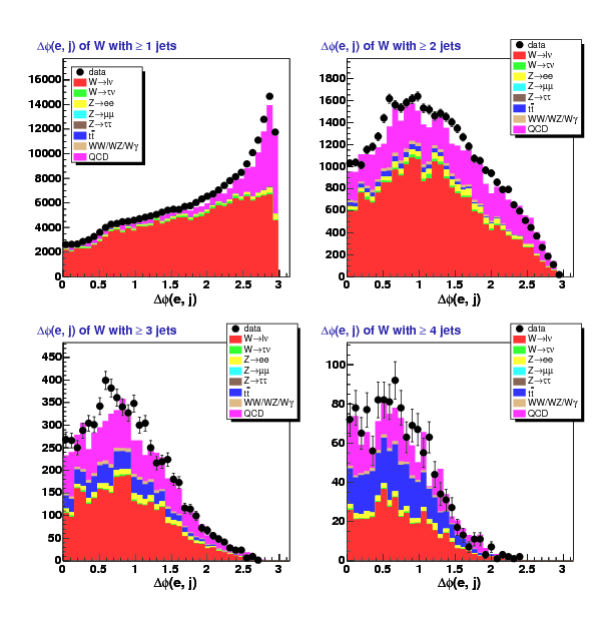


Figure 128: The  $\Delta \phi$  between the electron and the closest jet for  $W \to e\nu + \geq n$  jets. Upper-left plot is for  $\geq 1$  jets, upper-right for  $\geq 2$ , lower-left for  $\geq 3$ , and lower-right for  $\geq 4$ .

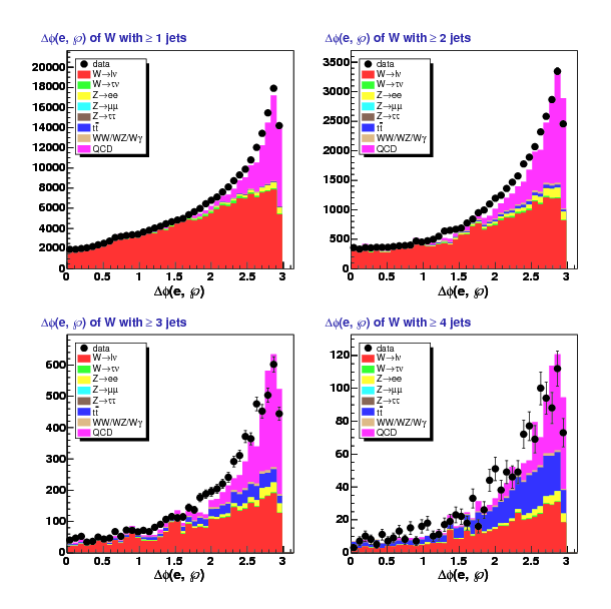


Figure 129: The  $\Delta \phi$  between the electron and the jet vector sum,  $\wp$  (as defined in equation 12 on page 29), for  $W \to e\nu + \geq n$  jets. Upper-left plot is for  $\geq 1$  jets, upper-right for  $\geq 2$ , lower-left for  $\geq 3$ , and lower-right for  $\geq 4$ .

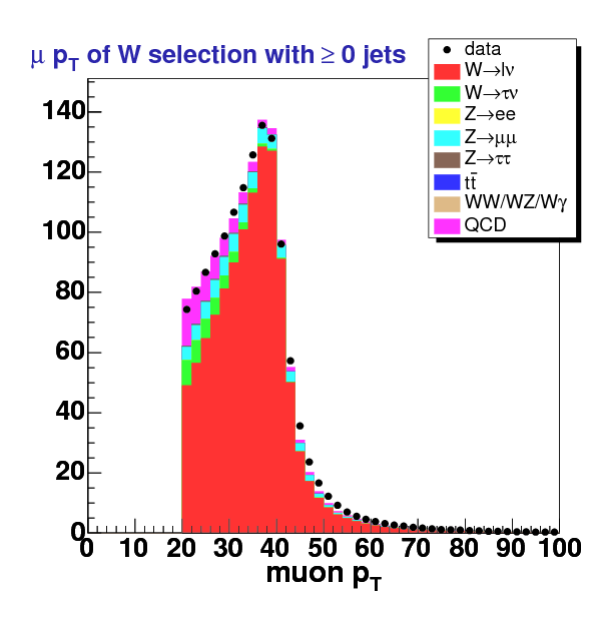


Figure 130: Muon transverse momentum  $(p_T)$  for  $W \to \mu\nu + \ge 0$  jets.

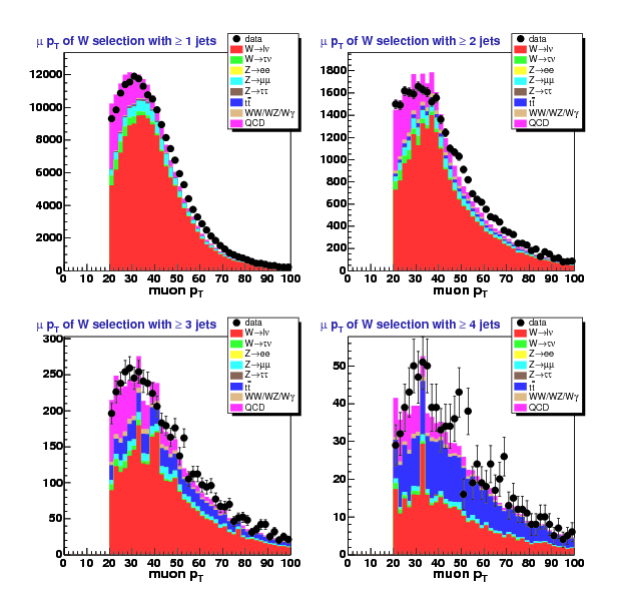


Figure 131: Muon transverse momentum  $(p_T)$  for  $W \to \mu\nu + \geq n$  jets. Upper-left plot is for  $\geq 1$  jets, upper-right for  $\geq 2$ , lower-left for  $\geq 3$ , and lower-right for  $\geq 4$ .

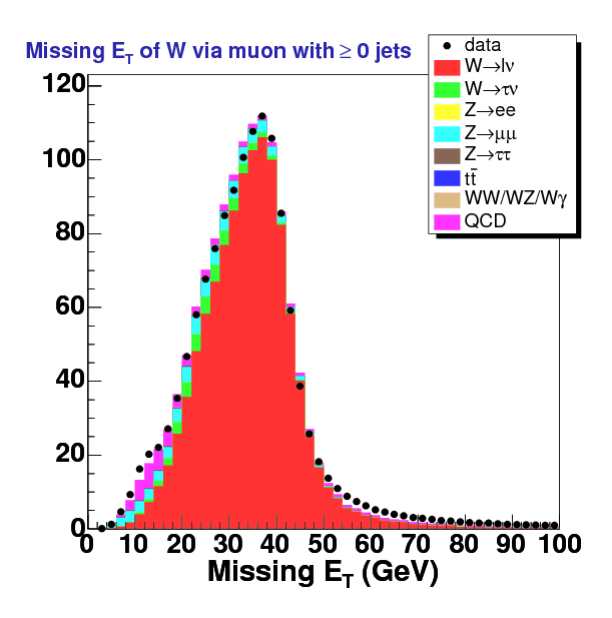


Figure 132: Missing transverse energy  $(\not\!\!E_T)$  for  $W \to \mu \nu + \ge 0$  jets.

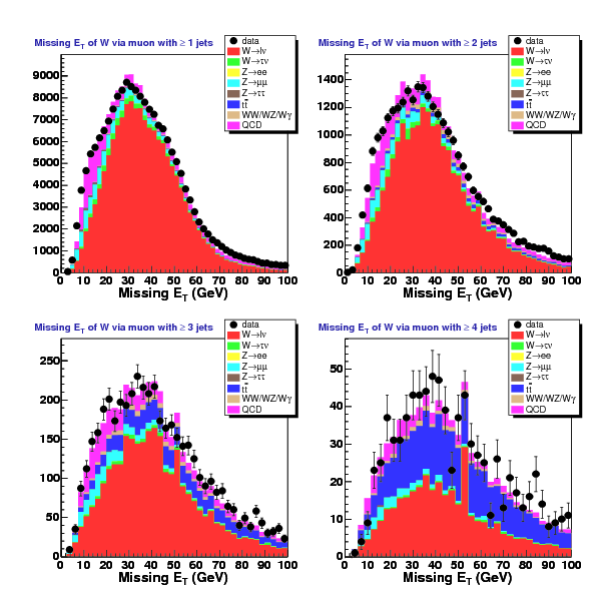


Figure 133: Missing transverse energy  $(\not\!E_T)$  for  $W \to \mu\nu + \geq n$  jets. Upper-left plot is for  $\geq 1$  jets, upper-right for  $\geq 2$ , lower-left for  $\geq 3$ , and lower-right for  $\geq 4$ .

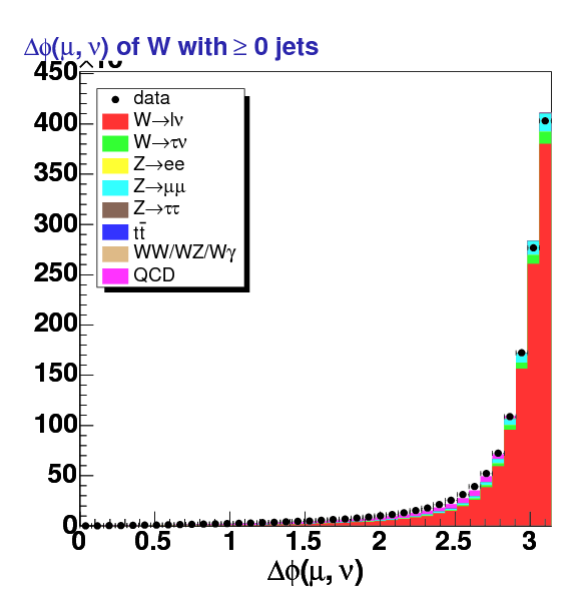


Figure 134:  $\Delta \phi$  between missing transverse energy and the muon  $(\Delta \phi(\mu, \nu))$  for  $W \to \mu \nu + \geq 0$  jets.

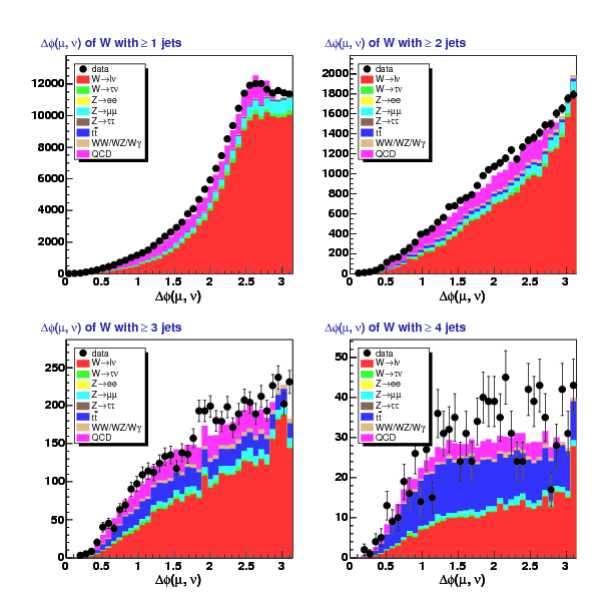


Figure 135:  $\Delta \phi$  between missing transverse energy and the muon  $(\Delta \phi(\mu, \nu))$  for  $W \to \mu \nu + \geq n$  jets. Upper-left plot is for  $\geq 1$  jets, upper-right for  $\geq 2$ , lower-left for  $\geq 3$ , and lower-right for  $\geq 4$ .

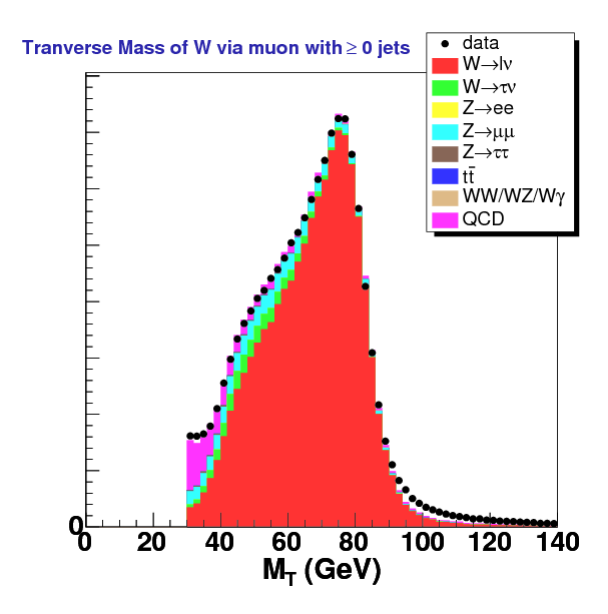


Figure 136: W transverse mass  $(M_T)$  for  $W \to \mu \nu + \geq 0$  jets.

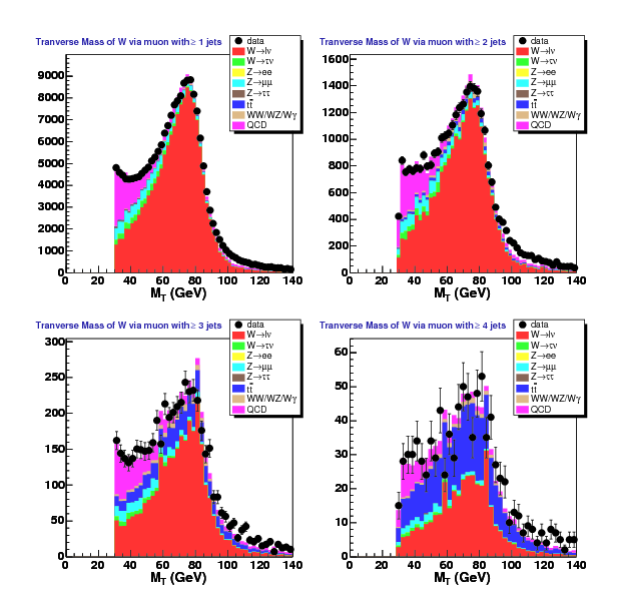


Figure 137: W transverse mass  $(M_T)$  for  $W \to \mu\nu + \geq n$  jets. Upper-left plot is for  $\geq 1$  jets, upper-right for  $\geq 2$ , lower-left for  $\geq 3$ , and lower-right for  $\geq 4$ .

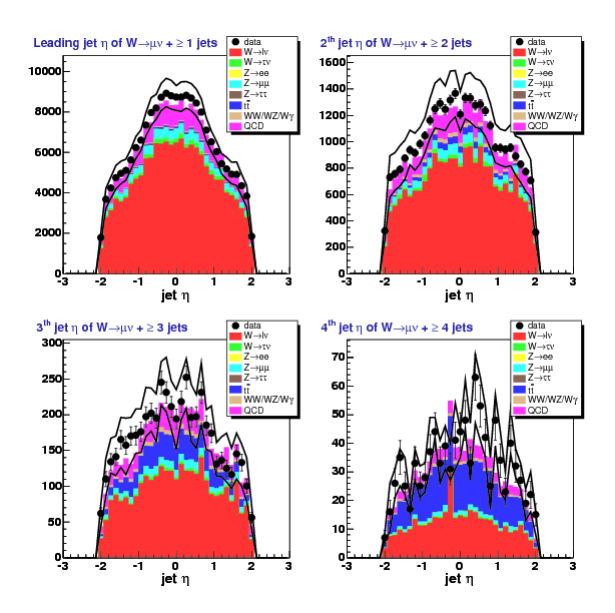


Figure 138:  $n^{\rm th}$  leading jet  $\eta$  for  $W \to \mu\nu + \geq n$  jets. The black lines represent the systematic on the jet energy scale. Upper-left plot is for  $\geq 1$  jets, upper-right for  $\geq 2$ , lower-left for  $\geq 3$ , and lower-right for  $\geq 4$ .

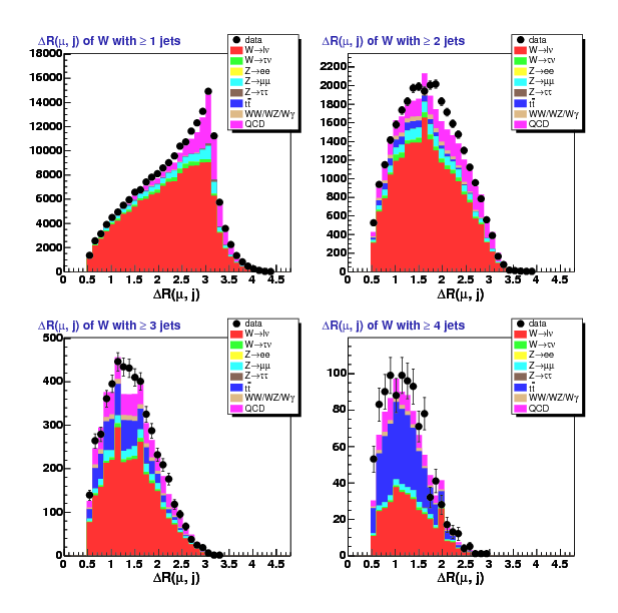


Figure 139: The  $\eta - \phi$  separation  $(\Delta R(\mu,j))$  with  $\Delta R_{a,b} = \sqrt{(\eta_a - \eta_b)^2 + (\phi_a - \phi_b)^2}$  for  $W \to \mu\nu + \geq n$  jets between the muon and the closest jet. Upper-left plot is for  $\geq 1$  jets, upper-right for  $\geq 2$ , lower-left for  $\geq 3$ , and lower-right for  $\geq 4$ .

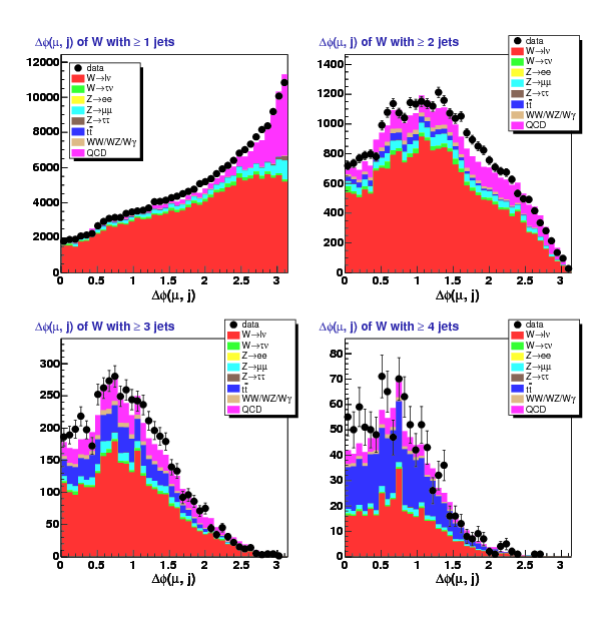


Figure 140: The  $\Delta \phi$  between the muon and the closest jet for  $W \to \mu \nu + \geq n$  jets. Upper-left plot is for  $\geq 1$  jets, upper-right for  $\geq 2$ , lower-left for  $\geq 3$ , and lower-right for  $\geq 4$ .

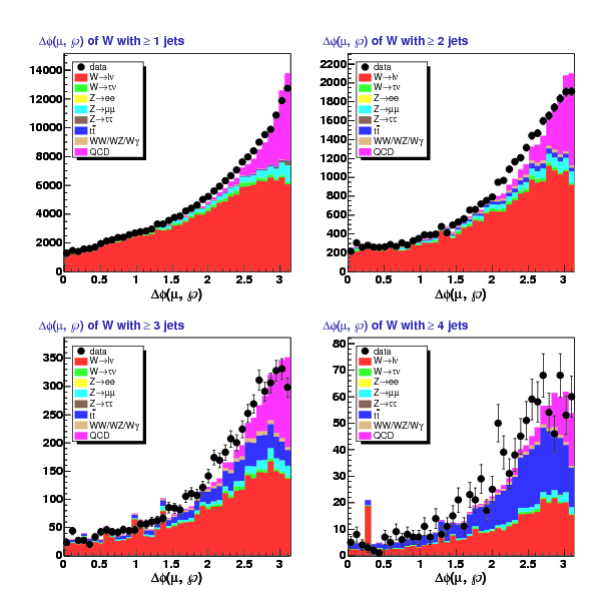


Figure 141: The  $\Delta \phi$  between the muon and the jet vector sum,  $\wp$  (as defined in equation 12 on page 29), for  $W \to \mu\nu + \geq n$  jets. Upper-left plot is for  $\geq 1$  jets, upper-right for  $\geq 2$ , lower-left for  $\geq 3$ , and lower-right for  $\geq 4$ .

## 4.6 MC Vertex Reweighing (Promotion)

As alluded to in sections 2.1 and 3.1 there is an additional background like effect that arises due to the potential for additional interactions to produce additional (that is non-primary vertex related) jets. For example, in the case of our signal sample we could have an event which has a candidate W (without loss of generalization, decaying to a muon and its neutrino) with 2 jets passing defining cuts. However, if one of these jets did not come from the primarily interactions it is not a W+2 jets event but rather a W+1 jet event with an additional jet via a separate interaction:

$$\langle p\bar{p} \to (W+1\mathrm{jet}) \rangle \oplus \langle p\bar{p} \to (X+\mathrm{jet}) \rangle$$

This possibility for our signal to be "promoted" to higher jet multiplicities (e.g. n to n+1) is called promotion. We can think as this as an additional background like effect where we have to adjust our expectation modulo the relevant event information (luminosity, number of vertices, etc.).

The overall goal of this section is to survey and understand the problem piece by piece and then proceed to explain our treatment. First we will discuss the relevant details to the number of vertices (hereafter "# vertices") and jet multiplicity distributions in data as a mean to our end of understanding the number of interactions. Then we will examine the comparison between data and MC and formulate a better criteria for the number of additional interactions in an event. This together with a method for correcting (reweighting) the MC on the basis for this criteria serves as a means to our end in accounting for the promotion background. We deal with systematic associated with the variation between reweighting and our refitting of backgrounds later in section 6.4.

Consider figures 142 and 143 which show the luminosity dependence on the number of quality 12 vertices for inclusive  $W \to e\nu$  and  $W \to \mu\nu$ , respectively. As these figures show, the luminosity has a clear effect on the number of additional quality 12 (or greater) vertices which in turn could manifest via promotion. The conclusion is that this is real effect that has to be quantified and dealt with. The previous version of this analysis [1] looked at the mini-bias sample and use this to construct a conversion matrix between the number of vertices (a good metric for additional interactions as explained later in this section) and jet multiplicity.

These plots demand a better understanding outside of our eventual goal of accounting for the jet promotion background/effect. A similar set of plots for the jet multiplicity is shown in Fig. 144 for electrons and Fig. 145. These are not particularly instructive by themselves so figures 146-147 were produce. In these plots the jet multiplicity for 4 different luminosity bins is normalized to the total (all luminosity) jet multiplicity so that they effectively have the same number of events. We note that in this approach, each jet bin is treated independently. These distributions are then divided by the nominal jet multiplicity. For example, if we measured the  $\geq 2$  jets multiplicity using only the  $L > 150^{30}$  cm<sup>-2</sup>/s sample it would be about 50% larger relative to our composite luminosity sample.

We now shift focus to the comparison between the MC and data. We first note that the previous MC sets for our W + np came via Alpgen(v1.3)+Herwig. We observed a rather lackluster performance in the MC (with full CDF simulation) in generating events with additional vertices.

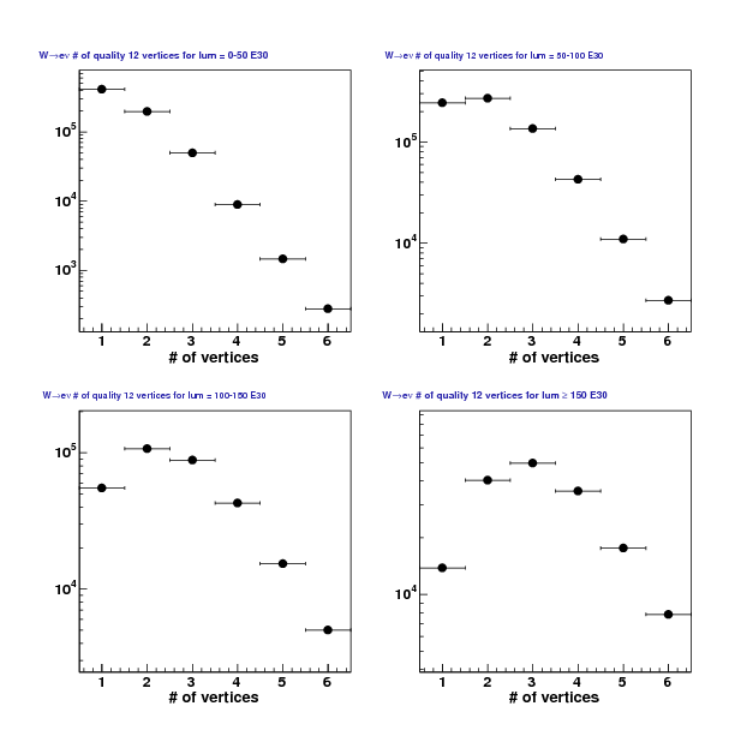


Figure 142: # of quality 12 vertices in  $W \to e\nu$  Candidates for instantaneous luminosities (in units of  $\times 10^{30}$  cm<sup>-2</sup>/s) of 0-50 (upper-left), 50-100 (upper-right), 100-150 (lower-left), and  $\geq 150$  (lower-right).

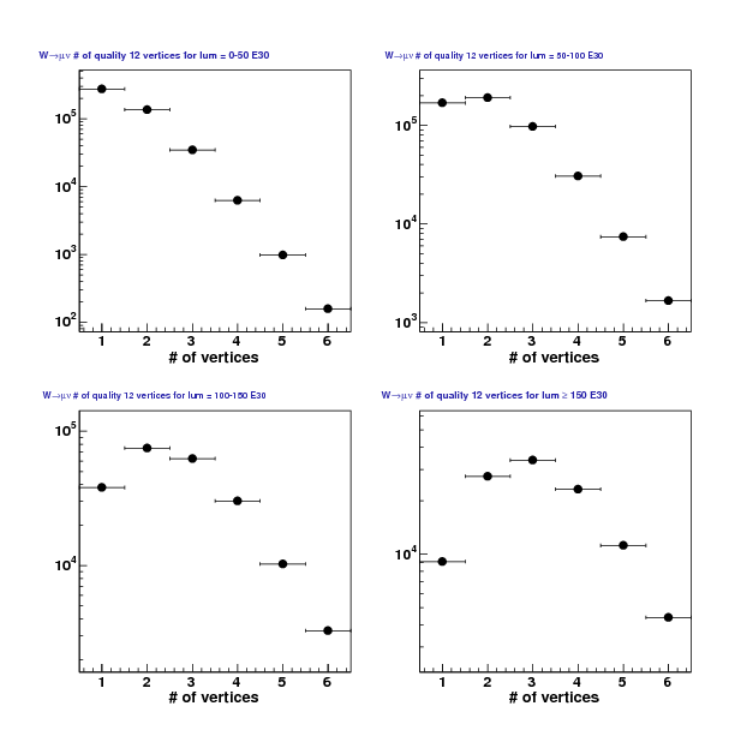


Figure 143: # of quality 12 vertices in  $W \to \mu\nu$  Candidates for instantaneous luminosities (in units of  $\times 10^{30}$  cm<sup>-2</sup>/s) of 0-50 (upper-left), 50-100 (upper-right), 100-150 (lower-left), and  $\geq 150$  (lower-right).

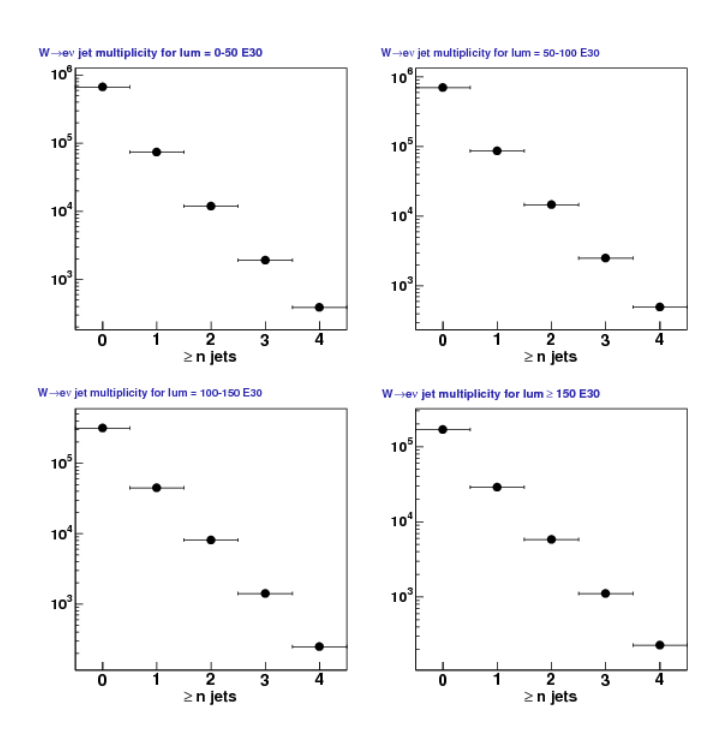


Figure 144: Jet Multiplicity for  $W \to e\nu$  Candidates for instantaneous luminosities (in units of  $\times 10^{30}$  cm<sup>-2</sup>/s) of 0-50 (upper-left), 50-100 (upper-right), 100-150 (lower-left), and  $\geq 150$  (lower-right).

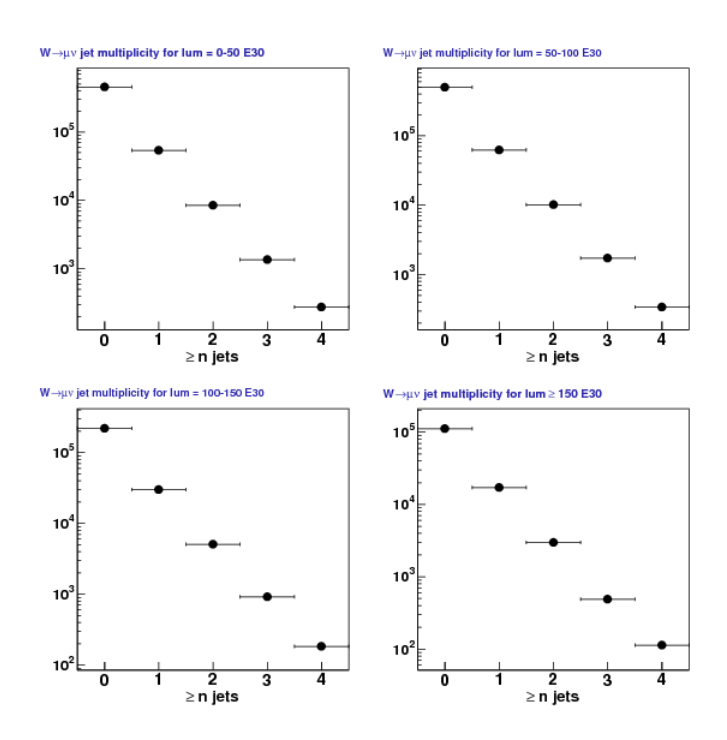


Figure 145: Jet Multiplicity for  $W \to \mu\nu$  Candidates for instantaneous luminosities (in units of  $\times 10^{30}$  cm<sup>-2</sup>/s) of 0-50 (upper-left), 50-100 (upper-right), 100-150 (lower-left), and  $\geq 150$  (lower-right).

The newer incarnation is much improved but still was not been tuned to give good agreement for moderate (1-4) number of vertices falls off very quickly for higher number of vertices. In figures 148 and 149 we show the # of quality 12 vertices for  $W \to e\nu + \geq n$  jets. We present the same distributions for  $W \to \mu\nu + \geq 0$  and n jets in figures 150 and 151. Again the prediction in the MC does not match up for the lower number of vertices and under performs for the higher number. On the positive side, in the case of the electrons, the data based QCD falls off roughly as the data does suggesting no # vertices dependence/bias.

In order to better understand the disagreement between MC and data we took the data based components (data candidates and QCD prediction) and compared them to the sum MC based predictions. We also simplified the # vertices to run to 1-6. Figures 152 and 153 are the (data-QCD) vs. MC version of figures 148 and 149, respectively, for the electron channel. We produce the same (data-QCD) vs. MC plots for the muon channel and these are shown in figures 154 and 155 for  $\geq 0$  jets and  $\geq 1$ -4 jets, respectively. In order to help make these comparisons with the # vertices, a Data/MC plot is shown in figures 156 and 157 for the electron channel and the muon channel results are given in figures 158 and 159 again for the  $\geq 0$  jets and  $\geq 1$ -4 jets cases, respectively. These Data/MC are literally the histogram division between are simplified data (minus QCD) and MC estimation.

## 

Figure 146: Jet Multiplicity for different instantaneous luminosity bins [0-50 ( $\bullet$ ), 50-100 ( $\blacktriangledown$ ), 100-150 ( $\blacksquare$ ), and  $\geq$ 150 ( $\blacktriangle$ ) in units of  $\times 10^{30}$  cm<sup>-2</sup>/s] normalized to and then divided by the total luminosity sample for  $W \to e\nu$  Candidates

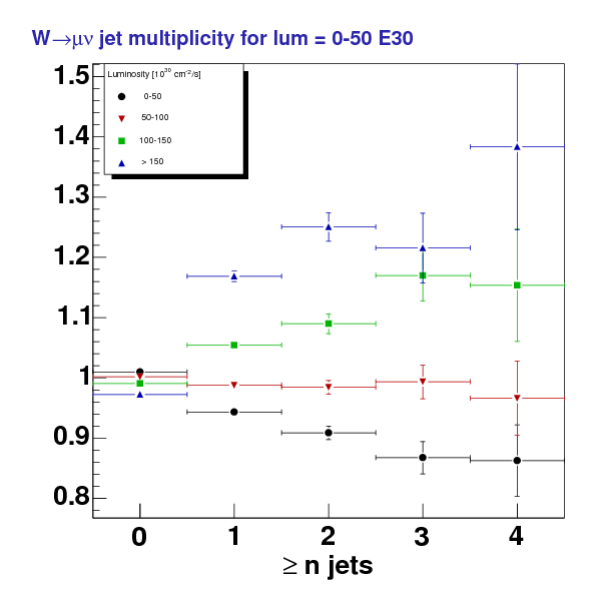


Figure 147: Jet Multiplicity for different instantaneous luminosity bins [0-50 ( $\bullet$ ), 50-100 ( $\blacktriangledown$ ), 100-150 ( $\blacksquare$ ), and  $\geq$ 150 ( $\blacktriangle$ ) in units of  $\times 10^{30}$  cm<sup>-2</sup>/s] normalized to and then divided by the total luminosity sample for  $W \to \mu\nu$  Candidates

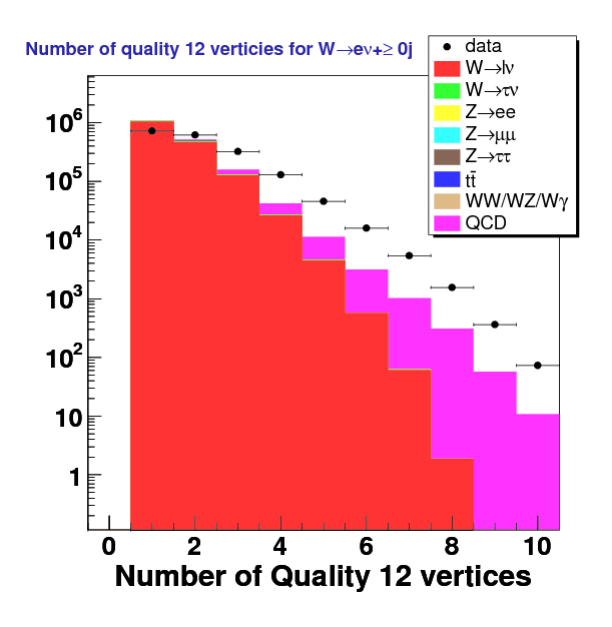


Figure 148: # quality 12 vertices for  $W \to e\nu + \geq 0$  jets

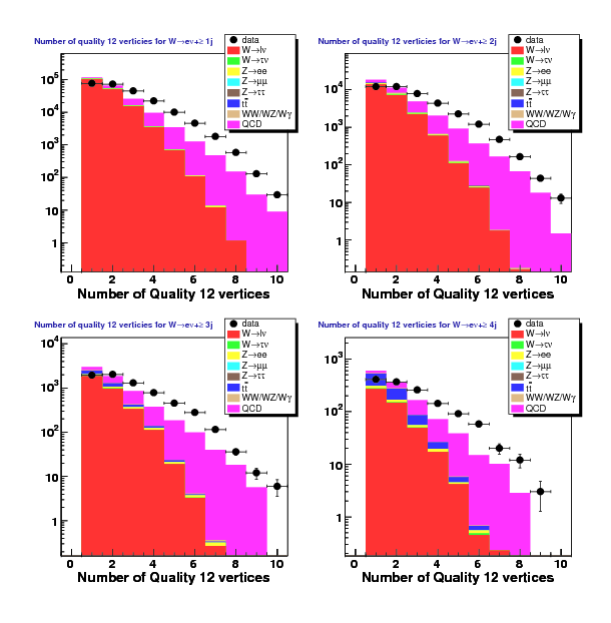


Figure 149: # quality 12 vertices for  $W \to e\nu + \ge 1$ -4 jets

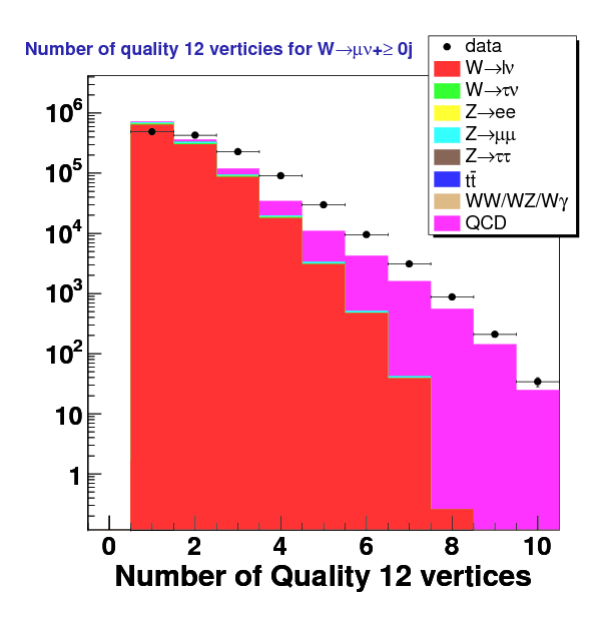


Figure 150: # quality 12 vertices for  $W \to \mu \nu + \geq 0$  jets

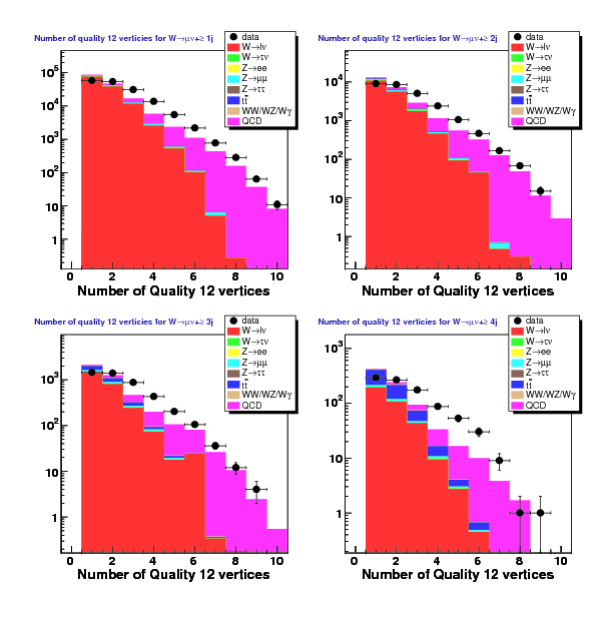


Figure 151: # quality 12 vertices for  $W \to \mu \nu + \ge 1\text{-}4$  jets

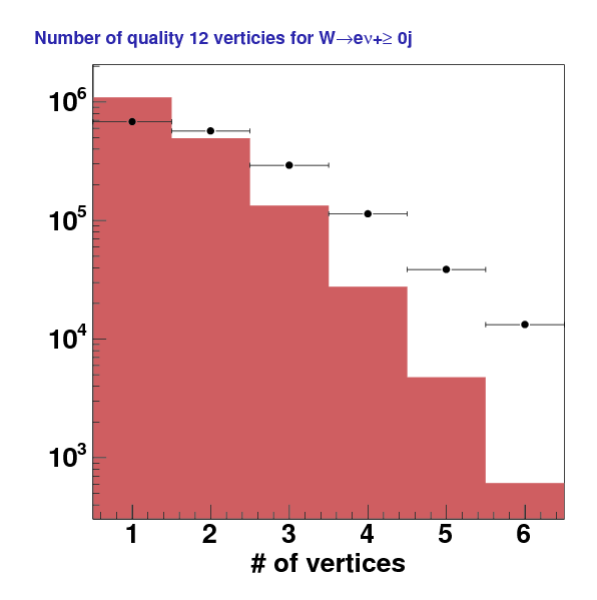


Figure 152: # quality 12 vertices for  $W \to e\nu + \ge 0$  jets. Here the red histogram represents the sum MC predictions of Fig. 148 while the data points represent Data-QCD

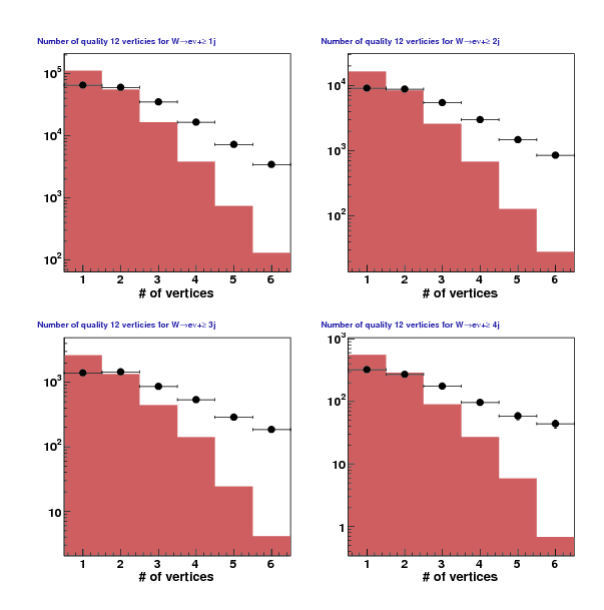


Figure 153: # quality 12 vertices for  $W \to e\nu + \ge 1$ -4 jets. Here the red histogram represents the sum MC predictions of Fig. 149 while the data points represent Data-QCD

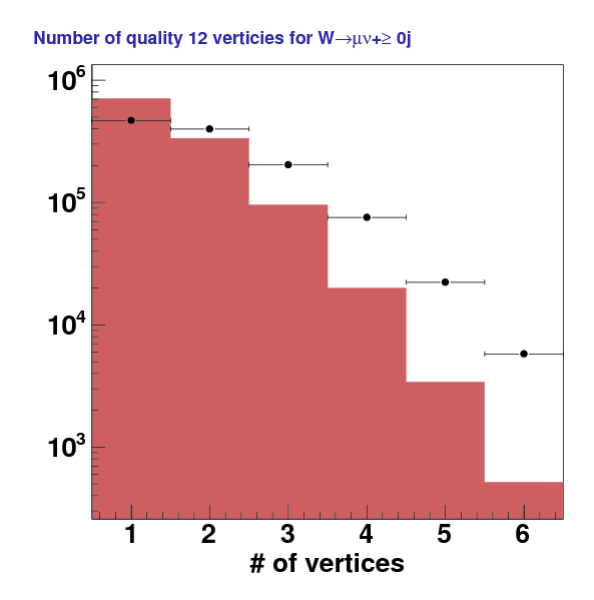


Figure 154: # quality 12 vertices for  $W \to \mu\nu + \ge 0$  jets. Here the red histogram represents the sum MC predictions of Fig. 150 while the data points represent Data-QCD

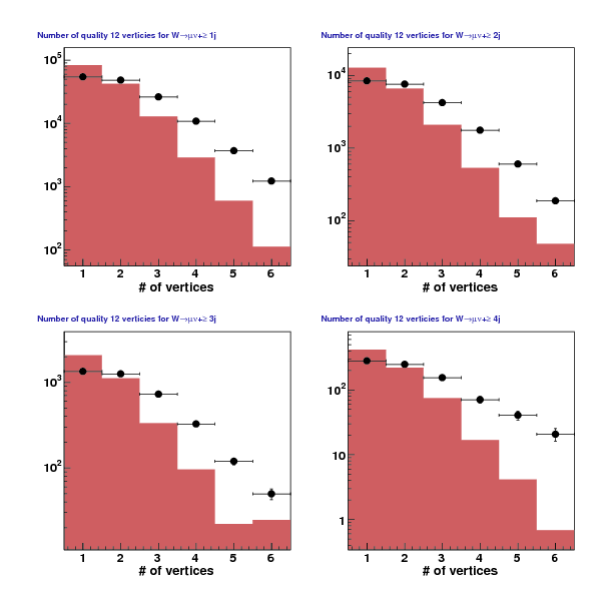


Figure 155: # quality 12 vertices for  $W \to \mu\nu + \ge 1$ -4 jets. Here the red histogram represents the sum MC predictions of Fig. 151 while the data points represent Data-QCD

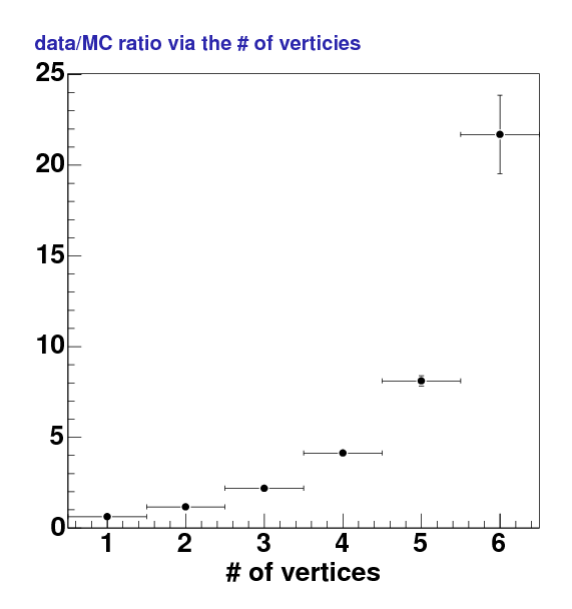


Figure 156: Data/MC comparison of # quality 12 vertices for  $W \to e\nu + \ge 0$  jets. This is a ratio of Data-QCD vs. MC from the Fig. 152.

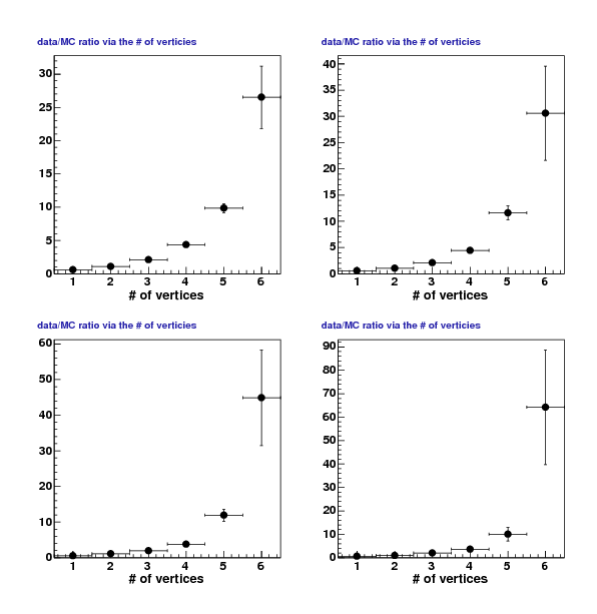


Figure 157: Data/MC comparison of # quality 12 vertices for  $W \to e\nu + \ge 1$ -4 jets. This is a ratio of Data-QCD vs. MC from the Fig. 153.

## data/MC ratio via the # of verticles 12 10 8 4 2 1 2 3 4 5 6 # of vertices

Figure 158: Data/MC comparison of # quality 12 vertices for  $W \to \mu\nu + \ge 0$  jets. This is a ratio of Data-QCD vs. MC from the Fig. 154.

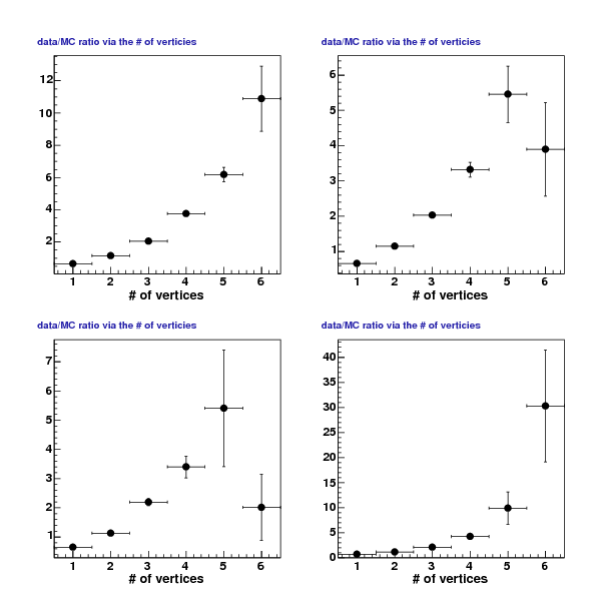


Figure 159: Data/MC comparison of # quality 12 vertices for  $W \to \mu\nu + \ge 1$ -4 jets. This is a ratio of Data-QCD vs. MC from the Fig. 155.

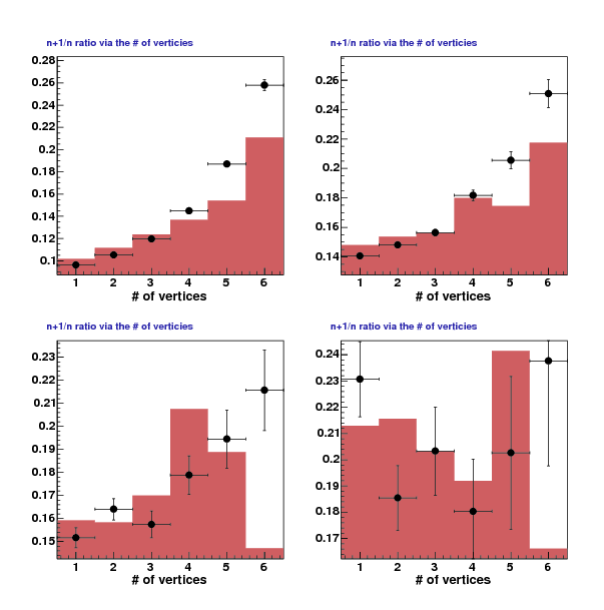


Figure 160: (n+1)/n jet multiplicity ratio comparison of # quality 12 vertices for  $W \to e\nu + \geq n$  jets. Here the red histogram represents the MC prediction while the data points represent Data-QCD for each jet multiplicity ratio. Upper-left: 1/0, upper-right: 2/1, lower-left: 3/2, and lower-right: 4/3.

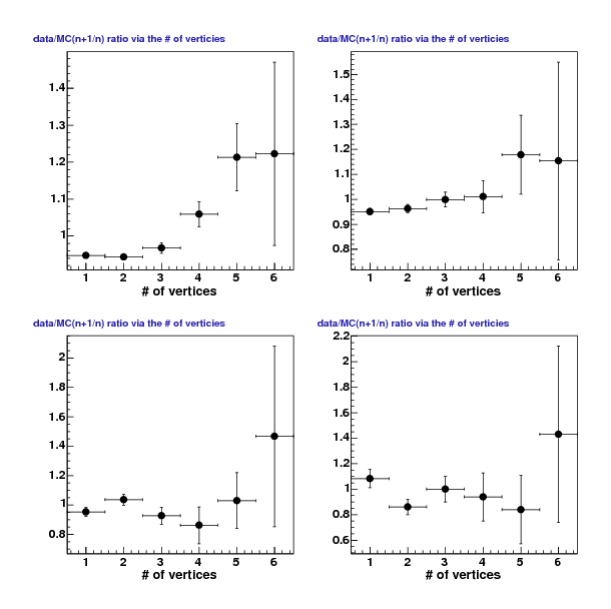


Figure 161: Data/MC ratio of the (n+1)/n jet multiplicity ratio comparison of # quality 12 vertices for  $W \to e\nu + \geq n$  jets. This is a Data/MC ratio of Fig. 160. Upper-left: 1/0, upper-right: 2/1, lower-left: 3/2, and lower-right: 4/3.

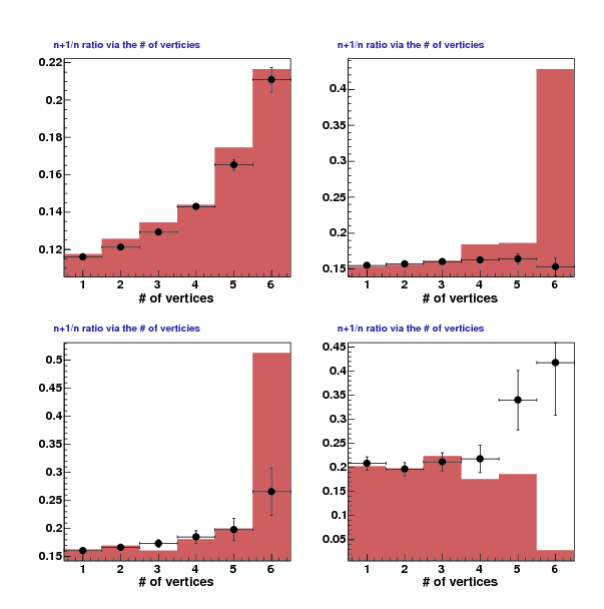


Figure 162: (n+1)/n jet multiplicity ratio comparison of # quality 12 vertices for  $W \to \mu\nu + \geq n$  jets. Here the red histogram represents the MC prediction while the data points represent Data-QCD for each jet multiplicity ratio. Upper-left: 1/0, upper-right: 2/1, lower-left: 3/2, and lower-right: 4/3.

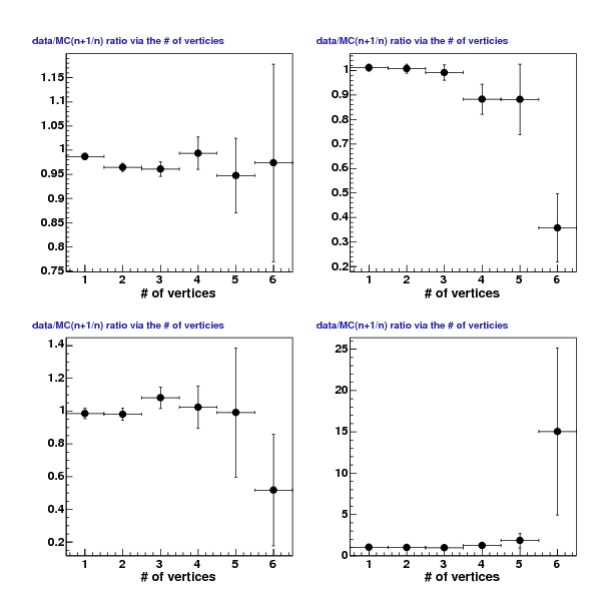


Figure 163: Data/MC ratio of the (n+1)/n jet multiplicity ratio comparison of # quality 12 vertices for  $W \to \mu\nu + \geq n$  jets. This is a Data/MC ratio of figure 162. Upper-left: 1/0, upper-right: 2/1, lower-left: 3/2, and lower-right: 4/3.

These plots (figures 148-159) make it clear that the MC does a poor job of describing the # vertices distribution. However, our direct concern was whether or not there was a possible jet multiplicity dependence; i.e. was the discrepancy consistent verses the number of jets such that we could simply scale up the MC to resolve the issue. To this end, we also produced a set of jet multiplicity ratio plots between consecutive bins. Here we still plot the # vertices distribution but each plot represents a (n+1)/n jet multiplicity ratio. For example, "2/1" represents the ratio between the # vertices shapes for  $\geq 2$  and  $\geq 1$  jets. Section 7.3 explains the motivation for this observable.

Figure 160 and its Data/MC comparison in figures 161 show the # vertices comparison where each plot represents a different (n + 1)/n jet multiplicity ratio for the electron channel. The results for the muon channel are similarly presented in figures 162 (data vs. MC) and 161 (data/MC). This observable speaks to the effect of promotion or more directly how well the MC could be use to describe the number of vertices for different jet multiplicities. The basic agreement is decent but less than stellar and past  $\geq 3$  or 4 vertices the MC would be limited in event size to describe the data. This result prompted us to study this further in order to get derive a method that would address these concerns as outline so far.

Before we describe our handling of the # vertices description and background promotion we consider two profile histogram plots and an additional set of plots dealing with our vertex description. The first (figure 164) is a histogram of the jet multiplicity plotted against the average # of quality 12 vertices for data and MC. The second (figure 165) is just the flipped version where the x-axis is the number of vertices and the jet multiplicity has been averaged for the profile histogram. Both plots are for the electron channel but the effect would not be appreciably different in the muon channel. Next we looked at the sum  $p_T$  of each vertex ordered in descending values for vertexes #1-5. The first vertex will almost always be the triggered candidate high  $p_T$  lepton and this is shown in figures 166 and 168 for the total inclusive sample for the electrons and muons, respectively. Figures 167 (electron channel) and 169 (muon channel) shows the sum vertex  $p_T$  for vertices 2-5 and our predictions poorly describes the data. Finally we look at the difference between each non-primary vertex's z-position ( $z_{vtx}$ ) with the primary vertex's z-position ( $z_0$ ). This quantity,  $z_0 - z_{vtx}$ , is plotted over a wide range for the total inclusive case in figure 170 and then for inclusive jet multiplicities 1-4 in figure 171 for our electron results. The muons results are presented, likewise, in figures 172 and 173.

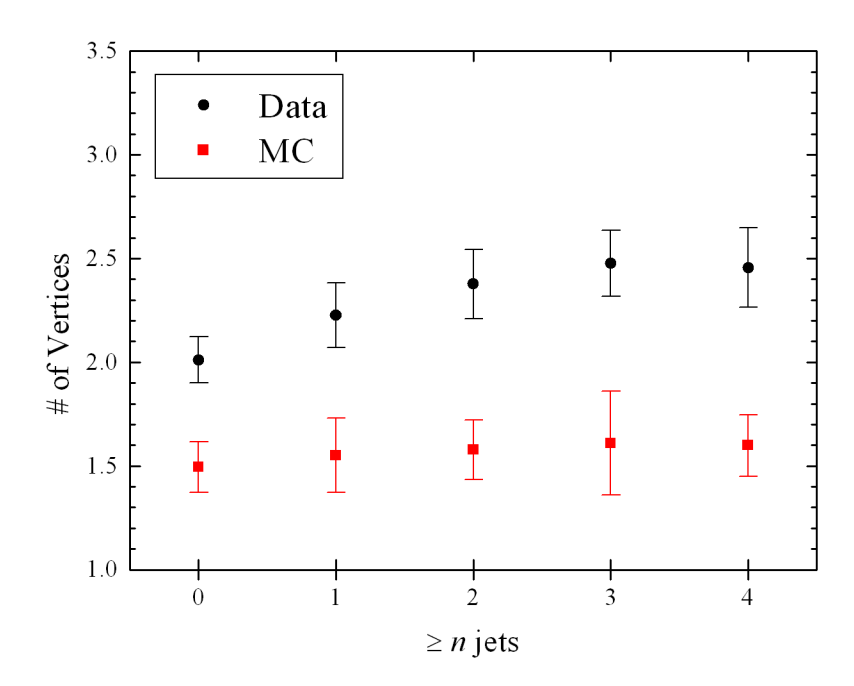


Figure 164: Profile histogram for the number of quality 12 vertices verses the jet multiplicity for  $W \to e\nu + \geq n$  jets.

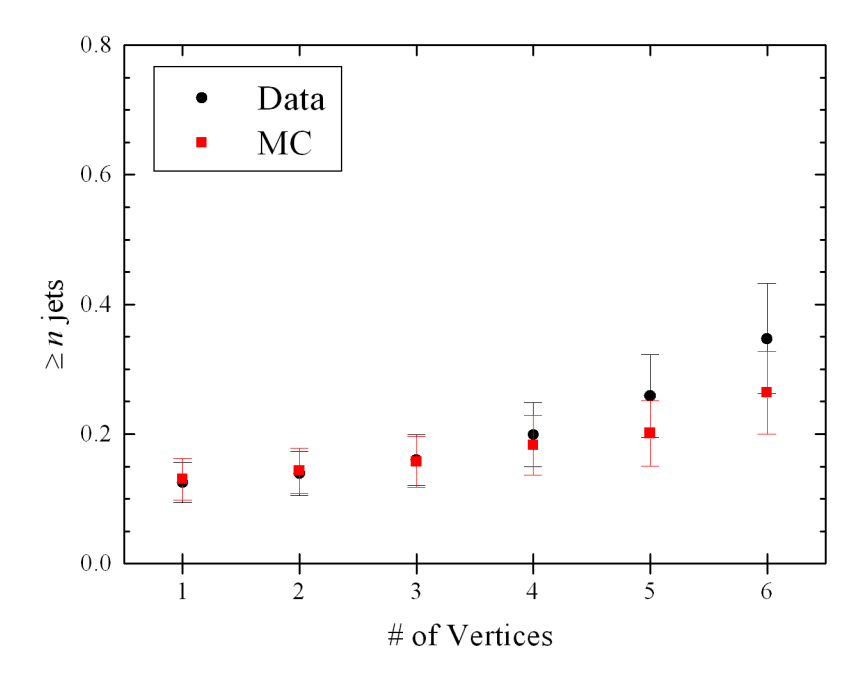


Figure 165: Profile histogram for the jet multiplicity verses the number of quality 12 vertices for  $W \to e\nu + \geq n$  jets.

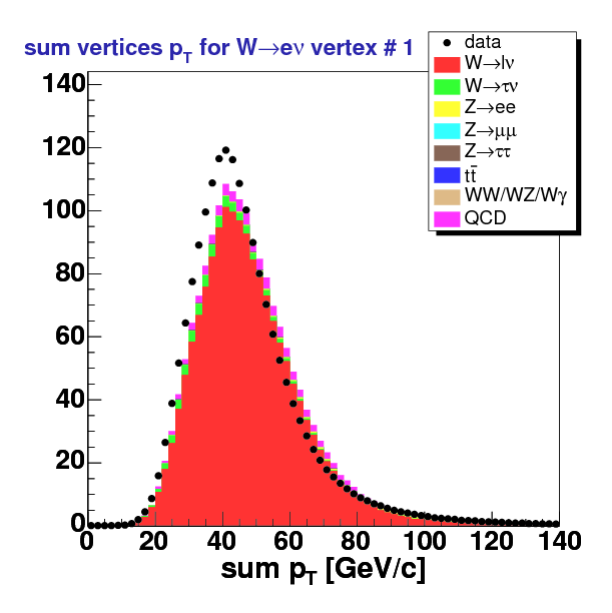


Figure 166: Vertex sum  $p_T$   $(\sum p_T^{vtx})$  for the leading order vertex for  $W \to e\nu + \ge 0$  jets

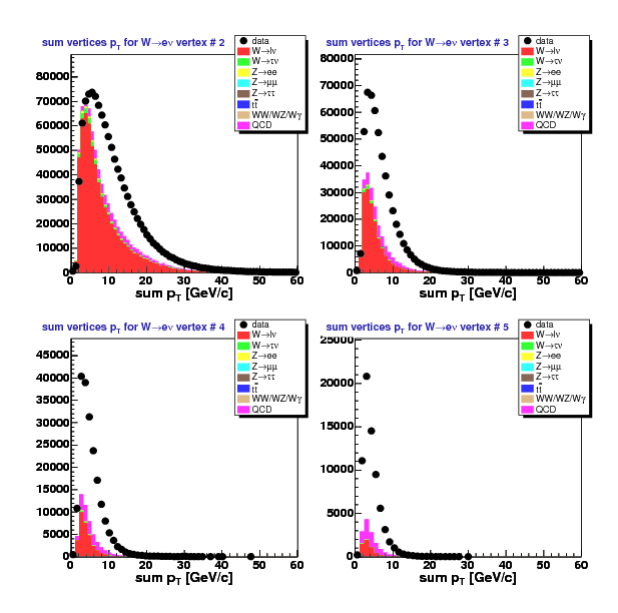


Figure 167: Vertex sum  $p_T$   $(\sum p_T^{vtx})$  for ordered vertexes 2-5 for  $W \to e\nu + \ge 0$  jets

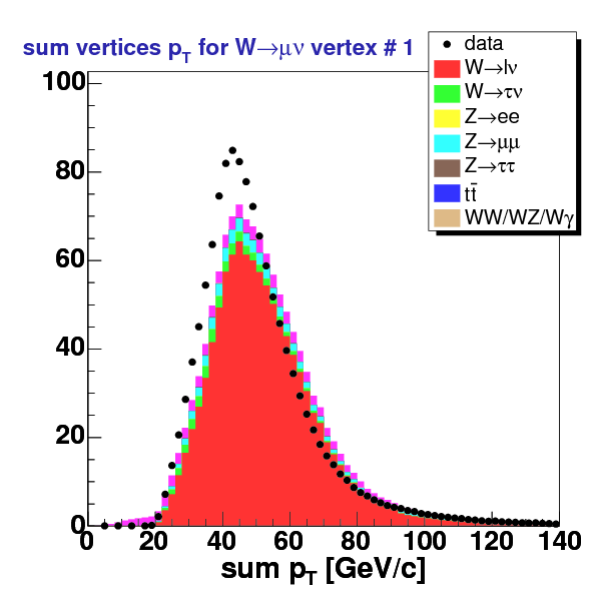


Figure 168: Vertex sum  $p_T$   $(\sum p_T^{vtx})$  for the leading order vertex for  $W \to \mu\nu + \ge 0$  jets

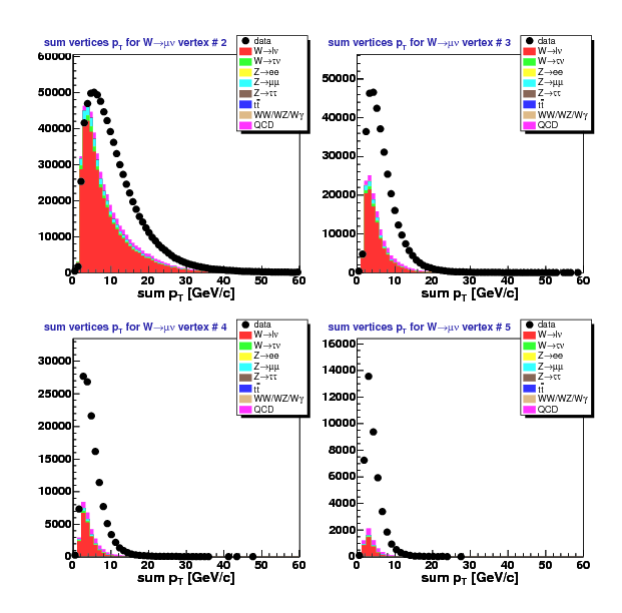


Figure 169: Vertex sum  $p_T$   $(\sum p_T^{vtx})$  for ordered vertexes 2-5 for  $W \to \mu\nu + \geq 0$  jets

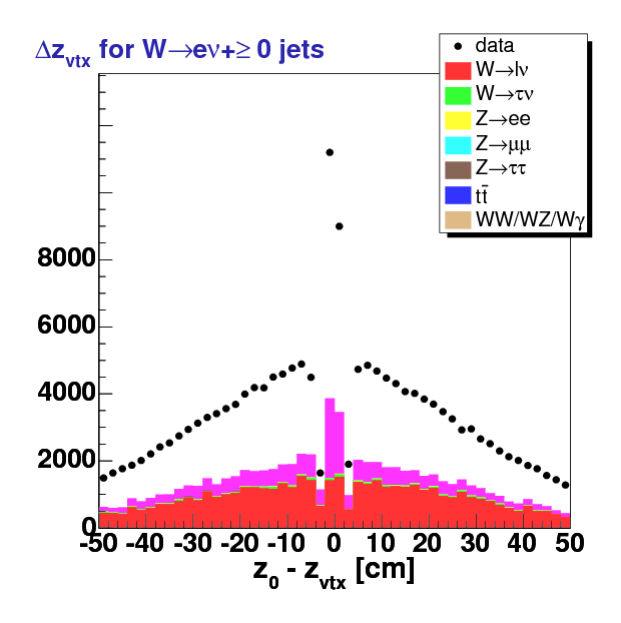


Figure 170:  $z_0-z_{vtx}$  for each vertex omitting the primary for  $W\to e\nu+\ge 0$  jets

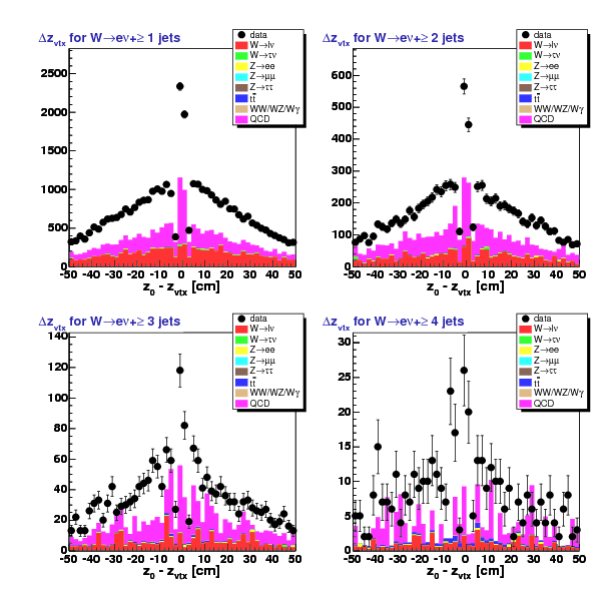


Figure 171:  $z_0-z_{vtx}$  for each vertex omitting the primary for  $W\to e\nu+\ge 1$ -4 jets

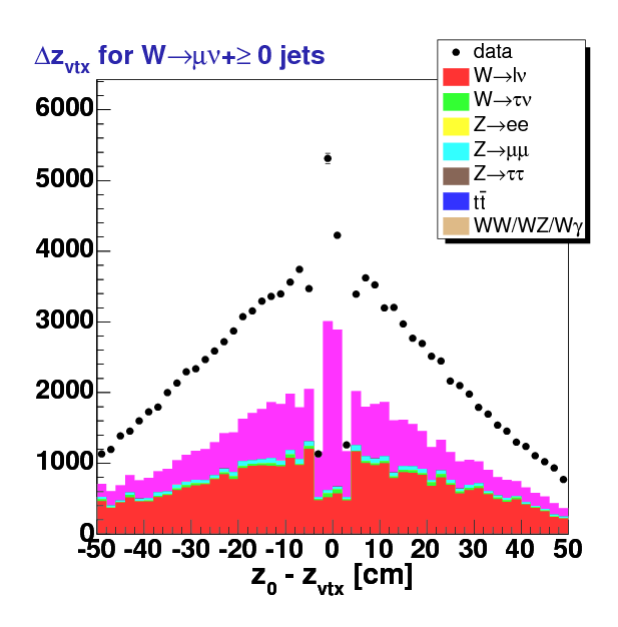


Figure 172:  $z_0-z_{vtx}$  for each vertex omitting the primary for  $W\to\mu\nu+\ge 0$  jets

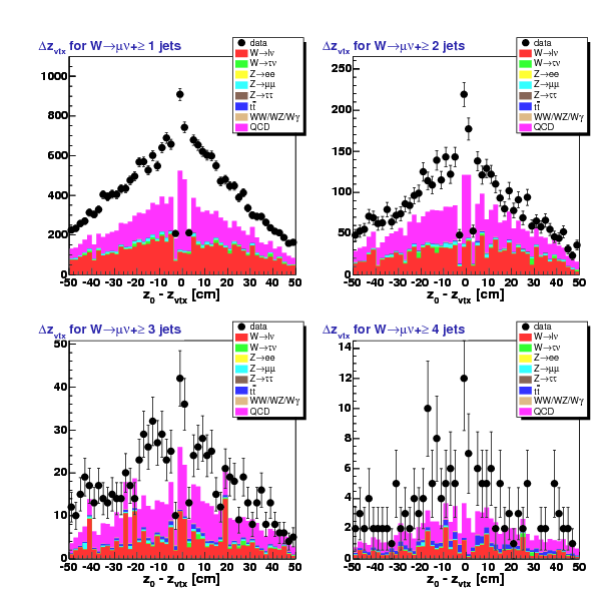


Figure 173:  $z_0-z_{vtx}$  for each vertex omitting the primary for  $W\to \mu\nu+\geq 1$ -4 jets

First we note that our jet transverse momentum requirement,  $p_T^{jet} > 20 \text{ GeV/c}$ , greatly reduces the possible effect of promotion. As noted at the beginning of the section, the promotion background will be heavily biased at low  $p_T$  [1]. Therefore, the simplest solution (at the cost of reducing the sample sizes at higher jet multiplicities) would be to just increase the  $p_T$  cut. However, with this knowledge we wondered if we could better quantify the number of additional interactions (e.g. via # vertices). We tested setting different  $p_T$  cuts to the vertex definition. Here the vertex momentum is defined by the sum track momentums with a common vertex. We denote the transverse momentum of the vertex via  $\sum p_T^{vtx}$ .

In figures 174 and 175, we present the same number of quality 12 vertices plots broken up into different instantaneous luminosities as done previously in figures 142 and 143 but with the additional requirement that  $\sum p_T^{vtx} > 18 \text{ GeV/c}$ . The limit of 18 GeV/c was chosen as an upper-limit for testing the sensitivity of this variable as this is the trigger threshold. The plots with the redefined vertex criteria no longer have the extreme luminosity dependence. In particular this definition makes events with higher number of vertices more meaningful in terms of actually indicating additional activity outside of the triggered lepton. In the case of the electron channel, our lower luminosity cohort  $(0-50\times10^{30}~\text{cm}^{-2}/\text{s})$  shows a 3 order of magnitude drop between 1 and 3 vertices with the additional  $\sum p_T^{vtx}$  cut (see figure 174). For the  $100-150\times10^{30}~\text{cm}^{-2}/\text{s}$  cohort, it is a full 2 orders of magnitude between 1 and 3. Contrast this to figure 142 where the difference is a factor of 10 for the lower luminosity results and a factor of 2 increase for 1 to 3 vertices. The same analysis on the muon channel (contrast figure 175 to figure 143) yields the same result.

We tested various  $\sum p_T^{vtx}$  cuts (8, 10, 15, and 18 GeV/c). We present results for  $\sum p_T^{vtx} > 15$  GeV/c and limit the number of vertices in the event to 6 or less. We note that this upper number of vertices cut was chosen to basically make the MC based W acceptance unchanged. Figures 176 and 177 show the data verses prediction comparison for  $W \to e\nu + \geq n$  jets. Based off of later comparisons with the muon channel, we expect consistent results but omit these plots for brevity. We make a data (i.e. data candidates minus QCD prediction) verses MC (i.e. MC signal+background predictions) in figures 178 and 179. We then show the (n+1)/n jet multiplicity ratio (compare to the "no cut" versions in Fig. 160 and Fig. 161) between data components and MC in figure 180 and a ratio of said components in 181.

Ultimately we found the  $\sum p_T^{vtx} > 10$  GeV/c to be optimal (modulo an additional constraint) for describing the data verses MC results and discussion that follow. Figures 182 and 183 are an updated version of the profile histograms (for  $W \to e\nu + \geq n$  jets) noted before in 164 and 165 where we have included the  $\sum p_T^{vtx} > 10$  GeV/c requirement. With respect to the MC the concern was whether we could adequately describe the effect of additional interactions for our promotion background. This meant having good relative agreement in # vertices for each different jet multiplicity. The limitation (as shown in figures 176-181) is that the MC starts to do poorly pass the third vertex. However this raised a different question with respect to the data, namely: what was the motivation for keeping events with many additional energetic vertices? Given our new  $\sum p_T^{vtx}$  discriminate, we could veto events with high # vertices and thus take a small hit in our data candidate yield and W signal acceptance while removing events that are not descriptive of W+jets.

In table 23 we show the reduction in the yield of data candidates for both electrons and muons

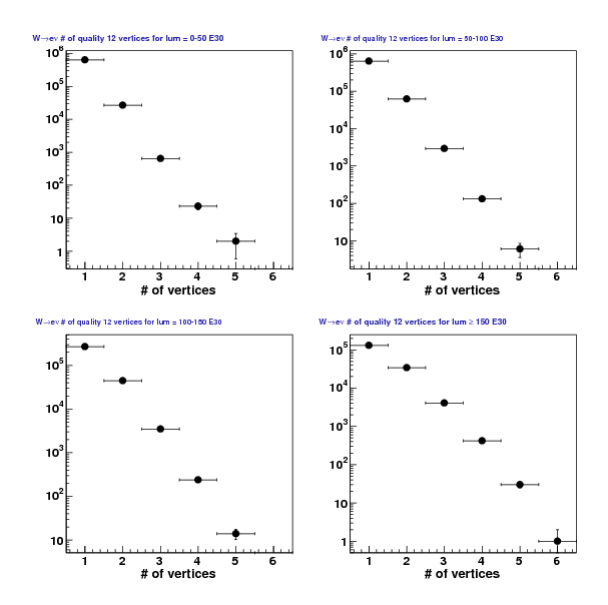


Figure 174: # of quality 12 vertices with  $\sum p_T^{vtx} > 18$  GeV/c in  $W \to e\nu$  Candidates for instantaneous luminosities (in units of  $\times 10^{30}$  cm<sup>-2</sup>/s) of 0-50 (upper-left), 50-100 (upper-right), 100-150 (lower-left), and  $\geq 150$  (lower-right). Compare to the no  $\sum p_T^{vtx}$  cut version in Fig. 142

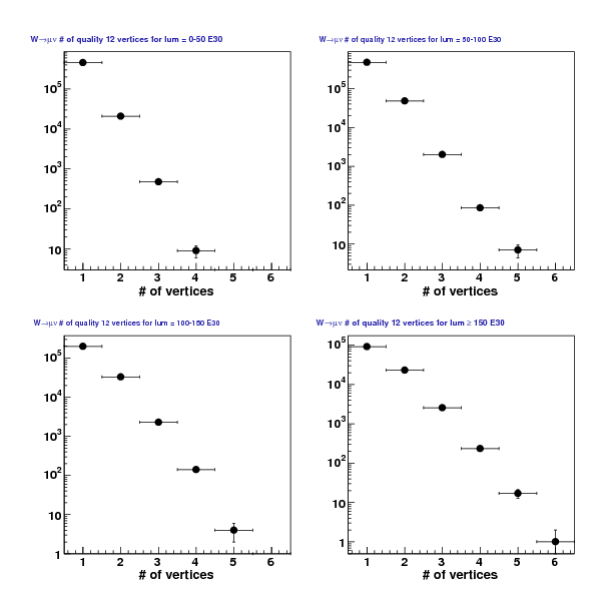


Figure 175: # of quality 12 vertices with  $\sum p_T^{vtx} > 18$  GeV/c in  $W \to \mu\nu$  Candidates for instantaneous luminosities (in units of  $\times 10^{30}$  cm<sup>-2</sup>/s) of 0-50 (upper-left), 50-100 (upper-right), 100-150 (lower-left), and  $\geq 150$  (lower-right). Compare to the no  $\sum p_T^{vtx}$  cut version in Fig. 143

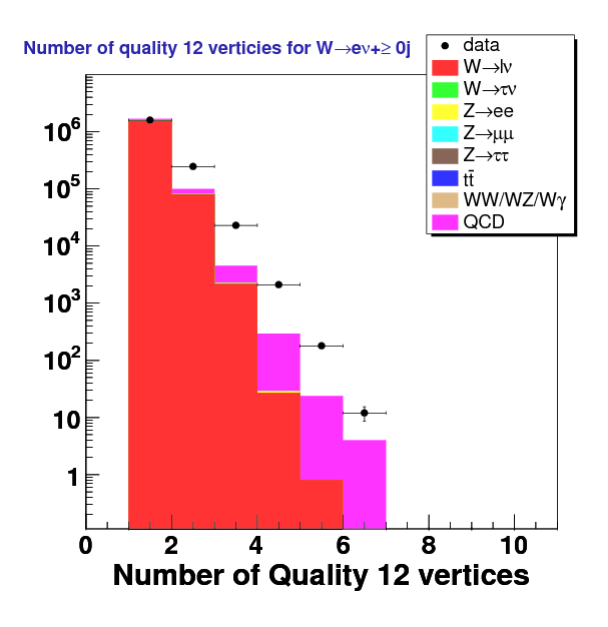


Figure 176: # quality 12 vertices (veto >6) with  $\sum p_T^{vtx} >$  15 GeV/c for  $W \to e\nu + \ge 0$  jets

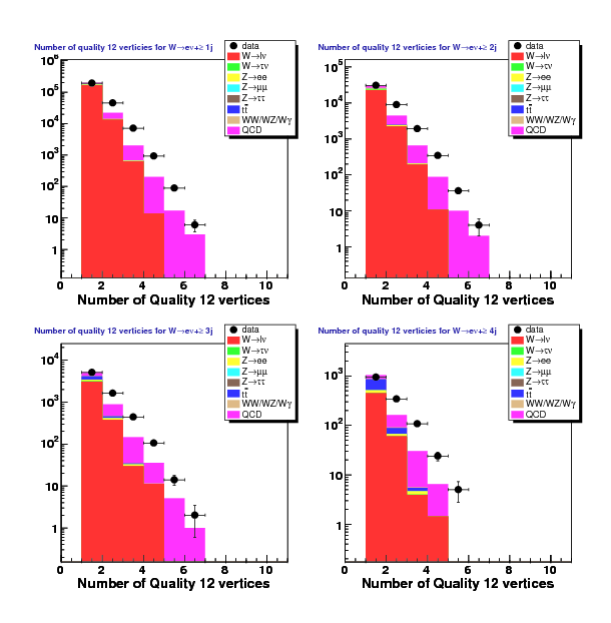


Figure 177: # quality 12 vertices (veto >6) with  $\sum p_T^{vtx} >$  15 GeV/c for  $W \to e\nu + \ge 1$ -4 jets

# data/MC ratio via the # of verticies 400 350 300 250 200 150 100 50 1 2 3 4 5 6 # of vertices

Figure 178: (Data-QCD)/MC comparison of # quality 12 vertices (veto >6) with  $\sum p_T^{vtx} > 15$  GeV/c for  $W \to e\nu + \ge 0$  jets.

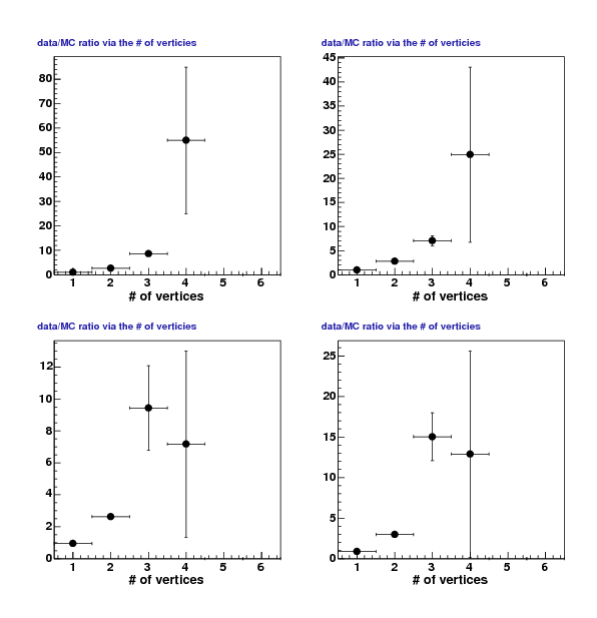


Figure 179: (Data-QCD)/MC comparison of # quality 12 vertices (veto >6) with  $\sum p_T^{vtx} > 15$  GeV/c for  $W \to e\nu + \ge 1$ -4 jets.

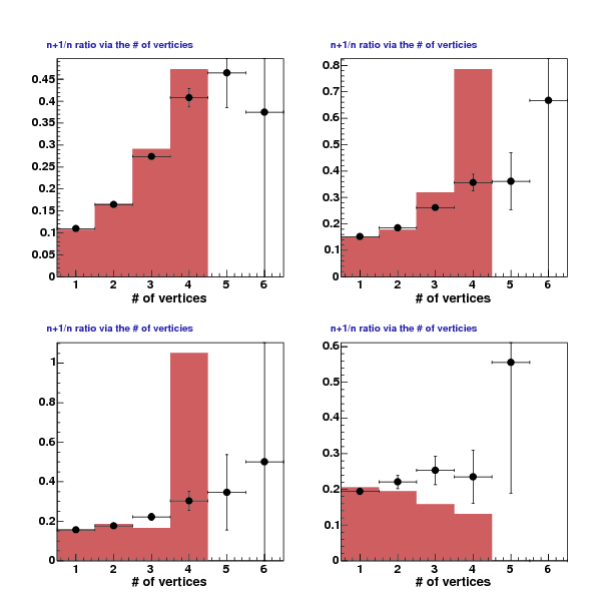


Figure 180: (n+1)/n jet multiplicity ratio comparison of # quality 12 vertices (veto >6) with  $\sum p_T^{vtx} > 15 \text{ GeV/c}$  for  $W \to e\nu + \geq n$  jets. Here the red histogram represents the MC prediction while the data points represent Data-QCD for each jet multiplicity ratio. Upper-left: 1/0, upper-right: 2/1, lower-left: 3/2, and lower-right: 4/3.

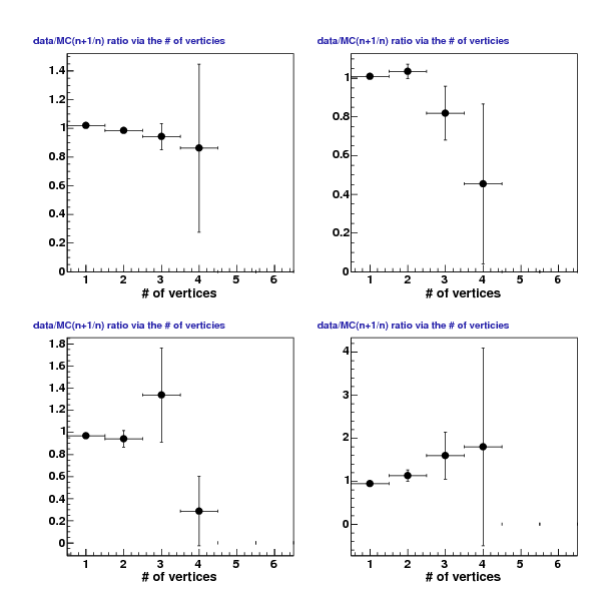


Figure 181: Data/MC ratio of the (n+1)/n jet multiplicity ratio comparison of # quality 12 vertices (veto >6) with  $\sum p_T^{vtx} > 15$  GeV/c for  $W \to e\nu + \geq n$  jets. This is a Data/MC ratio of Fig. 180. Upper-left: 1/0, upper-right: 2/1, lower-left: 3/2, and lower-right: 4/3.

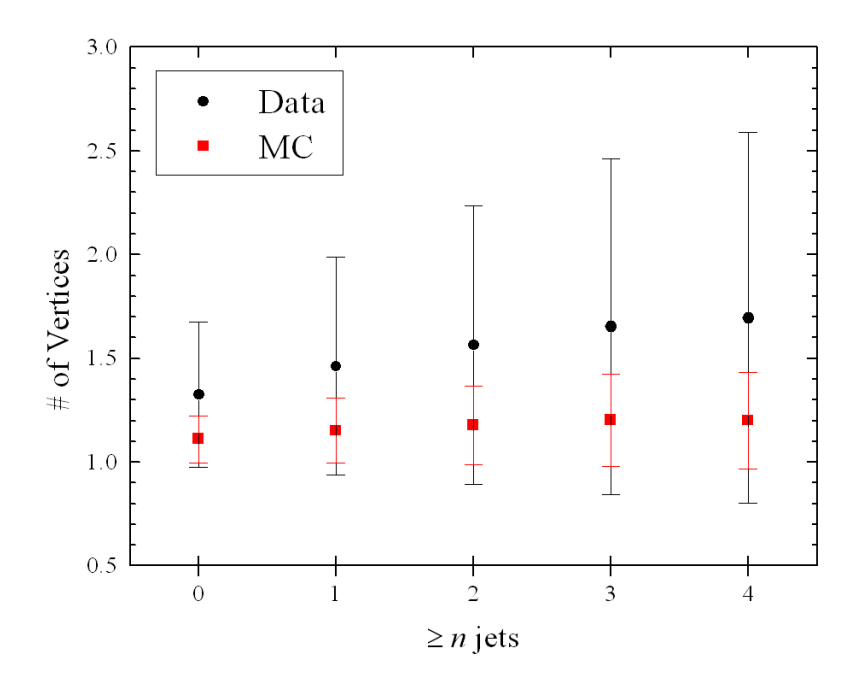


Figure 182: Profile histogram for the number of quality 12 vertices with  $\sum p_T^{vtx} > 10 \text{ GeV/c}$  verses the jet multiplicity for  $W \to e\nu + \geq n$  jets.

using quality 12 vertices defined with  $\sum p_T^{vtx} > 10 \text{ GeV/c}$  after vetoing events with # vertices  $\leq 3$ . In absolute terms, we lose about 16k events in the  $\geq 0$  jet bin and 94 events for  $\geq 4$  jets in the electron channel. We also note the that our electron sample shows an obvious linear drop off (approximately 1.45% per inclusive jet). The vertex number veto described here barely effects our acceptance; the largest reduction is in the  $\geq 1$  jet bin which measures less than 0.7%. The efficiency drop off for muons is larger and constant ( $\approx 8\%$ ) for one or more jet. This likely an artifact of the muon selection process where the # of vertices cut is biased toward cutting fakes (e.g. semi-leptonic decays). This was made explicit in an earlier version of our anti-selection muon procedure which included allowing the impact parameter ( $d_0$ ) to fail. For example, this gave events with additional vertices that saturated the low  $\sum p_T^{vtx}$  spectrum (the phenomena is still noticeable in figure 168 below 20 GeV/c).

Figures 184 and 186 show the (n+1)/n jet multiplicity ratio taking using  $\sum p_T^{vtx} > 10 \text{ GeV/c}$  with a >3 vertices veto for the electron and muon channel, respectively. A data/MC version is also reproduced in figures 185 (electrons) and 187 (muons). These jet multiplicity ratio plots show that there is no strong jet dependence or correlation and decent agreement at this stage between data and MC between 1 and 3 vertices.

At this point, we implement a fit of our # vertices distribution between data components and MC. The idea here is to reweight the MC (on subsequent passes in the analysis) so that it has the right profile. In effect, the MC will be corrected additional interactions and we simply fold in the promotion into our background and signal with this reweighting correction. Although we could reweight each vertex bin for each jet multiplicity, an ideal solution is to conduct the

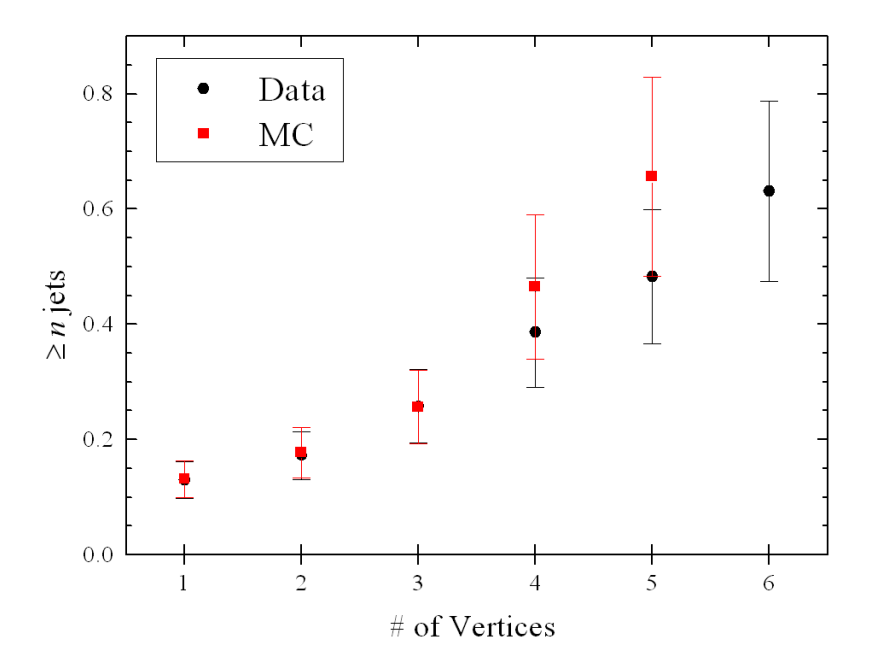


Figure 183: Profile histogram for the jet multiplicity verses the number of quality 12 vertices with  $\sum p_T^{vtx} > 10 \text{ GeV/c}$  for  $W \to e\nu + \geq n$  jets.

fit for the inclusive case and then apply it to the higher jet multiplicities which is feasible based on the results and discussion of figures 184-187. To do this we produce a plot like figure 156 or 178 were we have separated the data components from the MC and apply a reweight to the MC based on the ratio between Data and MC (i.e. Data/MC).

There are a few important details to this vertex "fitting" and reweighting. The first is with respect to our vertex fitting procedure and reweighting is that the QCD background needs to be further split into components. Recall that the QCD estimation comes from a template made from the anti-lepton selection of the data minus the MC contamination from the same anti-lepton selection. If we ignore this the fitting iterations start to be divergent on the third vertex relative to the first two and we will always be systematically off in trying to describe the # vertices distribution. Thus the vertex reweighting correction (w(#vertex)) is the weight applied to all jet multiplicities for the # number of vertices using the number of events in the total inclusive ( $\geq 0$ ) jet multiplicity. We define our base reweighting factor,  $w_0(\#\text{vertex})$ , as

$$w_0(\#\text{vertex}) = \frac{N_{\text{data}} - N_{\text{QCD-data}}}{N_{\text{MC}} + N_{\text{QCD-MC}}}$$
(20)

Here,  $N_{\rm data}$  is the number of candidate W events in data,  $N_{\rm QCD-data}$  is the estimated QCD background without the MC contamination subtraction,  $N_{\rm MC}$  is the sum of the signal W MC and all the MC based backgrounds, and  $N_{\rm QCD-MC}$  is the estimated contamination from non-QCD (i.e. MC) sources. For convenience we have suppressed the vertex dependence of these variables. Equation 20 needs a renormalization scale factor (see equation 21) which we now elaborate on.

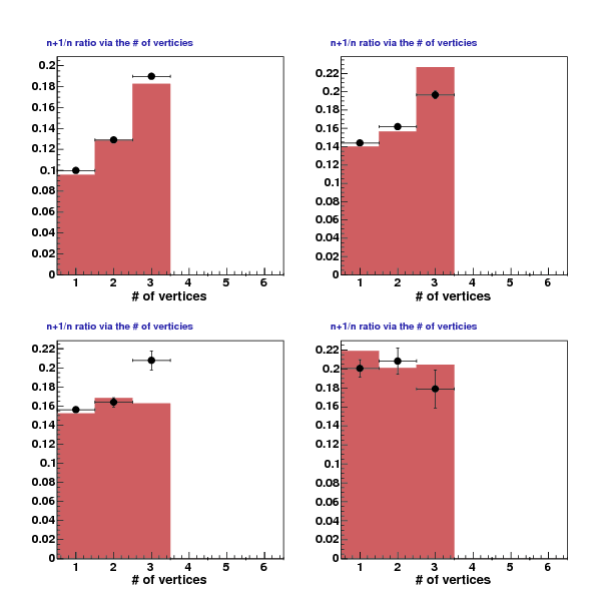


Figure 184: (n+1)/n jet multiplicity ratio comparison of # quality 12 vertices (veto >3) with  $\sum p_T^{vtx} > 10 \text{ GeV/c}$  for  $W \to e\nu + \geq n$  jets. Here the red histogram represents the MC prediction while the data points represent Data-QCD for each jet multiplicity ratio. Upper-left: 1/0, upper-right: 2/1, lower-left: 3/2, and lower-right: 4/3.

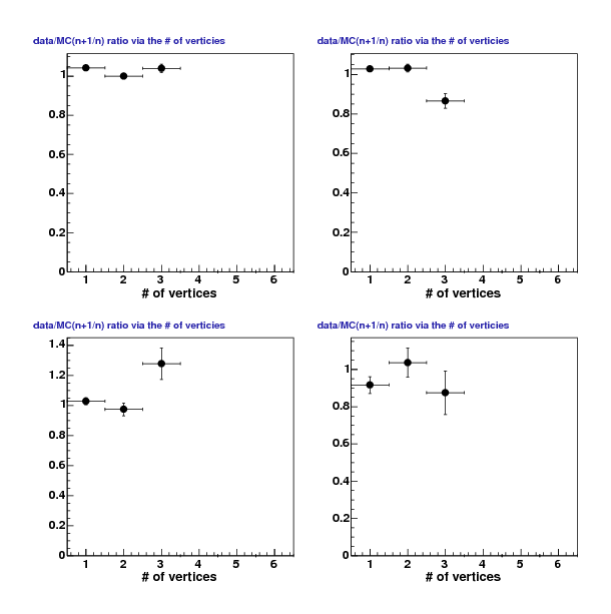


Figure 185: Data/MC ratio of the (n+1)/n jet multiplicity ratio comparison of # quality 12 vertices (veto >3) with  $\sum p_T^{vtx} > 10 \text{ GeV/c}$  for  $W \to e\nu + \geq n$  jets. This is a Data/MC ratio of Fig. 184. Upper-left: 1/0, upper-right: 2/1, lower-left: 3/2, and lower-right: 4/3.

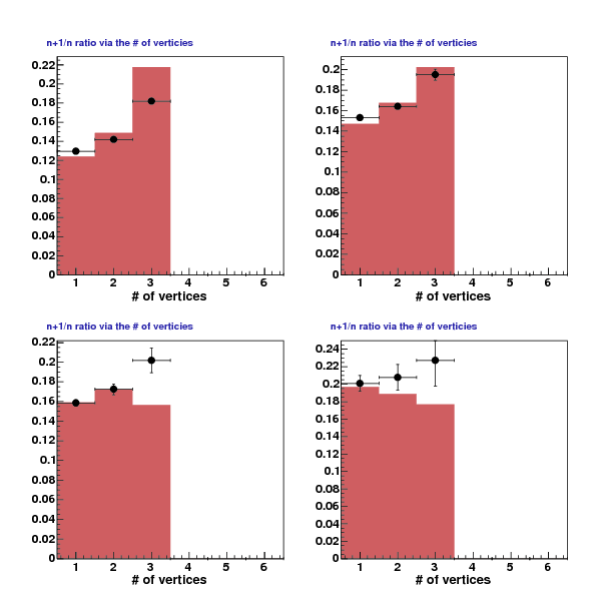


Figure 186: (n+1)/n jet multiplicity ratio comparison of # quality 12 vertices (veto >3) with  $\sum p_T^{vtx} > 10 \text{ GeV/c}$  for  $W \to \mu\nu + \geq n$  jets. Here the red histogram represents the MC prediction while the data points represent Data-QCD for each jet multiplicity ratio. Upper-left: 1/0, upper-right: 2/1, lower-left: 3/2, and lower-right: 4/3.

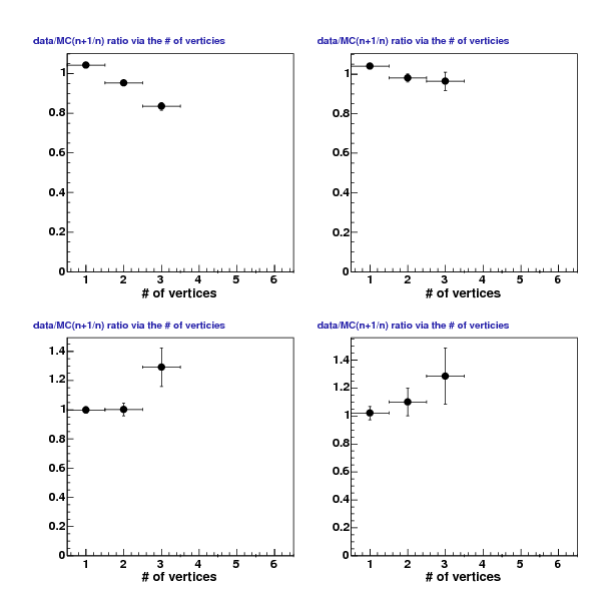


Figure 187: Data/MC ratio of the (n+1)/n jet multiplicity ratio comparison of # quality 12 vertices (veto >3) with  $\sum p_T^{vtx} > 10$  GeV/c for  $W \to \mu\nu + \geq n$  jets. This is a Data/MC ratio of Fig. 186. Upper-left: 1/0, upper-right: 2/1, lower-left: 3/2, and lower-right: 4/3.

	Electron Channel	Muon Channel
$\geq n$ jets	Reduction (%)	Reduction (%)
0	0.8	3.7
1	2.1	7.7
2	3.6	8.0
3	5.2	8.8
4	6.6	7.9

Table 23: Data Candidate Event Yield Reduction (%) using  $\sum p_T^{vtx} > 10$  GeV/c and # vertices  $\leq 3$  for  $W \to \ell \nu + \geq n$  jets

The second vertex fitting detail is that the procedure invites re-running the analysis a few times to make sure it is stable. The reason for this is that our background fitting estimation (see section 4.4) has the potential to shift a bit after we reweight the MC. The result is that the agreement will never be perfect but a first pass should lock it in to a good agreement with marginal improvements with subsequent re-runnings of the analysis with updated vertex weight values on the MC. In particular, equation 20 can acquire an additional degree of freedom where the number of events in the MC are not constrained in our vertex fit calculation and part of our desired weights are absorbed in our general background fitting. Our solution is to simply enforce the total number of events in the total inclusive case in the total MC sample. This effectively checks that the normalization of MC events is consistent iteration to iteration. We apply a correction factor using our initial weights  $(w_0(k))$  of equation 20 to get our final normalized vertex weight

$$w(\text{#vertex}) = \left(\frac{\sum_{k=1}^{3} N_{\text{MC}}}{\sum_{k=1}^{3} w(k) N_{\text{MC}}}\right) w_0(\text{#vertex})$$
(21)

where k is the # of vertices. This scale factor is by construction close to unity but it is important in order to achieve stability over multiple fitting iterations and between both lepton channels.

$\geq n$ jets	Vertex 1	Vertex 2	Vertex 3
0	0.8032	2.2180	6.3950
1	0.8336	2.2098	6.6951
2	0.8540	2.2907	6.2240
3	0.8669	2.1801	8.1484
4	0.8070	2.2794	6.9911
Average	0.8329	2.2356	6.8907
Std. Dev.	0.0281	0.0475	0.7616

Table 24: MC reweighting correction for the number of quality 12 vertices with  $\sum p_T^{vtx} > 10$  GeV/c for  $W \to e\nu + \geq n$  jets

In tables 24 and 25 we present our final results after 4 full iterations for our MC reweighting

$\geq n$ jets	Vertex 1	Vertex 2	Vertex 3
0	0.8425	2.1120	4.9630
1	0.8723	2.0297	4.4379
2	0.9103	1.9742	3.7948
3	0.9275	1.9336	4.1604
4	0.9480	2.0535	6.0549
Average	0.9001	2.0206	4.6822
Std. Dev.	0.0426	0.0694	0.8778

Table 25: MC reweighting correction for the number of quality 12 vertices with  $\sum p_T^{vtx} > 10$  GeV/c for  $W \to \mu\nu + \geq n$  jets

correction factors for # vertices (1-3) and for each inclusive jet multiplicity. The former is our electron results while the latter gives the muon channel results. We only use the total inclusive ( $\geq 0$  jets) case to reweight the MC but present results for the higher jet multiplicities as well. In each table, as an added convenience for comparison and consistency checking, are the (unweighted) average and standard deviation (abbreviated "Std. Dev.") for each inclusive jet multiplicity for each vertex number.

It is important to make sure that our fitting procedure in converging well and to this end we show the MC reweighting correction results for each vertex. Table 26 gives the results over 4 fitting iterations for  $W \to e\nu + \ge 0$  jets while table 27 likewise gives the results for  $W \to \mu\nu + \ge 0$  jets. Both lepton channel results converge quickly; more so with the muon channel which has a smaller QCD background estimation and MC contamination and thus less interplay between our background estimation template fitting and our vertex reweighting procedure described here.

Fitting Iteration	Vertex 1	Vertex 2	Vertex 3
$1^{\rm st}$	0.8201	2.286	6.724
$2^{\mathrm{nd}}$	0.8077	2.231	6.457
$3^{\rm rd}$	0.8032	2.218	6.395
$4^{ m th}$	0.8034	2.219	6.449
Average	0.8086	2.238	6.506
Std. Dev.	0.008	0.032	0.148

Table 26: MC reweighting correction for the number of quality 12 vertices with  $\sum p_T^{vtx} > 10$  GeV/c for  $W \to e\nu + \ge 0$  jets over 4 fitting iterations

Finally, we want to resurvey our various # vertices related observables we began with at the start of this section and note the improvement and overall consistency in our results. First, we note that the Data verses MC mismatch (see figures 198 and 200 for the electron and muon channel, respectively), the variation across each jet multiplicity (table 24 for the electrons and 25 for the muons), and the variation between multiple iterations of fitting, reweighting, and re-running (tables 26 and 27) are all on the order of 2.5% for the first vertex. The conclusion is that method is stable with respect to our reweighting procedure over 3 iterations. We continue this discussion of the effect of our reweighting on our cross-section in section 6.4 (page 195)

Fitting Iteration	Vertex 1	Vertex 2	Vertex 3
1 <sup>st</sup>	0.8337	2.099	4.882
$2^{\mathrm{nd}}$	0.8445	2.113	4.778
$3^{\rm rd}$	0.8425	2.112	4.963
$4^{ m th}$	0.8427	2.111	4.866
Average	0.8409	2.109	4.872
Std. Dev.	0.005	0.007	0.076

Table 27: MC reweighting correction for the number of quality 12 vertices with  $\sum p_T^{vtx} > 10$  GeV/c for  $W \to \mu\nu + \ge 0$  jets over 4 fitting iterations

where we give our systematic with respect to this procedure and our results.

As a crosscheck we also looked directly at the relative change between no vertex reweighting (original/default) and with the latest set of vertex corrections in the first and second leading jet  $p_T$  cross-sections. For reference, the final cross-section plots are presented in figures 266-267 (electrons) and 270-271 (muons) with their description starting on page 232. We construct the relative difference observable  $(\sigma_{vtx} - \sigma_{org})/\sigma_{vtx}$  where  $\sigma_{org}$  refers to the non-reweighted cross-section while  $\sigma_{vtx}$  is the fully reweighted. For our purpose here we present only the electron channel  $(W \to e\nu)$  although the trend is the same in the muon channel. The result for the first leading jet  $p_T$  is presented in figure 188 while the second leading jet  $p_T$  is shown in 189. The relative error  $(\Delta \sigma/\sigma)$  for  $\sigma_{vtx}$  is use as error bar for the observable. We see a relatively flat distribution that is consistent with our quoted 4.5% systematic of section 6.4.

In figures 190 and 191 we show our final results for the # vertices distribution for  $W \to e\nu + \geq n$  jets using our  $\sum p_T^{vtx} > 10 \text{ GeV/c}$  requirement where we veto events with more than 3 vertices. Likewise, the  $W \to \mu\nu + \geq n$  jets results are shown in figures 192 and 193. A simplified version of these plots with the data and MC components put together are shown in figures 194 and 195 (electrons) and 196 and 197 (muons). The ratio of the data components to the MC are presented in figures 198 and 199 for the electron channel as well as 200 and 201 for the muon channel. The (n+1)/n jet multiplicity ratio for the electron channel was already shown in figure 184 (data verses MC) and in figure 185 (data/MC ratio). In the same manner, the muon version of these plots are given in figures 186 (data verses MC) and in figure 187 (data/MC ratio).

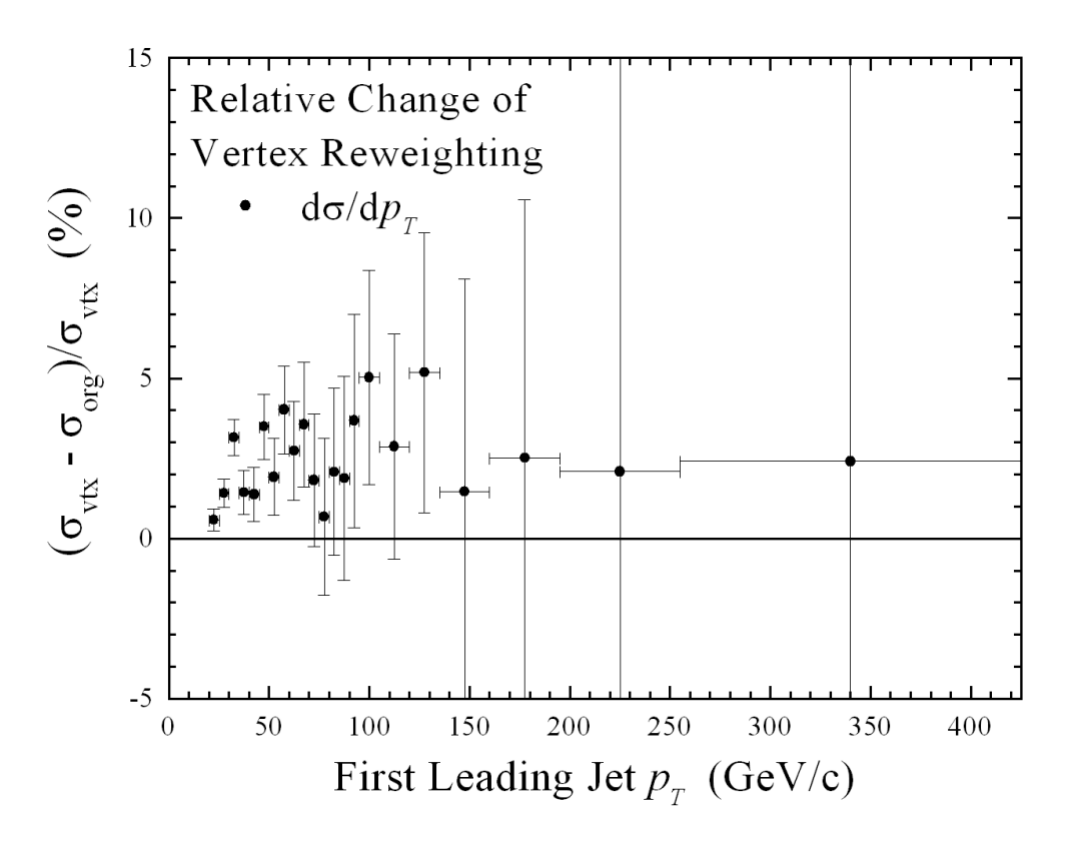


Figure 188: Relative change (%) in the first leading jet  $p_T$  for  $W \to e\nu + \ge 1$  jets.  $\sigma_{org}$  refers to the non-reweighted cross-section while  $\sigma_{vtx}$  is the fully reweighted. Note that the relative difference  $((\sigma_{vtx} - \sigma_{org})/\sigma_{vtx})$  has been converted into a percentage and the error shown is the relative Poisson uncertainty on  $\sigma_{vtx}$ .

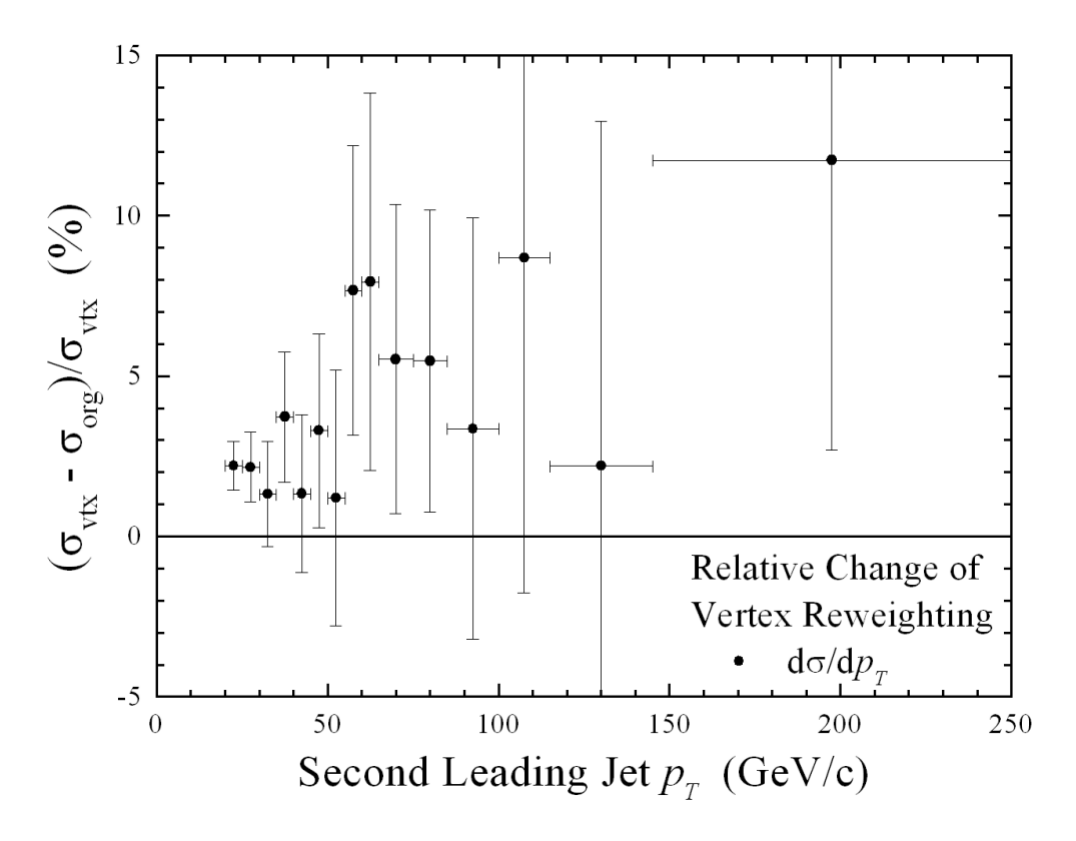


Figure 189: Relative change (%) in the second leading jet  $p_T$  for  $W \to e\nu + \geq 2$  jets.  $\sigma_{org}$  refers to the non-reweighted cross-section while  $\sigma_{vtx}$  is the fully reweighted. Note that the relative difference  $((\sigma_{vtx} - \sigma_{org})/\sigma_{vtx})$  has been converted into a percentage and the error shown is the relative Poisson uncertainty on  $\sigma_{vtx}$ .

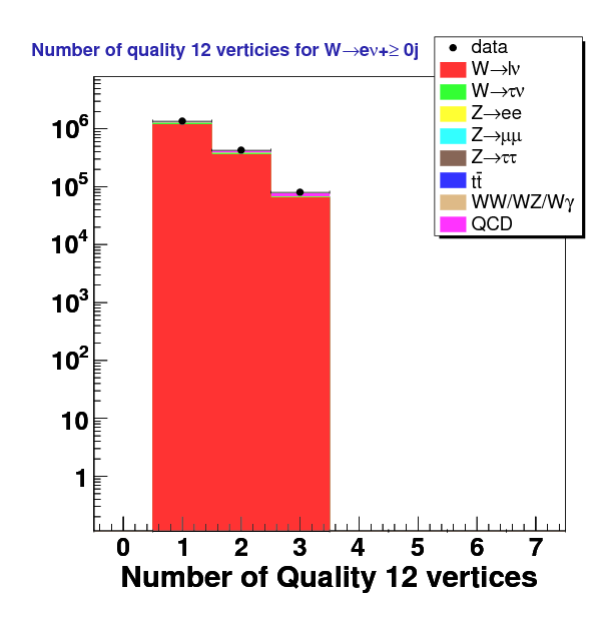


Figure 190: # quality 12 vertices with  $\sum p_T^{vtx} > 10$  GeV/c for  $W \to e\nu + \ge 0$  jets

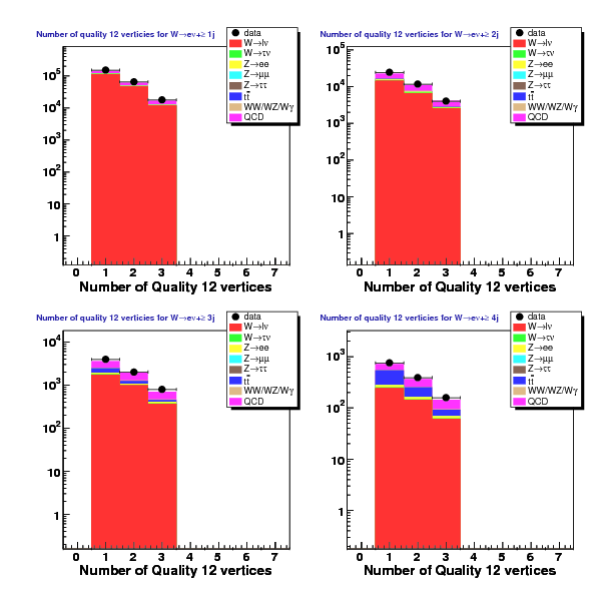


Figure 191: # quality 12 vertices with  $\sum p_T^{vtx} >$  10 GeV/c for  $W \to e\nu + \ge$ 1-4 jets

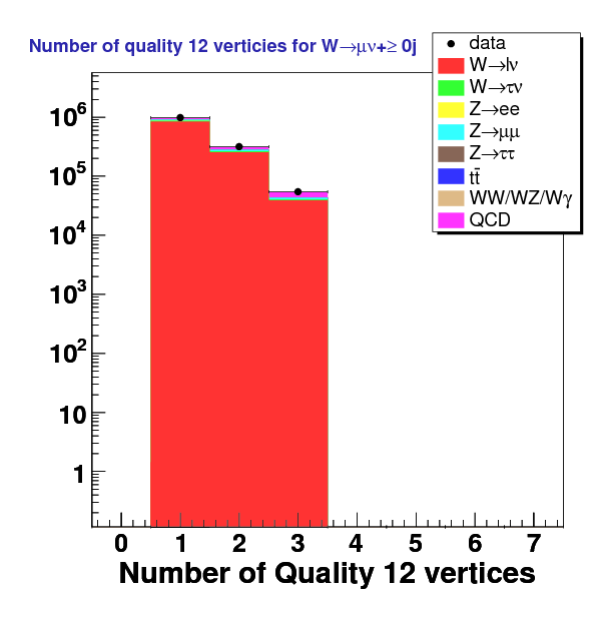


Figure 192: # quality 12 vertices with  $\sum p_T^{vtx} >$  10 GeV/c for  $W \to \mu \nu + \ge 0$  jets

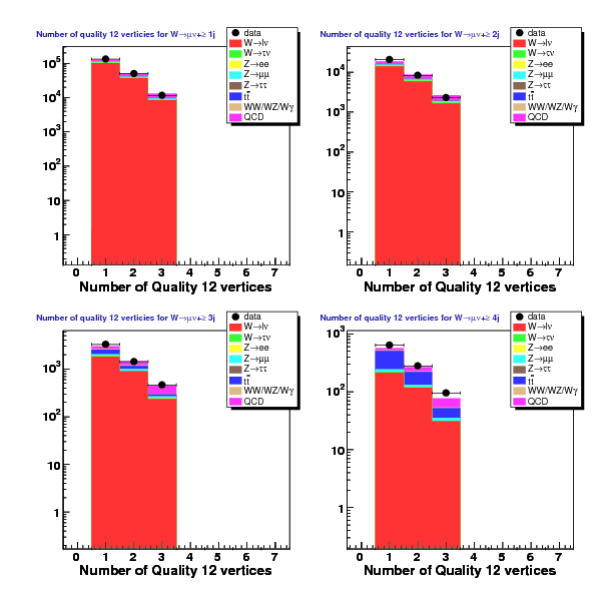


Figure 193: # quality 12 vertices with  $\sum p_T^{vtx} > 10$  GeV/c for  $W \to \mu\nu + \ge 1$ -4 jets

## Number of quality 12 verticies for W→ev+≥ 0j 10<sup>6</sup> 1 2 3 4 5 6 # of vertices

Figure 194: # quality 12 vertices with  $\sum p_T^{vtx} > 10$  GeV/c for  $W \to e\nu + \ge 0$  jets. We veto events with more than 3 vertices. Here the red histogram represents the sum MC predictions of figure 190 while the data points represent Data-QCD

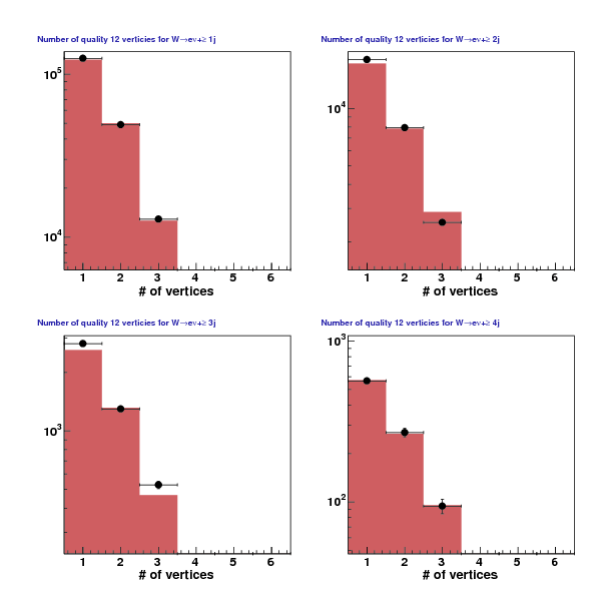


Figure 195: # quality 12 vertices with  $\sum p_T^{vtx} > 10$  GeV/c for  $W \to e\nu + \ge 1$ -4 jets. We veto events with more than 3 vertices. Here the red histogram represents the sum MC predictions of figure 191 while the data points represent Data-QCD

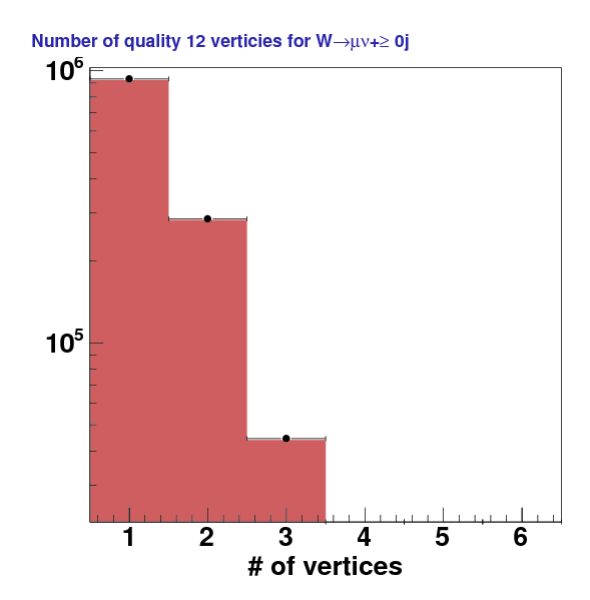


Figure 196: # quality 12 vertices with  $\sum p_T^{vtx} > 10$  GeV/c for  $W \to \mu\nu + \ge 0$  jets. We veto events with more than 3 vertices. Here the red histogram represents the sum MC predictions of figure 192 while the data points represent Data-QCD

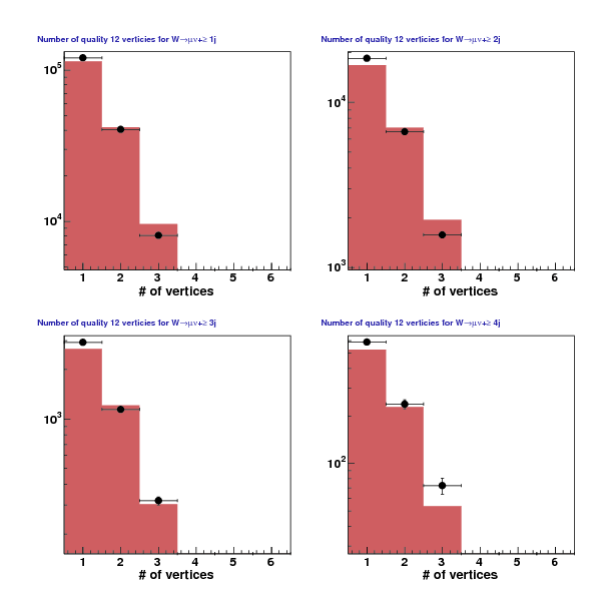


Figure 197: # quality 12 vertices with  $\sum p_T^{vtx} > 10$  GeV/c for  $W \to \mu\nu + \ge 1$ -4 jets. We veto events with more than 3 vertices. Here the red histogram represents the sum MC predictions of figure 193 while the data points represent Data-QCD

### data/MC ratio via the # of verticies

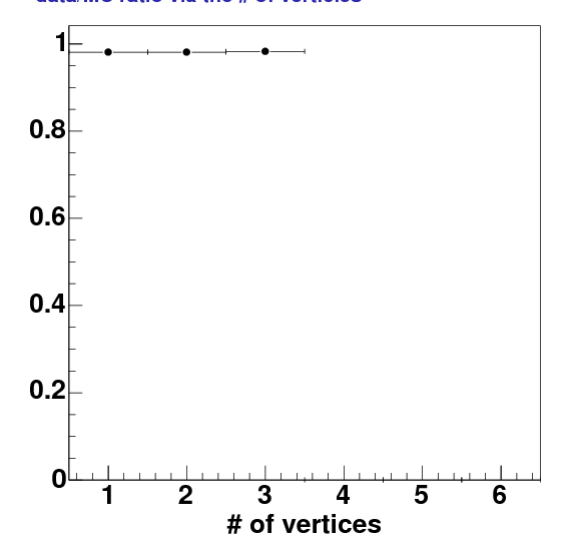


Figure 198: (Data-QCD)/MC comparison of # quality 12 vertices with  $\sum p_T^{vtx} > 10 \text{ GeV/c}$  for  $W \to e\nu + \geq 0$  jets. We veto events with more than 3 vertices. This is a ratio plot of Fig. 194.

As final cross check we also looked our two vertex related observables: the sum vertex transverse momentum  $(\sum p_T^{vtx})$  for ordered vertexes 1-3 in the total inclusive case and the difference in the z-position between all non-primary vertices to the primary  $(z_0 - z_{vtx})$  for all jet multiplicities. The non-reweighted no vertex cut/veto plots were given in figures 166-173. The post vertex reweighting  $\sum p_T^{vtx}$  plots for  $W \to e\nu + \geq 0$  jets are in figure 202 (leading vertex) and figure 203 (ordered vertexes 2-3). Likewise, the results for  $W \to \mu\nu + \geq 0$  jets are given in figures 204 and 205. The updated  $z_0 - z_{vtx}$  plots are shown in figures 206 and 207 for  $W \to e\nu + \geq 0$  jets and  $\geq 1$ -4 jets, respectively. The same version of these plots is show for the muon channel in figures 208 and 209, respectively. We note that the agreement is good and there are no signs of bias.

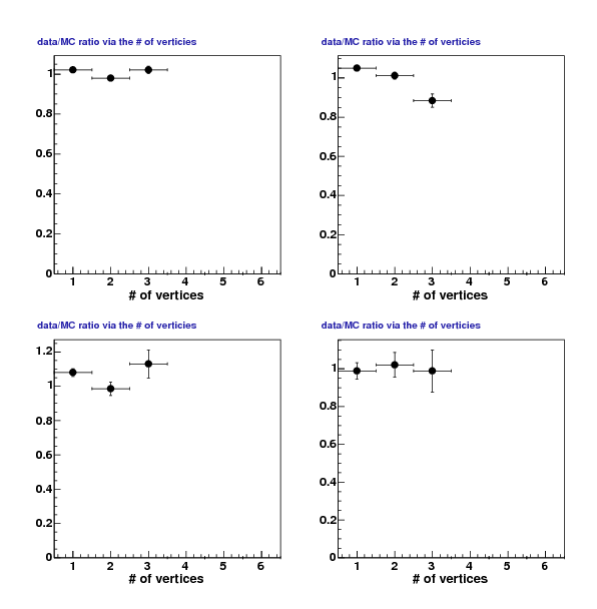


Figure 199: (Data-QCD)/MC comparison of # quality 12 vertices with  $\sum p_T^{vtx} > 10$  GeV/c for  $W \to e\nu + \geq 1$ -4 jets. We veto events with more than 3 vertices. This is a ratio plot of Fig. 195.

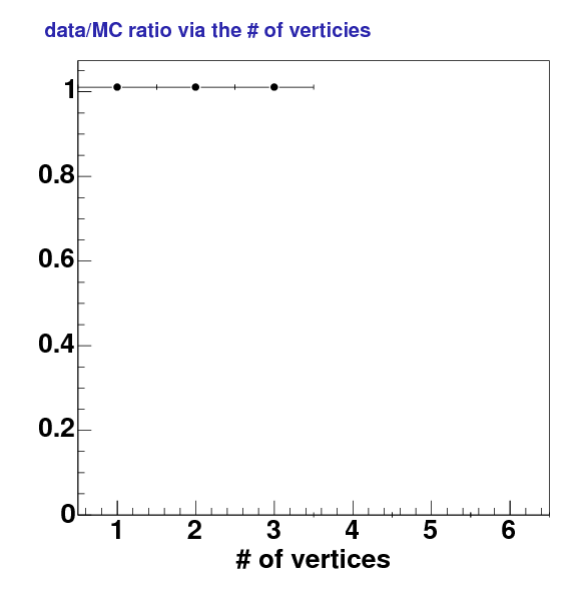


Figure 200: (Data-QCD)/MC comparison of # quality 12 vertices with  $\sum p_T^{vtx} > 10 \text{ GeV/c}$  for  $W \to \mu\nu + \geq 0$  jets. We veto events with more than 3 vertices. This is a ratio plot of figure 196.

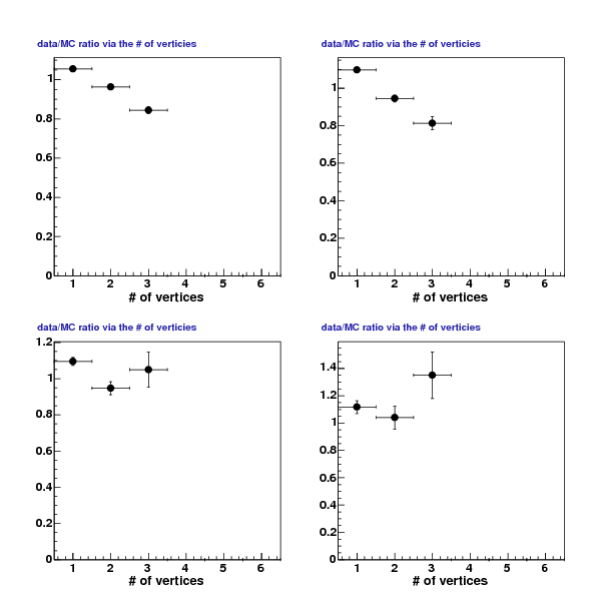


Figure 201: (Data-QCD)/MC comparison of # quality 12 vertices with  $\sum p_T^{vtx} > 10$  GeV/c for  $W \to \mu\nu + \geq 1$ -4 jets. We veto events with more than 3 vertices. This is a ratio plot of figure 197.

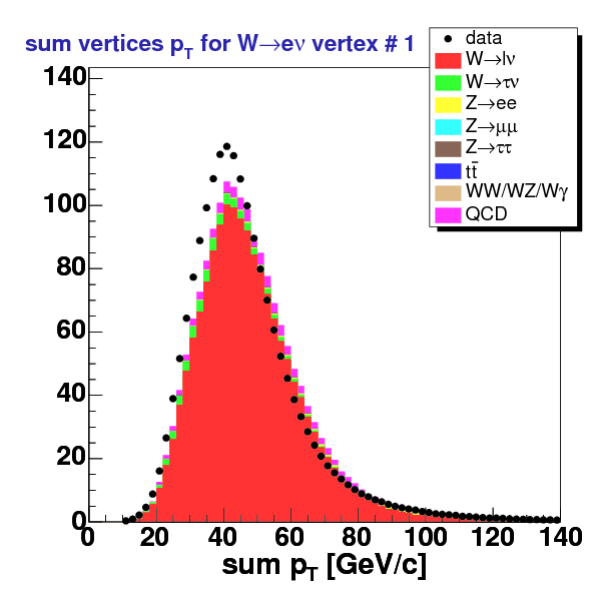


Figure 202: Vertex sum  $p_T$   $(\sum p_T^{vtx})$  for the leading order vertex for  $W\to e\nu+\ge 0$  jets with  $\sum p_T^{vtx}>10$  GeV/c.

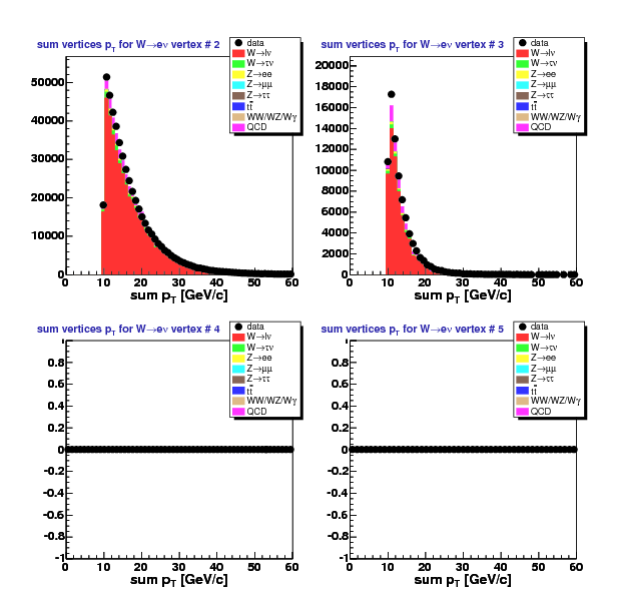


Figure 203: Vertex sum  $p_T$   $(\sum p_T^{vtx})$  for ordered vertexes 2-3 for  $W\to e\nu+\ge 0$  jets with  $\sum p_T^{vtx}>10$  GeV/c and vertexes 4-5 vetoed

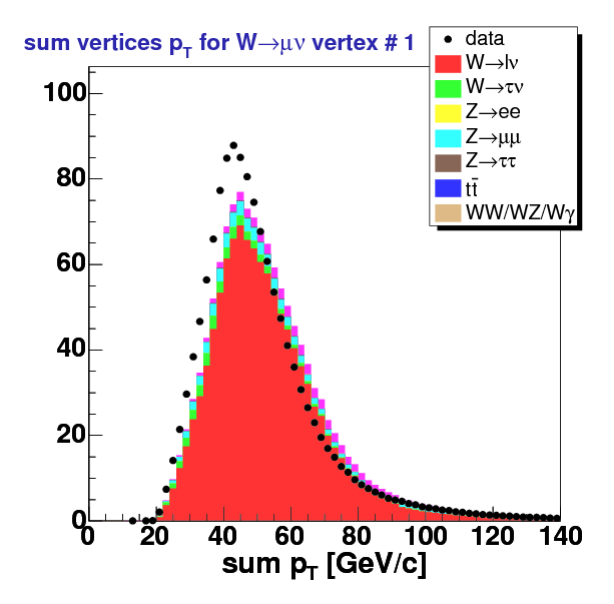


Figure 204: Vertex sum  $p_T$   $(\sum p_T^{vtx})$  for the leading order vertex for  $W \to \mu\nu + \ge 0$  jets with  $\sum p_T^{vtx} > 10$  GeV/c.

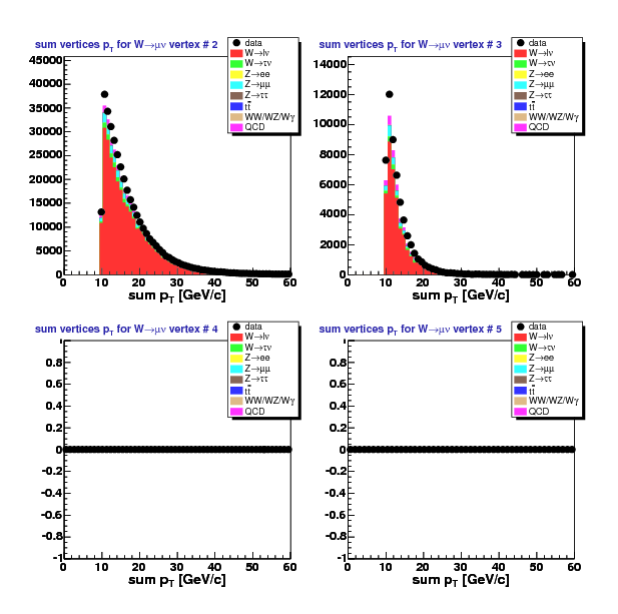


Figure 205: Vertex sum  $p_T$  ( $\sum p_T^{vtx}$ ) for ordered vertexes 2-3 for  $W\to \mu\nu+\ge 0$  jets with  $\sum p_T^{vtx}>10$  GeV/c and vertexes 4-5 vetoed

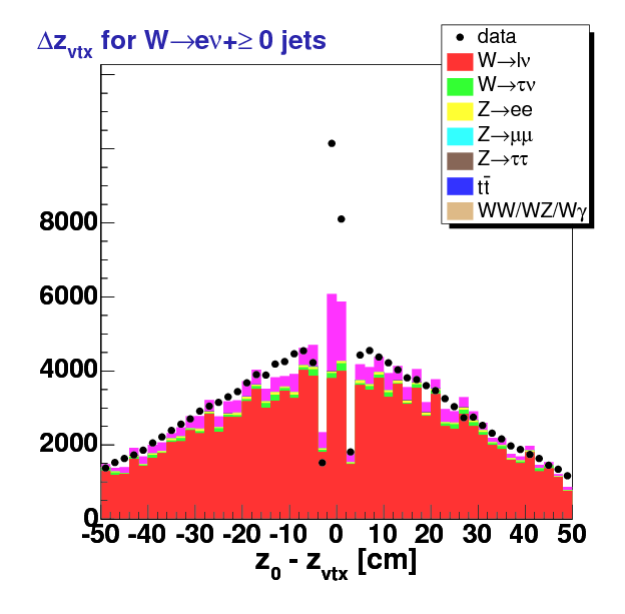


Figure 206:  $z_0 - z_{vtx}$  for each vertex omitting the primary for  $W \to e\nu + \ge 0$  jets with  $\sum p_T^{vtx} > 10 \text{ GeV/c}$ .

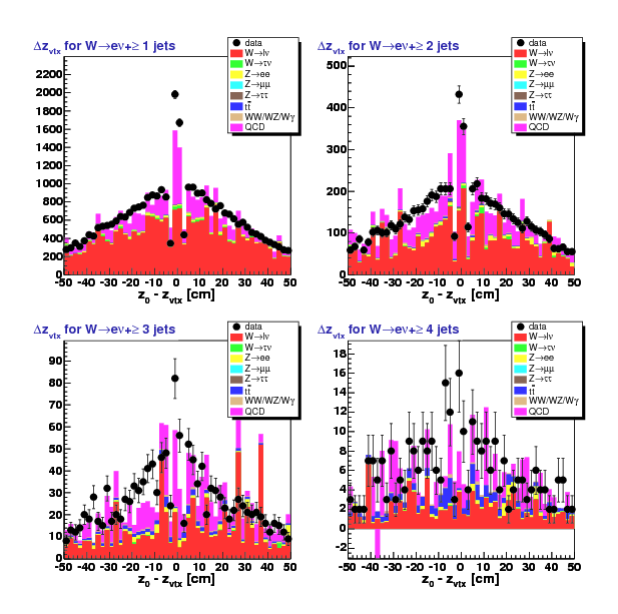


Figure 207:  $z_0 - z_{vtx}$  for each vertex omitting the primary for  $W \to e\nu + \ge 1$ -4 jets with  $\sum p_T^{vtx} > 10 \text{ GeV/c}$ .

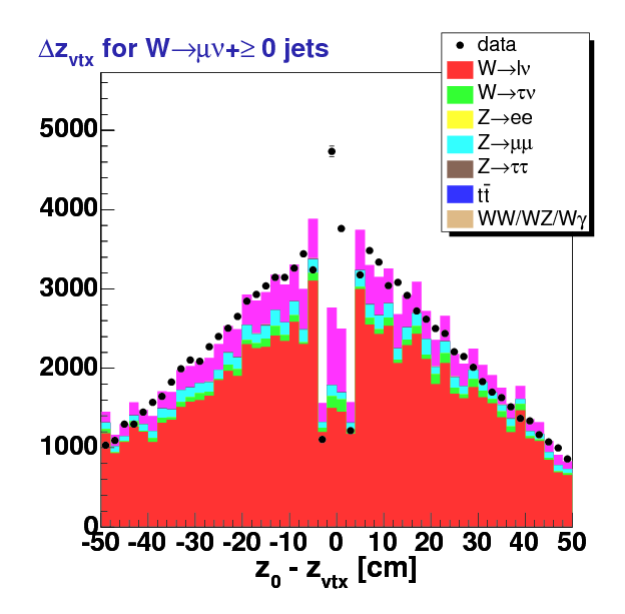


Figure 208:  $z_0 - z_{vtx}$  for each vertex omitting the primary for  $W \to \mu\nu + \ge 0$  jets with  $\sum p_T^{vtx} > 10 \text{ GeV/c}$ .

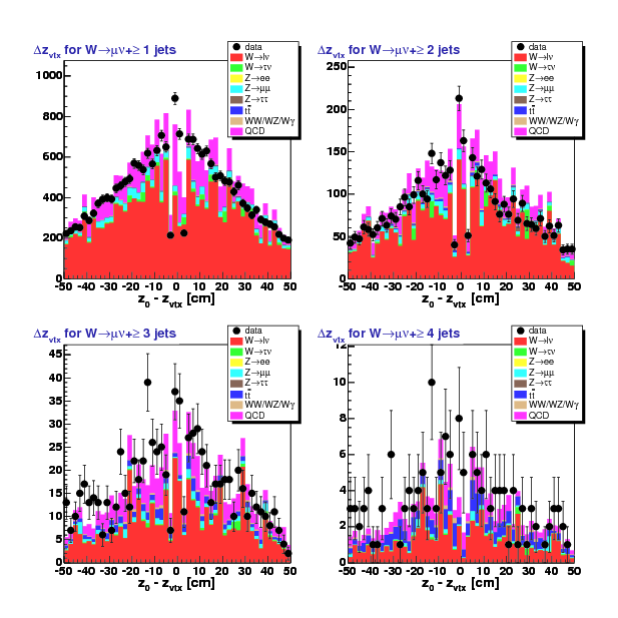


Figure 209:  $z_0 - z_{vtx}$  for each vertex omitting the primary for  $W \to \mu\nu + \ge 1$ -4 jets with  $\sum p_T^{vtx} > 10 \text{ GeV/c}$ .

## 5 Acceptance and Efficiency

In this chapter we describe our W+jets acceptance and lepton efficiencies. These will be used in our final cross-section definition in section 7.1. Although the procedure is straightforward there are several details that are worth keeping in mind. The first is that our acceptance in addition to having a detector dependence based on the lepton sub-detector type (i.e. CEM, CMUP, CMX-Arch, and CMX-Mini) has the potential to have a jet multiplicity dependence as well.

Another acceptance issue is the potential bias due to the W + np Alpgen MC and the fact that we do not know the *a priori* cross-section. The absolute cross-section is irrelevant but technically the relative weight between the *n* parton samples could bias the result and we wish to avoid this. We explain our solution to this in section 5.2 after giving an overview of the general procedure in 5.1.

A different acceptance concern deals with our desire to produce a more theory friendly cross-section (see section 7.1 for details). In additional to the typical "production level" acceptance, we define a reduced acceptance in section 5.4. Our nominal results are shown in section 5.3 while our modified reduced acceptance is presented in section 5.5.

Section 5.6 present our efficiency results for central (CEM) electrons and (CMUP and CMX) muons. Here the only concern is correctly apply the various lepton efficiencies for each run period with the corresponding luminosity. Finally in section 5.7 we describe how we combine the luminosity (L), the acceptance (A), and total efficiency  $(\epsilon)$  in to a final effective luminosity  $(LA\epsilon)$  by taking into account the lepton, jet multiplicity, and run period dependence.

### 5.1 Acceptance Procedure

Our acceptance procedure is straightforward. We use our signal MC, Alpgen W+np, to systematically run through our W selection cuts and see what fraction of the generated number of events are accepted. As noted in chapter 2 our W selection cuts take on the basic kinematic and geometric cuts on the triggered lepton and missing energy in addition to some event level vetos (e.g. no cosmics). However, the effect of trigger as well as lepton reconstruction and identification are categorized as efficiencies and are measured with the data as noted later in section 5.6.

We can refer to the acceptance of a cut or a group of sequential cuts together by taking the quotient of the number of events accepted (passed) verses the number of events before cutting. For example, let (cut 1) and (cut 2) be two sequential cuts needed for the signal acceptance. Let N(cut 1) and N(cut 2) represent the number of events that pass the corresponding cut. Then the acceptance of (cut 2) relative to (cut 1) is

$$A(\text{cut } 2) = \frac{N(\text{cut } 2)}{N(\text{cut } 1)} \tag{22}$$

and if (cut 1) really represents the first cut then trivially,

$$A(\text{cut }1) = \frac{N(\text{cut }1)}{N(\text{GEN})}$$
 (23)

where N(GEN) is the number of events generated for the MC sample. Assuming the cuts are taken in a consistent order one can denote the total acceptance of two sets of cuts by simply taking the product (i.e. the acceptance is homomorphic). Continuing with our examples from equations 22 and 23, let A(cut 1) and A(cut 2) be the relative acceptances for two sequential sets of cuts. Then

$$A(\operatorname{cut} 1 + 2) = A(\operatorname{cut} 1)A(\operatorname{cut} 2) \tag{24}$$

$$A(\operatorname{cut} 1+2) = \left(\frac{N(\operatorname{cut} 1)}{N(\operatorname{GEN})}\right) \left(\frac{N(\operatorname{cut} 2)}{N(\operatorname{cut} 1)}\right)$$

$$A(\operatorname{cut} 1+2) = \frac{N(\operatorname{cut} 2)}{N(\operatorname{GEN})}$$
(25)

$$A(\text{cut } 1+2) = \frac{N(\text{cut } 2)}{N(\text{GEN})}$$
 (26)

where A(cut 1+2) is the combined acceptance for both sets of cuts.

For reasons which will become clear in the next section, we define the p number of partons sample acceptance for j exclusive number of jets as  $A_p(j)$ . For our conveyance, we can omit the j jet dependence for  $A_p$  and our exclusive and inclusive jet multiplicity (parton dependence removed) total acceptance. We do this for both electrons (i.e. candidate tight CEM electrons) and muons and have the ability to divide the muons into their respective sub-detector types (candidate tight CMUP, CMX-Arch, and CMX-Mini muons). These parton and jet dependent acceptances are shown later in tables 40-43.

	$W \to e\nu$	$W \to \mu\nu$
n jets	N(GEN)	N(GEN)
0	1524842	1412970
1	1424120	1301665
2	1146287	1187073
3	651802	779158
4	251888	331232

Table 28: Number of MC events generated (N(GEN)) summed over all parton samples for each inclusive jet multiplicity in  $W \to \ell \nu + \geq n$  jets

Finally in this section, we present the raw numbers for our acceptance calculation. Due to the need to be independent of any ad hoc scaling of the relative p parton sample we do not use these numbers directly but follow the definition and procedure outlined in the next section. Table 28 gives the number of events generated summed over all the parton MC samples for each inclusive jet multiplicity for both the electron and muon channel. In other words,

$$N(\text{GEN}, n) = N(\text{GEN}) \equiv \sum_{\forall p} N_p^{\text{GEN}}$$
 (27)

where  $N_p^{\text{GEN}} = N_p^{\text{GEN}}(n)$  is the number of events generated via W+p parton MC with  $\geq n$ jets. We note that these are the proper number of events generated and that our MC selection does not have any good run list requirement as was noted in section 1.3. Table 29 defines the name of each cut which will be used in tables 30-33 which serve as a raw cut-by-cut breakdown of the acceptance for each lepton sub-detector type.

Cut Label (X)	Cut Definition for $A(X)$
CDL	Central Detector Lepton; in the lepton collection
$\eta$	Electron $ \eta  < 1.1$ cut
$\rho$	Muon COT exit radius cut $(\rho)$
fid	Fiducial detector lepton check
$z_0$	primary vertex cut; $ z_0  < 60$ cm
vtx	# of vertices $\leq 3$ with $\sum p_T^{vtx} > 10 \text{GeV/c}$
$p_T$	Electron or muon high $p_T$ requirement
$E_T$	Electron transverse energy cut
$M_T$	W transverse mass cut
e-jet	Electron-Jet separation requirement
$\mu ext{-jet}$	Muon-Jet separation requirement
$\Delta \phi$	$\Delta\phi(\ell,\wp)$ cut
Total	This is the total acceptance across all cuts

Table 29: Acceptance cut label and definitions as used in tables 30-33 for A(X)

### 5.2 Exclusive and Inclusive Acceptance Definitions

In this section we describe the process in which we take the acceptance for each (exclusive) jet multiplicity and parton sample combine this into a total (inclusive) jet multiplicity acceptance without parton dependence. As was our stated goal, we note that this procedure does not apply any special cross-section weight to the various Alpgen p number of partons samples. We begin by making an exclusive jet multiplicity acceptance calculation and then build on this to get our final inclusive jet multiplicity acceptance which then will be combined into our effective luminosity and in turn our cross-section measurements.

We define the acceptance for exclusive n jet multiplicity,  $A^{ex} = A^{ex}(n)$ , via the know distribution of the number of jets for each Alpgen+Pythia MC sample.

$$A^{ex} = \sum_{\forall p} c_p^{ex} A_p \tag{28}$$

where  $A_p$  is the exclusive jet multiplicity dependent acceptance for the p parton MC sample and  $c_p^{ex}$  is proportional to the probability of getting n jets using a p parton MC sample and is normalized to give the composition of each parton sample for n jets. We define  $c_p^{ex}$  as

$$c_p^{ex} \equiv \frac{\tilde{c}_p}{\sum_{\forall p} \tilde{c}_p} \tag{29}$$

	n jets	A(cdl)	$A(\eta)$	A(fid)	$A(z_0)$	A(vtx)	$A(p_T)$	$A(E_T)$	$A(M_T)$	$A(e ext{-jet})$	$A(\Delta\phi)$	A(Total)
Ì	0	0.961	0.833	0.939	0.654	0.952	0.794	0.832	0.971	1.000	1.000	0.300
	1	0.957	0.911	0.965	0.717	0.950	0.705	0.833	0.893	0.997	0.957	0.287
	2	0.967	0.947	0.978	0.764	0.949	0.671	0.826	0.857	0.992	0.958	0.293
	3	0.970	0.966	0.985	0.797	0.948	0.662	0.825	0.831	0.985	0.957	0.298
	4	0.970	0.980	0.990	0.832	0.941	0.664	0.843	0.833	0.979	0.954	0.322

Table 30: Raw CEM acceptance for each exclusive n jet multiplicity summed over all W+mp MC samples

n jets	A(cdl)	$A(\rho)$	A(fid)	$A(z_0)$	A(vtx)	$A(p_T)$	$A(M_T)$	$A(\mu$ -jet)	A(Total)
0	0.311	1.000	0.511	0.961	0.988	0.823	0.986	1.000	0.122
1	0.393	1.000	0.527	0.960	0.982	0.815	0.915	0.959	0.140
2	0.427	1.000	0.543	0.959	0.975	0.795	0.890	0.914	0.140
3	0.447	0.999	0.556	0.957	0.970	0.775	0.871	0.863	0.134
4	0.463	0.999	0.570	0.954	0.963	0.751	0.857	0.785	0.122

Table 31: Raw CMUP acceptance for each  $\it exclusive~n$  jet multiplicity summed over all W+mp MC samples

n jets	A(cdl)	$A(\rho)$	A(fid)	$A(z_0)$	A(vtx)	$A(p_T)$	$A(M_T)$	$A(\mu$ -jet)	A(Total)
0	0.099	0.768	0.966	0.976	0.988	0.846	0.988	1.000	0.059
1	0.122	0.775	0.966	0.976	0.985	0.831	0.922	0.960	0.065
2	0.131	0.781	0.963	0.974	0.980	0.811	0.895	0.919	0.063
3	0.136	0.787	0.962	0.974	0.974	0.792	0.878	0.873	0.059
4	0.141	0.792	0.961	0.972	0.970	0.775	0.864	0.797	0.054

Table 32: Raw CMX-Arch acceptance for each  $exclusive\ n$  jet multiplicity summed over all W+mp MC samples

n jets	A(cdl)	$A(\rho)$	A(fid)	$A(z_0)$	A(vtx)	$A(p_T)$	$A(M_T)$	$A(\mu\text{-jet})$	A(Total)
0	0.015	0.803	0.952	0.979	0.988	0.846	0.988	1.000	0.009
1	0.018	0.813	0.951	0.978	0.986	0.832	0.920	0.963	0.010
2	0.020	0.810	0.952	0.976	0.982	0.820	0.895	0.916	0.010
3	0.021	0.817	0.946	0.976	0.978	0.802	0.882	0.865	0.009
4	0.022	0.817	0.951	0.973	0.970	0.776	0.866	0.795	0.008

Table 33: Raw CMX-Mini acceptance for each exclusive n jet multiplicity summed over all W+mp MC samples

with

$$\tilde{c}_p = \frac{N_p^{\text{GEN}}}{\sum_{\forall i} N_p^{\text{GEN}}} \tag{30}$$

As noted in the previous section (see equation 27),  $N_p^{\text{GEN}}$  represents the number of generated events from the p parton MC samples for (exclusive) n jets. Equation 30 for  $\tilde{c}_p = \tilde{c}_p(n)$  is just the number of events generated for a given p parton sample for exclusive jet multiplicity n normalized to the total number of events in the generated sample.

Some additional details for our methodology are as follows. The parton sum runs over all 5 W+mp samples with  $m \in \{0, 1, 2, 3, 4\}$  and the exclusive jet number likewise with  $n \in \{=0, =1, =2, =3, \geq 4\}$ . Note that the 4 jet case is by default defined to be  $\geq 4$  jets. This is trivial to our inclusive jet multiplicity acceptance framework below but is a non-issue here as well. Recall that the Alpgen W+4p samples match to the inclusive  $\geq 4$  jet bin while W+mp is exclusively match for  $m \neq 4$ .

Tables 35 and 5.3 show the exclusive weight matrix  $(c_p^{ex})$  for  $W \to e\nu$  and  $W \to \mu\nu$ , respectively. These tables derive from the composition of generated events  $(\tilde{c}_p)$  which are shown in tables 34 for electrons and table 37 for muons. We omit our tables for the total acceptance defined with exclusive jet multiplicity for brevity.

We define the acceptance for inclusive  $\geq n$  jet multiplicity,  $A = A(\geq n)$ , to be consistent with what is given in Equation 28. The idea is to use the exclusive acceptance frame work to produce our desired inclusive acceptance by summing over the higher jet bins. Consider for example the inclusive 2 jet case which would symbolically look like:

$$(\geq 2) \Leftrightarrow (=2) \cup (=3) \cup (\geq 4)$$

This is our nominal acceptance that we will be using for all of our cross-section measurements modulo the discussion in section 5.4. We define A via

$$A = \sum_{\forall j > n} \sum_{\forall p} c_p^{in}(j, n) A_p(j)$$
(31)

with implicit inclusive  $\geq n$  jets dependence and where

$$c_p^{in}(j,n) \equiv \frac{\tilde{c}_p(j)}{\sum_{\forall j > n} \sum_{\forall m} \tilde{c}_m}$$
(32)

The normalization to  $\tilde{c}_p$  is a function of the inclusive jet bin. We note that  $\tilde{c}_p$  and  $A_p$  depend on the *exclusive* number of jets (j) and parton sample and that the former was defined in equation 30.

Tables 36 and 39 are the equivalent weight matrix for inclusive jet multiplicity case. As noted before, the Alpgen+Pythia MC for W+4p is setup to match to  $\geq 4$  jets. Thus the results in the  $\geq 4$  jet bin will be equal by construction to the results given in the exclusive scenario. With equations 32 and 30 we just need to apply our exclusive jet multiplicity and parton number dependent acceptance to fully compose our final acceptance.

### 5.3 Electron and Muon Acceptance Results

We present our electron and muon channel acceptances in this section. First we present, for each lepton detector type, the  $A_p(j)$  acceptances which are the p parton total acceptance for exclusive j jets. Using these along with the results from the previous section, we derive the total acceptance for  $\geq n$  jets,  $A=A(\geq n)$ , via equation 31. Table 40 presents the CEM  $A_p(j)$  while tables 41, 42, and 43 refer to the CMUP, CMX-Arch, and CMX-Mini  $A_p(j)$  acceptances, respectively.

Finally we present our electron (CEM) and muon (CMUP, CMX-Arch, and CMX-Mini) total acceptance results in table 44. The average CEM acceptance works out to  $0.308 \pm 0.012$  while the combined  $\mu$  detector acceptance averages to  $0.205 \pm 0.013$ . We also note that the acceptance is roughly flat with jet multiplicity dependence. The relative error (standard deviation divided by average) in the spread of jet bins for the CEM is 4.0% while for the  $\mu$  detectors it is 6.4%.

n jets	0p	1p	2p	3p	4p
0	0.9190	0.4154	0.1409	0.0416	0.0093
1	0.0777	0.5331	0.4631	0.2507	0.0937
2	0.0031	0.0491	0.3575	0.4392	0.2976
3	0.0002	0.0023	0.0367	0.2408	0.3748
4	0.0000	0.0002	0.0018	0.0276	0.2245

Table 34: Acceptance  $\tilde{c}_m$  matrix (mp verses n jets) for  $W\!\to\!e\nu+m{\rm p~MC}$ 

n jets	0p	1p	2p	3p	4p
0	0.6021	0.2722	0.0924	0.0273	0.0061
1	0.0548	0.3759	0.3265	0.1768	0.0661
2	0.0027	0.0428	0.3118	0.3831	0.2596
3	0.0003	0.0035	0.0561	0.3678	0.5723
4	0.0001	0.0007	0.0071	0.1087	0.8835

Table 35: Acceptance  $c_m^{ex}$  matrix (mp verses n jets) for  $W \to e\nu + mp$  MC. These results are derived from equation 29 and the  $\tilde{c}_p$  results of table 34.

j	$\geq n$ jets	0p	1p	2p	3p	4p
0	0	0.5299	0.2395	0.0813	0.0240	0.0054
1	0	0.0058	0.0394	0.0343	0.0186	0.0069
2	0	0.0000	0.0006	0.0042	0.0052	0.0035
3	0	0.0000	0.0000	0.0001	0.0005	0.0008
4	0	0.0000	0.0000	0.0000	0.0000	0.0001
1	1	0.0480	0.3289	0.2857	0.1547	0.0578
2	1	0.0003	0.0048	0.0352	0.0432	0.0293
3	1	0.0000	0.0000	0.0006	0.0042	0.0065
4	1	0.0000	0.0000	0.0000	0.0001	0.0007
2	2	0.0024	0.0386	0.2814	0.3457	0.2343
3	2	0.0000	0.0003	0.0051	0.0335	0.0521
4	2	0.0000	0.0000	0.0000	0.0007	0.0059
3	3	0.0003	0.0032	0.0523	0.3428	0.5335
4	3	0.0000	0.0000	0.0005	0.0074	0.0599
4	4	0.0001	0.0007	0.0071	0.1087	0.8835

Table 36: Acceptance  $c_p^{in}(j,n)$  matrix (mp/ verses=j jets) as defined in equation 32 for  $W\to e\nu+mp$  MC

n jets	0p	1p	2p	3p	4p
0	0.9653	0.3305	0.0833	0.0184	0.0031
1	0.0323	0.6403	0.4100	0.1663	0.0460
2	0.0023	0.0275	0.4791	0.4509	0.2268
3	0.0001	0.0016	0.0261	0.3413	0.4131
4	0.0000	0.0001	0.0015	0.0230	0.3111

Table 37: Acceptance  $\tilde{c}_m$  matrix (mp verses n jets) for  $W \to \mu \nu + m {\rm p~MC}$ 

n jets	0p	1p	2p	3p	4p
0	0.6892	0.2360	0.0595	0.0131	0.0022
1	0.0249	0.4945	0.3166	0.1285	0.0355
2	0.0019	0.0232	0.4038	0.3800	0.1911
3	0.0002	0.0020	0.0334	0.4363	0.5281
4	0.0000	0.0003	0.0046	0.0686	0.9265

Table 38: Acceptance  $c_m^{ex}$  matrix (mp verses n jets) for  $W \to \mu\nu + mp$  MC. These results are derived from equation 29 and the  $\tilde{c}_p$  results of table 37.

j	$\geq n$ jets	0p	1p	2p	3p	4p
0	0	0.6045	0.2070	0.0522	0.0115	0.0019
1	0	0.0026	0.0519	0.0332	0.0135	0.0037
2	0	0.0000	0.0004	0.0064	0.0060	0.0030
3	0	0.0000	0.0000	0.0001	0.0008	0.0010
4	0	0.0000	0.0000	0.0000	0.0000	0.0001
1	1	0.0213	0.4223	0.2704	0.1097	0.0303
2	1	0.0003	0.0030	0.0521	0.0491	0.0247
3	1	0.0000	0.0000	0.0005	0.0069	0.0083
4	1	0.0000	0.0000	0.0000	0.0001	0.0010
2	2	0.0017	0.0205	0.3570	0.3360	0.1690
3	2	0.0000	0.0002	0.0036	0.0473	0.0572
4	2	0.0000	0.0000	0.0000	0.0005	0.0069
3	3	0.0002	0.0019	0.0312	0.4081	0.4939
4	3	0.0000	0.0000	0.0003	0.0044	0.0599
4	4	0.0000	0.0003	0.0046	0.0686	0.9265

Table 39: Acceptance  $c_p^{in}(j,n)$  matrix (mp/ verses=j jets) as defined in equation 32 for  $W\to \mu\nu+mp$  MC

# 5.4 Reduced Acceptance Definition

The results of the previous section represent the typical acceptances for production level cross-sections. This means the cross-section for  $p\bar{p}$  goes to some process X (we will omit the branching ratio and simply take X to represent a final state) takes the form

$$\sigma(p\bar{p} \to X) = \frac{N_{\text{data}} - N_{\text{bkgd}}}{LA\epsilon}$$
(33)

where the acceptance, A, is the acceptance via MC for process  $p\bar{p}$  goes to final state X with full detector simulation. Clearly,  $N_{\rm data}$  is the number of candidate W events in data while  $N_{\rm bkgd}$  (or simply B, for brevity in later chapters) is the sum of all of our background estimation.

In this section we want to introduce the concept of a cross-section based on the reduced production phase space for our signal. The main motivation for our use of a reduce acceptance is to present a cross-section which is friendly to various theoretical predictions. In addition, the restriction of phase-space negates the potential problem of trusting the MC outside of the area of measurement in terms of a geometric and pure kinematic acceptance. Although we do not have to make any assumption about the MC treatment about the non-central, low  $M_T$ , etc. events, we do have to deal with an addition set of selection cuts made before CDF detector simulation.

In contrast to equation 33, we have

$$\sigma(p\bar{p} \to X|[a_{\text{hepg}}]) = \frac{N_{\text{data}} - N_{\text{bkgd}}}{L\bar{A}\epsilon}$$
 (34)

where  $[a_{\text{hepg}}]$  represents a set of cuts (as the variable implies, these cuts will be at the hepg level) that reduces of the available MC decay space for the process going to X and  $\bar{A}$  represents the acceptance of X in simulation given the MC set already has  $[a_{\text{hepg}}]$  applied. Our luminosity and efficiency components (L and  $\epsilon$ , respectively) are unchanged and our handling of the equivalent total effective luminosity,  $L\bar{A}\epsilon$ , is otherwise unchanged with respect to the procedure of the last section of this chapter (see section 5.7). Effectively equations 23 and 26 replace their usage of N(GEN) with the number of events passing these generator (e.g. hepg variables) level cuts.

We construct this redefined cross-section by making the (potentially lepton dependent) cuts outlined in table 45. These cuts obviously mirror our detector level cuts in selecting the W. While it is possible to subdivide the muons into detector types, this is not called for when dealing with a global MC acceptance correction. We will explain the procedure in section 5.7.

Functionally, we select the leptons via there particle ID number in order to get the needed 4-momentum information in the hepg bank. We use the second pair of leptons that have as their parent the original leptons from the W decay. These daughters particles represent a post radiation correction state. The potential effect on the reduce acceptance relative to selecting the original (pre-radiation) leptons that are proper daughters of the original W in the collection is given as a systematic and described in section 6.3.

We define our reduced acceptance correction as  $a_{\text{hepg}}$  which is symbolically given by

$$a_{\text{hepg}} = \frac{N(M_T)}{N(\text{GEN})} \tag{35}$$

Table 40: CEM  $A_p(j)$ 

n jets	0p	1p	2p	3p	4p
0	0.2817	0.3210	0.3441	0.3471	0.3344
1	0.2256	0.2565	0.3042	0.3237	0.3267
2	0.2578	0.2836	0.2627	0.3012	0.3185
3	0.3373	0.2839	0.3330	0.2767	0.3084
4	0.2942	0.3385	0.3565	0.3702	0.3151

Table 41: CMUP  $A_p(j)$ 

n je	ets	0p	1p	2p	3p	4p
0		0.1171	0.1311	0.1400	0.1484	0.1426
1		0.0806	0.1373	0.1447	0.1480	0.1469
2		0.1035	0.0894	0.1390	0.1424	0.1436
3		0.0780	0.1045	0.0941	0.1332	0.1377
4		0.1248	0.0882	0.0961	0.0959	0.1245

Table 42: CMX Arches (CMX-Arch)  $A_p(j)$ 

			,	,	1 - /- /
n jets	0p	1p	2p	3p	4p
0	0.0568	0.0623	0.0688	0.0652	0.0692
1	0.0373	0.0638	0.0664	0.0676	0.0653
2	0.0582	0.0390	0.0626	0.0638	0.0627
3	0.0303	0.0449	0.0397	0.0596	0.0607
4	0.0000	0.0189	0.0434	0.0404	0.0551
	0 1 2 3	0 0.0568 1 0.0373 2 0.0582 3 0.0303	0         0.0568         0.0623           1         0.0373         0.0638           2         0.0582         0.0390           3         0.0303         0.0449	0         0.0568         0.0623         0.0688           1         0.0373         0.0638         0.0664           2         0.0582         0.0390         0.0626           3         0.0303         0.0449         0.0397	0         0.0568         0.0623         0.0688         0.0652           1         0.0373         0.0638         0.0664         0.0676           2         0.0582         0.0390         0.0626         0.0638           3         0.0303         0.0449         0.0397         0.0596

Table 43: CMX Miniskirt (CMX-Mini)  ${\cal A}_p(j)$ 

				,	P(O)
n jets	0p	1p	2p	3p	4p
0	0.0089	0.0095	0.0102	0.0104	0.0090
1	0.0061	0.0099	0.0103	0.0104	0.0116
2	0.0079	0.0066	0.0098	0.0100	0.0101
3	0.0141	0.0103	0.0070	0.0093	0.0094
4	0.0000	0.0000	0.0072	0.0060	0.0086

Table 44: Total Acceptance for each lepton detector type for  $W \to \ell \nu + \geq n$  jets

n jets	A(CEM)	A(CMUP)	A(Arch)	A(Mini)
0	0.308	0.128	0.061	0.009
1	0.298	0.145	0.066	0.010
2	0.300	0.142	0.063	0.010
3	0.306	0.136	0.060	0.009
4	0.329	0.125	0.055	0.009

Generator Level Cut	$W \to e\nu$	$W \to \mu\nu$
$ \eta_e  < 1.1$	✓	
$ \eta_{\mu}  < 1.0$		✓
$p_T^{\ell} > 20 \; \mathrm{GeV/c}$	✓	✓
$M_T^W > 40 \text{ GeV/c}^2$	✓	
$M_T^{W} > 30 \text{ GeV/c}^2$		✓

Table 45: Generator level cuts for the reduced acceptance  $\bar{A}$  for  $W \to \ell \nu + m$  partons MC

where  $N(M_T)$  represents the number of generated events that passed our final generator level cut. Of course, our actual procedure is to make a parton (MC sample) and exclusive jet multiplicity dependent acceptance to mirror that of our  $A_p(j)$  term in equation 31. Following the same procedure and using the same definitions for  $c_p^{in}$  and  $\tilde{c}_p$  in equations 32 and 30. This pseudo acceptance,  $a_{\text{hepg}}$ , is then a correction to our normally defined production acceptance, A, which becomes our reduced acceptance,  $\bar{A}$ . Then

$$\bar{A} = \frac{A}{a_{\text{hepg}}} \tag{36}$$

which suggests with respect to equations 33 and 36 that

$$\sigma(p\bar{p} \to X | [a_{\text{hepg}}]) = (a_{\text{hepg}}) \, \sigma(p\bar{p} \to X)$$
 (37)

# 5.5 Reduced Acceptance Results

In table 46 we present the results for our acceptance correction factor,  $a_{\text{hepg}}$ , as defined in the previous section for both lepton channels. The variation in the acceptance values is 2.7% for the muons and 1.4% for the electrons. Regrettably the acceptance values for our reduced cross-section are different enough to make it unlikely that the electron and muons results could combined together. This is somewhat expected given that the cuts are not entirely equivalent (see table 45) and thus making them different cross-sections. The reduced acceptance,  $\bar{A}$ , results follow from the nominal acceptance results in table 44 which are simply scaled via equation 36. They are presented for completeness in table 47.

	$W \rightarrow e\nu$	$W \rightarrow \mu\nu$
n jets	$a_{\text{hepg}}$	$a_{ m hepg}$
0	0.578	0.600
1	0.578	0.582
2	0.568	0.575
3	0.562	0.568
4	0.562	0.558

Table 46: Reduced acceptance correction  $(a_{hepg})$  for  $W \to \ell \nu + n$  jets

n jets	$\bar{A}(CEM)$	$\bar{A}(\mathrm{CMUP})$	$\bar{A}({ m Arch})$	$\bar{A}(\mathrm{Mini})$
0	0.533	0.213	0.102	0.015
1	0.516	0.249	0.113	0.017
2	0.528	0.247	0.110	0.017
3	0.544	0.239	0.106	0.016
4	0.585	0.224	0.099	0.016

Table 47: Total Reduced Acceptance for each lepton detector type for  $W \to \ell \nu + \geq n$  jets

# 5.6 Lepton Efficiencies

In this section we present the various lepton efficiencies based on the work done by the Lepton and Joint Physics working groups [49][10]. Unlike our acceptance results which we take from MC, we define efficiencies as a data measured component (for high  $p_T$  leptons this is typically done with Zs) that would result in missing events. The procedure for electron efficiencies is described fully in [50]. These results (up to and including period 17) are taken from [51]. Likewise [52] describes the procedure for the central muon efficiencies which are derived via [53].

Efficiencies for a given detector break down into several categories. First is the trigger efficiency  $(\epsilon_{\text{trig}})$  which is the efficiency for triggering a high  $p_T$  lepton. The second is the ID (identification) efficiency  $(\epsilon_{\text{ID}})$  which represents the efficiency of a lepton passing its set of quality cuts (e.g. CES  $\Delta z$ , HAD/EM, and isolation, etc.). Next we consider two muon only related efficiencies. The first is the reconstruction efficiency  $(\epsilon_{\text{reco}})$  which is a measurement of the stub-track/muon reconstruction efficiency. In order to match the results given by the joint physics we will always present the combined efficiency between the ID and reconstruction and call this the "ID Efficiency". There is an additional efficiency that we have trivially added for muons based on our  $\chi^2_{\text{COT}}$  cut. As noted in section 2.3, this cut was found to be extremely efficient for our data as well as in the signal MC. Luckily, the Joint Physics group has measured this  $\chi^2_{\text{COT}}$  efficacy  $(\epsilon_{\chi^2})$  and find it consistent with unity (100%) with (purely negative) uncertainties on the order of 0.04-0.08%. We trivially combine this with our ID efficiency for the purpose of book-keeping.

We also account for our additional  $\Delta z_{vtx}$  cut which is applied both lepton channels. We reproduce the Joint Physics/Lepton group procedure of selecting tight leptons via Z selection and noting the efficiency of our final  $|\Delta z_{vtx}| < 2.0$  cm cut. The efficiency is denoted as  $\epsilon_{\Delta z}$  and averages 98.7% (99.2%) for electrons (muons) over all run periods [54]. We did not estimate or include any systematic uncertainty for this track based efficiency. Finally, there is an lepton independent efficiency that we apply with respect to the vertex position cut ( $|z_0| < 60$  cm) which we will reference with  $\epsilon_{z_0}$ . The details on this final measurement are documented in [55].

The total efficiency ( $\epsilon_{\text{total}}$  or simply  $\epsilon$ ) is just the product of all the various efficiencies for each lepton detector type.

$$\epsilon = \epsilon_{\text{total}} \equiv (\epsilon_{\text{trig}})(\epsilon_{\text{ID}})(\epsilon_{\text{reco}})(\epsilon_{\Delta z})(\epsilon_{z_0})$$
 (38)

We have for each of the 13 different run periods (see section 1.2) the corresponding set of efficiencies as well as scale factors as was already noted in section 1.4 and follow from the general procedure of [9]. The total run period dependent efficiency for each lepton detector

Run	$\epsilon_{ m ID}$	$\epsilon_{ m trig}$	$\epsilon$
Period	ID Efficiency	Trigger Efficiency	Total Efficiency
0d	$0.802 \pm 0.003$	$0.962 \pm 0.007$	$0.739 \pm 0.006$
0h	$0.796 \pm 0.003$	$0.976 \pm 0.006$	$0.744 \pm 0.006$
5-7	$0.786 \pm 0.004$	$0.979 \pm 0.004$	$0.737 \pm 0.005$
8	$0.788 \pm 0.005$	$0.959 \pm 0.007$	$0.732 \pm 0.007$
9	$0.789 \pm 0.005$	$0.960 \pm 0.002$	$0.733 \pm 0.005$
10	$0.787 \pm 0.004$	$0.959 \pm 0.002$	$0.731 \pm 0.004$
11	$0.777 \pm 0.004$	$0.961 \pm 0.004$	$0.723 \pm 0.005$
12	$0.772 \pm 0.005$	$0.960 \pm 0.003$	$0.720 \pm 0.005$
13	$0.784 \pm 0.004$	$0.957 \pm 0.003$	$0.729 \pm 0.004$
14	$0.805 \pm 0.010$	$0.960 \pm 0.030$	$0.751 \pm 0.025$
15	$0.792 \pm 0.005$	$0.963 \pm 0.005$	$0.741 \pm 0.006$
16	$0.790 \pm 0.006$	$0.961 \pm 0.005$	$0.738 \pm 0.007$
17	$0.781 \pm 0.005$	$0.962 \pm 0.003$	$0.730 \pm 0.005$

Table 48: CEM Efficiencies

type will then be combined with the luminosity in each period along with the total acceptance into a combined effective luminosity which we discuss in the next section.

In table 48 we present the ID and trigger efficiency results for CEM electrons. The results for CMUP are shown in table 49. The CMX muon efficiencies are broken down for arches (CMX-Arch) and miniskirt (CMX-Mini) in tables 50 and 51, respectively. Recall that we will present the ID and reconstruction efficiencies together and for convenience and consistency refer to it as the ID efficiency. We do not present the efficiencies for our muon based  $\chi^2_{\text{COT}}$  cut separately and as also noted before combine this with our formal ID efficiency. In each of the four tables (48-51) the total efficiency includes the lepton vertex position  $(z_0)$  efficiency. These results are individually given in table 52.

# 5.7 Effective Luminosity $(LA\epsilon)$

We currently have a detector dependent acceptance based off of our two sets of W MC for each lepton channel, and a detector and run dependent set of efficiencies and luminosities over our 13 different run periods. Here we are going to combine these pieces together into our effective luminosity term. This will then basically become our dominator term for our cross-section measurements (see section 7.1). The second goal for this section is to explain the resulting error propagation which will become important in the next chapter (in particular, sections 6.2-6.3).

First we recall tables 1 and 2 which define our run periods and the luminosity in each period. Let  $L_i$  be the luminosity and  $\epsilon_i$  the total CEM efficiency for enumerated period i and let  $A_{CEM} = A(CEM)$  be total acceptance for electrons. Then the effective luminosity  $(LA\epsilon)$  goes

$$(LA\epsilon)_e \equiv \sum_{\forall i} (L_i \epsilon_i) A_{CEM}$$
 (39)

Run	$\epsilon_{ m ID}$	$\epsilon_{ m reco}$	$\epsilon_{ m trig}$	$\epsilon$
Period	ID Efficiency	Reconstruction Efficiency	Trigger Efficiency	Total Efficiency
0d	$0.846 \pm 0.005$	$0.927 \pm 0.004$	$0.902 \pm 0.004$	$0.678 \pm 0.006$
0h	$0.850 \pm 0.005$	$0.916 \pm 0.003$	$0.919 \pm 0.004$	$0.686 \pm 0.005$
5-7	$0.825 \pm 0.006$	$0.918 \pm 0.004$	$0.918 \pm 0.005$	$0.666 \pm 0.007$
8	$0.814 \pm 0.008$	$0.931 \pm 0.005$	$0.913 \pm 0.006$	$0.670 \pm 0.009$
9	$0.836 \pm 0.008$	$0.927 \pm 0.005$	$0.927 \pm 0.007$	$0.696 \pm 0.009$
10	$0.845 \pm 0.006$	$0.913 \pm 0.005$	$0.866 \pm 0.007$	$0.647 \pm 0.008$
11	$0.797 \pm 0.007$	$0.905 \pm 0.005$	$0.862 \pm 0.010$	$0.602 \pm 0.009$
12	$0.816 \pm 0.008$	$0.916 \pm 0.006$	$0.842 \pm 0.012$	$0.612 \pm 0.011$
13	$0.834 \pm 0.006$	$0.913 \pm 0.005$	$0.828 \pm 0.009$	$0.613 \pm 0.009$
14	$0.843 \pm 0.016$	$0.904 \pm 0.012$	$0.894 \pm 0.022$	$0.662 \pm 0.022$
15	$0.830 \pm 0.009$	$0.892 \pm 0.007$	$0.879 \pm 0.010$	$0.633 \pm 0.011$
16	$0.821 \pm 0.010$	$0.893 \pm 0.009$	$0.894 \pm 0.013$	$0.637 \pm 0.014$
17	$0.839 \pm 0.008$	$0.890 \pm 0.006$	$0.889 \pm 0.010$	$0.645 \pm 0.010$

Table 49: CMUP Efficiency

Run	Crn			$\epsilon$
	$\epsilon_{\mathrm{ID}}$	$\epsilon_{ m reco}$	$\epsilon_{ m trig}$	-
Period	ID Efficiency	Reconstruction Efficiency	Trigger Efficiency	Total Efficiency
0d	$0.877 \pm 0.007$	$0.994 \pm 0.002$	$0.967 \pm 0.004$	$0.807 \pm 0.007$
0h	$0.853 \pm 0.007$	$0.991 \pm 0.002$	$0.955 \pm 0.004$	$0.773 \pm 0.007$
5-7	$0.859 \pm 0.008$	$0.987 \pm 0.003$	$0.954 \pm 0.005$	$0.775 \pm 0.009$
8	$0.846 \pm 0.011$	$0.989 \pm 0.004$	$0.946 \pm 0.007$	$0.766 \pm 0.012$
9	$0.861 \pm 0.011$	$0.980 \pm 0.005$	$0.930 \pm 0.008$	$0.760 \pm 0.012$
10	$0.859 \pm 0.008$	$0.986 \pm 0.003$	$0.929 \pm 0.009$	$0.762 \pm 0.010$
11	$0.820 \pm 0.010$	$0.982 \pm 0.004$	$0.927 \pm 0.010$	$0.723 \pm 0.012$
12	$0.843 \pm 0.012$	$0.981 \pm 0.005$	$0.900 \pm 0.014$	$0.723 \pm 0.016$
13	$0.838 \pm 0.009$	$0.977 \pm 0.004$	$0.893 \pm 0.009$	$0.710 \pm 0.011$
14	$0.872 \pm 0.025$	$0.989 \pm 0.011$	$0.890 \pm 0.027$	$0.747 \pm 0.032$
15	$0.854 \pm 0.012$	$0.968 \pm 0.006$	$0.923 \pm 0.013$	$0.741 \pm 0.015$
16	$0.816 \pm 0.015$	$0.966 \pm 0.009$	$0.894 \pm 0.024$	$0.686 \pm 0.023$
17	$0.789 \pm 0.011$	$0.963 \pm 0.006$	$0.898 \pm 0.014$	$0.662 \pm 0.015$

Table 50: CMX-Arch Efficiency

Run	$\epsilon_{ m ID}$	$\epsilon_{ m reco}$	$\epsilon_{ m trig}$	$\epsilon$
Period	ID Efficiency	Reconstruction Efficiency	Trigger Efficiency	Total Efficiency
0d	$0.000 \pm 0.000$	$0.000 \pm 0.000$	$0.000 \pm 0.000$	$0.000 \pm 0.000$
0h	$0.817 \pm 0.014$	$0.926 \pm 0.009$	$0.772 \pm 0.014$	$0.560 \pm 0.015$
5-7	$0.836 \pm 0.017$	$0.926 \pm 0.012$	$0.744 \pm 0.019$	$0.552 \pm 0.019$
8	$0.849 \pm 0.025$	$0.880 \pm 0.022$	$0.884 \pm 0.009$	$0.639 \pm 0.026$
9	$0.850 \pm 0.027$	$0.821 \pm 0.025$	$0.866 \pm 0.008$	$0.585 \pm 0.027$
10	$0.846 \pm 0.021$	$0.858 \pm 0.018$	$0.929 \pm 0.009$	$0.653 \pm 0.022$
11	$0.830 \pm 0.023$	$0.820 \pm 0.020$	$0.927 \pm 0.010$	$0.611 \pm 0.023$
12	$0.858 \pm 0.028$	$0.832 \pm 0.024$	$0.900 \pm 0.014$	$0.624 \pm 0.029$
13	$0.824 \pm 0.022$	$0.849 \pm 0.020$	$0.893 \pm 0.009$	$0.607 \pm 0.022$
14	$0.935 \pm 0.059$	$0.894 \pm 0.052$	$0.890 \pm 0.027$	$0.724 \pm 0.066$
15	$0.806 \pm 0.030$	$0.882 \pm 0.023$	$0.923 \pm 0.013$	$0.638 \pm 0.031$
16	$0.812 \pm 0.041$	$0.873 \pm 0.035$	$0.894 \pm 0.024$	$0.616 \pm 0.043$
17	$0.839 \pm 0.026$	$0.912 \pm 0.020$	$0.898 \pm 0.014$	$0.668 \pm 0.027$

Table 51: CMX-Mini Efficiency

Run	$\epsilon_{z_0}$
Period	$z_0$ Cut Efficiency
0d	$0.958 \pm 0.002$
0h	$0.958 \pm 0.002$
5-7	$0.958 \pm 0.002$
8	$0.968 \pm 0.002$
9	$0.968 \pm 0.002$
10	$0.968 \pm 0.002$
11	$0.968 \pm 0.002$
12	$0.972 \pm 0.001$
13	$0.972 \pm 0.001$
14	$0.972 \pm 0.001$
15	$0.972 \pm 0.001$
16	$0.972 \pm 0.001$
17	$0.972 \pm 0.001$

Table 52: Vertex position cut efficiency  $(\epsilon_{z_0})$ 

When we have multiple sub-detectors as is the case for the muons things are slightly more involved:

$$(LA\epsilon)_{\mu} = \sum_{\forall k} (LA\epsilon)_{k} \tag{40}$$

$$= \sum_{\forall k} \sum_{i} (L_{i,k} \epsilon_{i,k}) A_k \tag{41}$$

where k represents the three muon sub-detectors such that

$$k \in \{\text{CMUP}, \text{CMX-Arch}, \text{CMX-Mini}\}$$

For the purpose of understanding how the errors propagate we note that the error on the run period luminosity and efficiency are independent of other periods. Thus the error goes linearly for the efficiency. We take the acceptances to be independent as well. We note that the trivial luminosity error is easy to deal with (see section 6.1 for details) as it will be taken as a universal relative error. As such we will only derive the dependence of the less trivial acceptance and efficiency calculations.

Let  $\Delta A_k$  be the absolute acceptance error (with possible sub-detector dependence k) and  $\Delta \epsilon_{i,k}$  is the absolute error on the total lepton efficiency for run period i and sub-detector lepton k. We denote the effective luminsoity error (due to  $\Delta A$  and  $\Delta \epsilon_i$ ) error via  $\Delta (LA\epsilon)_{\ell}$ . For electrons,

$$\Delta(LA\epsilon)_e = (LA\epsilon)_e \sqrt{\left(\frac{\Delta A}{A}\right)^2 + \left(\frac{\sum_{\forall i} L_i \Delta \epsilon_i}{\sum_{\forall i} L_i \epsilon_i}\right)^2}$$
(42)

while for the muons,

$$\Delta(LA\epsilon)_{\mu} = \sum_{\forall k} (LA\epsilon)_{k} \left(\frac{(LA\epsilon)_{k}}{(LA\epsilon)_{\mu}}\right) \sqrt{\left(\frac{\Delta A_{k}}{A_{k}}\right)^{2} + \left(\frac{\sum_{\forall i} L_{i,k} \Delta \epsilon_{i,k}}{\sum_{\forall i} L_{i,k} \epsilon_{i,k}}\right)^{2}}$$
(43)

Table 53 notes the numerical values for our effective luminosities for electrons and combined muons. The error included is the Poisson based error which we have been sighting from table 48-52. This random error is very small and will be shown to be negligible to the 6.0% luminosity, the parton distribution functions (PDF), and final state radiation (FSR) systematics (see sections 6.1, 6.2, and 6.3, respectively).

$\geq n$	$(LA\epsilon)_e \text{ (pb}^{-1})$	$(LA\epsilon)_{\mu} \; (pb^{-1})$
0	$593 \pm 11.7$	$364 \pm 7.0$
1	$580 \pm 14.6$	$369 \pm 8.5$
2	$595 \pm 9.4$	$360 \pm 6.4$
3	$625 \pm 9.9$	$347 \pm 6.5$
4	$709 \pm 9.9$	$330 \pm 5.8$

Table 53: Effective Luminosity  $((LA\epsilon)_{\ell})$  for  $W \to \ell\nu + \geq n$  jets. The given uncertainties are due to the associated (run dependent) total efficiency uncertainty  $(\Delta\epsilon)$  and do not include the universal 6% uncertainty nor the PDF or FSR acceptance related systematics of sections 6.1-6.3.

# 6 Systematics

In this chapter we detail the various systematics we consider that will go into our final cross-section measurements. Some of these considerations are straightforward (e.g. the luminosity systematic uncertainty) while others are unique to this analysis (e.g. vertex reweighing/promotion systematic). It is useful to generalize about the nature of systematics and how they effect our final cross-section measurements. Consider the following "blue-print" for our treatment of systematics in forming a final cross-section (compare to equation 82),

$$\Delta \sigma = \Delta(\text{Unfolding}) \left[ \Delta(\text{JES}) \left[ \frac{\Delta(\text{Promotion}) \left[ \Delta(\text{Background}) \right]}{\Delta(\text{Luminosity} + \text{Acceptance})} \right] \right]$$
(44)

Here  $\Delta(\text{Unfolding})$  and  $\Delta(\text{JES})$  represents a bin-by-bin systematic in our unfolding correction and jet energy scale corrections to our total cross-section which are presented in sections 6.8 and 6.7, respectively. The former represents a systematic for the whole cross-section via the response in the signal MC while the latter individually effects our candidates in data, the background estimation, and our acceptance.

The  $\Delta$ (Background) term in equation 44 represents the two systematics for the background estimation which are also bin-by-bin effects on our final cross-section histograms. First we present our general background fitting estimation systematic in section 6.5. Secondly, we consider the top ( $t\bar{t}$  theoretical cross-section based) background estimation in section 6.6. The  $\Delta$ (Promotion) term signifies an additional treatment/correction for promotion which can be thought of as a background. This is actually our vertex reweighting systematic and is described in section 6.4. Finally  $\Delta$ (Luminosity+Acceptance) represents two sets of contributions to our effective luminosity. First the straightforward contribution of the systematic on the effective luminosity which is dominated by the actual luminosity detector uncertainty as noted in section 6.1. The second set of contributions effect our acceptance and efficiency calculation and deal with our methodological handling and assumptions concerning our use of PDFs (parton distribution functions) and FSR (final state radiation of the leptonic W decay). We describe these systematics in sections 6.2 and 6.3, respectively.

Special considerations, such as addressing cancellation of systematics in our normalized cross-sections will be addressed. In particular, we highlight in section 6.9 our treatment of how we combined systematics to obtain a total systematic. In the last section 6.10, we show the relative uncertainty for each systematic for each nontrivial cross-section which is in parallel to our presentation of our cross-section results in the next chapter.

### 6.1 Luminosity Measurement

Our final cross-section measurements involve our effective luminosity term was the effective product of the CLC luminosity, W acceptance, and various lepton efficiencies as defined in section 5.7. In that section we gave an uncertainty term,  $\Delta(LA\epsilon)$ , (equations 42 and 43) which was defined in terms of uncertainties in our acceptance ( $\Delta A$ ) and efficiency ( $\Delta \epsilon$ ). This section deals with the direct uncertainty in our measurement of the luminosity and not the other

components of the effective luminosity. More precisely this is the CLC detector uncertainty on the measured integrated luminosity [56].

The systematic due to the uncertainty in the luminosity measurement is straightforward to account for due to its placement in the dominator of our cross-section calculation and not having any lepton, jet multiplicity, or analysis observable dependence. We apply a 6.0% global uncertainty to all non-normalized cross-sections. To be pedagogical, the cross-section error  $(\Delta \sigma)$  for an abstract cross-section observable  $(\sigma)$  would simply be

$$\Delta_{\text{Lum}} \equiv \Delta \sigma = (0.06)\sigma \tag{45}$$

In the case of cross-section ratios (such as normalized cross-section), this luminosity uncertainty completely cancels due to its independence. Note that the luminosity systematic is not presented in any of the relative uncertainty plots in section 6.10 as it is completely trivial. We will later denote the pure luminosity (as oppose to the total effective luminosity) systematic via  $\Delta_{\text{Lum}}$ .

The two dominate acceptance and efficiency related systematics follow in the next two sections. The first (section 6.2) deals with the systematic due to our choice of parton distribution function and its associated error. We also naturally incorporate the uncertainties in our efficiency via our effective luminosity calculation mentioned above. The second section of note (section 6.3) deals with the variation with our given choice of pre- or post-radiation lepton selection in our reduced cross-section (as defined in section 7.1) as well as its indirect effect on the PDF acceptance systematic.

### 6.2 Parton Density Function (PDF) Acceptance

The acceptance systematic described in this section comes from our knowledge of the parton distribution functions (PDF) we use. The general procedure we followed is given here [57]. The basic concept is to vary different PDF sets and apply a weight based off of the relative value of the default CTEQ5L set to each event. We then calculate the acceptance for each PDF variation and compute a systematic based off of the spread in that distribution. There is an additional PDF and acceptance related systematic based on our knowledge of the strong coupling constant,  $\alpha_S$ . We also fold in the uncertainty in our efficiency measurements the results of which was presented in section 5.6.

The general procedure begins by running over each MC sample (taking care to run in the same event number order) and produce a PDF root file that has a weight value for each event and for each PDF set used. We look at a total of 46 sets: CTEQ5L (weight values are 1.0000 by definition), MRST72, MRST75, CTEQ6L, CTEQ6L1, CTEQ6M (central value), and the 20 pairs of orthogonal CTEQ6M eigen vectors that represent  $\pm$  90% CL [58].

In order to produce a relative weight one needs to reproduce the event's squared momentum transfer,  $Q^2$ , and the parton momentum fractions for the initial patrons,  $x_1$  and  $x_2$ . Although this information is not saved during generation it is possible to reconstruct the values by looking at the hepg bank. In the case of the Alpgen MC the choice of generator  $Q^2$  is chosen via the

iqopt option which is set to 1 in this case. This (default) option sets  $\mathbb{Q}^2$  to

$$Q^2 = M_W^2 + \sum_{\text{y jets}} p_T^2 \tag{46}$$

Here,  $M_W^2$  is the squared mass of the W in the hepg bank. Pedagogically, we always take the "second" W in the bank which has as its parent the generated W (we use the PDG Monte Carlo particle numbering scheme[60]). However, the W mass by construction does not change (only its 4-momentum components as needed relative to the changes in the final state radiation leptons) and thus there is no final state radiation (FSR) correction due to our choice in  $Q^2$ . Note that we consider the additional effect of our choice in the post-final radiation state verses pre-final state radiation with respect to our reduced acceptance (see section 5.4) as a separate systematic to be described in the next section.

The sum in equation 46 is over all the generated partons that are quarks or gluons. While these are not jets per se, the notation is hopefully clear that these are hadronic partons and that the  $p_T$  of the W nor its leptons is used. We calculate the squared transverse momentum in the normal way via the hepg momentum components:  $p_T^2 = p_x^2 + p_y^2$ . Although we do not have a say in the matter, we note that this is a logical choice in  $Q^2$  with  $M_W^2$  and  $M_W^2 + p_{T(W)}^2$  as the typical sighted values in the Run I CDF W+jets paper [61].

For the momentum fractions, unfolding the initial values proves to be more involved. The method by some is not particularly rigorous [62], e.g.

$$x_1 = \frac{E_1 + |p_{1,z}|}{\sqrt{s_0}}$$

We derive  $x_1$  and  $x_2$  by using a similar method outlined in [63]. The notation and discussion in [64] is also instructive.

$$x_F = x_1 - x_2 \tag{47}$$

$$\tau = x_1 x_2 \tag{48}$$

 $x_F$  is the Feynman x which is chosen, without loss of generality, to be the difference between the proton based parton  $(p_1)$  momentum fraction and the anti-proton based parton  $(p_2)$  momentum fraction. The product of the momentum fractions is defined to be  $\tau$ .

We can then write  $x_1$  and  $x_2$  in terms of these quantities:

$$x_1 = +\frac{1}{2} \left( x_F + \sqrt{x_F^2 + 4\tau} \right) \tag{49}$$

$$x_2 = -\frac{1}{2} \left( x_F - \sqrt{x_F^2 + 4\tau} \right) \tag{50}$$

In order to calculate Equations 49 and 50 we need use the 4-momentum of the patrons  $p_1$  and  $p_2$  via the hepg bank in combination with  $\tau$  and  $x_F$ . For the former, recall that the momentum fraction is defined via the relationship  $p_i = x_i P_i$  where  $P_i$  is the proton or anti-proton 4-momentum and is taken to be  $P_{1,2} = (980, 0, 0, \pm 980)$ , without loss of generality. Substituting

 $x_i P_i$  in for  $p_i$  for

$$\hat{s} = (p_1 + p_2)^2 \tag{51}$$

$$\hat{s} = s_0(x_1x_2) + (m_1^2 + m_2^2) \tag{52}$$

Ignoring the minor mass correction which is small relative to the beam energy,  $\tau$  can thus be written as the quotient of the square of the center of mass energy of the event  $(\hat{s})$  and the square of the total beam-on-beam energy  $(s_0 = (2 \times 980 \text{ GeV})^2)$  or

$$\tau = \frac{\hat{s}}{s_0} \tag{53}$$

Therefore, we use Equation 53 via Equation 51 to calculate  $\tau$ .

For  $x_F$ , again recall  $p_i = x_i P_i$ . It is not kosher to define a scaler quantity in terms of a ratio of 4-momentums so we begin with

$$x_1 - x_2 = \frac{P_1 P_2}{P_1 P_2} (x_1 - x_2) \tag{54}$$

$$= \frac{p_1 P_2 - P_1 p_2}{P_1 P_2} \tag{55}$$

$$= \frac{980(E_1 + p_{1z}) - 980(E_2 - p_{2z})}{2(980)^2}$$
 (56)

$$x_F = \frac{(E_1 - E_2) + (p_{1z} + p_{2z})}{2(980)} \tag{57}$$

The  $x_F$  quantity has the behavior one would expect for various simple test cases. It is also similar to the result in equation 12 in [63]. Using the above, it is simply a matter of calling the needed PDF libraries via Pythia and CTEQ6 methods to obtain the desired structure function weight for each event.

Initially we investigated the two MRST sets PDF sets: MRST72 and MRST75 [59]. This proved to be a useful exercise in understanding the effect of the PDF on the acceptance but does not use the more rigorous CTEQ6M method which we outline below. However, under this frame work we could measure the PDF uncertainty via the difference between the nominal CTEQ5L and MRST72 acceptances. An additional acceptance related systematic, this time for  $\alpha_S$ , came via the difference of MRST72 and MRST75 acceptances [57].

In figure 210 we plot the acceptance for six PDF sets normalized to the default CTEQ5L acceptance for  $W \rightarrow e\nu + 0$  jets. The behavior for muons was the same though there was an expected error dependence due to the  $\eta$  coverage of the different muon detectors. There was no effect in the relative acceptance pattern between jet multiplicities though the acceptance differences were largest for > 1 jet.

The method for determining the PDF uncertainty and which will be the dominate acceptance systematic came via using CTEQ6M and its 20 eigen vector/parameter pairs. The motivation came from the fact that the old paradigm on focusing on the older PDF sets was out of date and most groups defaulted to this method. The procedure allows for an asymmetric error and is dependent on the relative difference to the central value (CTEQ6M). We denote the central

value via  $A_0$  and the 40 additional acceptances via  $A_i^{\pm}$  with i=1-20. The PDF uncertainty,  $\Delta A^{\pm}$  is given by [57]

$$\Delta A^{+} = \sqrt{\sum_{i=1}^{20} \left( \text{Max}[(A_{i}^{+} - A_{0}), (A_{i}^{-} - A_{0}), 0] \right)^{2}}$$

$$\Delta A^{-} = \sqrt{\sum_{i=1}^{20} \left( \text{Max}[(A_{0} - A_{i}^{+}), (A_{0} - A_{i}^{-}), 0] \right)^{2}}$$
(58)

$$\Delta A^{-} = \sqrt{\sum_{i=1}^{20} \left( \text{Max}[(A_0 - A_i^+), (A_0 - A_i^-), 0] \right)^2}$$
 (59)

We calculate  $\Delta A^{\pm}$  for each jet multiplicity and for each lepton/detector type. For comparison purposes only, we look at the raw combined muon results which are taken by throwing caution to the wind and treating the muons as a single detector sample. The electron (CEM) and combined muon  $(\mu)$  results are presented in table 54 while the proper muon results (CMUP, CMX-Arch, and CMX-Mini) are shown in table 55. The errors presented and more generally all the acceptance uncertainties (in the form of  $\Delta A$ ) are given as a percent and are relative to the cross-section measurement or the nominal acceptance, equivalently. The corresponding plot for tables 54-55 is shown in Fig. 211 where the positive (negative) error maps to the positive (negative) acceptance uncertainty axis. The notation and convention here is straightforward; the acceptance uncertainty due to our CTEQ6M PDF method is given by  $\pm \Delta A^{\pm}$ .

$\geq n$ jets	$\Delta A_{CEM}^+$	$\Delta A^{CEM}$	$\Delta A_{\mu}^{+}$	$\Delta A_{\mu}^{-}$
0	0.91	1.54	0.49	0.74
1	1.19	1.99	0.75	1.11
2	0.69	1.25	0.40	0.75
3	0.70	1.26	0.43	0.92
4	0.64	0.95	0.37	0.61

Table 54: Asymmetric PDF Acceptance Uncertainty (%) for Electrons and Combined Muons Using CTEQ6M

$\geq n$ jets	$\Delta A_{CMUP}^{+}$	$\Delta A^{-}_{CMUP}$	$\Delta A_{Arch}^{+}$	$\Delta A^{-}_{Arch}$	$\Delta A_{Mini}^{+}$	$\Delta A_{Mini}^{-}$
0	0.64	0.95	0.49	0.75	0.38	0.67
1	0.91	1.32	0.74	1.12	0.65	1.21
2	0.49	0.80	0.40	0.77	0.36	0.81
3	0.50	0.93	0.41	0.94	0.41	1.04
4	0.49	0.75	0.38	0.67	0.33	0.46

Table 55: Asymmetric PDF Acceptance Uncertainty (%) for Muons Using CTEQ6M

In general the negative systematic uncertainty for the PDF ( $\Delta A^{-}$ ) is larger than the positive  $(\Delta A^{+})$ . For convenience we take a conservative total acceptance based symmetric uncertainly by adding the errors in quadrature which we denote via  $\Delta A$ .

$$\Delta A = \sqrt{(\Delta A^+)^2 + (\Delta A^-)^2} \tag{60}$$

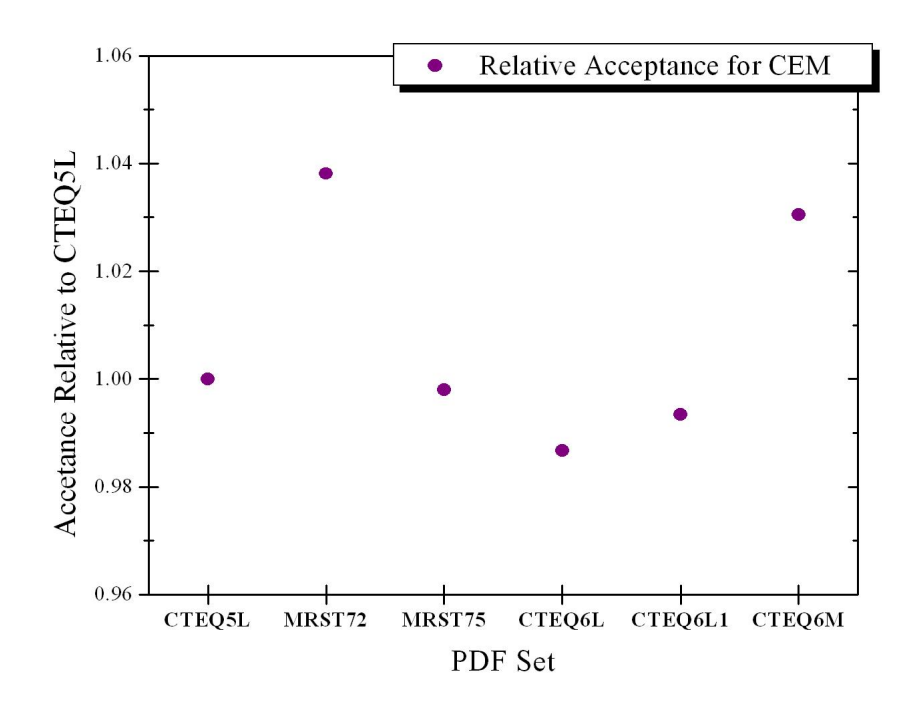


Figure 210: Total Inclusive CEM Acceptance for PDF Sets Relative to CTEQ5L Acceptance for  $W \rightarrow e\nu + \geq 0$  jets

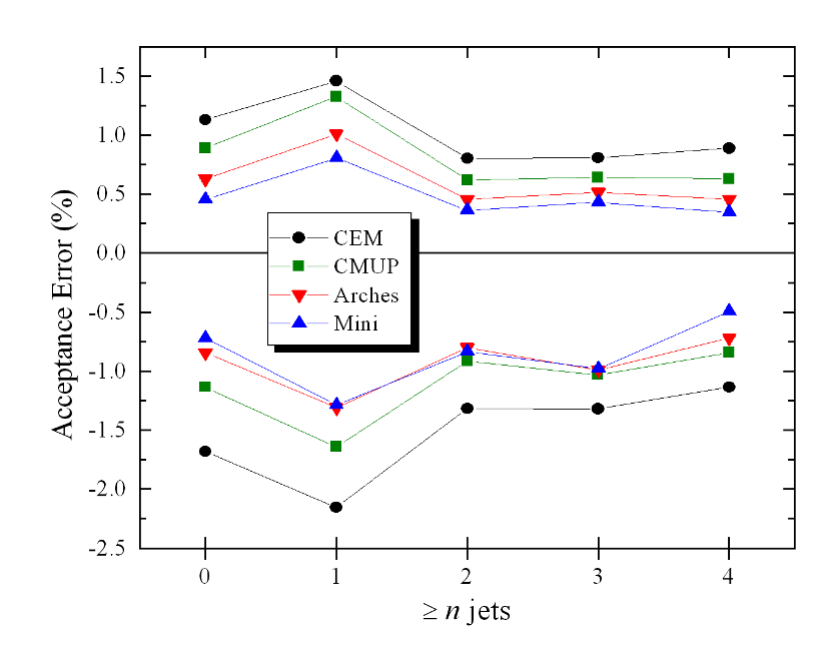


Figure 211: Asymmetric PDF Systematic Uncertainty (%) for each lepton detector vs.  $\geq n$  jets

$\geq n$ jets	$\Delta A_{CEM}^{\alpha_S}$	$\Delta A_{CMUP}^{\alpha_S}$	$\Delta A_{Arch}^{\alpha_S}$	$\Delta A_{Mini}^{\alpha_S}$
0	0.67	0.61	0.39	0.25
1	0.85	0.98	0.70	0.49
2	0.41	0.38	0.22	0.11
3	0.41	0.40	0.30	0.17
4	0.61	0.39	0.25	0.05

Table 56:  $\alpha_S$  Acceptance Uncertainty (%) for  $W \to \ell \nu + \geq n$  Jets Using CTEQ6L/L1

We note that  $\Delta A$  is still taken to be detector and jet multiplicity dependent. These combined results is shown in figure 212 and again in table 57. Consistent with our previous presentation of this section, these acceptance based systematics uncertainties are relative to the acceptance.

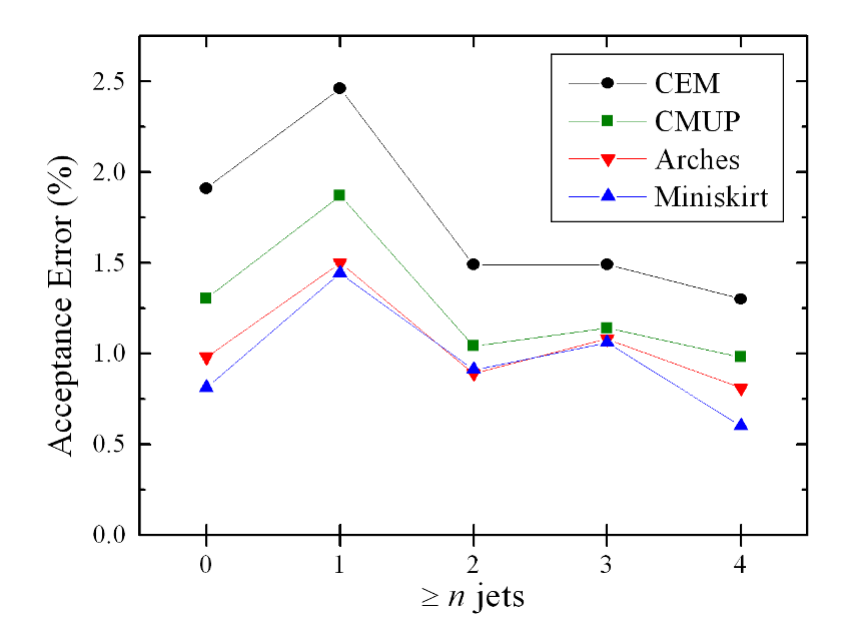


Figure 212: Final Acceptance Systematic Uncertainty for each lepton detector vs.  $\geq~n$  jets

The total PDF error,  $\Delta A$ , on our cross-section will follow from our treatment of the effective luminosity (see section 5.7) via equation 42 (page 184) for electrons (CEM) and equation 43 for muons (CMUP, CMX-Arch, and CMX-Mini). As noted above, the acceptance uncertainty given in this section have been relative to the appropriate lepton and jet multiplicity acceptance and measured as a percentage whereas equations 42 and 43 denote  $\Delta A$  as an absolute error in the acceptance. We directly apply  $\Delta A_{CEM}$ , etc. to the relative acceptance error term  $(\Delta A/A)$  in those equations. We combine this with the systematic associated with our total efficiency information  $(\Delta \epsilon)$  as described in section 5.6. The systematic error  $(\Delta \sigma)$  for a given cross-section  $(\sigma)$  is given by

$$\Delta_{\rm PDF} \equiv \Delta \sigma = \left(\frac{\Delta (LA\epsilon)_{\ell}}{(LA\epsilon)_{\ell}}\right) \sigma \tag{61}$$

We will later use  $\Delta_{PDF}$  to signify our general acceptance (PDF and  $\alpha_S$ ) systematic as well as

$\geq n$ jets	$\Delta A_{CEM}$	$\Delta A_{CMUP}$	$\Delta A_{Arch}$	$\Delta A_{Mini}$
0	1.8	1.2	0.9	0.8
1	2.3	1.6	1.3	1.3
2	1.4	1.0	0.9	0.9
3	1.4	1.1	1.0	1.0
4	1.2	0.9	0.8	0.6

Table 57: Total PDF Acceptance Uncertainty (%) for  $W \rightarrow \ell \nu + \geq n$  Jets Using CTEQ6M

our jet multiplicity independent efficiency uncertainty.

# 6.3 Final State Radiation (FSR)

This section deals with another aspect of our acceptance systematic which recursively effects our PDF calculation and directly effects our reduced acceptance of section 5.4. At tree level for a 2 to 2 particle process (for reference see the W decay diagram in figure 213) there is no accounting for the higher order effects such as bremsstrahlung[65] of the charged lepton via photon emission given in QED or the equivalent radiation of the initial state partons which includes emission of additional partons as described in QCD. We described these higher order contributions as ISR and FSR for initial state and final state radiation, respectively.

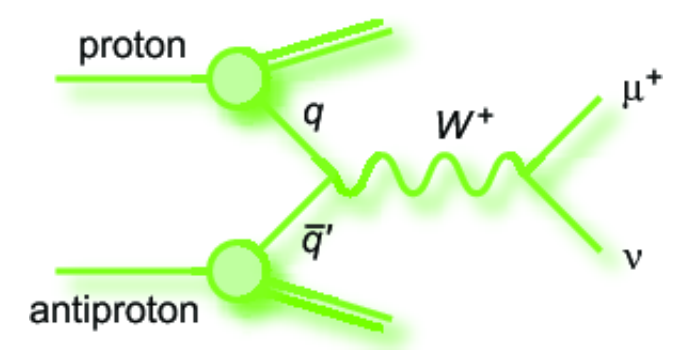


Figure 213: Tree level (leading order) Feynman digram for  $p\bar{p} \to W \to \mu\nu$  [66]

The potential effect of the initial state radiation (ISR) of our observables is affirmatively and explicitly ignored in this analysis as our measurement (the jet kinematics of W events) is this effect. In other words, since we tag the event via the leptonic decay of W to electrons and muons (with their associated neutrinos) the jets we measure necessarily come from radiation of the initial (color charged) partons from the  $p\bar{p}$  interaction. Potentially, our results can inform perturbative quantum chromodynamics (pQCD) and this very effect.

Final state radiation (FSR) in the case of a W decay to a charged lepton and its neutrino would be represented by photon emission on the charged member. FSR is an observable detector effect [67] but for our purpose here it also impacts our methodological use of PDFs of the previous section. For our PDF systematic analysis we selected the post-FSR generated W and we observed how different PDF choices varied our acceptance via our signal MC. Here we want to apply an additional systematic due to our choice of post-FSR verses pre-FSR leptons on our reduced acceptance definition of section 5.4. As noted in the previous section, there is no FSR dependence on our momentum transfer and thus no effect on our signal MC via full detector simulation. However, for our reduced acceptance, the cuts we make on the charged lepton and on the transverse W mass (explicit cuts given in table 45 on page 179) are affected by our selection at the hepg bank.

We define two reduced acceptances by our systematic choice in which 4-momentums we use for the lepton decay pair. We do this by selecting leptons via their particle ID as well as their parent (particle) ID. The pre-FSR reduced acceptance ( $\bar{A}_{pre}$ ) uses the "original" leptons that have the W as its parent. By default, we use the post-FSR variables for our reduced acceptance ( $\bar{A} = \bar{A}_{post}$ ). These are the daughter particles of the pre-FSR lepton pair.

We assign a FSR systematic uncertainty ( $\Delta \sigma$ ) to our reduced cross-section ( $\sigma$ ) based off of the relative difference in the calculated reduced acceptance cross-section:

$$\Delta_{\text{FSR}} \equiv \Delta \sigma = |\sigma_{\text{post-FSR}} - \sigma_{\text{pre-FSR}}| \tag{62}$$

where the cross-section terms ( $\sigma = \sigma_{\text{post-FSR}}$  and  $\sigma_{\text{pre-FSR}}$ ) use the respective reduced acceptances ( $\bar{A}_{\text{post}}$  and  $\bar{A}_{\text{pre}}$ ) as described in section 7.1. This is effectively just the relative difference of a pre/post  $a_{\text{hepg}}$  (see equations 35 and 36 on page 177). We will denote this FSR error as  $\Delta_{\text{FSR}}$ .

	$W \rightarrow e\nu$	$W \rightarrow \mu\nu$
$\geq n$ jets	$\Delta\sigma/\sigma$ (%)	$\Delta\sigma/\sigma$ (%)
0	4.5	2.6
1	4.7	3.4
2	4.8	3.3
3	5.3	3.6
4	5.6	4.7

Table 58: The relative final state radiation (FSR) systematic uncertainty on the reduced acceptance cross-section (as defined in section 5.4) for  $W \to \ell \nu + \geq n$  jets as defined by equation 62. For non-reduced acceptance cross-sections where we use the normal CDF detector acceptance without limiting generator with cuts at the hepg level, there is no associated FSR systematic.

Table 58 give our FSR (reduced acceptance) systematic for each jet multiplicity and both lepton channels. There is a modest jet multiplicity dependence (1-2% difference between the 0 and 4 inclusive jet bins). The uncertainty is also systematically larger in the electron channel and this may be just an artifact of the difference in our hepg cuts we apply. This hypothesis is consistent with the PDF systematic of the previous section.

### 6.4 Vertex Reweighting

In this section we detail our systematic concerning our reweighing of the MC number of vertices distribution. As noted already in section 4.6, we reweight the MC based on the number of vertices ("# vertices") behavior seen in the data. To recount, the motivation is to remove the instantaneous luminosity dependence on the jet multiplicity and to account for the effect jet promotion. In the latter case, additional interactions in the event may produce additional jets which are not associated with the primary W interaction. The effect would show up as an event being "promoted" into a higher jet multiplicity. Our solution to reweight the MC was shown to mitigate this. Here, however, we wish to estimate a systematic based on the variation in our jet multiplicity cross-section due to the effect of different # vertices fittings and reweightings. Based off of the expected and observed (see figures 188 and 189 starting on page 156 for example)  $n^{\text{th}}$  leading jet  $p_T$  behavior, our vertex reweighting systematic does not warrant a bin-by-bin correction to our observables outside of the application of a jet multiplicity dependent systematic.

In section 4.6 we highlighted the results of 4 iterations where we would "fit" the # vertices distributions (for quality 12 vertices 1-3 with  $\sum p_T^{vtx} > 10 \text{ GeV/c}$ ) by effectively taking the ratio of our data (more precisely, candidate data minus QCD prediction) with our MC based signal and background estimations (see equation 20 on page 150). Once we verified basic consistency in the results for high jet multiplicity, we use the total inclusive ( $\geq 0$  jets) multiplicity results to then reweight the MC. This process was repeated 3 more times (iterations 2-4) such that we have the default reweighting cross-section results along with 3 potential variations in our cross-section results. The reweighting results were presented in tables 26 and 27 for the electron and muon channels, respectively. We will now present the jet multiplicity cross-section values normalized to the average cross-section for each jet multiplicity over the four iterations as well as the standard deviation of these values. The normalization to the average allows greater ease in comparison between different iterations and jet multiplicities. The electron channel results are present in table 59 while the muon channel results are given in 60.

	$0^{\mathrm{th}}$	$1^{\mathrm{st}}$	$2^{\mathrm{nd}}$	$3^{\mathrm{rd}}$	Standard
$\geq n$ jets	iteration	iteration	iteration	iteration	Deviation
0	1.003	1.004	0.996	0.997	0.004
1	1.006	1.015	0.989	0.990	0.013
2	1.012	1.019	0.984	0.986	0.018
3	1.031	1.016	0.975	0.978	0.028
4	1.044	1.037	0.958	0.961	0.047

Table 59:  $W \to e\nu + \geq n$  jet multiplicity cross-sections normalized to the average over all iterations. The three iterations (1<sup>st</sup>-3<sup>rd</sup>) are for the vertex fitting and subsequent MC reweighting while the 0<sup>th</sup> iteration represents the default reweighing. The standard deviation is taken over each of the four measurements for each jet multiplicity.

To obtain our final systematic for our vertex reweighting procedure to address the effect of multiple interactions and the potential for promotion, we looked at the relative difference between our final analysis result (i.e. 3<sup>rd</sup> iteration) and our default (no vertex redefinition and default

	$0^{\mathrm{th}}$	$1^{\mathrm{st}}$	$2^{\mathrm{nd}}$	$3^{\mathrm{rd}}$	Standard
$\geq n$ jets	iteration	iteration	iteration	iteration	Deviation
0	0.976	0.991	1.017	1.017	0.020
1	0.982	0.992	1.013	1.013	0.015
2	0.985	0.996	1.010	1.010	0.012
3	1.006	0.985	1.005	1.005	0.010
4	1.047	1.039	0.957	0.957	0.050

Table 60:  $W \to \mu\nu + \geq n$  jet multiplicity cross-sections normalized to the average over all iterations. The three iterations (1<sup>st</sup>-3<sup>rd</sup>) are for the vertex fitting and subsequent MC reweighting while the 0<sup>th</sup> iteration represents the default reweighing. The standard deviation is taken over each of the four measurements for each jet multiplicity.

MC weighting). Symbolically, our jet multiplicity dependent uncertainty would be

$$\frac{|\sigma_{\text{default}} - \sigma_{\text{final}}|}{2} \tag{63}$$

Of course, the standard deviation given in tables 59 and 60 is in good agreement with the prior approach but better captures the spread in the fitting procedure itself. We also note that the standard deviation calculation of the 4 different iterations is larger for all jet multiplicities. Therefore, we take the conservative of these two methods and use the standard deviation in the cited tables as our relative vertex reweighting systematic uncertainty. We will reference the systematic for a given cross-section using  $\Delta_{\text{Vtx}}$ . To be pedagogical, for each cross-section iteration  $(\sigma(i))$  for a given lepton and jet multiplicity the cross-section uncertainty  $(\Delta\sigma)$  is defined as

$$\Delta_{\text{Vtx}} = \Delta \sigma = \sum_{i=0}^{3} \frac{(\sigma(i) - \bar{\sigma})^2}{4 - 1}$$

$$\tag{64}$$

We performed an additional cross-check of our vertex reweighting procedure by looking at the relative difference in our results with respect to our jet energy corrections (as described in section 3.6). It is possible that after applying  $\pm \sigma_{\rm JES}$  variation we could have an additional systematic effect via the jet energy scale on our reweighting results outline here. As it turn out, the effect is hardly detectable: less than 0.05% change between the  $+\sigma_{\rm JES}$  and  $-\sigma_{\rm JES}$  results.

### 6.5 Background Estimation Fitting

Our background estimation procedure has the potential to systematically shift our result. Unlike previous systematics discussed so far, this would necessarily be dependent on the actual shape of our jet kinematic observables rather than effectively changing our acceptance which is simply jet multiplicity dependent. This systematic that we turn to now would be a bin-by-bin effect to our background estimation via our various histograms of analysis observables beyond the normal Poisson uncertainty associated with the number of events in each bin.

We consider two different concerns. First there is the systematic uncertainty associated with our actual background estimation fitting procedure as described in section 4.4. This method of using

our EWK and QCD templates (sections 4.2 and 4.3, respectively) to arrive at a jet multiplicity independent background estimation is dealt with in this section. Second, we have to consider the theoretical cross-section uncertainty in the case of our diboson and  $t\bar{t}$  backgrounds where we directly reweight events via an effective luminosity (see section 4.1). These "fixed" (i.e. not fitted) estimations which are dominated by the theoretical uncertainty in the  $t\bar{t}$  cross-section are dealt with in the next section.

In section 4.5 we presented our background fitting fractions via tables 19  $(W \to e\nu + \ge n \text{ jets})$  and 20  $(W \to \mu\nu + \ge n \text{ jets})$  which included the fitting uncertainty  $(\Delta k_{EWK} \text{ and } \Delta k_{QCD})$  for each jet multiplicity. We recalculate our cross-sections by varying the number of background events by

$$\Delta B_{\text{Fit}} = |\Delta k_{EWK}(N_{EWK}) - \Delta k_{QCD}(N_{QCD})| \tag{65}$$

where  $\Delta B_{\rm Fit}$  is the background estimation from our non-diboson and non-tt processes (i.e.  $W \to \tau \nu$ ,  $Z \to \ell \ell$ ,  $Z \to \tau \tau$ , and QCD). We note that  $N_{EWK}$  and  $N_{QCD}$  are the number of events in our EWK and QCD templates after we normalized via  $n_{EWK}$  and  $n_{QCD}$  (see tables 17 and 18), respectively. Equation 65 takes its form due to the fitting fraction being 100% anti-correlated. As a result, the uncertainty tends to be dominated by one of the templates which varies based on the number of events in each bin of our histogram observables.

Like our previous systematics outlined in this chapter, we abstractly define our background fitting cross-section uncertainty ( $\Delta \sigma$ ) based off of our nominal cross-section definition (section 7.1) as

$$\Delta_{\text{Fit}} \equiv \Delta \sigma = u \frac{\Delta B_{\text{Fit}}}{LA\epsilon} \tag{66}$$

where our effective luminosity (section 5.7) is noted with  $LA\epsilon$  and u is our unfolding fraction (section 3.8). We will reference the systematic uncertainty due to our non-t $\bar{t}$  background estimation and fitting via  $\Delta_{\rm Fit}$ .

The uncertainty is not technically flat due to the background being composed of events not from our EWK or QCD templates (e.g.  $t\bar{t}$  estimation) and hence the relative error is allowed to shift. As section 6.10 will show however, this systematic is smooth bin-by-bin and flat relative to a simple Poisson error of the expected signal. For the third and fourth inclusive jet bins, this is not the case in our second background estimation related systematic (as discussed in the next section) for the theoretical  $t\bar{t}$  cross-section uncertainty.

We investigated the potential for a correlation systematic effects in our vertex reweighting procedure as well as our jet energy scale systematic. Once we accounted for the expected change in the templates (i.e.  $N_{EWK}$  and  $N_{QCD}$  of equation 66) we found virtually identical results in both cases. This is an artifact of the procedure itself as our fitting is dependent on the W  $M_T$  shape for the EWK and QCD templates and not issues more sensitive to our jet related observables.

### 6.6 tt Background Estimation

The second background related uncertainty to our cross-section measurement comes from the a theoretical cross-sections we use to directly estimate the backgrounds for diboson and  $t\bar{t}$ 

production. These contributions which were "fixed" relative to our background fitting procedure were explained in section 4.1. We investigated the effect of varying the WW, WZ, and  $W\gamma^*$  cross-sections but found these to have almost no effect on our measurement. They are known to  $\approx 6-8\%$  (see table 16 on page 16) and only account for  $\approx 3\%$  of the total candidate number of events in data (see tables 21 and 22 starting on page 92). In addition, the jet related kinematics for an accepted event tends to overlap with the other electro-weak based backgrounds.

Conversely, we found that the  $t\bar{t}$  background estimation requires a formal procedure (this section) to account for the potential variation in our measurement given the  $\approx 12\%$  theoretical cross-section error and account for  $\approx 10\text{-}37\%$  of our events in the inclusive third and fourth jet bins. This fact alone would require us to understand the possible variation in our total background estimation for jet multiplicity cross-section. Equally distressing, top pair kinematics are fairly distinct due to producing energetic and heavy jets via a lepton+jets decay. Our goal in this section is to account for the potential discrepancy in our results due to our  $t\bar{t}$  cross-section being systematically off. Like the previous section, this systematic will be calculated bin-by-bin for each of our analysis histogram observables.

Our approach is to effectively rerun the entire analysis and vary the theoretical cross-section via its uncertainty as given in table 16. This then propagates as an effective MC weight change as described in section 1.6. The key here is that we are not free to just shift the cross-section universally as this change will can effect our fitting fractions for our EWK and QCD templates. As a result, we follow the same background estimation procedure where we derive new fitting fractions based off of the  $M_T$  spectrum in data minus the estimated contributions of dibosons and our weight modified  $t\bar{t}$  sample. We then calculate our W cross-section as normal (see section 7.1) for both the positive and negative deviations in the theory cross-section. We shall denote these recalculated cross-sections as  $\sigma_+$  and  $\sigma_-$ , respectively. This necessarily means that our  $t\bar{t}$  background estimation systematic is constructed to allow for asymmetric errors.

For a given cross-section ( $\sigma$ ) we define the spread in our  $t\bar{t}$  variation cross-section  $\sigma_{\pm}$  ( $\Delta\sigma$ ) as

$$\Delta \sigma = \frac{|\sigma_+ - \sigma_-|}{2} \tag{67}$$

The actual asymmetric cross-section error which we distinguish as  $\Delta_{\text{Top}}$  is given by

$$\Delta_{\text{Top}} \equiv \Delta \sigma \pm (\bar{\sigma}_{+} - \sigma) \tag{68}$$

where  $\bar{\sigma}_{\pm}$  is simply the average of both variations:

$$\bar{\sigma}_{\pm} = \frac{\sigma_{+} + \sigma_{-}}{2} \tag{69}$$

Methodologically, we check to make sure that our error band always contains the central value. Theoretically, it is possible to construct such a scenario but this never happens and our systematic uncertainty is effectively symmetric for our analysis observables. Indeed, the systematic of this section is also a general test of our theory independent background estimation procedure which was formally addressed in the previous section.

### 6.7 Jet Energy Scale Corrections

The dominate systematic in many analyses looking at jet kinematics is the jet energy scale (JES) and this is certainly true in ours. Jet energy corrections were discussed in section 3.6, in particular, along with our definition and treatment of jets in chapter 3, generally. This section overviews and describes the general procedure for the jet energy corrections systematic. We deal with the related issue of applying a systematic to our unfolding correction in the next section.

We are fortunate that the CDF jet energy correction group has a very streamlined procedure for applying jet energy correction and for getting appropriate  $\pm \sigma_{\rm JES}$  uncertainties for our JES systematic [33][35]. (We note that the  $\pm \sigma_{\rm JES}$  represents the plus-or-minus one standard deviation in the jet energy scale uncertainty and not the generic cross-section,  $\sigma$ , used elsewhere in this chapter.) We apply the level 5 (i.e. relative, multiple interactions, and absolute) jet corrections the via the procedure on the Jet Energy Corrections Systematic Uncertainties page via the ROOT interface.

From the technical point of view this simply requires us running the full analysis three times: once for the nominal (corrected) result and then once each changing the corrections by  $\pm \sigma_{\rm JES}$ . This amounts to inputing a simple systematic flag ( $\pm 1$  for  $\pm \sigma_{\rm JES}$  or 0 for the default correction) when we set up our jet corrections for each event. From this we construct three sets of cross-sections in parallel (see section 7.1 for our cross-section definition discussion). The cross-sections can deviate bin-by-bin with respect to the nominal based on the variation in the number of candidates in data as well as our background estimation and even a change in our acceptance. We account for all of these considerations.

In order to calculate the JES systematic we construct a bin-by-bin error based on the deviation between the nominal "central" result and our two systematic variations. We define the latter cross-sections to be  $\sigma_{\pm}$ . Let  $\sigma$  be the cross-section measurement for one of our observables (e.g.  $n^{\text{th}}$  leading jet  $p_T$ ) and let  $\Delta \sigma$  be the prescribed JES systematic uncertainty for  $\sigma$ . We construct  $\Delta \sigma$  via  $\sigma_+$  and  $\sigma_-$  as follows,

$$\Delta \sigma = \frac{|\sigma_+ - \sigma_-|}{2} \tag{70}$$

However, for some distributions bin-by-bin variations may produce  $\Delta \sigma$  values where the central value is outside of the range of  $\sigma_+$  and  $\sigma_-$ . In order to correct for this, our final uncertainly is scaled by twice the distance to the nearest variation. The two cases are as follows:

$$if(\sigma_{+} < \sigma) \Rightarrow \Delta\sigma = (\sigma - \sigma_{+}) + \frac{|\sigma_{+} - \sigma_{-}|}{2}$$
(71)

$$if(\sigma_{-} > \sigma) \Rightarrow \Delta \sigma = (\sigma_{-} - \sigma) + \frac{|\sigma_{+} - \sigma_{-}|}{2}$$
 (72)

The notation in equation 70 (likewise equations 71 and 72) suggests a symmetric systematic error and indeed it is just the variation between the mean value between  $\sigma_{+}$  and  $\sigma_{-}$ . Like our  $t\bar{t}$  systematic we account for the difference in the average via  $\bar{\sigma}_{\pm}$  (equation 69 in the previous section) and define our asymmetric error of  $\sigma$  using

$$\Delta_{\rm JES} \equiv \Delta \sigma \pm (\bar{\sigma}_{\pm} - \sigma) \tag{73}$$

which takes the same form as equation 68. In order to account for all the systematics together, we will later refer to our jet energy systematic uncertainty as  $\Delta_{\rm JES}$ .

# 6.8 Hadron Level Unfolding Correction

Our final systematic deals with our unfolding of our calorimeter based measurements into a hadronic cross-section. This hadron level unfolding was explained in section 3.8. Using equation 16 (page 57) we are using the W MC to get a bin-by-bin or universal but jet multiplicity dependent correction via the quotient of the pre-simulation hadron level based jets with the normal detector reconstructed (via full simulation) jets. As a result, our systematic is primarily limited to the Poisson random fluctuation of the components of the ratio to form our unfolding fraction u.

In addition, we use an averaged unfolding fraction (as described in section 3.9) when we have a relative flat distribution. As a result, our unfolding systematic on our cross-sections,  $\Delta \sigma$ , is calculated using one of the two  $\Delta u$  calculation. In the case of a bin-by-bin unfolding (e.g. jet  $p_T$ ) we use equation 17 for  $\Delta u$  and derive our cross-section systematic uncertainty for the unfolding as

$$\Delta \sigma = \sigma \Delta u = \sigma \sqrt{\left(\frac{\Delta \sigma_{HAD}}{\sigma_{HAD}}\right)^2 + \left(\frac{\Delta \sigma_{CAL}}{\sigma_{CAL}}\right)^2}$$
 (74)

with  $\sigma$  being our final cross-section measurement (bin-by-bin for our analysis observables as appropriate) using the calorimeter based cross-section via the data with the unfolding fraction, u, applied. Similarly, we apply equation ?? using  $\Delta u$  to obtain our systematic when the unfolding is consistent with 0-slope line of order unity:

$$\Delta \sigma = \sigma \bar{\Delta u} \tag{75}$$

In either case, we will signify our unfolding systematic from the others in this chapter via  $\Delta_u \equiv \Delta \sigma$  using equation 74 or 75 as appropriate.

We observe in passing that since  $\sigma_{HAD}$  and  $\sigma_{CAL}$  are psudeo-cross-sections (their acceptances are not calculated as they are by definition equal and will cancel) they really amount to a number of events in each bin for each jet definition. Thus the relative error for the terms effectively goes as the square root of one over the number of events  $(1/\sqrt{N})$ . On a different note, there are no observables that we deem (based on their behavior) needing an additional shape systematic. Thus, we are ignoring potential correlations and dependence at this stage and hence the uncertainty in  $\Delta_{\rm u}$  is being taken simply in quadrature. Since the unfolding fraction, u or  $\bar{u}$  is a ratio we regard this as a conservative estimation. However, we do consider and factor in possible correlations with the jet energy scale correction systematic in the next section.

### 6.9 Systematics Combination and Correlated Systematics Treatment

The focus of this section is to describe the treatment of combining our systematics. The procedure here will give us our final total systematic error. There are actually two different

concerns here. The first is that for a given differential cross-section we want to account for nondiagonal terms in our error matrix. The second issue is when we normalize our cross-sections or otherwise take ratios between two of them (e.g.  $\sigma_{n+1}/\sigma_n$  of section 7.3). The resulting quotients can have rather substantial and intentional correlations that need to be accounted for.

For convenience we will denote these two concerns via the following short hand. Let f be a differential cross-section given by

 $f = \frac{\mathrm{d}\sigma}{\mathrm{d}X} \tag{76}$ 

With respect to our normalized cross-sections we refer to these as  $f/\sigma$  where this is understood as

$$\frac{f}{\sigma} = \frac{f}{\sigma_n} = \frac{\mathrm{d}\sigma/\mathrm{d}X}{\mathrm{d}\sigma/\mathrm{d}n} \tag{77}$$

where  $d\sigma/dn$  is the jet multiplicity cross-section via the notation of section 7.2. As noted previously there are also two observables (the afore mentioned  $\sigma_{n+1}/\sigma_n$  and  $r_{\Delta\eta}$  of section 7.7) that are effectively ratios of full differential cross-sections. We will note these special considerations later in this section.

For the most part systematics are done in such a way as to minimize any directly "induced" correlation. In addition, we have directly investigated the potential interplay of our systematics in the proceeding sections save the one mentioned at the end of the previous section. For example, when varying the  $t\bar{t}$  cross-section (see section 6.6) we effectively repeat the analysis and allow for a different background fitting and this is independent of our background fitting systematic (section 6.5). The jet energy scale (JES) systematic also has this feature of being independent of the background systematic and we even recalculate the acceptance when coming up with our  $\sigma_{\pm}$  (see section 6.7, equation 70). Likewise, our vertex reweighting scheme of section 6.4 accounted for the potential interplay when we would refit our background estimations after applying the last iterations of weights. We also observed that varying the jet energy scale even in the highest jet multiplicities had a <0.2% effect on our MC vertex weight calculation.

The one combination of systematics that we would expect full correlation (more precisely full anti-correlation) and have not addressed is in the unfolding factor being applied with the jet energy scale. This follows as the jet energy scale effects our calorimeter based cross-section and in our unfolding via the MC (see equation 16 on page 57). A similar correlation was internally address for our background fitting estimation systematic which had our fitting fractions completely correlated due to their sum being unity. Taking all the other systematics as uncorrelated we have the total (bin-by-bin) systematic uncertainty,  $\Delta f$ , as

$$\Delta f = \sqrt{\Delta_{\text{Lum}}^2 + \Delta_{\text{Vtx}}^2 + \Delta_{\text{PDF}}^2 + \Delta_{\text{FSR}}^2 + \Delta_{\text{Fit}}^2 + \Delta_{\text{Top}}^2 + (\Delta_{\text{JES}} - \Delta_{\text{u}})^2}$$
 (78)

Here we have denoted the various error components of  $\Delta f$  as  $\Delta_{\rm sys}$  for each systematic, sys  $\in$  {Lum, Vtx, PDF, FSR, Fit, Top, JES, u} via each of the proceeding section of this chapter. The mapping of the systematics is straightforward. The key here is that we have accounted for the effect of the anti-correlation between the jet energy scale (JES) and the unfolding (u) in equation 78 while the remaining systematic errors are taken in quadrature.

We now consider  $\Delta(f/\sigma)$  the error for our differential cross-sections normalized to the relevant inclusive jet multiplicity cross-section. Technically we are still applying the resulting ratio  $(f/\sigma)$ 

to the basic formulation of equation 78 but now we have to consider the total correlation of the same systematics. For example, the jet energy scale systematics for the jet multiplicity for  $\geq 1$  cross-section  $(\sigma_1)$  will obviously correlate (positively) with the first leading jet  $p_T$  cross-section  $(d\sigma_1/dp_T^{1st})$ .

We calculate the uncertainty for a given systematic by varying both numerator and dominator together and noting the difference. Let  $\Delta f$  be the systematic uncertainty on the differential cross-section for a given systematic and like wise for  $\Delta \sigma$  for the jet multiplicity cross-section. The the uncertainty on the quotient,  $\Delta(f/\sigma)$ , goes as

$$\Delta\left(\frac{f}{\sigma}\right) = \frac{1}{2} \left| \frac{f + \Delta f}{\sigma + \Delta \sigma} - \frac{f - \Delta f}{\sigma - \Delta \sigma} \right| \tag{79}$$

which can also be written in terms of an absolute difference between the relative errors:

$$\Delta\left(\frac{f}{\sigma}\right) = \left(\frac{f/\sigma}{1 - (\Delta\sigma/\sigma)^2}\right) \left|\frac{\Delta f}{f} - \frac{\Delta\sigma}{\sigma}\right| \tag{80}$$

The latter equation without the  $(\Delta \sigma/\sigma)^2$  term would be identical to the case where we have 100% negative correlation. Once  $\Delta(f/\sigma)$  has been calculated for all systematics via equation 79 we then treat the measurement as we did in equation 78. We note, as advertised in section 6.1 that the pure luminosity systematic will completely cancel since there is no dependence jet multiplicity or otherwise. As a result,  $\Delta_{\text{Lum}}$  will uniformly negated in our (bin-by-bin) relative error. The acceptance related systematics will also cancel out if the differential cross-section (f) and  $(\sigma)$  are of the same jet multiplicity. This is true for our PDF, FSR (if applicable), and vertex reweighting (Vtx). An example where acceptance does not go to zero is  $(d\sigma/dn)/\sigma_0$  for the  $n \neq 0$  bins.

The are two additional ratio measurements that we make that we will note in passing. First the  $\sigma_{n+1}/\sigma_n$  and secondly  $r_{\Delta\eta}$ . It turns out that the basic solution is to follow the procedure outline above (using equation 79) by noting that now the dominator caries a bin-by-bin error rather than a flat error to be compared to the nominator bin-by-bin. Let us define f and g to be differential cross-sections with the same basic observable and histogram binning. Furthermore, let  $\Delta f$  and  $\Delta g$  be their respected error for a given systematic. We account for the systematic uncertainty in f/g via  $\Delta(f/g)$  defined by

$$\Delta\left(\frac{f}{g}\right) = \frac{1}{2} \left| \frac{f + \Delta f}{g + \Delta g} - \frac{f - \Delta f}{g - \Delta g} \right| \tag{81}$$

We then combine the systematics as normal via equation 78.

On a final note when dealing with potentially asymmetric systematic errors (such as the jet energy) we always check to guarantee that the positive and negative errors bracket the central value. In the rare cases where this is not the case we revert to the procedure use for the jet energy scale using equations 71 and 72 where  $\sigma_{\pm}$  are the respective upper and bottom limit for the error bar.

### 6.10 Relative Systematic Uncertainties

In this section we present our systematic uncertainties for each cross-section distribution (see the next chapter). In these plots the systematic uncertainties are presented as the relative error to the cross-section measurement (i.e.  $\Delta \sigma/\sigma$ ). We do this across the range of the observable in question (e.g.  $m_{jj}$  for  $d\sigma/dm_{jj}$ ) to show the potential bin-by-bin dependence. The total systematic (which is potentially asymmetric) is added together via the prescription in the previous section and this systematic (absent the luminosity which is held separate) is then present in our final cross-section plots which are detailed in the next section. Appendix A will feature this total systematic uncertainty in table form.

As noted in section 6.1, the luminosity error is not shown due to it having no dependence variable. For a similar reason, we also omit the global systematic we apply via our vertex reweighting in section 6.4 and likewise for FSR (assuming it is applicable). We do include the acceptance error (denoted as **Acceptance**) via our PDF,  $\alpha_S$ , and efficiency uncertainties as described section 6.2 which only has a jet multiplicity dependence but is otherwise flat in our jet kinematic related differential cross-sections. We reiterate that these last four systematics completely cancel out in many of our ratio cross-section/observables or reduced cross-sections (see section 7.1).

For comparison, we include the natural random uncertainty in the bin-by-bin sample size and denote this as the **Poission** error. The background fitting systematic of section 6.5 will be noted as **Background**. The other background systematic comes from the  $t\bar{t}$  cross-section of section 6.6 which we label as  $t\bar{t}$   $\sigma$ (**Theory**). The jet energy scale systematic discussed in section 6.7 we refer to as **Jet Energy**. Finally the unfolding systematic from section 6.8 is unimaginatively called **Unfolding**.

Our relative systematic uncertainties or, more simply, our relative errors start at figure 214 and end at figure 257. Rather than write out a description of each figure in detail we provide a mapping via table 61 for our relative errors with respect to their corresponding cross-sections. The Cross-section and Section columns of the table describe the differential cross-section (or ratio of) and its corresponding section in the next chapter. Table 61 then provides the relative error plot's figure number (#) and then its associated cross-section. The third and fourth columns are for the electrons results while the latter two are for the muons. There are no direct systematic error plots corresponding with the results of figures 282 through 289 as these are identical to our normalized results for  $d\sigma/dp_T^{\rm nth}$ . In other words, figures 228-235 map to 282-289, correspondingly.

		$W \to e\nu$	$W \to e\nu$	$W \to \mu\nu$	$W \to \mu\nu$
Cross-section	Section #	$\Delta\sigma/\sigma$	$\sigma$	$\Delta \sigma / \sigma$	$\sigma$
	,,	/	Figure #	Figure #	Figure #
$\frac{\mathrm{d}\sigma}{\mathrm{d}n}$	7.2	214	260	215	261
$\frac{\sigma_n}{\sigma_0}$	7.2	216	262	217	263
$\frac{\sigma_{n+1}}{\sigma_n}$	7.3	218	264	219	265
$\frac{\mathrm{d}\sigma}{\mathrm{d}p_T^{1st}}$	7.4	220	266	224	270
$\frac{\mathrm{d} p_T^{}}{\mathrm{d} p_T^{2nd}}$	7.4	221	267	225	271
$\frac{\mathrm{d}\sigma}{\mathrm{d}p_T^{3rd}}$	7.4	222	268	226	272
$\frac{\mathrm{d}\sigma}{\mathrm{d}p_T^{4th}}$	7.4	223	269	227	273
$\frac{\mathrm{d}\sigma/\mathrm{d}p_T^{1^{st}}}{\sigma}$	7.4	228	274	232	278
$\frac{\mathrm{d}\sigma/\mathrm{d}p_T^{2^{nd}}}{\sigma_2}$	7.4	229	275	233	279
$\frac{\mathrm{d}\sigma/\mathrm{d}p_T^{3^{rd}}}{\sigma_3}$	7.4	230	276	234	280
$\frac{\mathrm{d}\sigma/\mathrm{d}p_T^{4^{th}}}{\sigma_4}$	7.4	231	277	235	281
$\frac{\mathrm{d}\sigma}{\mathrm{d}m_{ij}}$	7.5	236	290	237	291
$\frac{\mathrm{d}\sigma/\mathrm{d}m_{jj}}{\sigma_2}$	7.5	238	292	239	293
$d\sigma$	7.6	240	294	241	295
$\frac{\mathrm{d} \overline{\mathrm{d}}_{jj}}{\mathrm{d} \sigma/\mathrm{d} R_{jj}} = \frac{\mathrm{d} \sigma/\mathrm{d} R_{jj}}{\sigma_2}$	7.6	242	296	243	297
$\frac{\mathrm{d}\sigma_2}{\mathrm{d}\Delta\eta}$	7.7	244	298	245	299
$\frac{\mathrm{d}\sigma_2/\mathrm{d}\Delta\eta}{\sigma^2}$	7.7	246	300	247	301
$\frac{\mathrm{d}\sigma_3}{\mathrm{d}\Delta\eta}$	7.7	248	302	249	303
$\frac{\mathrm{d}\sigma_3/\mathrm{d}\Delta\eta}{\sigma_3}$	7.7	250	304	251	305
$r_{\Delta\eta} \text{ (Eq. 86)}$	7.7	252	306	253	307
$d\sigma$	7.8	254	308	255	309
$\frac{\overline{\mathrm{d}\eta^*}}{\mathrm{d}\sigma/\mathrm{d}\eta^*}$	7.8	256	310	257	311

Table 61: The mapping of each relative error  $(\Delta \sigma/\sigma)$  figure with its corresponding cross-section  $(\sigma)$  figure for each cross-section observable

# pet multiplicity of W event via electron 0.45 Poisson Background It (Theory) Acceptance Promotion Juntolding 0.35 0.1 0.05 0 1 2 3 4 ≥ n jets

Figure 214: Relative Errors for  $W \to e \nu$  jet multiplicity (companion of Fig. 260)

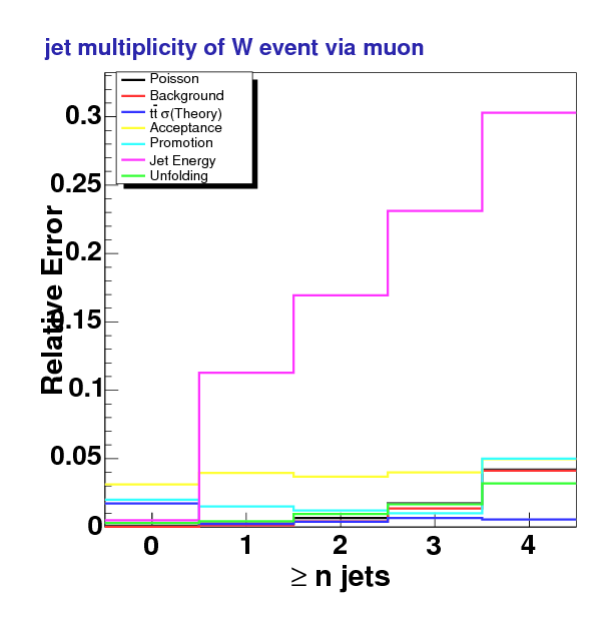


Figure 215: Relative Errors for  $W \to \mu \nu$  jet multiplicity (companion of Fig. 261)

# 

Figure 216: Relative Errors for  $W \to e \nu$  jet multiplicity (companion of Fig. 262)

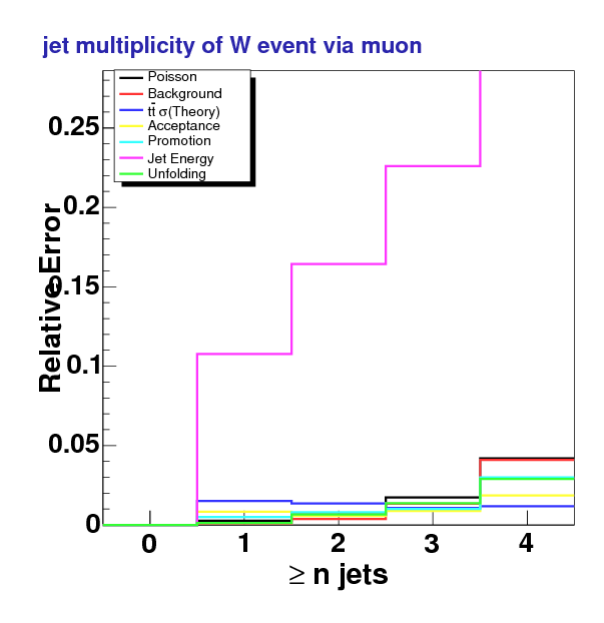


Figure 217: Relative Errors for  $W \to \mu \nu$  jet multiplicity (companion of Fig. 263)

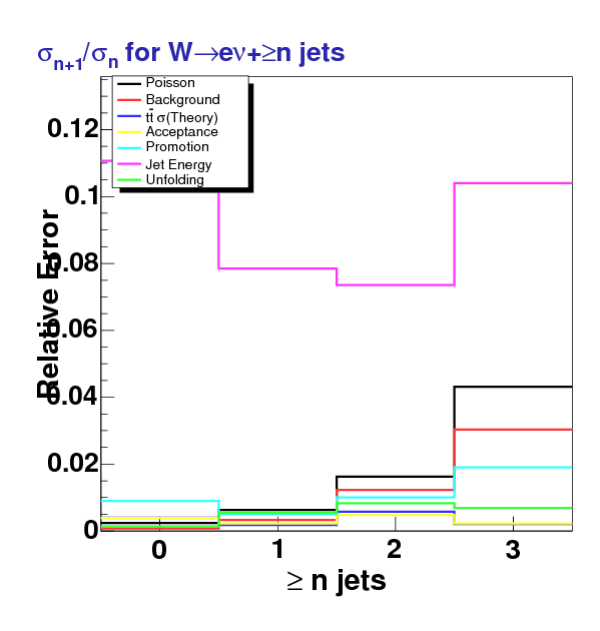


Figure 218: Relative Errors for  $W \to e\nu \ \sigma_{n+1}/\sigma_n$  (companion of Fig. 264)

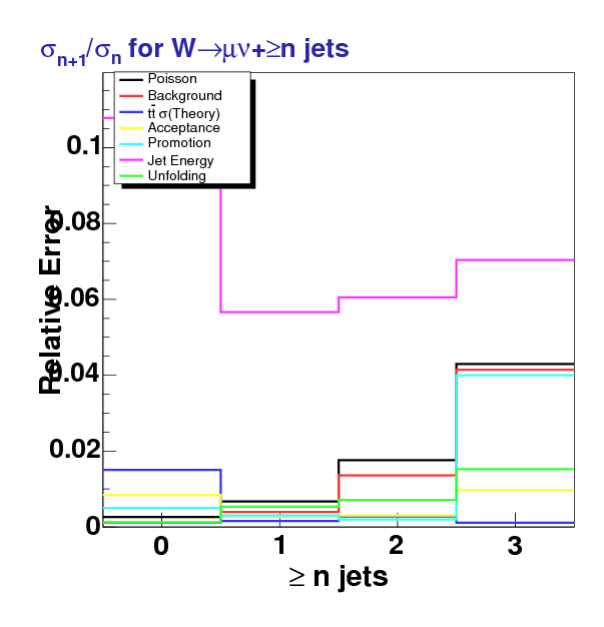


Figure 219: Relative Errors for  $W \to \mu\nu~\sigma_{n+1}/\sigma_n$  (companion of Fig. 265)

# jet p<sub>T</sub> for leading jet with electron via W 0.2 Poisson Background it or(Theory) 0.18 Promotion Jet Energy 0.16 Promotion Jet Energy 0.10 12 Poisson 0.16 Poisson Background O.16 Poisson Background O.17 Poisson O.18 Poisson O

Figure 220: Relative Errors for Leading jet  $p_T$  for  $W \to e\nu + \geq 1$  jet (companion of Fig. 266)

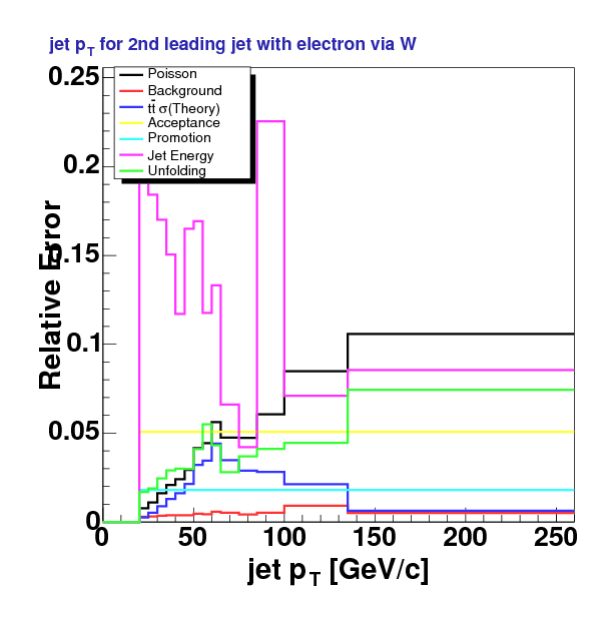


Figure 221: Relative Errors for  $2^{nd}$  leading jet  $p_T$  for  $W \to e\nu + \geq 2$  jets (companion of Fig. 267)

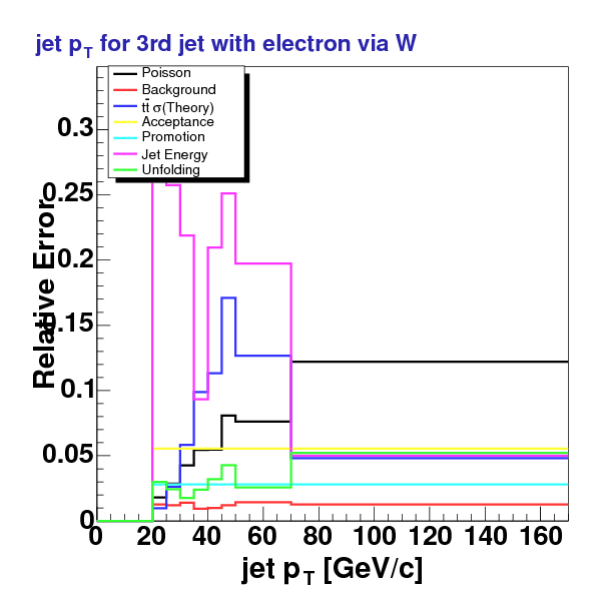


Figure 222: Relative Errors for  $3^{rd}$  leading jet  $p_T$  for  $W \to e\nu + \geq 3$  jets (companion of Fig. 268)

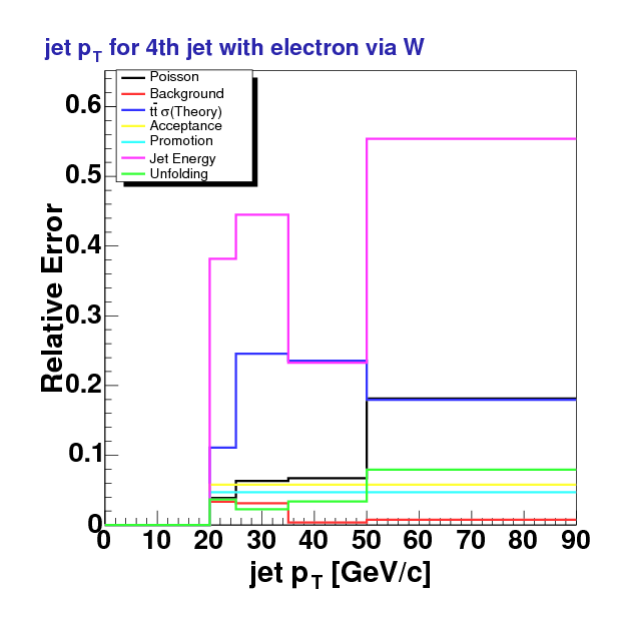


Figure 223: Relative Errors for  $4^{th}$  leading jet  $p_T$  for  $W \to e\nu + \geq 4$  jets (companion of Fig. 269)

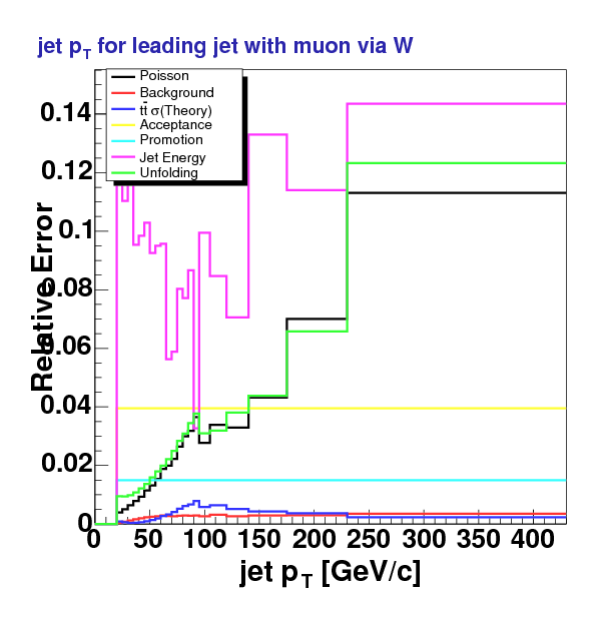


Figure 224: Relative Errors for Leading jet  $p_T$  for  $W \to \mu\nu + \geq 1$  jet (companion of Fig. 270)

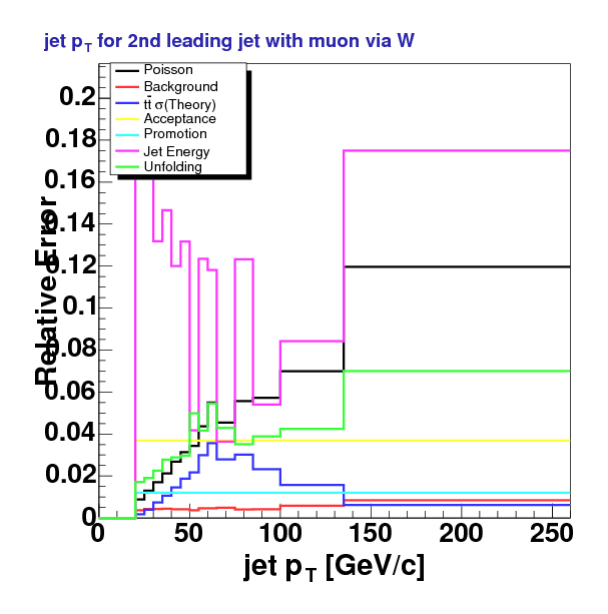


Figure 225: Relative Errors for  $2^{nd}$  leading jet  $p_T$  for  $W \to \mu\nu + \geq 2$  jets (companion of Fig. 271)

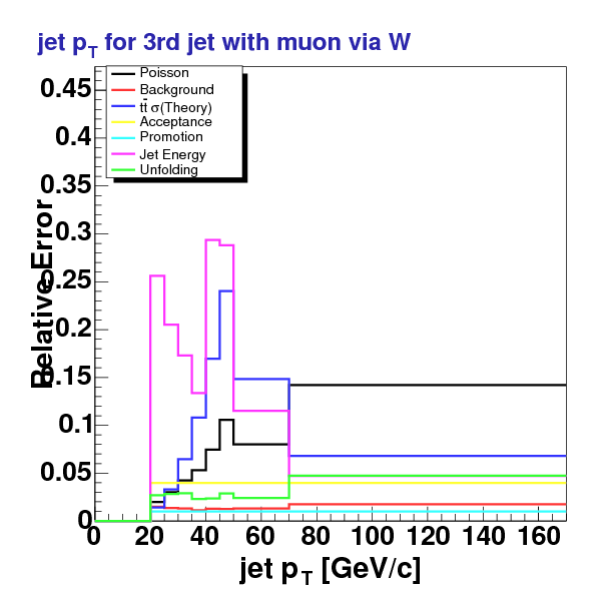


Figure 226: Relative Errors for  $3^{rd}$  leading jet  $p_T$  for  $W \to \mu\nu + \geq 3$  jets (companion of Fig. 272)

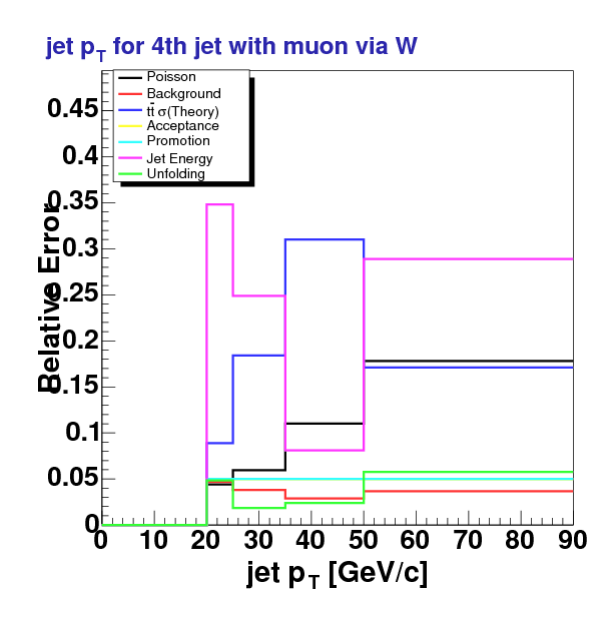


Figure 227: Relative Errors for  $4^{th}$  leading jet  $p_T$  for  $W \to \mu\nu + \geq 4$  jets (companion of Fig. 273)

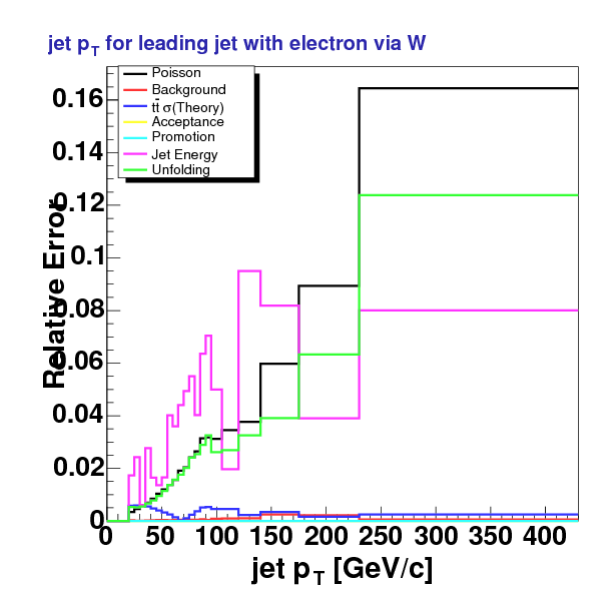


Figure 228: Relative Errors for Leading jet  $p_T$  for  $W \to e\nu + \geq 1$  jet (companion of Fig. 274)

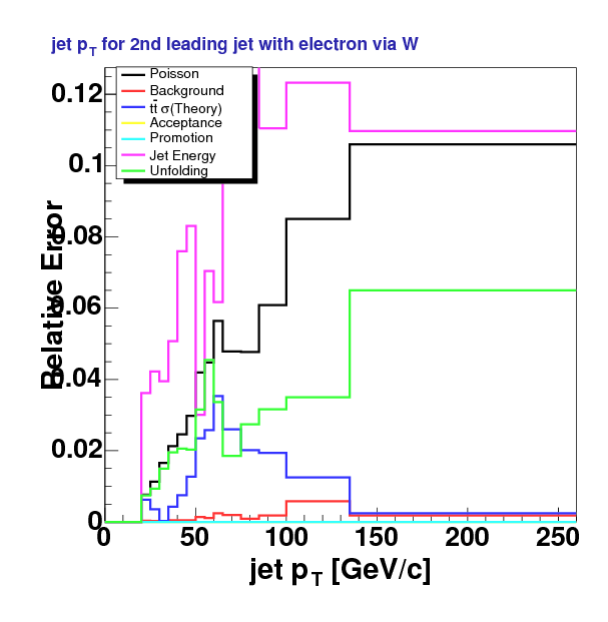


Figure 229: Relative Errors for  $2^{nd}$  leading jet  $p_T$  for  $W \to e\nu + \geq 2$  jets (companion of Fig. 275)

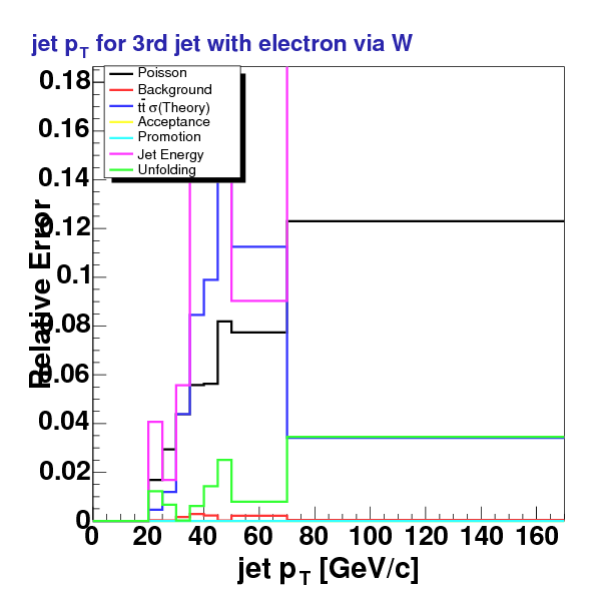


Figure 230: Relative Errors for  $3^{rd}$  leading jet  $p_T$  for  $W \to e\nu + \geq 3$  jets (companion of Fig. 276)

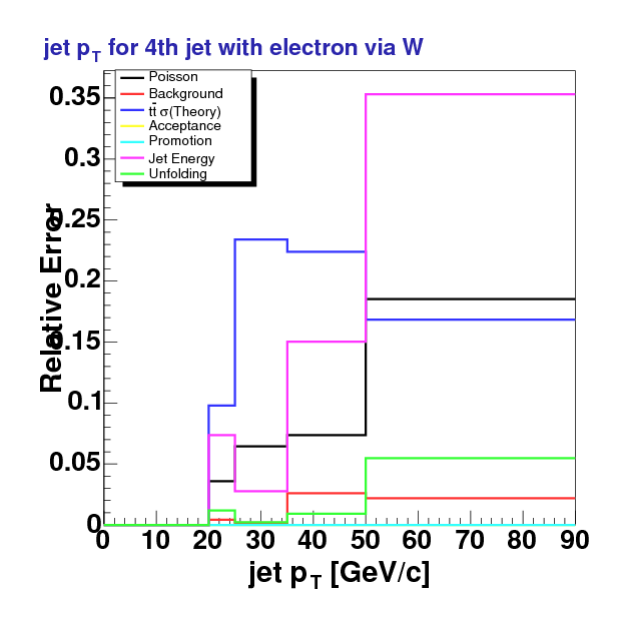


Figure 231: Relative Errors for  $4^{th}$  leading jet  $p_T$  for  $W \to e\nu + \geq 4$  jets (companion of Fig. 277)

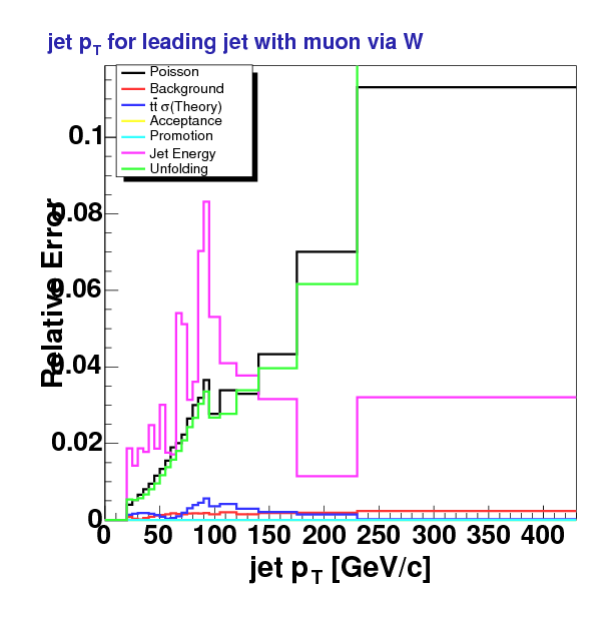


Figure 232: Relative Errors for Leading jet  $p_T$  for  $W \to \mu\nu + \geq 1$  jet (companion of Fig. 278)

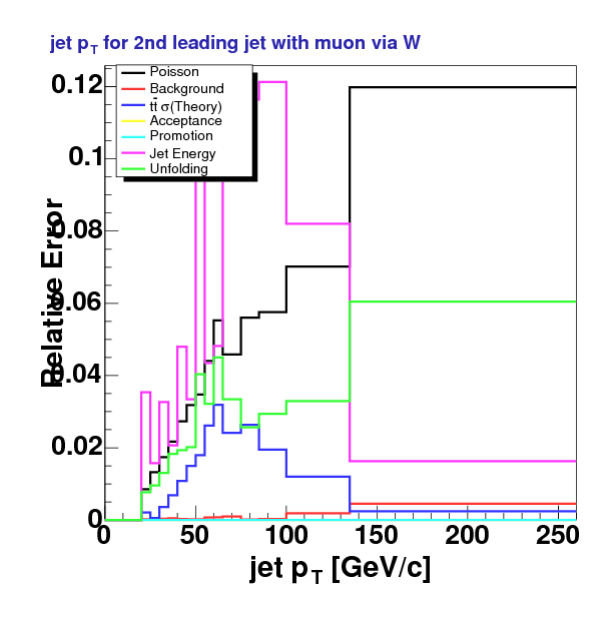


Figure 233: Relative Errors for  $2^{nd}$  leading jet  $p_T$  for  $W \to \mu\nu + \geq 2$  jets (companion of Fig. 279)

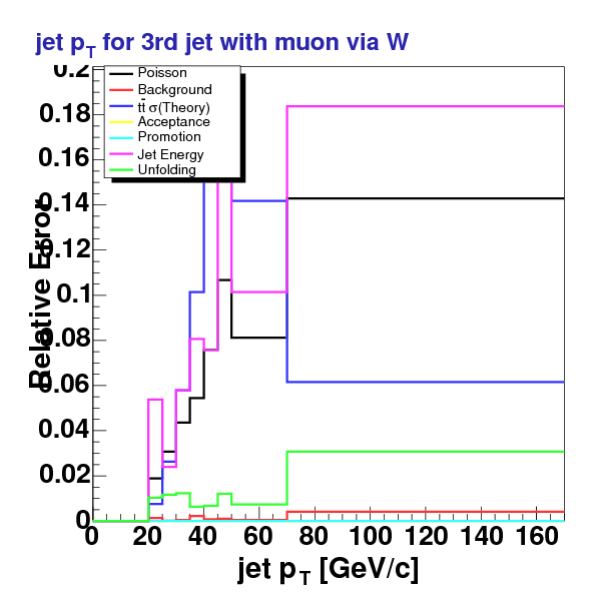


Figure 234: Relative Errors for  $3^{rd}$  leading jet  $p_T$  for  $W \to \mu\nu + \geq 3$  jets (companion of Fig. 280)

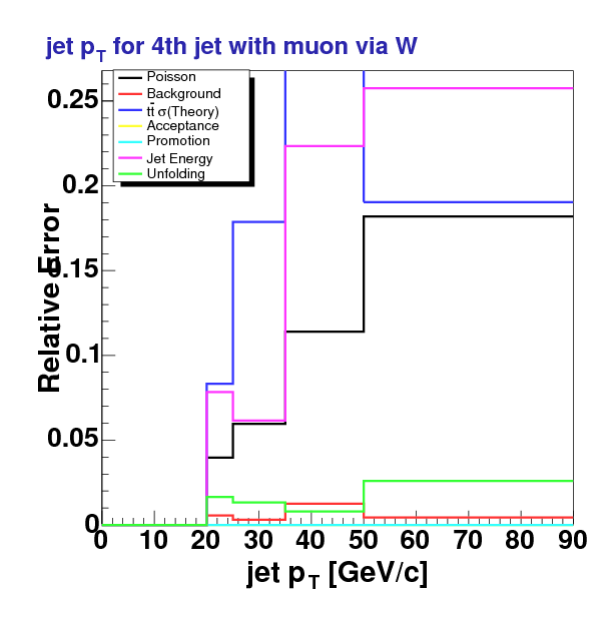


Figure 235: Relative Errors for  $4^{th}$  leading jet  $p_T$  for  $W \to \mu\nu + \geq 4$  jets (companion of Fig. 281)

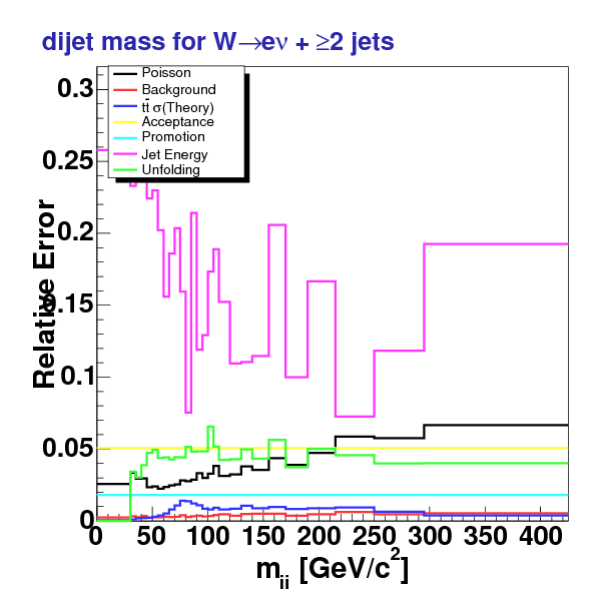


Figure 236: Relative Errors for Dijet Mass Cross-section for  $W \to e\nu + \geq 2$  jets (companion of Fig. 290)

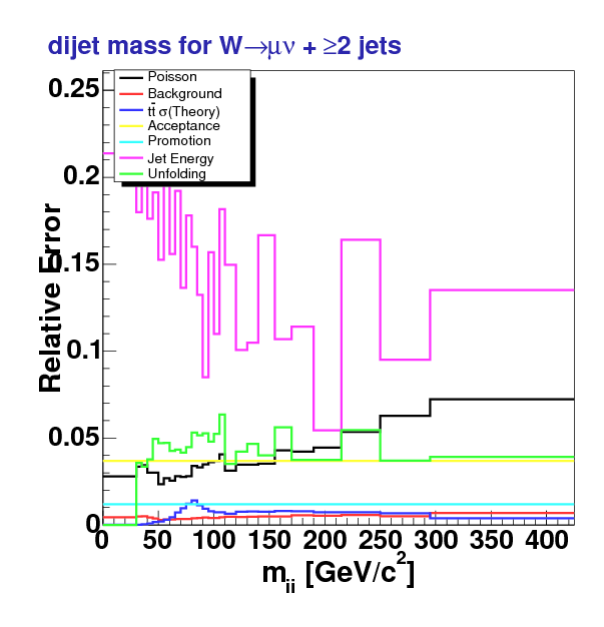


Figure 237: Relative Errors for Dijet Mass Cross-section for  $W \to \mu\nu + \geq 2$  jets (companion of Fig. 291)

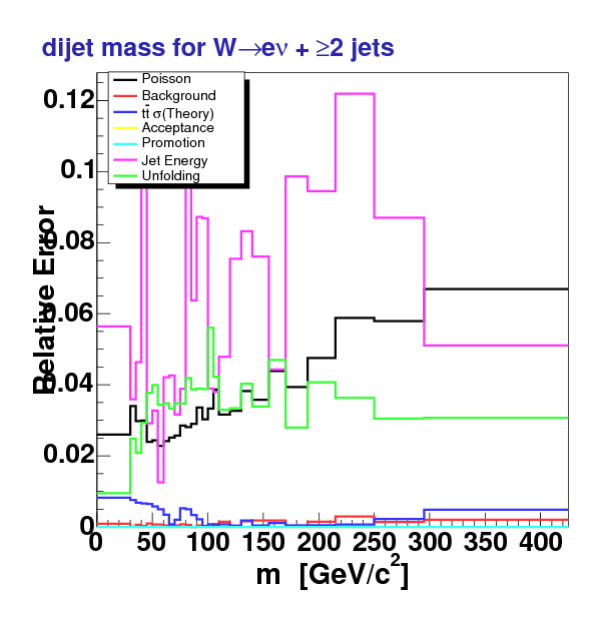


Figure 238: Relative Errors for Dijet Mass Cross-section for  $W \to e\nu + \geq 2$  jets (companion of Fig. 292)

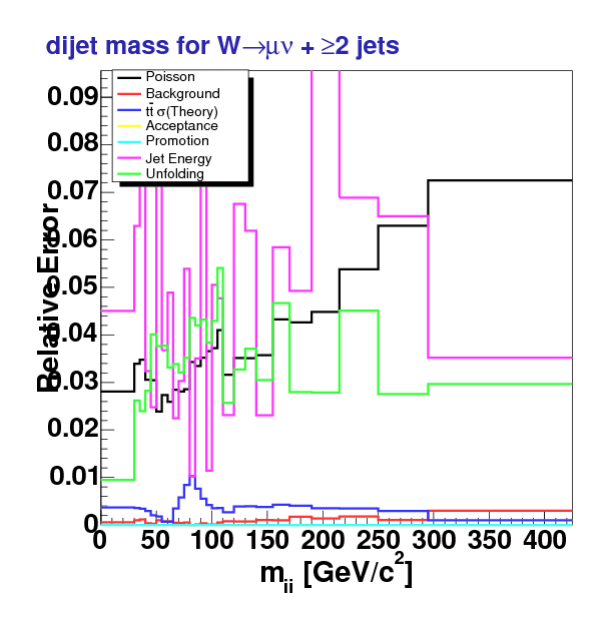


Figure 239: Relative Errors for Dijet Mass Cross-section for  $W \to \mu\nu + \geq 2$  jets (companion of Fig. 293)

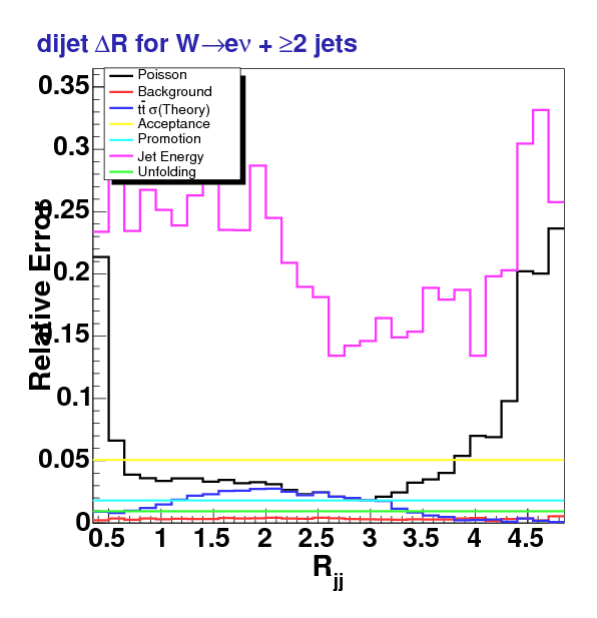


Figure 240: Relative Errors for Dijet Separation Cross-section for  $W \to e\nu + \geq 2$  jets (companion of Fig. 294)

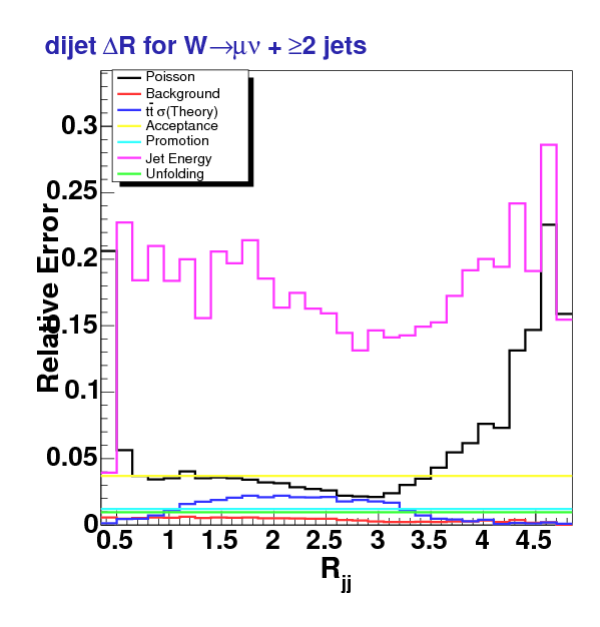


Figure 241: Relative Errors for Dijet Separation Cross-section for  $W\to \mu\nu+\geq 2$  jets (companion of Fig. 295)

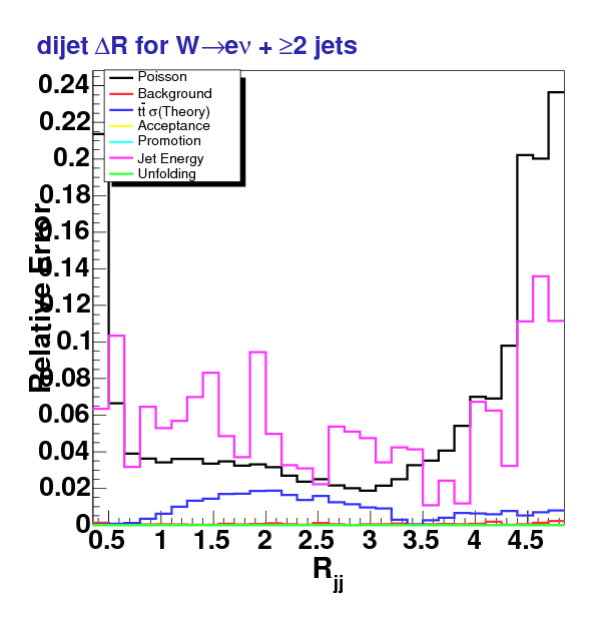


Figure 242: Relative Errors for Dijet Separation Cross-section for  $W \to e\nu + \geq 2$  jets (companion of Fig. 296)

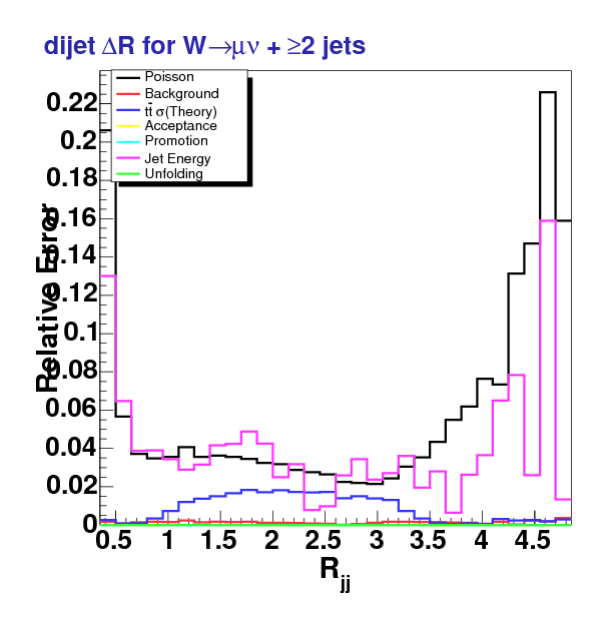


Figure 243: Relative Errors for Dijet Separation Cross-section for  $W \to \mu\nu + \geq 2$  jets (companion of Fig. 297)

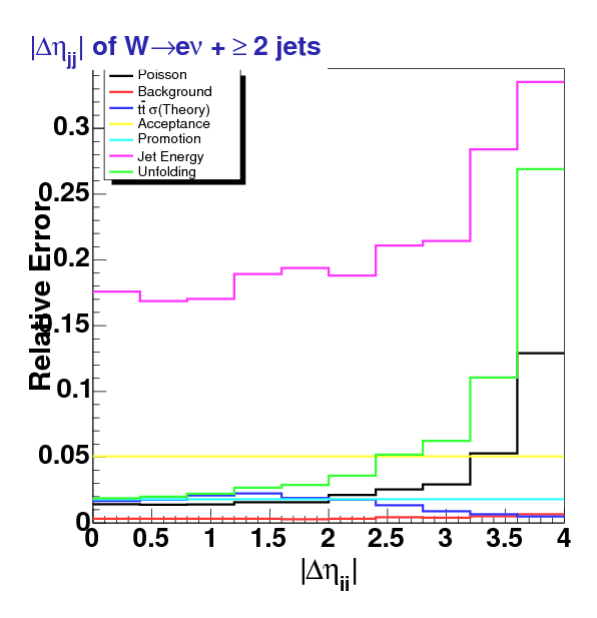


Figure 244: Relative Errors for  $\Delta \eta$  Cross-section for  $W \to e\nu + \geq 2$  jets (companion of Fig. 298)

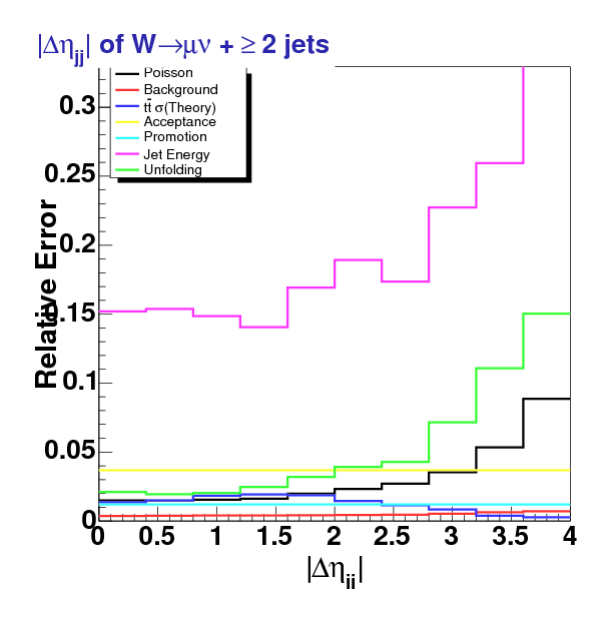


Figure 245: Relative Errors for  $\Delta \eta$  Cross-section for  $W \to \mu \nu + \geq 2$  jets (companion of Fig. 299)

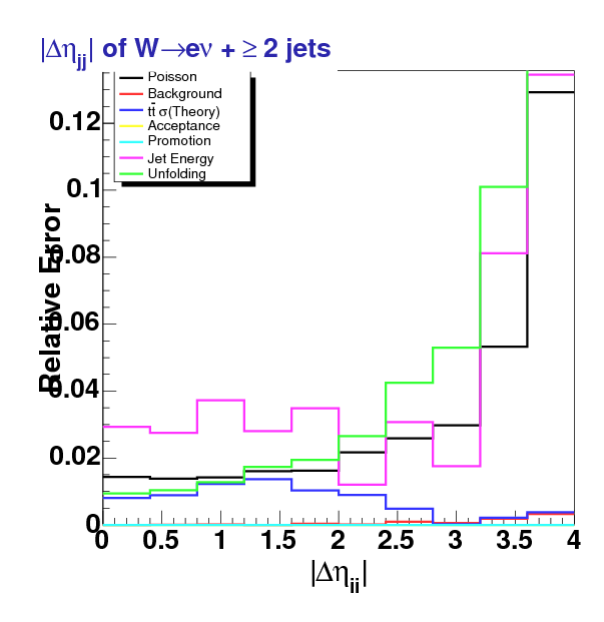


Figure 246: Relative Errors for  $\Delta \eta$  Cross-section for  $W \to e\nu + \geq 2$  jets (companion of Fig. 300)

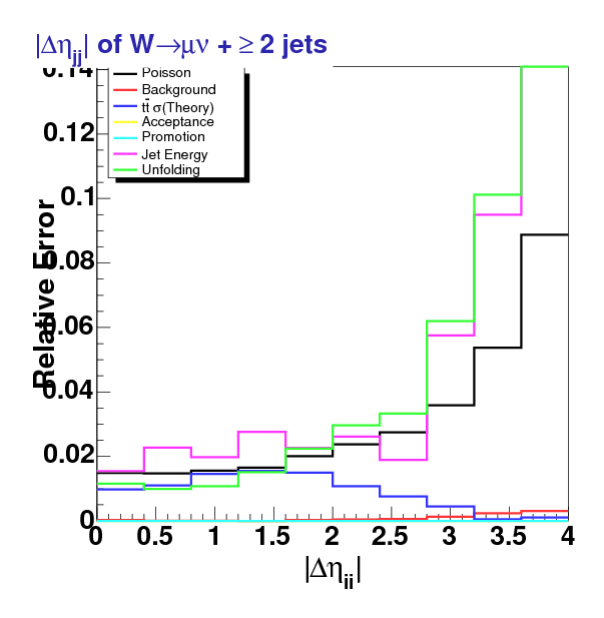


Figure 247: Relative Errors for  $\Delta \eta$  Cross-section for  $W \to \mu \nu + \geq 2$  jets (companion of Fig. 301)

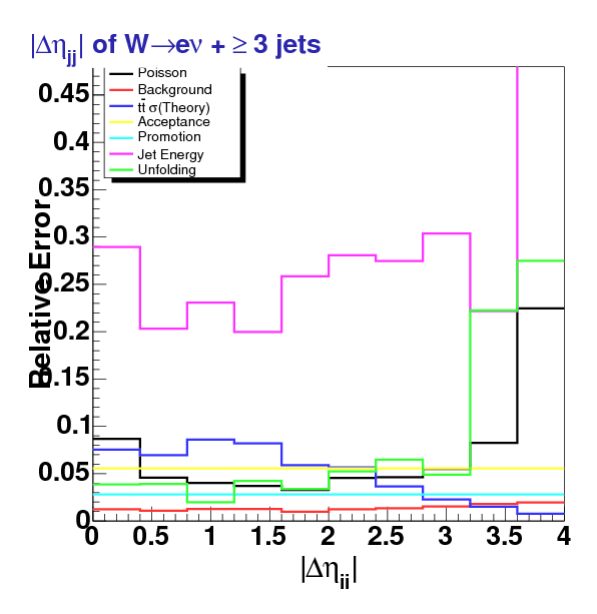


Figure 248: Relative Errors for  $\Delta \eta$  Cross-section for  $W \to e\nu + \geq 3$  jets (companion of Fig. 302)

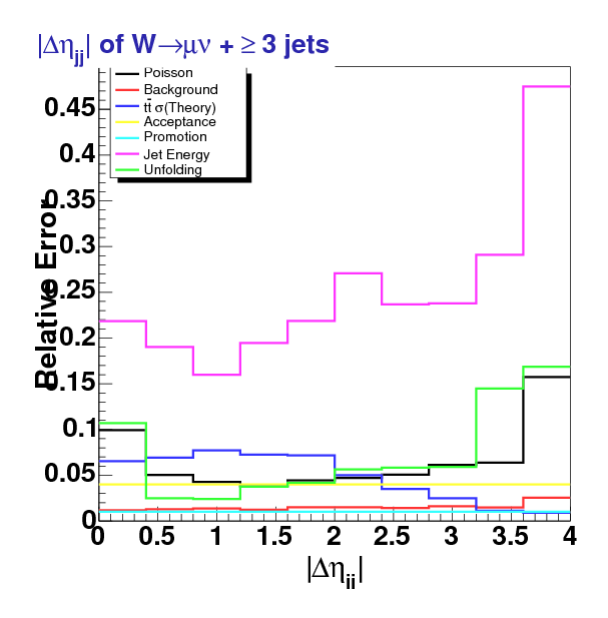


Figure 249: Relative Errors for  $\Delta \eta$  Cross-section for  $W \to \mu \nu + \geq 3$  jets (companion of Fig. 303)

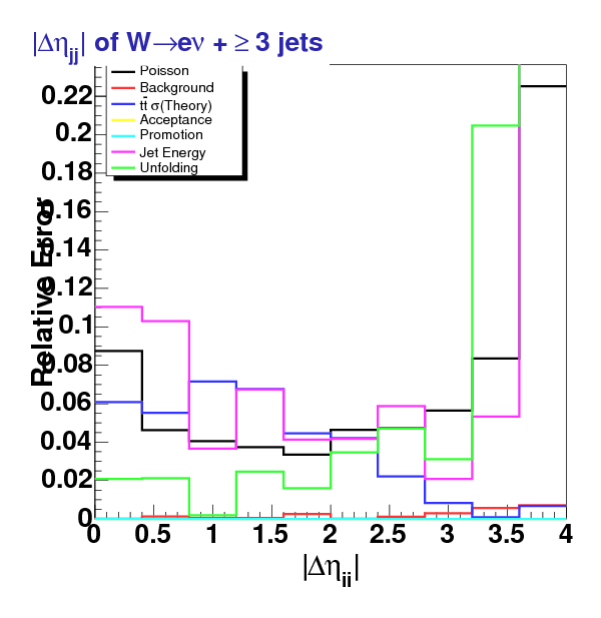


Figure 250: Relative Errors for  $\Delta \eta$  Cross-section for  $W \to e\nu + \geq 3$  jets (companion of Fig. 304)

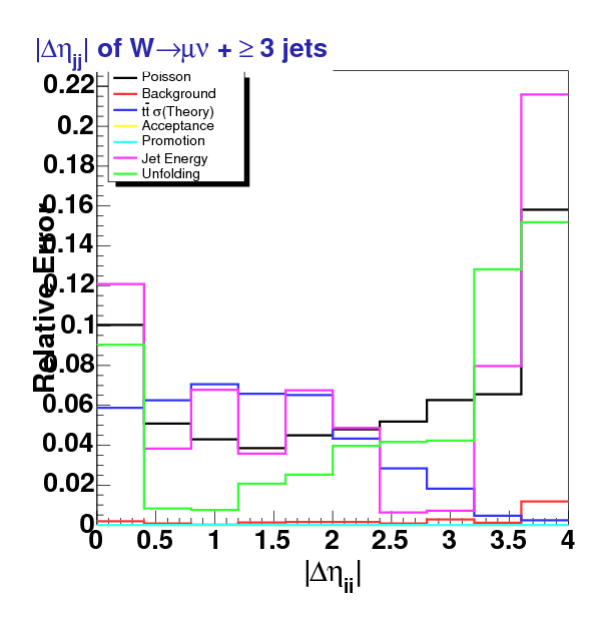


Figure 251: Relative Errors for  $\Delta \eta$  Cross-section for  $W \to \mu \nu + \geq 3$  jets (companion of Fig. 305)

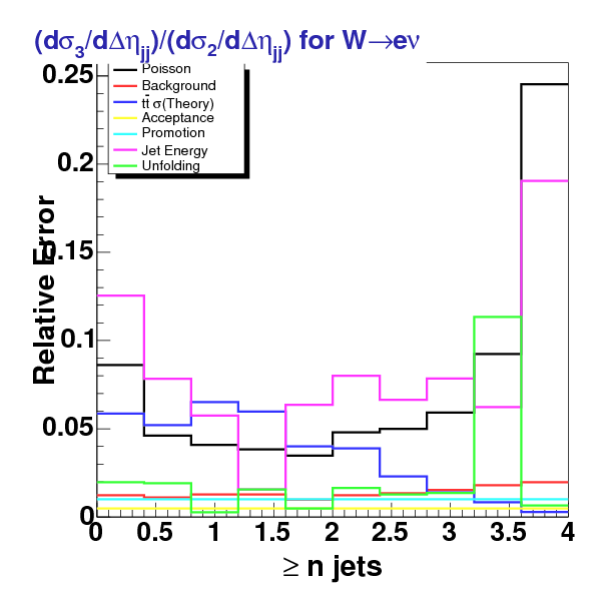


Figure 252: Relative Errors for  $\Delta \eta$  Cross-section for  $W \to e\nu + \geq 3$  jets (companion of Fig. 306)

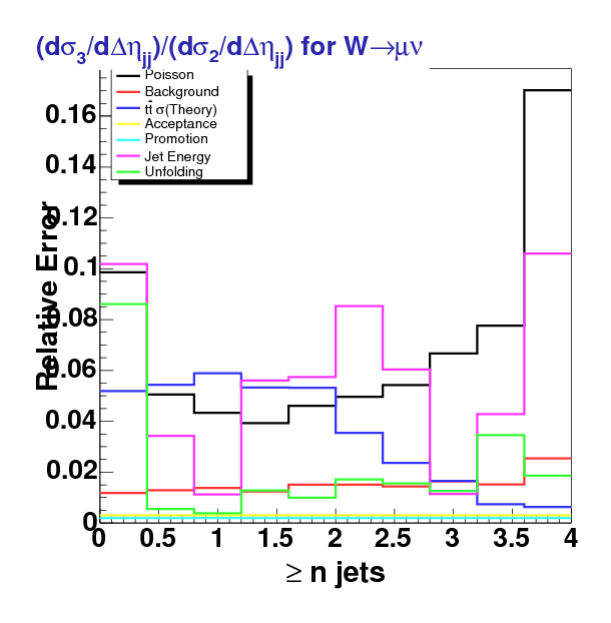


Figure 253: Relative Errors for  $\Delta \eta$  Cross-section for  $W \to \mu \nu + \geq 3$  jets (companion of Fig. 307)

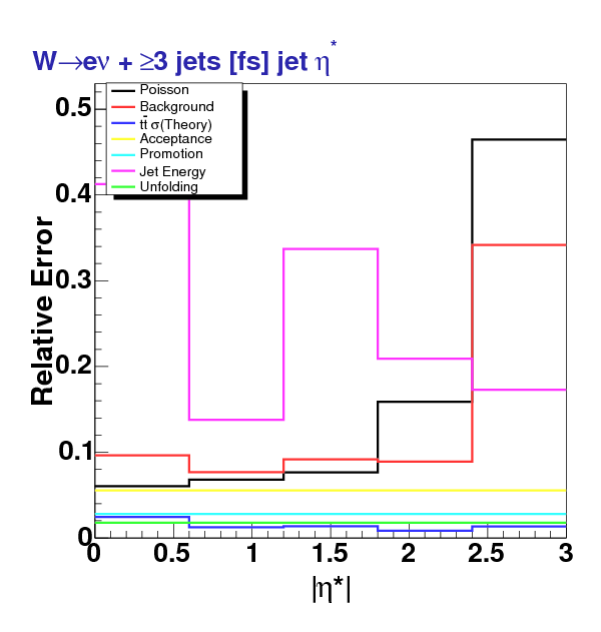


Figure 254: Relative Errors for  $|\eta^*|$  Cross-section for  $W \to e\nu + \geq 3$  jets with  $\Delta \eta_{jj} > 2.0$  (companion of Fig. 308)

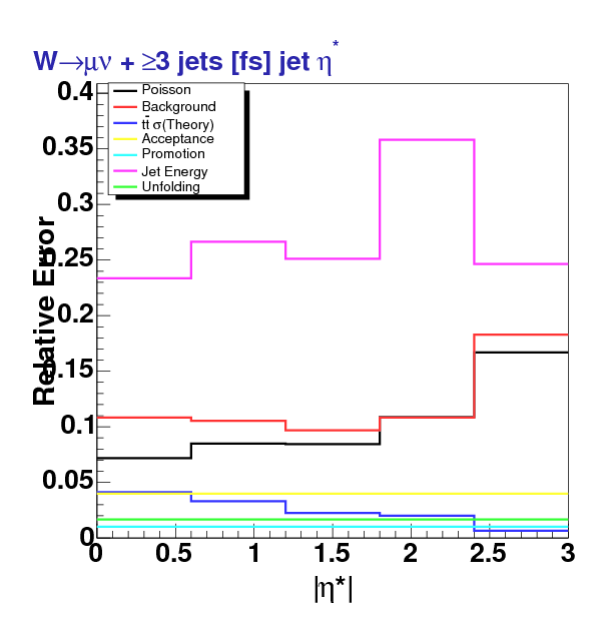


Figure 255: Relative Errors for  $|\eta^*|$  Cross-section for  $W \to \mu\nu + \geq 3$  jets with  $\Delta \eta_{jj} > 2.0$  (companion of Fig. 309)

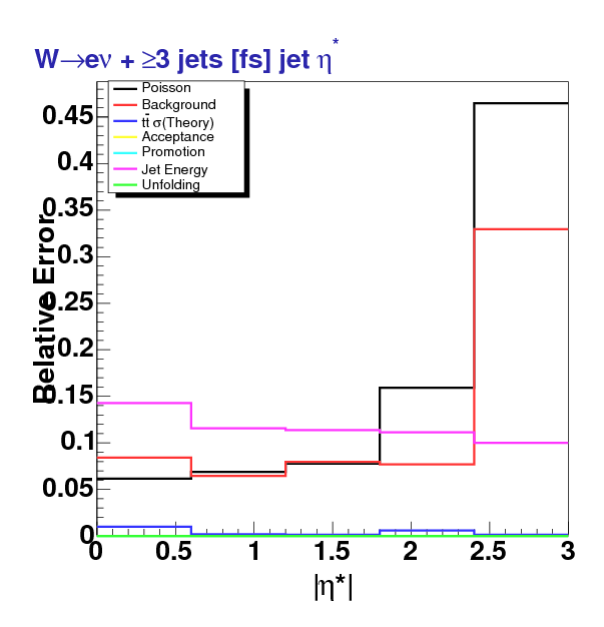


Figure 256: Relative Errors for  $|\eta^*|$  Cross-section for  $W \to e\nu + \geq 3$  jets with  $\Delta \eta_{jj} > 2.0$  (companion of Fig. 310)

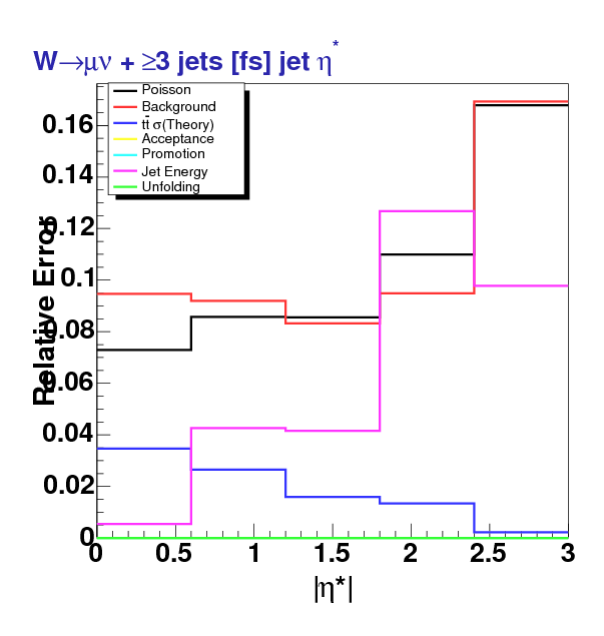


Figure 257: Relative Errors for  $|\eta^*|$  Cross-section for  $W\to \mu\nu+\geq 3$  jets with  $\Delta\eta_{jj}>2.0$  (companion of Fig. 311)

# 7 Results

In this chapter we present our final results. These include various differential cross-sections for jet kinematic variables. Cross-section measurements can be defined as production level (e.g.  $\sigma(p\bar{p} \to W+ \geq n \text{ jets}))$  or as an acceptance limited cross-section where the reduced acceptance as defined in Section 5.4. The motivation for the former is to have the actual extrapolated production cross-section at the Tevatron. While slightly unorthodox, the latter reduced cross-section definition is motivated as a way to remove any MC acceptance dependence for non-acceptable Ws at the hepg level and to generally provide a more theory friendly result for comparison. In particular, this cross-section definition can be used to compare to NLO theoretical results assuming the same W acceptance space definition.

In addition, we present normalized cross-sections that are normalized to the respective inclusive  $n^{\rm th}$  jet multiplicity cross-section such that their integral is unity. Ergo these shape observables provided a means of comparison between predictions outside any universal scale factor. The other big motivation, is that normalizing to the inclusive jet multiplicity cross-section also cancels out or diminishes the systematic uncertainties. Luminosity, acceptance, efficiency, and vertex reweighing (promotion) systematics completely cancel as they are common in both measurements. We also account for the correlated effect between systematics as explained at the end of section 6.9. This effectively reduces our systematics for the dominate uncertainties like the jet energy scale and thus strengthening the power for comparison.

We present our general cross-section definition in the next section. The later section gives the appropriate definitions for our observables and then, typically, incorporates our observables into a differential cross-section. We begin presenting our results starting with the inclusive jet multiplicity cross-section of section 7.2. Also presented are some cross-section ratios between different quantiles. This includes the jet multiplicity ratios of section 7.3. Next we present the  $n^{\text{th}}$  leading jet  $p_T$  differential cross-sections for n=1-4 in section 7.4. That section also provides the results of comparing the bin-by-bin ratio of our result with a simple theoretical prediction from our W Alpgen MC.

Sections 7.5 and 7.6 deal with two of our dijet cross-sections. The former is the dijet mass  $(m_{jj})$  spectrum while the latter is for the dijet separation  $(R_{jj})$ . We discuss our  $\Delta \eta$  results in section 7.7 which includes results for both  $\geq 2$  and  $\geq 3$  results as well as a bin-by-bin ratio for said results. Finally we present our differential cross-section results for our  $\eta^*$  observable which requires an additional (jet based) selection cut. In addition, we present these same results in table form with the relevant observables (cross-sections, shapes, and ratios etc.) in appendix A. It includes the measured value from data and the total systematic error (generally asymmetric with respect to the central value) for each variable bin.

## 7.1 Cross-section definition

In this analysis we are looking for cross-sections which we denote as a production cross-section with branching ratio for the final state (which we write explicitly)

$$\sigma = \sigma(p\bar{p} \to W + \text{jets}) \times Br(W \to \ell\nu)$$

or via equation 37 (page 179)

$$\bar{\sigma} = \sigma(p\bar{p} \to W + \text{jets}|[a_{\text{hepg}}]) \times Br(W \to \ell\nu)$$

for our reduce cross-section. We define our cross-section (denoted here as simply  $\sigma$ )

$$\sigma = u \left( \frac{N_{data} - B}{LA\epsilon} \right) \tag{82}$$

where u is the unfolding scale factor of section 3.9,  $N_{data}$  is the number of candidate W events from data, B is the sum of all the estimated backgrounds, and  $LA\epsilon$  is the effective luminosity. The last quantity is the total summed product of the measured integrated luminosity, the W and jet acceptance via MC, and the detector and trigger efficiencies for each run period and subdetector types (the latter applicable to muons only) as defined in chapter 5.

The only difference between the nominal cross-section and the reduced version is in the acceptance as noted in section 5.4. Thus we substitute  $\bar{A} = A/a_{hepg}$  in the equation above for A and calculating the reduced cross-section. In point of fact we only consider the production level cross-section for our first observable: the inclusive jet multiplicity (see next section). Otherwise, all cross-sections (including derivative observables) use the reduce cross-section definition.

Derived observables using cross-section ratios (normalized cross-sections and quantities like  $\sigma_{n+1}/\sigma_n$  defined below) are calculated by simply performing the desire quotient. No simplification is used in eliminating terms that ought to cancel. This is done to have these results in lock step with the procedure for calculating systematics and the potential for systematics to cancel due to correlations. It also serves as good cross-check for the general procedure.

### 7.2 Jet Multiplicity Cross-section

In this section we show the results of the number of W events with an greater than or equal to n jets where  $n \in \{0, 1, 2, 3, 4\}$ . We formally note the jet multiplicity cross-section as a differential cross-section with  $\geq n$  jets as  $d\sigma/dn$ . However, for simplicity and ease of use with other results, we shall hereafter refer to the jet multiplicity cross-section as  $\sigma_n$ .

The jet multiplicity measurement is the base observable in this W+jets analysis and is used to normalize the cross-sections to get the shape of various jet kinematic variables that follow in later sections. Note that our measurement of the total inclusive  $(W+ \ge 0 \text{ jets})$  cross-section is not competitive to the already systematics limited analysis by CDF with 72 pb<sup>-1</sup> [68], however it provides a good benchmark for comparison with the pure EWK measurement. The production level cross-section for the inclusive jet multiplicity is given in figures 258  $(W \to e\nu)$  and 259  $(W \to \mu\nu)$ .

Figures 260 and 261 are the jet multiplicity cross-sections for the electron and muon channel, respectively. Figures 262 and 263 are normalized to the total inclusive cross-section  $(\sigma_n)$ . All of these results are set to a common log scale showing, to a first approximation, an exponential decay structure. A better method of comparing the rate of cross-section change verses jet multiplicity is done in the next section.

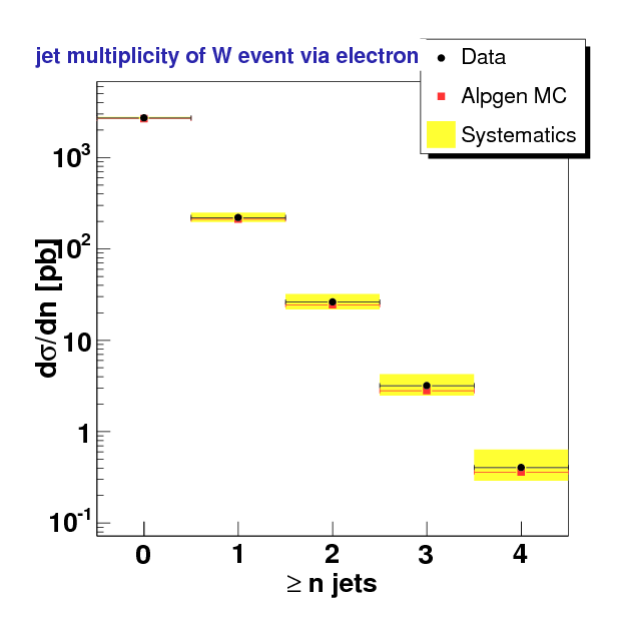


Figure 258:  $W \to e \nu$  jet multiplicity. This is a production level cross-section.

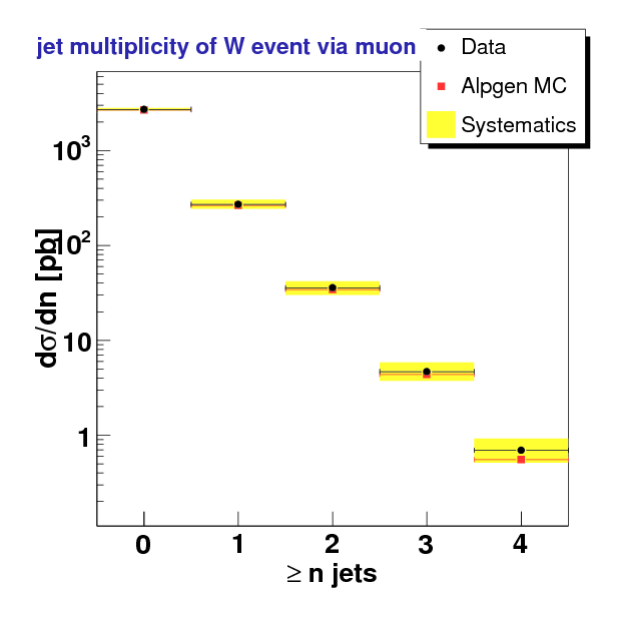


Figure 259:  $W \to \mu\nu$  jet multiplicity. This is a production level cross-section.

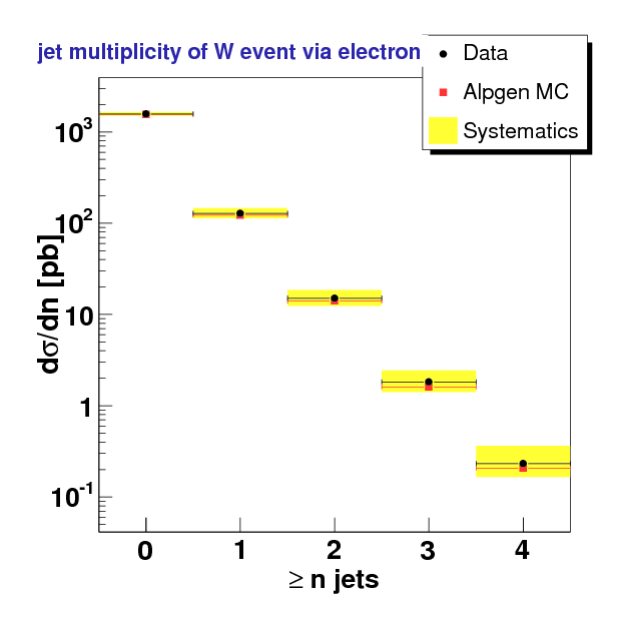


Figure 260:  $W \to e \nu$  jet multiplicity.

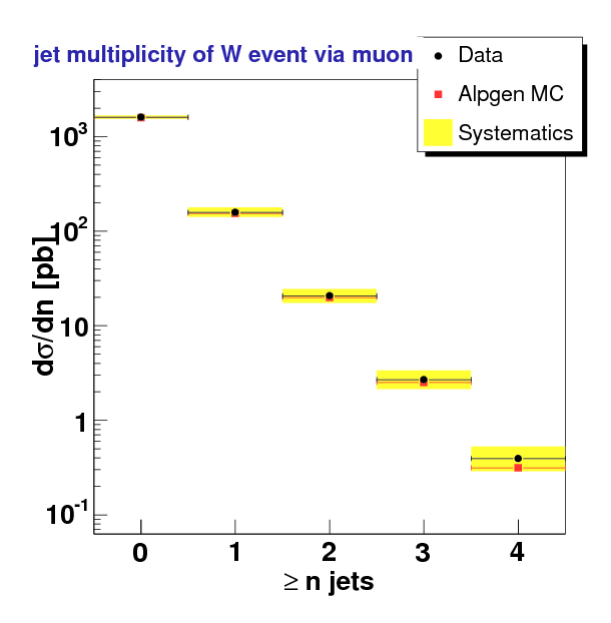


Figure 261:  $W \to \mu \nu$  jet multiplicity.

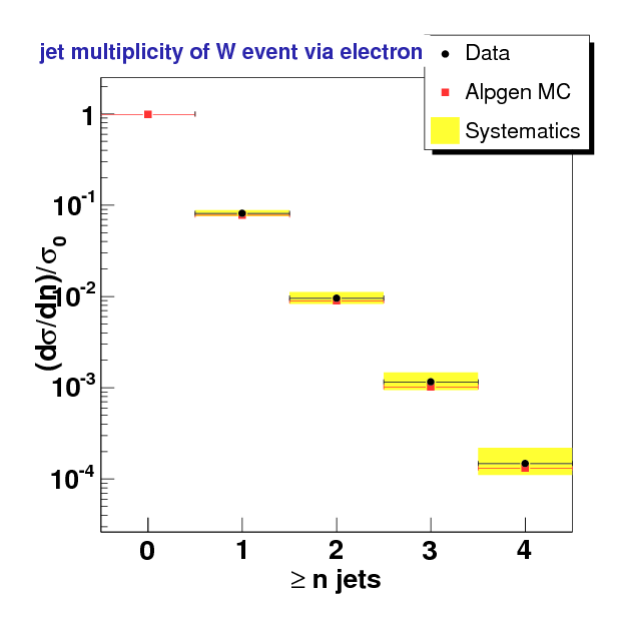


Figure 262:  $W \to e \nu$  jet multiplicity.

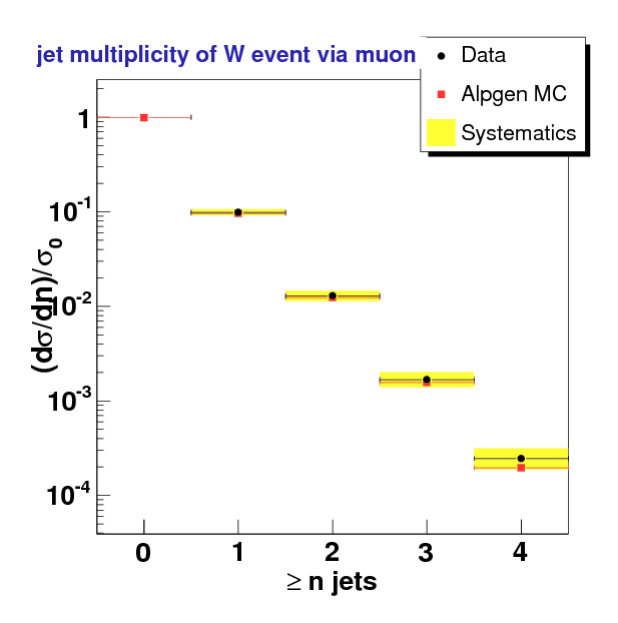


Figure 263:  $W \to \mu \nu$  jet multiplicity.

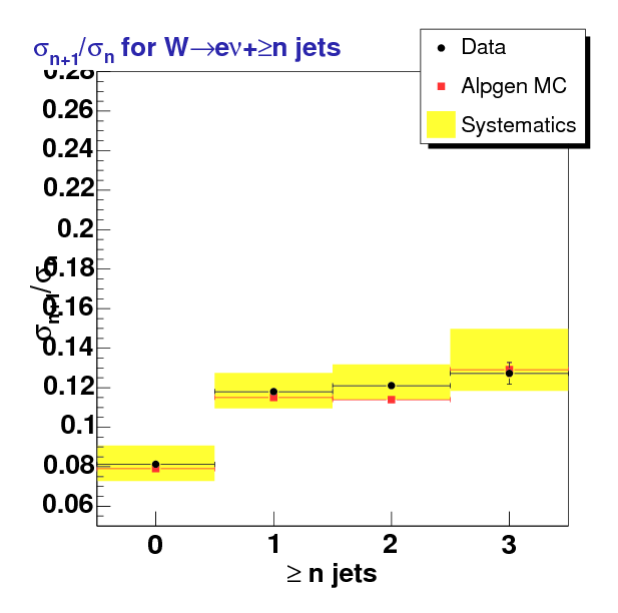


Figure 264:  $W \to e\nu \ \sigma_{n+1}/\sigma_n$ .

# 7.3 Jet Multiplicity Ratio, $\sigma_{n+1}/\sigma_n$

Via the results of the previous section, we construct a quotient based on the number of (inclusive) jets in a higher bin relative to the lower. Note that although systematics are reduced by this ratio as they were in the  $\sigma_n/\sigma_0$  the acceptance × efficiency does not completely cancel. The results are shown in Fig. 264 and Fig. 265 for the electrons and muons, respectively.

# 7.4 $n^{\text{th}}$ Leading Jet $p_T$ Differential Cross-section

The jet  $p_T$  spectrum for the  $n^{th}$  jet is the hallmark measurement for this analysis. Jets are ranked via their transverse momentum and based on its rank is assigned to the appropriate  $\geq n$  jets bin. This then forms the  $\mathrm{d}\sigma/\mathrm{d}p_T$  (or more pedagogically  $\mathrm{d}\sigma_n/\mathrm{d}p_T^{n^{th}}$ ) differential cross-section. The results are seen in Fig. 266 through 273.

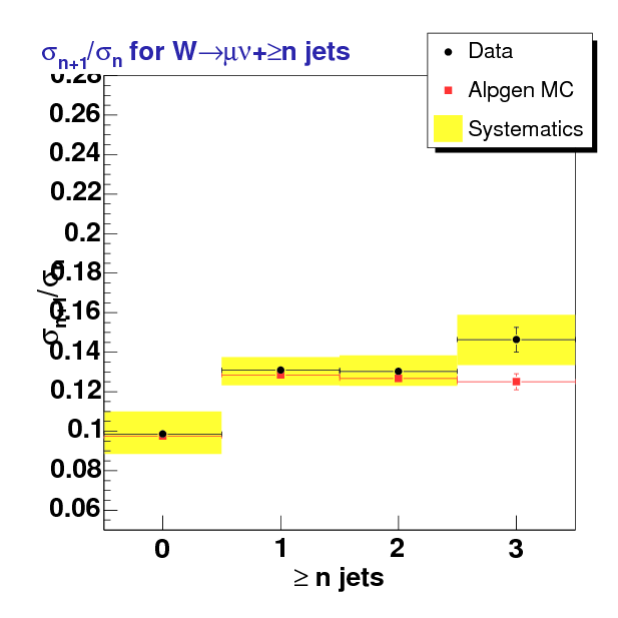


Figure 265:  $W \to \mu\nu \ \sigma_{n+1}/\sigma_n$ .

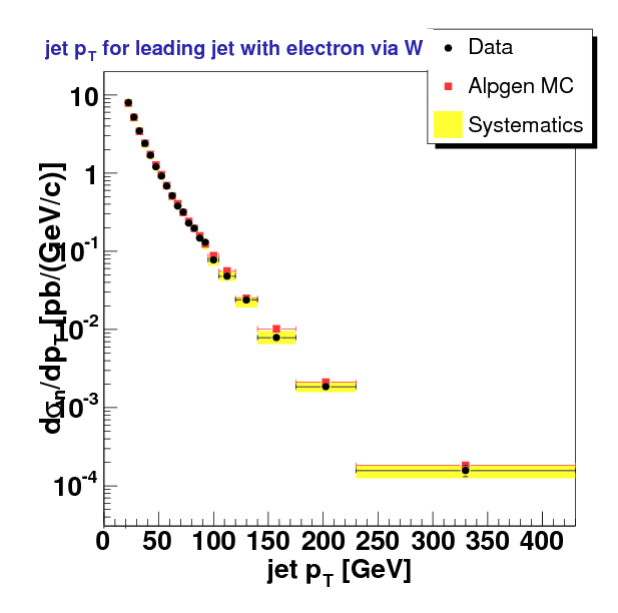


Figure 266: Leading jet  $p_T$  for  $W \to e\nu + \geq 1$  jet.

The jet energy scale, unfolding factor, and, for  $\geq 3$  or  $\geq 4$  jets,  $t\bar{t}$  background estimation are the dominate uncertainties. The systematics are largest at the highest momentum bins for each jet multiplicity and are generally larger for high multiplicities which is consistent with the previous sections. Systematics are reduced a bit by normalizing the to the total inclusive cross-section. For the purpose of comparing to theory (or direct full-simulation MC) this is fine as the relative shape difference is sufficient the hardness or softness of a given theoretical prediction.

We denote the normalized cross-section as  $(d\sigma/dp_T)/\sigma_n$ . These plots are shown in Fig. 274 through Fig. 281. Note that we use variable bins to keep systematics relatively flat throughout the spectra. Of course, the jet energy scale and  $t\bar{t}$  systematics along with poor event yield always conspires to make the highest jet bin's systematics large.

Due to the nature of the plots falling several orders of magnitude on a common log scale plot, it is advantageous to present the results by dividing the measurement in data to the theoretical prediction (currently this is Alpgen+Pythia MC). Note that this does not effect the systematics in anyway; the relative uncertainties remain unchanged while the result can be plotted linearly with results expected to fall roughly around unity. These Data/Theory plots for jet  $p_T$  are shown in Fig. 282 through 289.

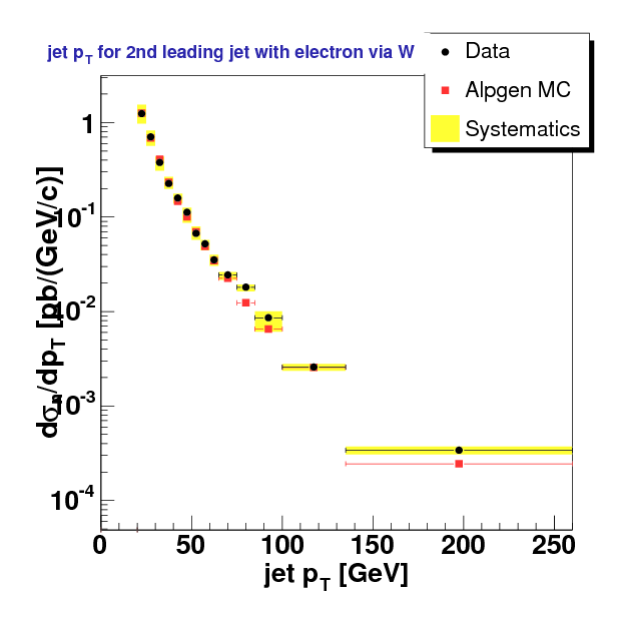


Figure 267:  $2^{nd}$  leading jet  $p_T$  for  $W \to e\nu + \geq 2$  jets.

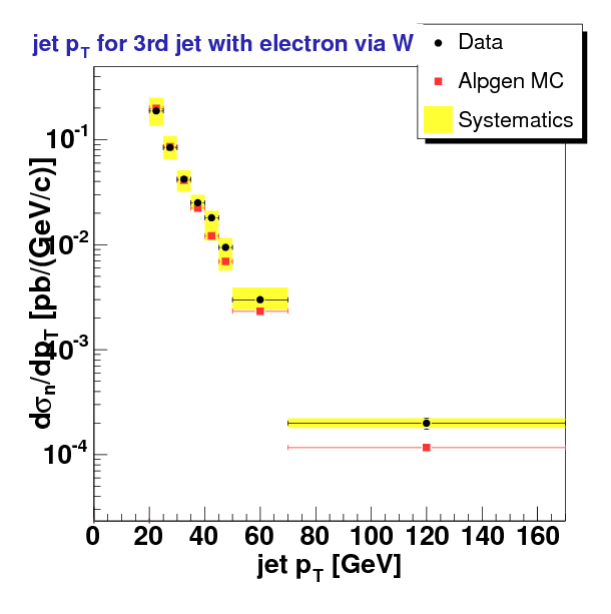


Figure 268:  $3^{rd}$  leading jet  $p_T$  for  $W \to e\nu + \geq 3$  jets.

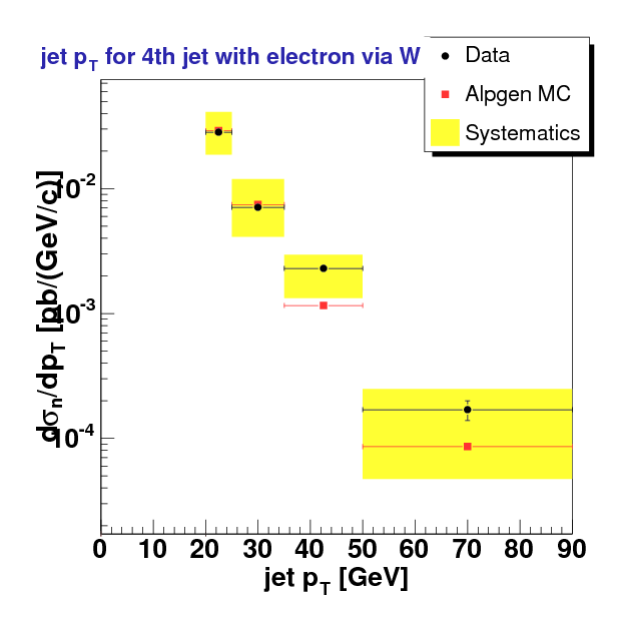


Figure 269:  $4^{th}$  leading jet  $p_T$  for  $W \to e\nu + \geq 4$  jets.

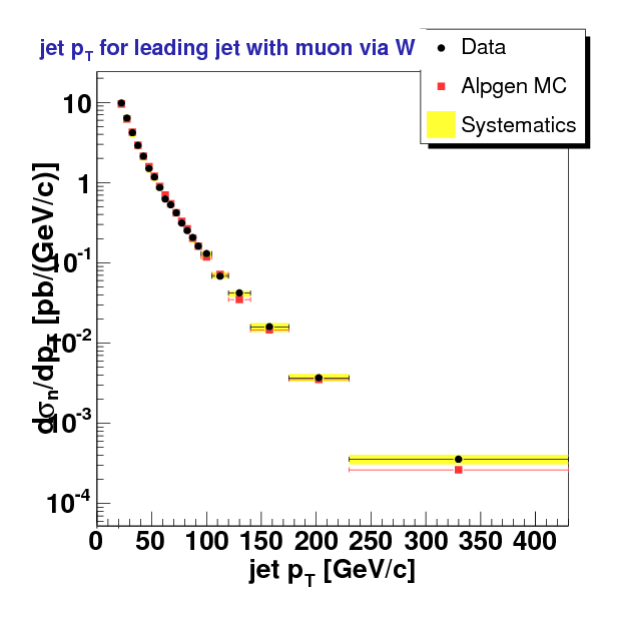


Figure 270: Leading jet  $p_T$  for  $W \to \mu \nu + \geq 1$  jet.

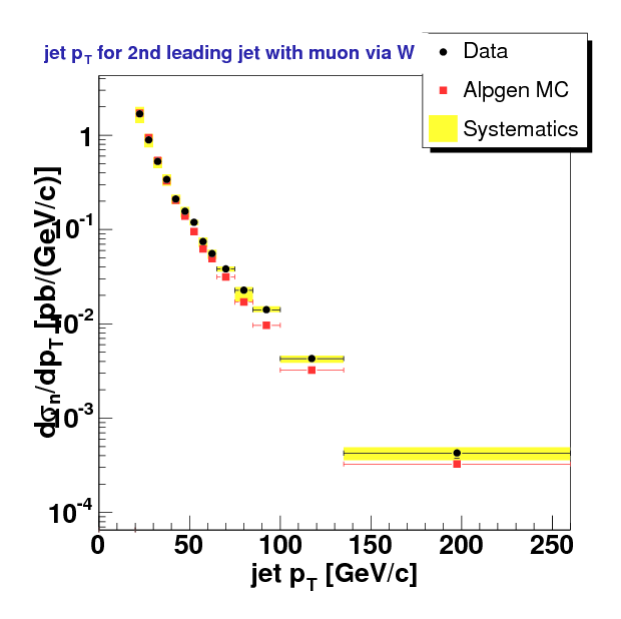


Figure 271:  $2^{nd}$  leading jet  $p_T$  for  $W \to \mu \nu + \geq 2$  jets.

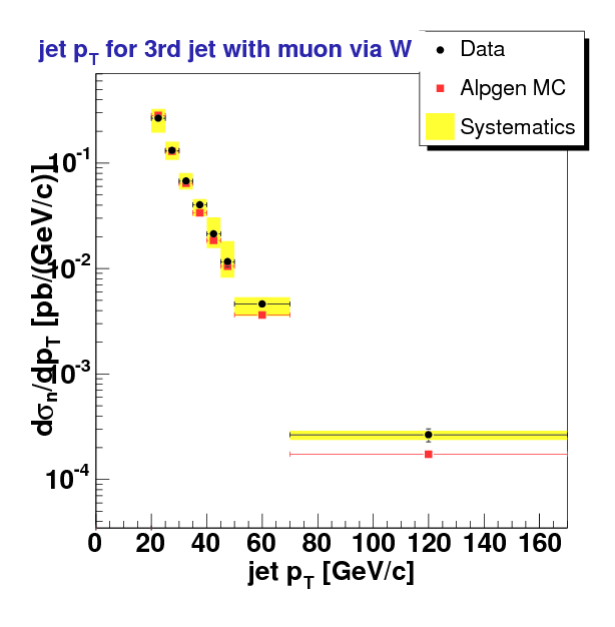


Figure 272:  $3^{rd}$  leading jet  $p_T$  for  $W \to \mu\nu + \geq 3$  jets.

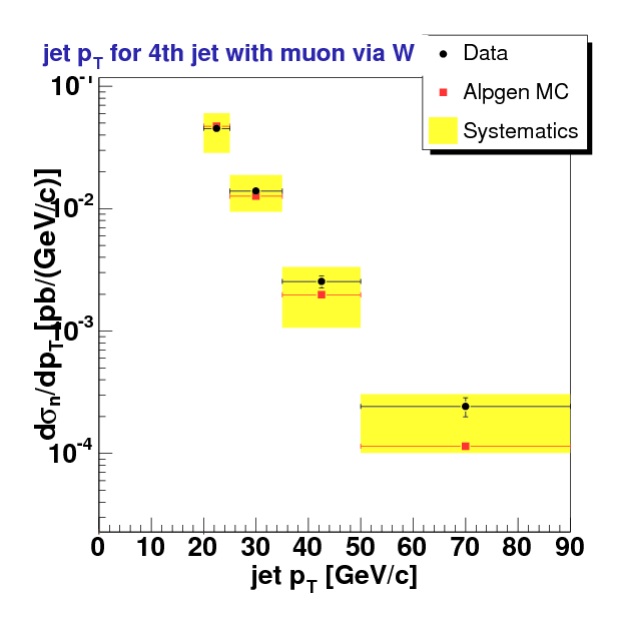


Figure 273:  $4^{th}$  leading jet  $p_T$  for  $W \to \mu\nu + \geq 4$  jets.

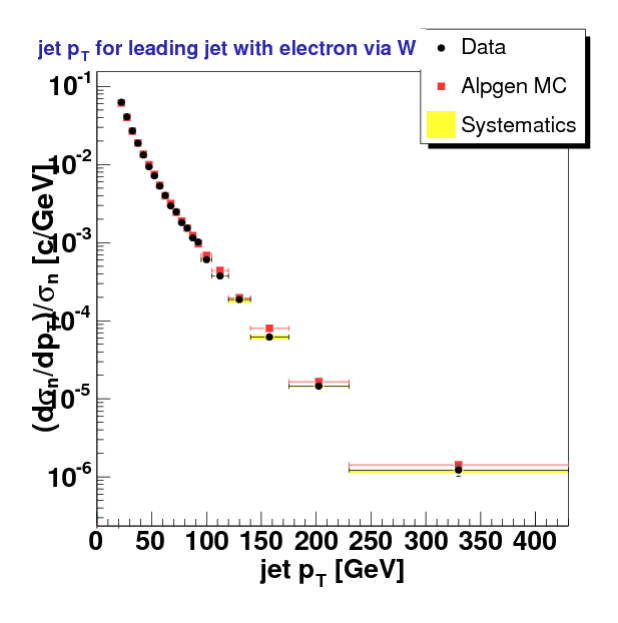


Figure 274: Leading jet  $p_T$  for  $W \to e\nu + \geq 1$  jet.

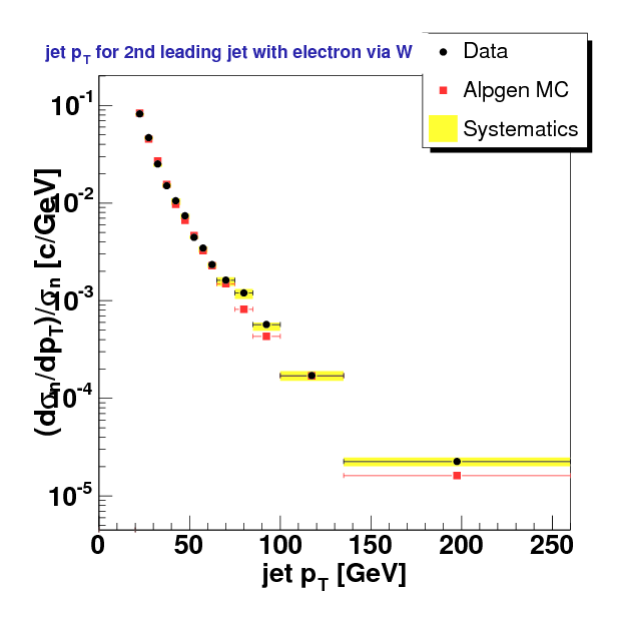


Figure 275:  $2^{nd}$  leading jet  $p_T$  for  $W \to e\nu + \geq 2$  jets.

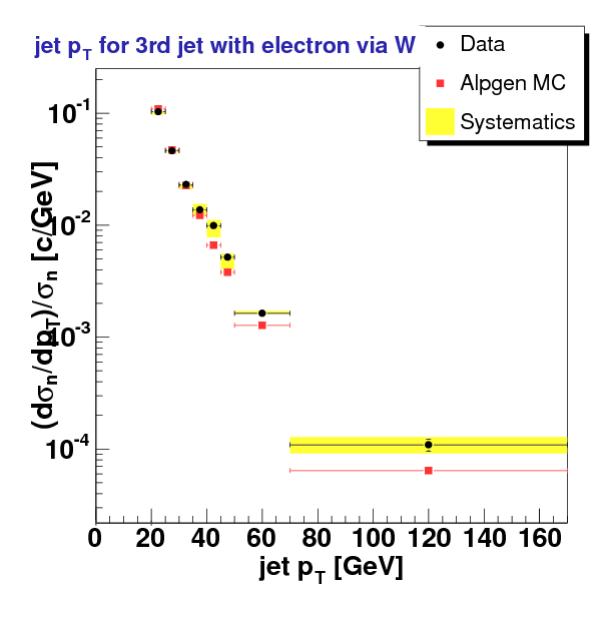


Figure 276:  $3^{rd}$  leading jet  $p_T$  for  $W \to e\nu + \geq 3$  jets.

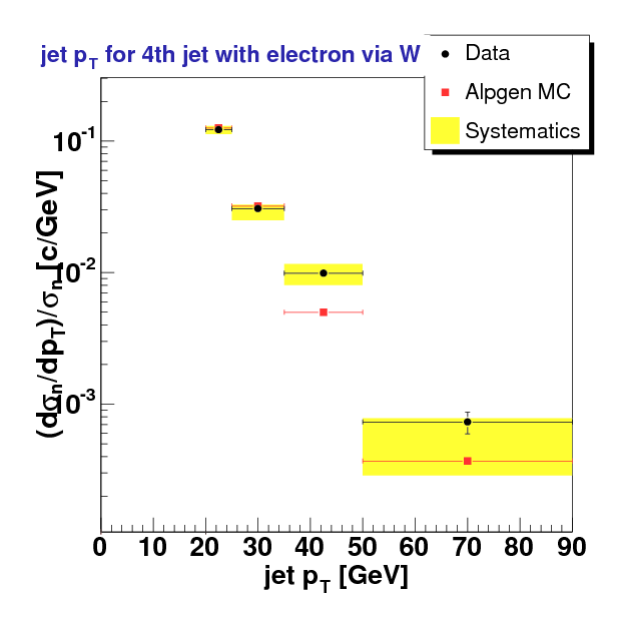


Figure 277:  $4^{th}$  leading jet  $p_T$  for  $W \to e\nu + \geq 4$  jets.

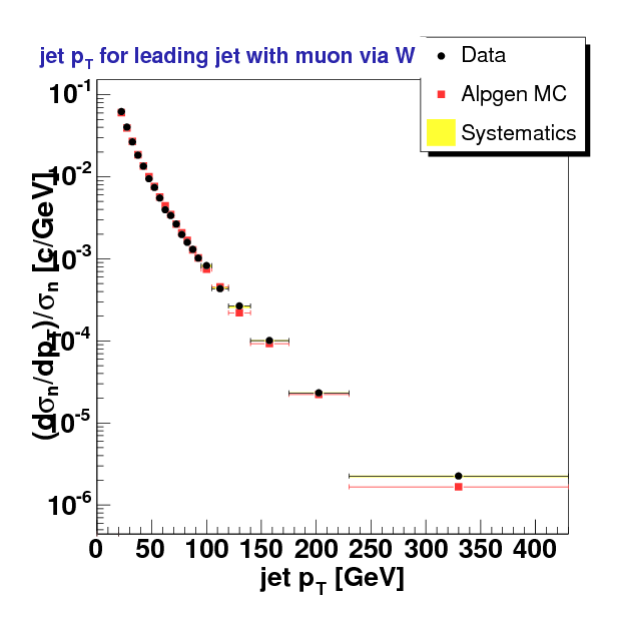


Figure 278: Leading jet  $p_T$  for  $W \to \mu \nu + \geq 1$  jet.

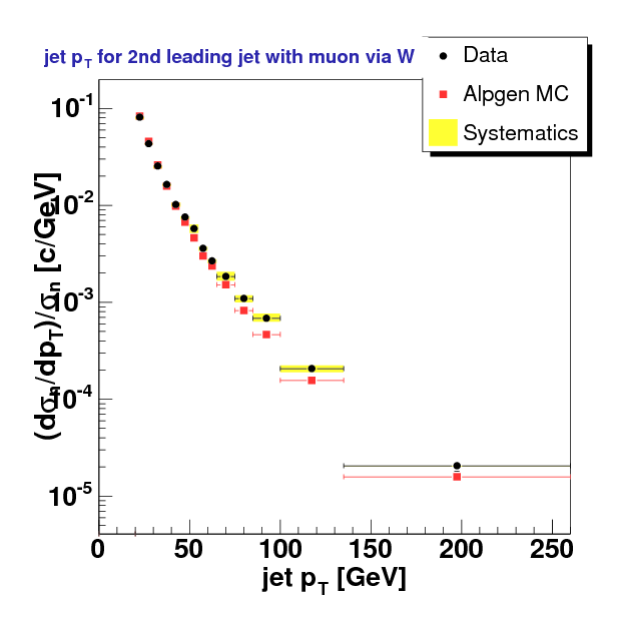


Figure 279:  $2^{nd}$  leading jet  $p_T$  for  $W \to \mu\nu + \geq 2$  jets.

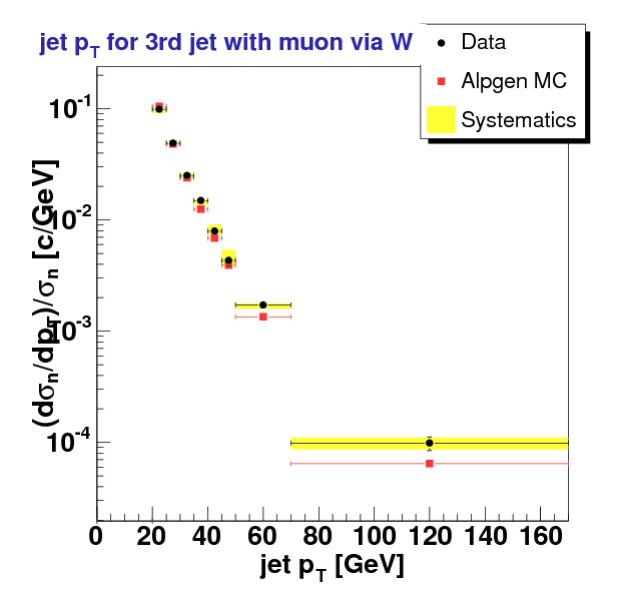


Figure 280:  $3^{rd}$  leading jet  $p_T$  for  $W \to \mu\nu + \geq 3$  jets.

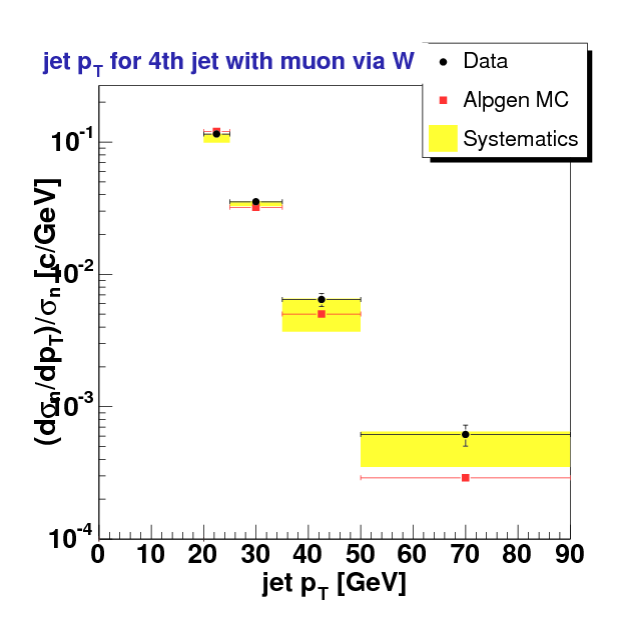


Figure 281:  $4^{th}$  leading jet  $p_T$  for  $W \to \mu\nu + \geq 4$  jets.

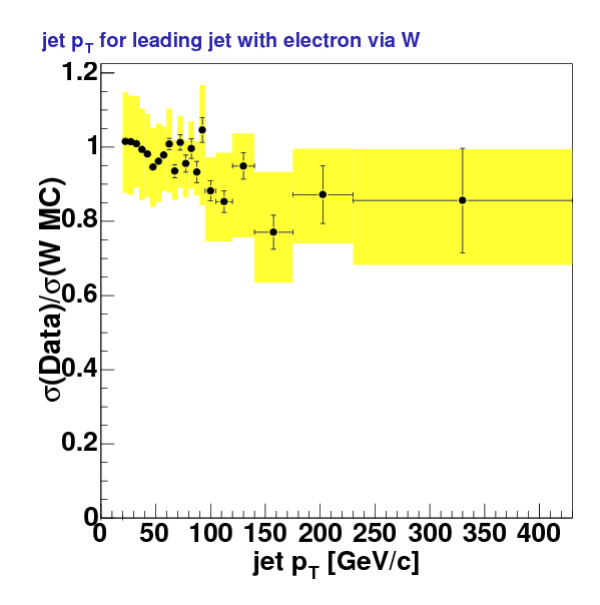


Figure 282: Data/Theory Leading jet  $p_T$  for  $W \to e\nu + \geq 1$  jet.

## 7.5 Dijet Mass Cross-section

In this section and the next we consider two dijet variables. Here we look at the dijet mass for event with  $\geq 2$  jets. We do this by selecting the two leading (largest) jets in  $p_T$ . We then construct a mass observable  $(m_{ij})$  for the jet pair via

$$m_{ij}^2 = (p_1 + p_2)^2 (83)$$

where  $p_j$  is the equivalent of the four-momentum from the detector,  $p_j = (E_j, \vec{p}_j)$ .

The results of the dijet mass differential cross-section are presented in Fig. 290 and Fig. 291 for the electron and muon results, respectively. We use the notation  $d\sigma/dm_{jj}$  to signify this cross-section. Similar to the jet  $p_T$  results, the we use variable bins (roughly optimized based on the systematic and statistical errors) and present the results normally on a common log scale.

As with the jet  $p_T$  cross-section, it is useful to remove the overall normalization in the plot by dividing by the inclusive 2 jet cross-section ( $\sigma_2$ ). The normalized version of these results are shown in Fig. ?? for electrons and Fig. ?? for muons.

### 7.6 Dijet Separation Cross-section

The second dijet cross-section we consider is the dijet separation cross-section. Taking the same highest jet  $p_T$  pair as before in events with  $\geq 2$  jets we construct an angular separation measurement  $(R_{jj})$  based on the jet  $\eta$  and  $\phi$ . We define the separation in the normal way via

$$R_{ij} = \sqrt{(\eta_1 - \eta_2)^2 + (\phi_1 - \phi_2)^2} \tag{84}$$

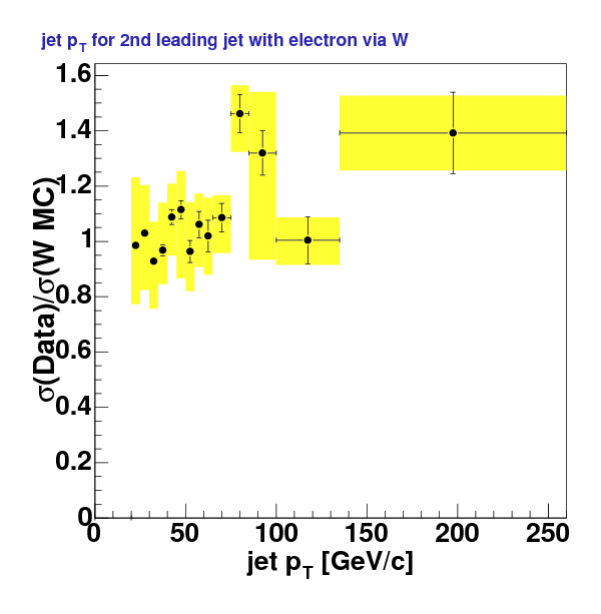


Figure 283: Data/Theory  $2^{nd}$  leading jet  $p_T$  for  $W \to e\nu + \geq 2$  jets.

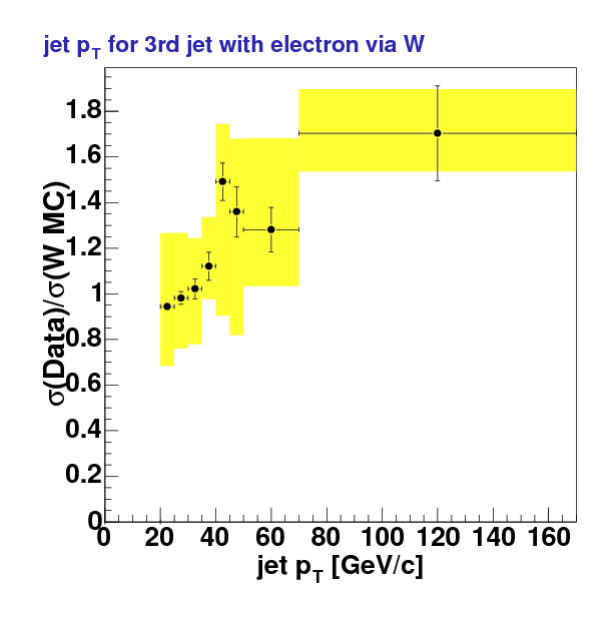


Figure 284: Data/Theory  $3^{rd}$  leading jet  $p_T$  for  $W \to e\nu + \geq 3$  jets.

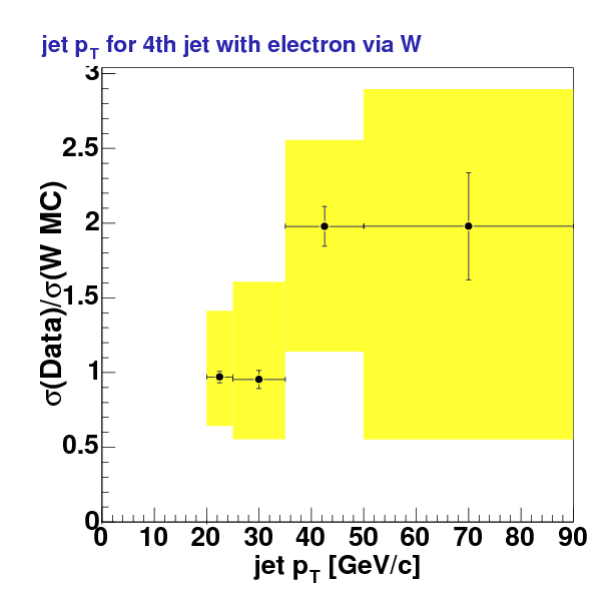


Figure 285: Data/Theory  $4^{th}$  leading jet  $p_T$  for  $W \to e\nu + \geq 4$  jets.

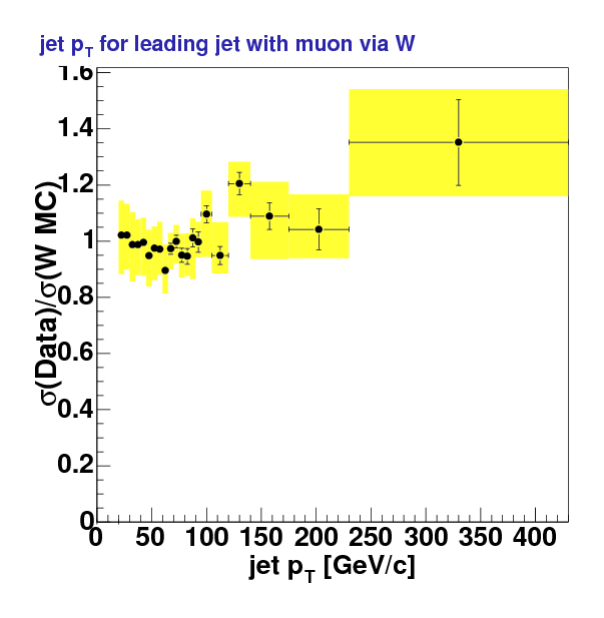


Figure 286: Data/Theory Leading jet  $p_T$  for  $W \to \mu \nu + \geq 1$  jet.

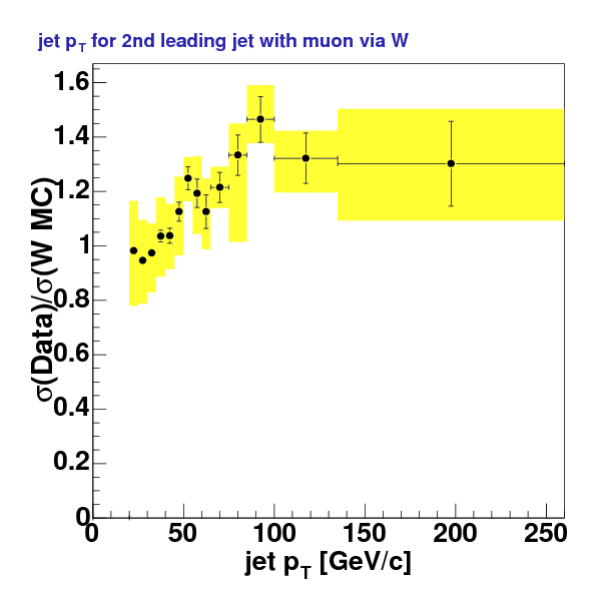


Figure 287: Data/Theory  $2^{nd}$  leading jet  $p_T$  for  $W \to \mu\nu + \geq 2$  jets.

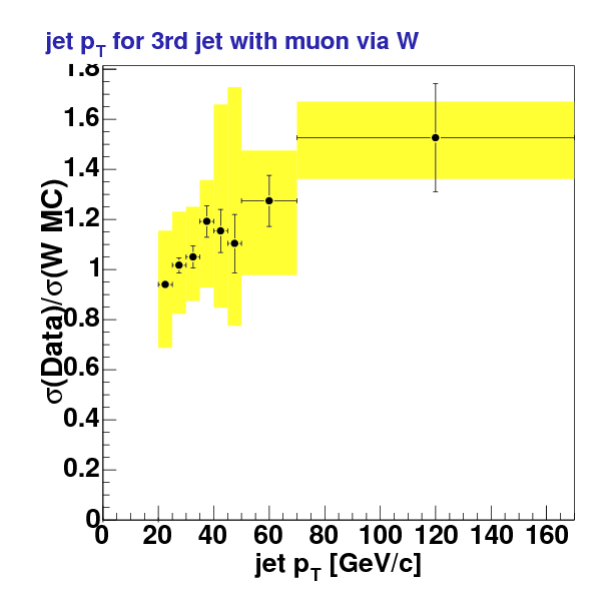


Figure 288: Data/Theory  $3^{rd}$  leading jet  $p_T$  for  $W \to \mu\nu + \geq 3$  jets.

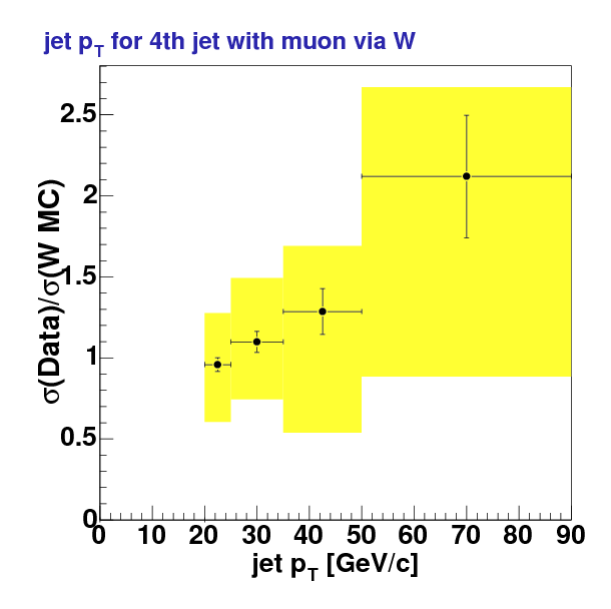


Figure 289: Data/Theory 4<sup>th</sup> leading jet  $p_T$  for  $W \to \mu\nu + \geq 4$  jets.

Note that the difference in the azimuthal angles  $(\Delta \phi)$  is done by taking the absolute value of the difference and then, if this value is larger than  $\pi$ , taking  $\Delta \phi = 2\pi - |\phi_1 - \phi_2|$ .

We denote this cross-section with  $d\sigma/dR_{jj}$  and its normalized (unitless) version with  $(d\sigma/dR_{jj})/\sigma_2$ . The nominal cross-section results are presented in Fig. 294 and Fig. 295 for electrons and muons, respectively. Similarly, the normalized cross-section results are showcased in Fig. 296 and Fig. 297. We note the reduction in the total systematic uncertainty in the latter pair of plots due to our method's power in canceling correlated systematics as explained in Section 6.9.

## 7.7 $\Delta \eta$ Cross-sections

In this and the next section we consider jet variables dealing with the forwardness of jets. This is interesting as it is complementary to looking at the jet  $p_T$  spectrum. In both cases, different theoretical predictions and methods may offer different results. See the discussion in section ??? in [1] for BNLK NLL predictions [69].

We define  $\Delta \eta$  as the absolute difference in pseudo-rapidity in the two farthest jets. We then consider two cross-sections based on this observable:  $d\sigma_2/d\Delta\eta$  and  $d\sigma_3/d\Delta\eta$ . Note that because of our definition of  $\Delta\eta$  (as appose to the procedure for the dijet separation) the inclusive 2 jet differential cross-section necessarily includes the inclusive 3 jet  $\Delta\eta$  events. We can see this by writing out the components as done in Equation 85.

$$\frac{\mathrm{d}\sigma_{\geq 2}}{\mathrm{d}\Delta\eta} = \frac{\mathrm{d}\sigma_{=2}}{\mathrm{d}\Delta\eta} + \frac{\mathrm{d}\sigma_{\geq 3}}{\mathrm{d}\Delta\eta} \tag{85}$$

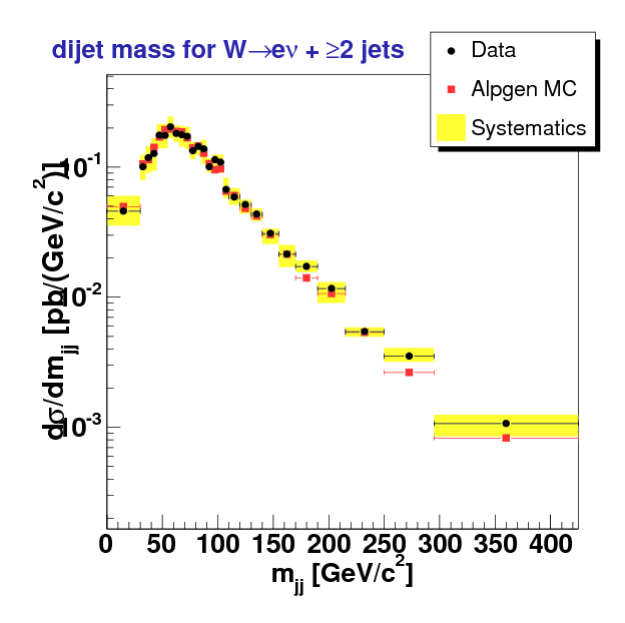


Figure 290: Dijet Mass Cross-section for  $W \to e\nu + \geq 2$  jets.

The electron and muon  $\Delta \eta$  cross-section results for the inclusive 2 jet case are shown in Fig. 298 and Fig. 299, respectively. The normalized plots are shown in Fig. 300 and Fig. 301.

The inclusive 3 jet case follows in Fig. 302 and Fig. 303 for the differential cross-section for electrons and muons while Fig. 304 and Fig. 305 show the normalized shape plots.

We next consider a ratio measurement that examines the behavior in  $\Delta \eta$  between 2 or  $\geq$  3 jets. We define  $r_{\Delta \eta}$  as the quotient of the previous measurements:

$$r_{\Delta\eta} = \frac{\mathrm{d}\sigma_{\geq 3}/\mathrm{d}\Delta\eta}{\mathrm{d}\sigma_{\geq 2}/\mathrm{d}\Delta\eta} \tag{86}$$

Note that the bin size is the same in the 2 and 3 inclusive jet case for  $\Delta \eta$  in order to make  $r_{\Delta \eta}$  relatively easy to produce. The results as shown in Fig. 306 and Fig. 307 for electrons and muons.

### 7.8 $\eta^*$ Cross-sections

Another distribution that is interesting to look at that is sensitive to different predictions in jet  $\eta$  is  $\eta^*$ . We define it as the  $\eta$  of the 3<sup>rd</sup> ordered jet minus the average of the leading jets,

$$\eta^* = \eta_3 - \frac{\eta_1 + \eta_2}{2} \tag{87}$$

This variable is of interest to processes like VBF (Vector Boson Fusion) [70] and may be instructive to use as a discriminate or to tag events for a Higgs signal with W+jets as a background.

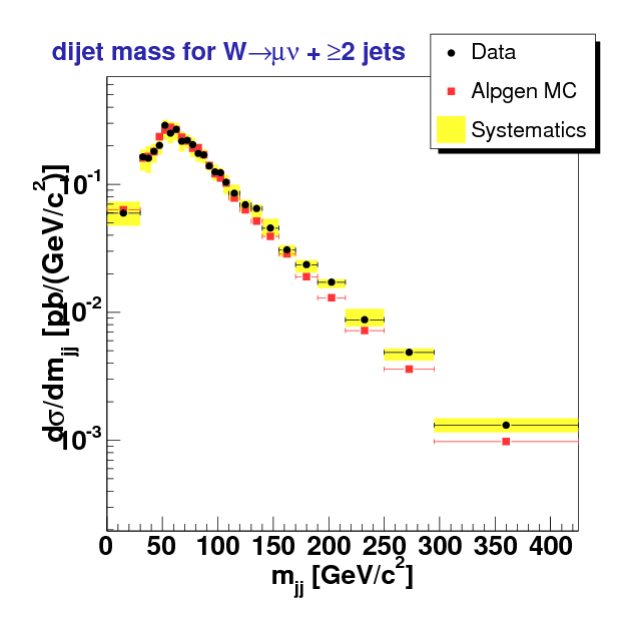


Figure 291: Dijet Mass Cross-section for  $W \to \mu\nu + \geq 2$  jets.

Detector	$\Delta \eta_{jj} > 2.0$	Acceptance
CEM	?	?
CMUP	?	?
CMX-Arch	?	?
CMX-Mini	?	?

Table 62:  $\eta^*$  Acceptance Results for all lepton detector types with  $\geq 3$  jets

With the above motivation in mind, we want to look at events where the leading jets are forward. For our convenience we define

$$\bar{\eta} = \frac{\eta_1 + \eta_2}{2}$$

$$\Delta \eta_{jj} = |\eta_1 - \eta_2|$$

$$(88)$$

$$\Delta \eta_{ij} = |\eta_1 - \eta_2| \tag{89}$$

where the former (88) is simply the average in equation 87 while the latter (89) is the  $\Delta \eta_{jj}$  of the leading jet pair and should not be confused with the  $\Delta \eta$  of section ??. Our selection for our  $\eta^*$  events requires  $\geq 3$  jets and  $\Delta \eta_{jj} > 2.0$ . Outside of being restrictive to our sample size,  $\Delta \eta_{ij}$  requires its own acceptance calculation and correction. Following the same procedures in our acceptance and efficiency section (Sec. 5) we add the additional jet requirement. The acceptance results are given in table 62 (luminosity and efficiency are unaffected).

We present our  $|\eta^*|$  results in figures 308 and 309 for electrons and muons, respectively. For the normalized cross-section shapes, we are careful to divide by the inclusive cross-section with the  $\Delta \eta_{jj}$  requirement. As such,  $(d\sigma_3/d\eta^*)/\sigma_3$  has an integral sum of unity. These normalized shape cross-section distributions are presented in figures 310 and 311

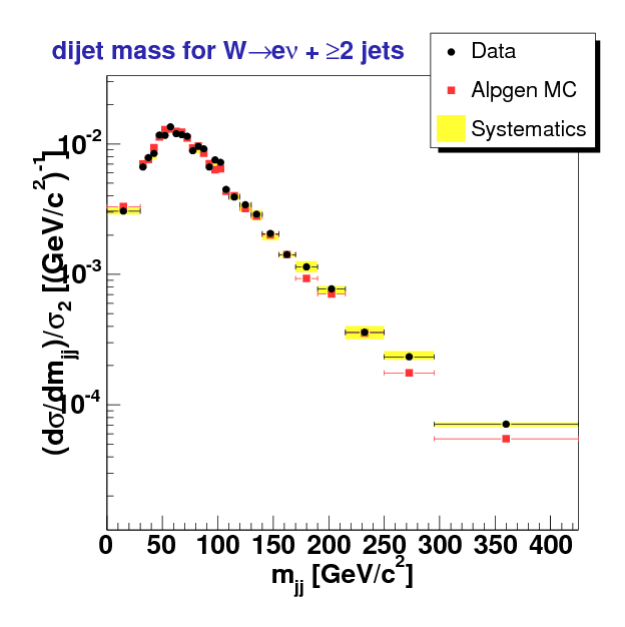


Figure 292: Dijet Mass Cross-section for  $W \to e\nu + \geq 2$  jets.

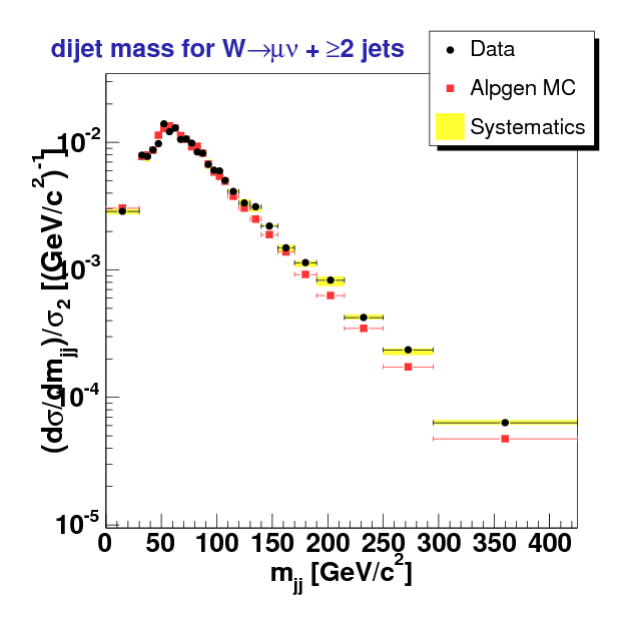


Figure 293: Dijet Mass Cross-section for  $W \to \mu \nu + \geq 2$  jets.

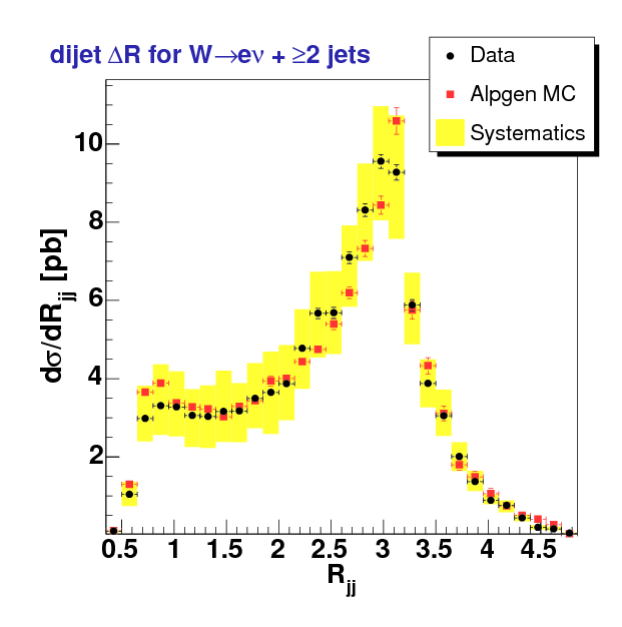


Figure 294: Dijet Separation Cross-section for  $W \to e\nu + \geq 2$  jets.

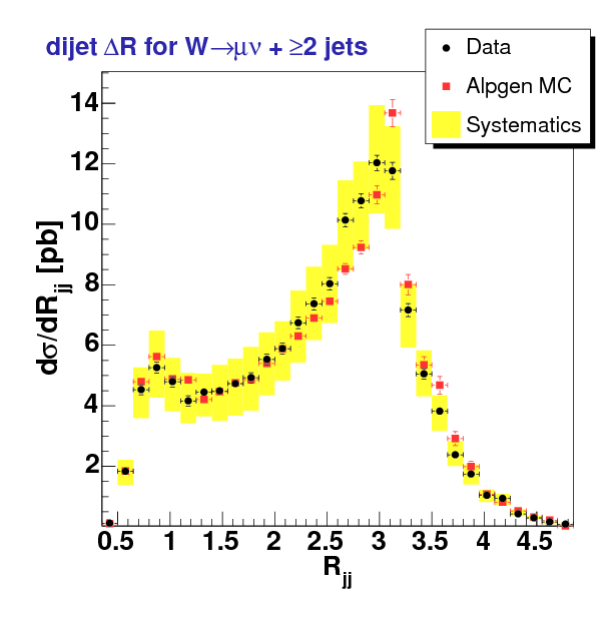


Figure 295: Dijet Separation Cross-section for  $W \to \mu \nu + \geq 2$  jets.

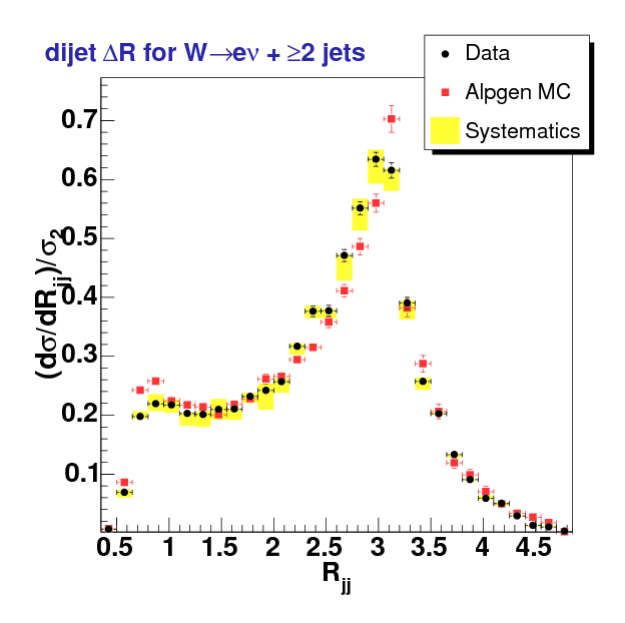


Figure 296: Dijet Separation Cross-section for  $W \to e\nu + \geq 2$  jets.

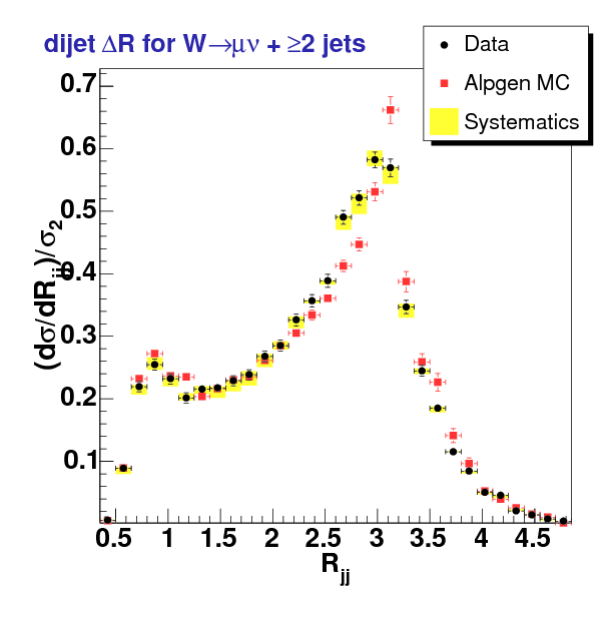


Figure 297: Dijet Separation Cross-section for  $W \to \mu\nu + \geq 2$  jets.

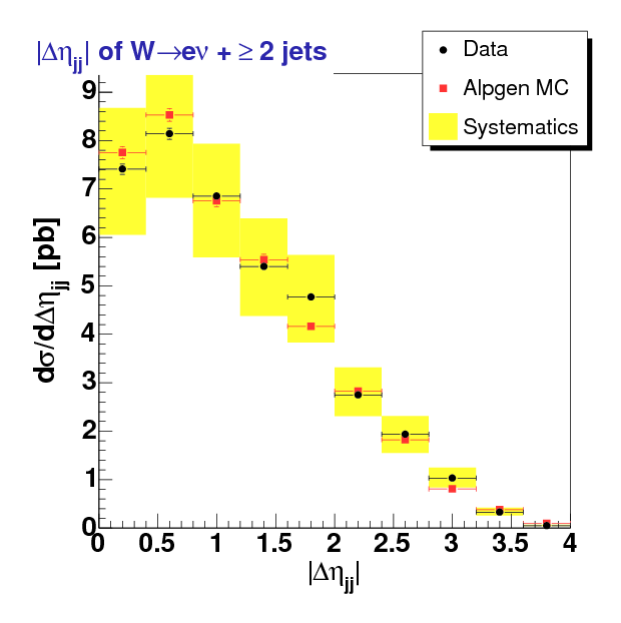


Figure 298:  $\Delta \eta$  Cross-section for  $W \to e \nu + \geq 2$  jets.

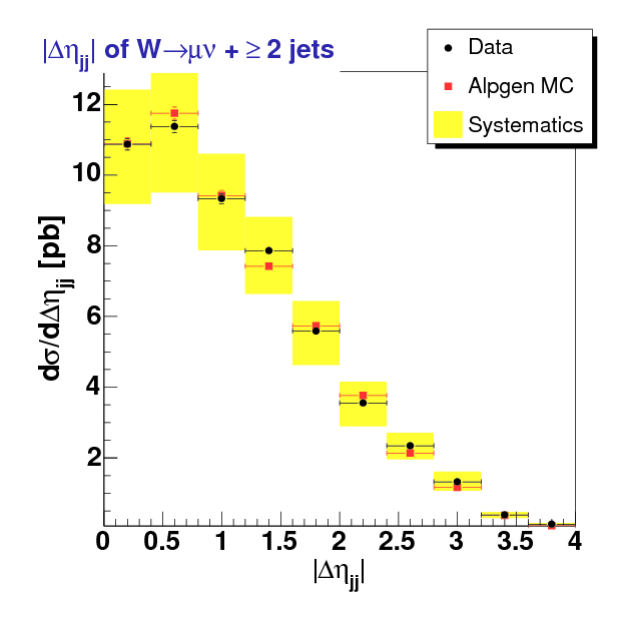


Figure 299:  $\Delta \eta$  Cross-section for  $W \to \mu \nu + \geq 2$  jets.

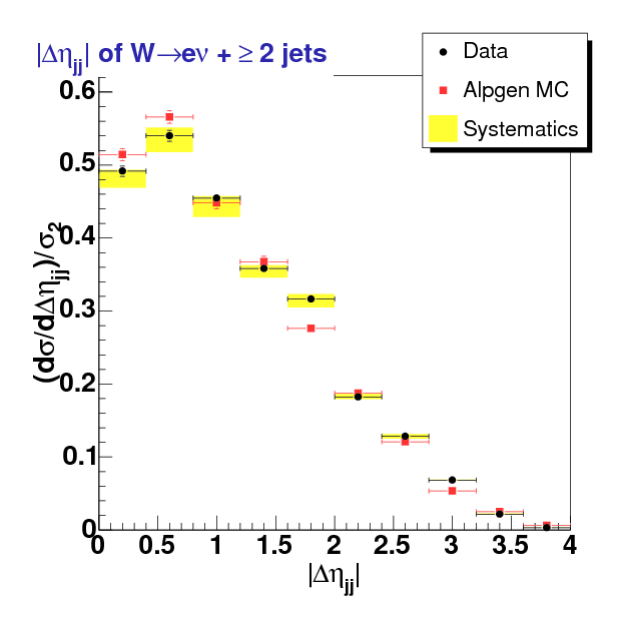


Figure 300:  $\Delta \eta$  Cross-section for  $W \to e \nu + \geq 2$  jets.

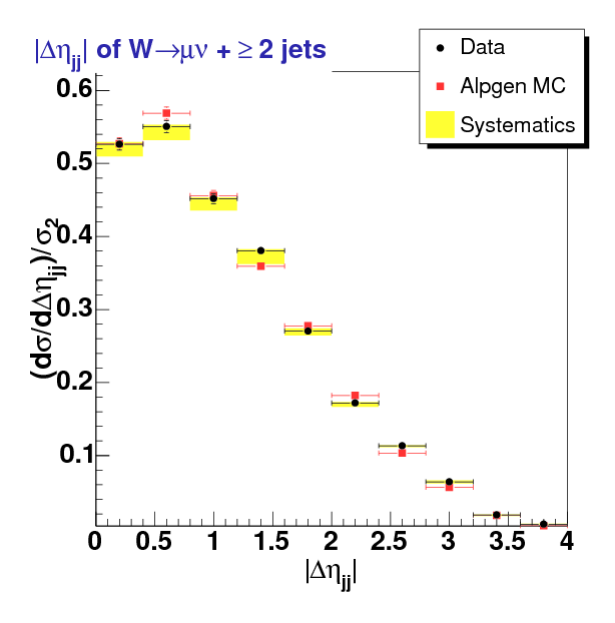


Figure 301:  $\Delta \eta$  Cross-section for  $W \to \mu \nu + \geq 2$  jets.

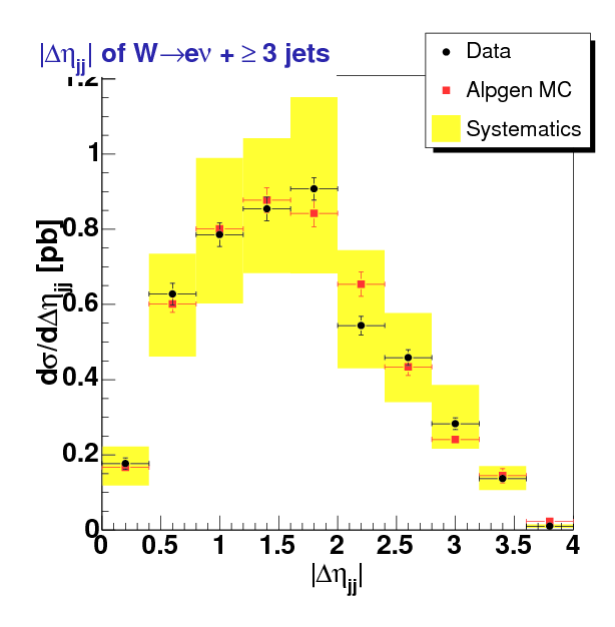


Figure 302:  $\Delta \eta$  Cross-section for  $W \to e \nu + \geq 3$  jets.

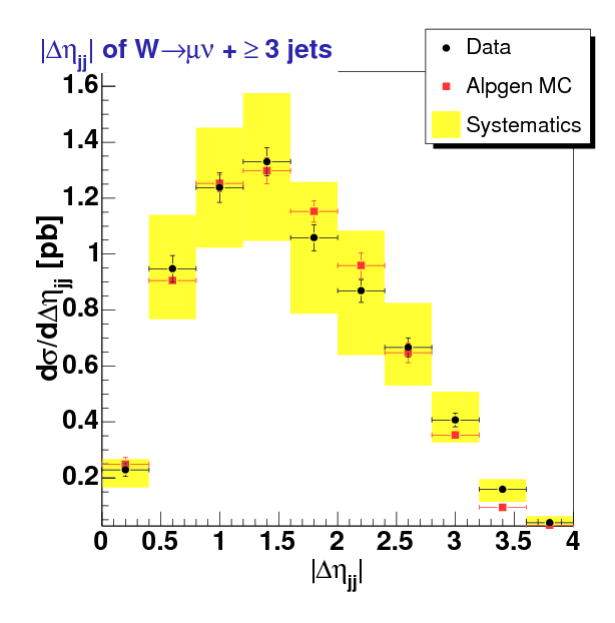


Figure 303:  $\Delta \eta$  Cross-section for  $W \to \mu \nu + \geq 3$  jets.

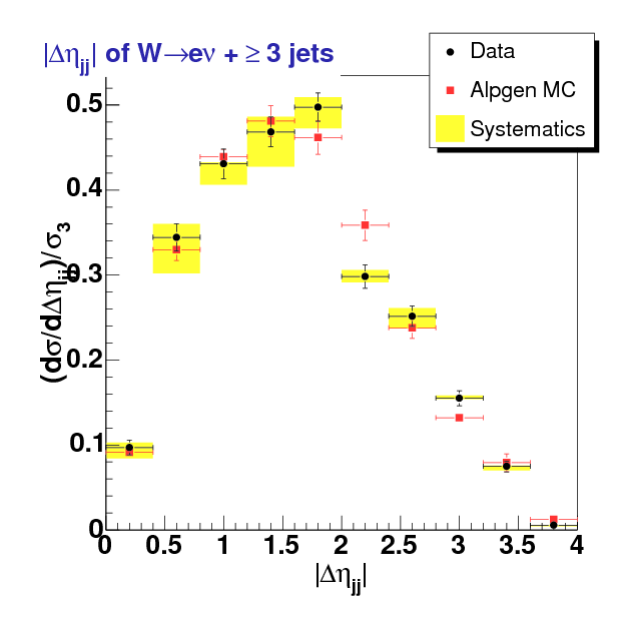


Figure 304:  $\Delta \eta$  Cross-section for  $W \to e \nu + \geq 3$  jets.

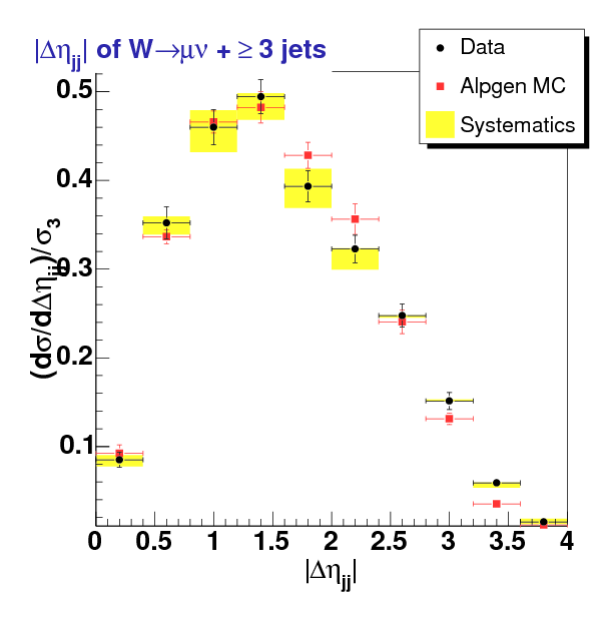


Figure 305:  $\Delta \eta$  Cross-section for  $W \to \mu \nu + \geq 3$  jets.

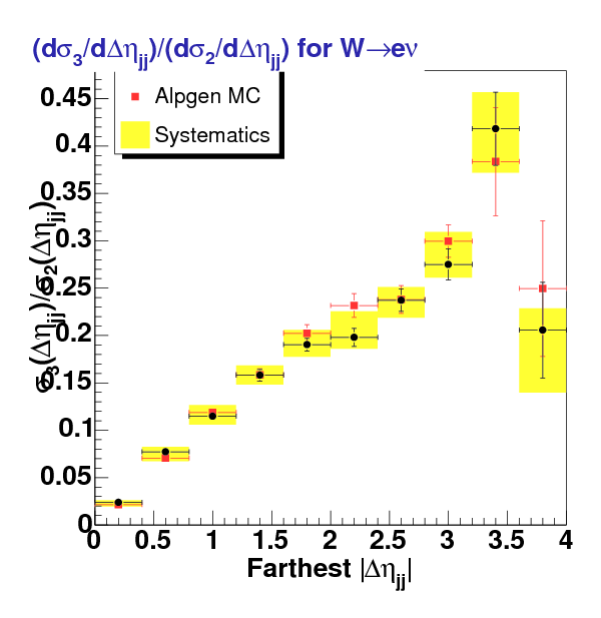


Figure 306:  $\Delta \eta$  Cross-section for  $W \to e \nu + \geq 3$  jets.

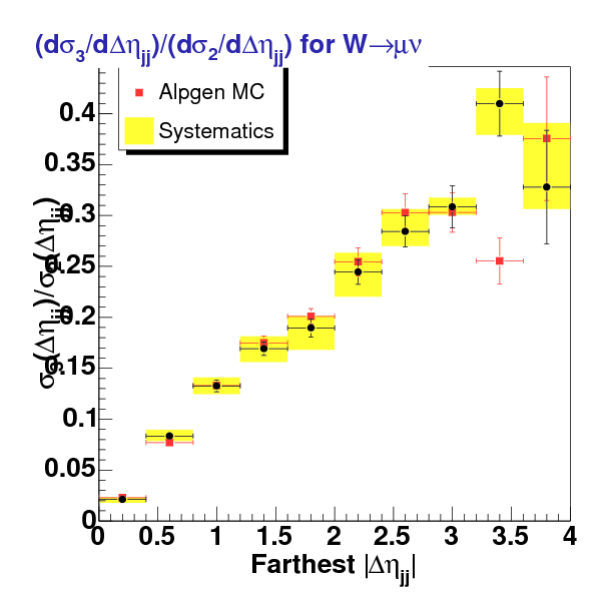


Figure 307:  $\Delta \eta$  Cross-section for  $W \to \mu \nu + \geq 3$  jets.

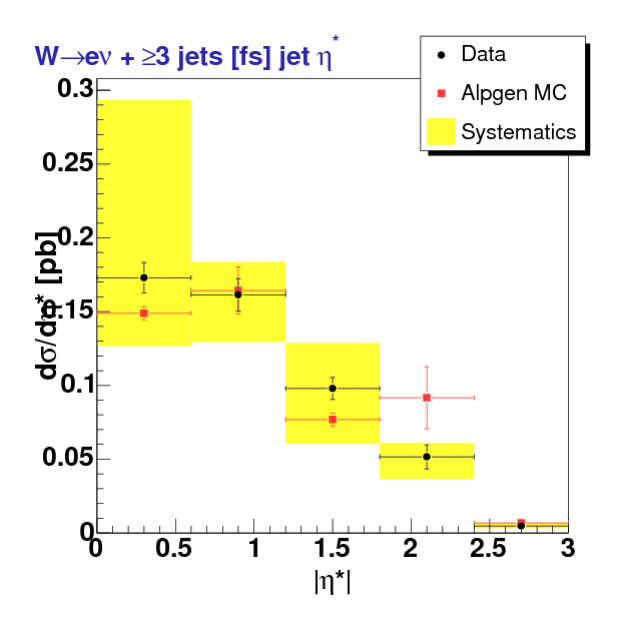


Figure 308:  $|\eta^*|$  Cross-section for  $W \to e\nu + \geq 3$  jets with  $\Delta \eta_{jj} > 2.0$ 

## 7.9 $H_T$ Cross-sections

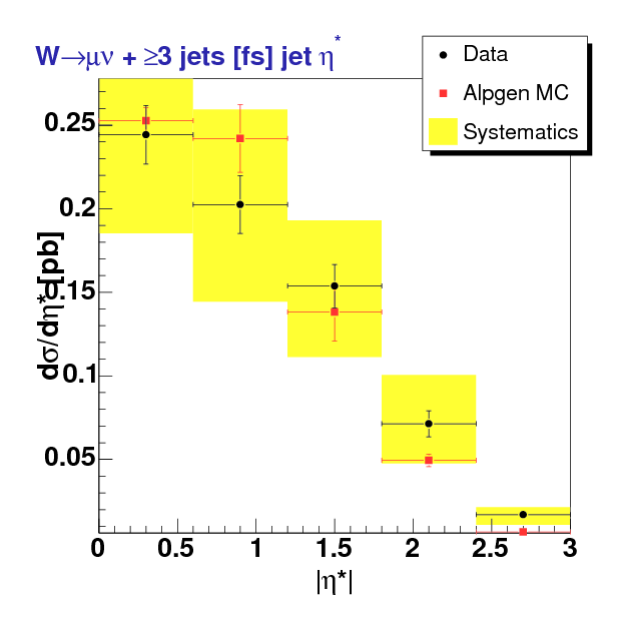


Figure 309:  $|\eta^*|$  Cross-section for  $W \to \mu\nu + \geq 3$  jets with  $\Delta \eta_{jj} > 2.0$ 

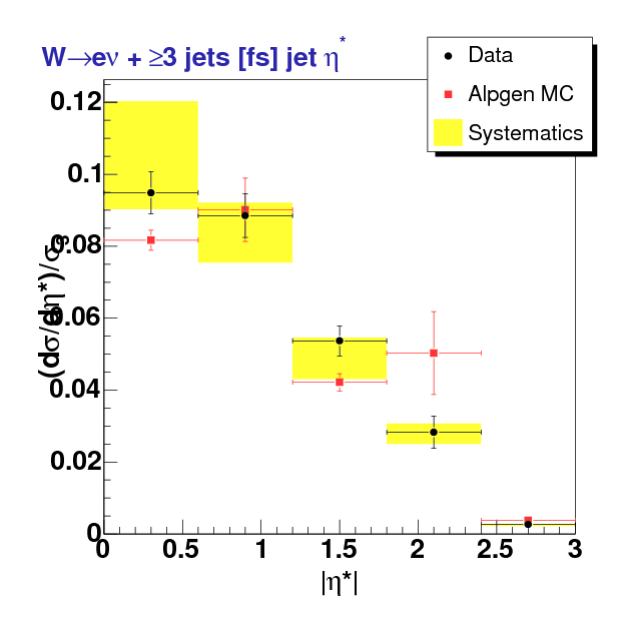


Figure 310:  $|\eta^*|$  Cross-section for  $W \to e\nu + \geq 3$  jets with  $\Delta \eta_{jj} > 2.0$ 

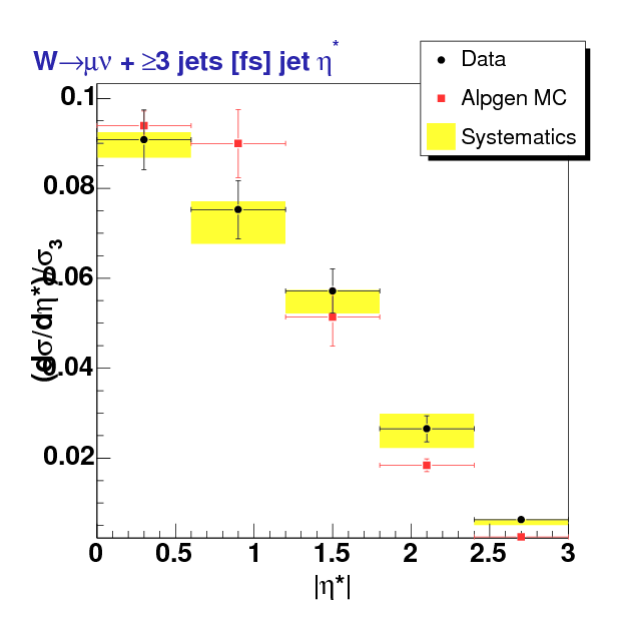


Figure 311:  $|\eta^*|$  Cross-section for  $W \to \mu\nu + \geq 3$  jets with  $\Delta \eta_{jj} > 2.0$ 

## References

- [1] B. Cooper, A. Messina, and D. Waters, CDF Internal Note 8046.
- [2] B. Cooper, A. Messina, and D. Waters, CDF Public Note 8381.
- [3] B. Cooper, Ph.D. thesis, University College London (2006); A. Messina, Ph.D. thesis, Universit'a di Roma La Sapienza (2004).
- [4] T. Aaltonen *et al.* (CDF Collaboration), Phys. Rev. D 77, 011108(R) (2008), hep-ex/0711.4044.
- [5] CDF Top Quark Physics Group (CDF internal webpage), http://www-cdf.fnal.gov/internal/physics/top/topnew.shtml.
- [6] Top Code (CDF internal webpage), http://www-cdf.fnal.gov/internal/physics/top/topcode.shtml; TopCodePrescriptions.FarmsTarball (CDF internal webpage) http://www-cdf.fnal.gov/tiki/tiki-index.php?page=TopCodePrescriptions.FarmsTarball.
- [7] ROOT http://root.cern.ch/; F. Rademakers and R. Brun, ROOT: An Object-Oriented Data Analysis Framework, Linux Journal, Issue 51, July (1998).
- [8] M. Martinez, GOOD RUN LIST v26 Page, http://www-cdf.fnal.gov/internal/dqm/goodrun/v26/goodv26.html.
- [9] Joint Physics Working Group, Joint Physics Scale Factor Class (CDF internal webpage), http://www-cdf.fnal.gov/internal/physics/joint\_physics/instructions/JPScaleFactor/index.html.
- [10] Joint Physics Working Group, *PerfIDia* (CDF internal webpage), http://ncdf70.fnal.gov:8001/PerfIDia/PerfIDia.html.
- [11] Top Group Gen 6 MC Production (CDF internal webpage), http://www-cdf.fnal.gov/internal/physics/top/RunIIMC/topmc6/index.shtml.
- [12] M.L. Mangano, M. Moretti, F. Piccinini, R. Pittau, A. Polosa, JHEP 0307:001,2003, http://arxiv.org/ps/hep-ph/0206293; M. L. Mangano, M. Moretti, F. Piccinini, R. Pittau, and A. Polosa, *ALPGEN V2.13*, mlm.home.cern.ch/mlm/alpgen.
- [13] Alpgen V2 validation for gen6, http://www-cdf.fnal.gov/tiki/tiki-index.php?page=Alpgen+gen6.
- [14] J. M. Campbell and R. K. Ellis, Phys. Rev. D 60, 113006 (1999), http://arxiv.org/abs/hep-ph/9905386v2; D. Acosta et al. CDF Collaboration, Phys. Rev. Lett. 94, 041803 (2005), http://arxiv.org/abs/hep-ex/0410008v2; U. Baur, T. Han and J. Ohnemus, Phys. Rev. D 57, 2823 (1998).
- [15] M. Cacciari, S. Frixione, M.L. Mangano, P. Nason, and G. Ridolfi, J. High Energy Phys. **04**, 068 (2004), http://arxiv.org/abs/hep-ph/0303085v1

- [16] CDF Top Quark Physics Public Results, http://www-cdf.fnal.gov/physics/new/top/public\_mass.html and http://www-cdf.fnal.gov/physics/new/top/public\_xsection.html.
- [17] D. Hare, E. Halkiadakis, and T. Spreitzer, CDF Internal Note **8614**; T. Spreitzer *et al.*, CDF Internal Note **7309**.
- [18] U. Grundler, L. Lovas, and A. Taffard, CDF Internal Note 8618; V. Martin, CDF Internal Note 7367.
- [19] CDF Run 2 Muon Detectors, http://www-cdfonline.fnal.gov/ops/cdf\_muon/chambers.html.
- [20] W. D. Dagenhart and D. Stentz, *Using CMX Muons*, CDF Internal Note **7989**.
- [21] V. Martin, CDF Internal Note **7031**, Appendix B.2.
- [22] K. Burkett, E. James, P. Beauchemin, and P. Savard, CDF Internal Note 8715; K. Burkett et al., CDF Internal Note 8722; T. Aaltonen et al., The CDF Collaboration, Phys. Rev. Lett. 101, 181602 (2008) http://arxiv.org/abs/0807.3132v1.
- [23] A. Sfyrla, CDF Internal Note 8989; A. Annovi et al., CDF Internal Note 9761; A. Annovi et al., CDF Internal Note 9807.
- [24] T. Aaltonen et al., The CDF Collaboration, Phys. Rev. Lett. 100, 071801 (2008) http://arxiv.org/abs/0710.4112; V. Bartsch et al., CDF Internal Note 8668; Private correspondence with Emily Nurse.
- [25] E. Lytken, A. Canepa, and D. Bortoletto, CDF Internal Note 8336.
- [26] This revelation was prompted by a study conducted by J. Strologas on the CMU efficiency between 7 and 3 cm; Private communication with John Strologas.
- [27] (CMIO and basic stubless muons details)
- [28] Private conversation with V. Martin; CDF Internal Note XXXX,
- [29] Midpoint paper and cdf info
- [30] Top (topNtuple) electron-jet removal
- [31] J. Strologas and S. Errede, CDF Internal Note **5877**; Also see [32]; Private communication with John Strologas.
- [32] K. Bloom, CDF Internal Note 6559.
- [33] Jet Energy and Resolution Group, http://www-cdf.fnal.gov/internal/physics/top/jets/corrections.html
- [34] A. Bhatti et al., Nucl. Instrum. Meth. A **566** 375-412 (2006) http://arxiv.org/abs/hep-ex/0510047v1.

- [35] Jet Energy Corrections How to Apply them, http://www-cdf.fnal.gov/internal/physics/top/jets/how-to-apply.html
- [36] Jet Energy Corrections Level 0, http://www-cdf.fnal.gov/internal/physics/top/jets/level0.html; L. Nodulman, CDF Internal Note 6728; H. S. Budd and W. K. Sakumoto, CDF Internal Note 6433; B. Heinemann, CDF Internal Note 6406; L. Nodulman, CDF Internal Note 6364.
- [37] J.-F. Arguin and B. Heinemann, CDF Internal Note 6239.
- [38] K. Hatakeyama and A. A. Bhatti, CDF Internal Note **7354**; A.A. Bhatti and K. Hatakeyama, CDF Internal Note **6854**.
- [39] A. Bhatti and F. Canelli, CDF Internal Note **7450**; J-F Arguin *et al.*, CDF Internal Note **6280**.
- [40] J.-F. Arguin and B. Heinemann, CDF Internal Note 6239.
- [41] J-F Arguin et al., CDF Internal Note 6565.
- [42] S. Pashapour and P. K. Sinervo, CDF Internal Note **7322**.
- [43] F. Canelli and B. Heinemann, CDF Internal Note **7451**.
- [44] Private correspondence with Kenichi Hatakeyama and Regis Lefevre via e-mail with Ben Kilminster and Jeannine Wagner.
- [45] Private communication with Tom Junk.
- [46] CDF Collaboration, Phys. Rev. Lett. **94** 091803 (2005), http://arxiv.org/abs/hep-ex/0406078v2; K. Copic, M. Schmitt, and V. Martin, CDF Internal Note **8195**.
- [47] http://root.cern.ch/root/htmldoc/TFractionFitter.html.
- [48] R. Barlow and C. Beeston, Comp. Phys. Comm. **77** 219-228 (1993); http://www.hep.man.ac.uk/~roger/hfrac.f.
- [49] Lepton Working Group, http://www-cdf.fnal.gov/internal/physics/joint\_physics/leptons/webpage.html.
- [50] D. Hare, E. Halkiadakis, and T. Spreitzer, CDF Internal Note 8614.
- [51] Results painstakingly taken from http://ncdf70.fnal.gov:8001/PerfIDia/HighElectronsID.
- [52] U. Grundler, L. Lovas, and A. Taffard, CDF Internal Note 8618.
- [53] Results painstakingly taken from http://ncdf70.fnal.gov:8001/PerfIDia/HighMuons.html.
- [54] In collaboration with John Strologas.
- [55] W. Sakumoto, CDF Internal Note **8318**; Efficiency of the Z-vertex cut of 60 cm, http://www-cdf.fnal.gov/internal/physics/joint\_physics/instructions/zvertex-efficiency.html

- [56] T. Affolder et al., The CDF Collaboration, Phys. Rev. D63, 072003 (2001).
- [57] PDF Uncertainties, http://www-cdf.fnal.gov/internal/physics/joint\_physics/instructions/PDFUncertainties/pdf.html
- [58] CTEQ (CTEQ6M + CTEQ5L) paper
- [59] MRST paper
- [60] K. Hagiwara *et al.*, Physical Review D66, 010001-1 (2002); PDG id table for fundamental particles, http://pdg.lbl.gov/mc\_particle\_id\_contents.html.
- [61] T. Affolder et al., The CDF Collaboration, Phys. Rev. D 63, 072003 (2001).
- [62] S. Miller, http://www-cdf.fnal.gov/internal/physics/joint\_physics/pdfs/.
- [63] O. Gonzalez and C. Rott, CDF Internal Note 7051.
- [64] D. H. Perkins, Introduction to High Energy Physics, 4th Edition, P. 174 (2000).
- [65] Literally, braking radiation.
- [66] Useful Diagrams of Top Signals and Backgrounds, http://www-d0.fnal.gov/Run2Physics/top/top-public\_web\_pages/top\_feynman\_diagrams.html
- [67] FSR detector results
- [68] CDF R measurement with  $72 \text{ pb}^{-1}$
- [69] BNLK predications
- [70] Zepenfiled  $\eta^*$

## A Cross-section Tables

This appendix gives the tabled version of the cross-section results presented in section 7. Each table includes the range (bin size) and cross-section for each cross-section histogram. The total and negative systematic error are included in the last pair of columns. For convenience we may used a simplified notation for the cross-section and the asymmetric error. Namely the cross-section will be  $\sigma$  and the total systematic noted by  $\pm \Delta \sigma$ . We will omit this notation for special ratio cross-sections like  $r_{\Delta \eta}$  and  $\sigma_{n+1}/\sigma_n$ .

We also present the complimentary set of tables for the normalized cross-sections. The central value follows dividing by the appropriate inclusive jet multiplicity cross-section but the total systematic needs to be presented to track the relative improvement in our description and understanding of the shape. Note however, the values cited here are not the reduced cross-section values and thus represents a total cross-section defined with the nominal acceptance definition. The acceptance restricted reduced cross-sections can be obtained using 46 and equation 34 on 177 (see sections 5.4 and 7.1 for further details).

In table 63 we reproduce a similar mapping table as was presented before showing our systematic results (section 6.10 table 61). Here we give each cross-section observable (including normalized cross-sections and other cross-section ratios), the corresponding section where the cross-section was defined/introduced, and then the table and companion figure number for each channel (electrons then muons).

Cross-section		$W \to e\nu$	$W \to e\nu$	$W \to \mu\nu$	$W \to \mu \nu$
Observable	Section	Table #	Figure #	Table #	Figure #
$\frac{\mathrm{d}\sigma}{\mathrm{d}n}$ †	7.2	64	258	65	259
$\frac{\mathrm{d}\sigma}{\mathrm{d}n}$	7.2	66	260	67	261
$\frac{\sigma_n}{\sigma_0}$	7.2	68	262	69	263
$\frac{\sigma_{n+1}}{\sigma_n}$	7.3	70	264	71	265
$\frac{\mathrm{d}\sigma}{\mathrm{d}p_{-T}^{1st}}$	7.4	72	266	76	270
$\frac{\mathrm{d}\sigma_{-T}}{\mathrm{d}p_{-T}^{2nd}}$	7.4	73	267	77	271
$\frac{\mathrm{d}\sigma}{\mathrm{d}p_{-T}^{3rd}}$	7.4	74	268	A	272
$\frac{\mathrm{d}\sigma}{\mathrm{d}p_{-T}^{4th}}$	7.4	75	269	79	273
$\frac{\mathrm{d}\sigma/\mathrm{d}p_{-T}^{1st}}{\sigma_{1}}$	7.4	80	274	84	278
$\frac{\mathrm{d}\sigma/\mathrm{d}p_{-T}^{2^{nd}}}{\sigma_2}$	7.4	81	275	85	279
$\frac{\mathrm{d}\sigma/\mathrm{d}p_{-T}^{3^{rd}}}{\sigma_{3}}$	7.4	82	276	86	280
$\frac{\mathrm{d}\sigma/\mathrm{d}p_{-T}^{4^{th}}}{\sigma_4}$	7.4	83	277	87	281
$\frac{\mathrm{d}\sigma}{\mathrm{d}m_{jj}}$	7.5	96	290	97	291
$\frac{\mathrm{d}\sigma/\mathrm{d}m_{jj}}{\sigma_2}$	7.5	98	292	99	293
$\frac{d\sigma}{dR_{dd}}$	7.6	100	294	101	295
$\frac{\mathrm{d}\sigma/\mathrm{d}R_{jj}}{\sigma_2}$	7.6	102	296	103	297
$\frac{\mathrm{d}\sigma_2}{\mathrm{d}\Delta\eta}$	7.7	104	298	108	299
$\frac{\mathrm{d}\Delta\eta}{\mathrm{d}\sigma_2/\mathrm{d}\Delta\eta}$	7.7	106	300	110	301
$\frac{\mathrm{d}\sigma_3}{\mathrm{d}\Delta\eta}$	7.7	105	302	109	303
$\frac{\mathrm{d}\sigma_3/\mathrm{d}\Delta\eta}{\sigma_3}$	7.7	107	304	111	305
$r_{\Delta\eta}$ (Eq. 86)	7.7	112	306	113	307
$\frac{\mathrm{d}\sigma}{\mathrm{d}n^*}$	7.8	114	308	115	309
$\frac{\mathrm{d}\sigma/\mathrm{d}\eta^*}{\sigma_3}$	7.8	116	310	117	311

Table 63: The mapping of each cross-section table with its corresponding cross-section figure for each cross-section observable. †: The first jet multiplicity results are defined at the production level without reduce acceptance (default for all other observables).

	Cross-section	Total Systematic
$\geq n$ jets	$\sigma_n \text{ (pb)}$	$\Delta \sigma_n \text{ (pb)}$
0	2707	$^{+70.}_{-62.} \pm 162.$
1	220.	$\frac{+30.}{-24.} \pm 13.$
2	26.2	$^{+70.}_{-62.} \pm 162.$ $^{+30.}_{-24.} \pm 13.$ $^{+5.8}_{-4.5} \pm 1.6$ $^{+1.06}_{-1.01} \pm 0.19$
3	3.18	$^{+1.06}_{-0.71} \pm 0.19$
4	0.41	$^{+0.23}_{-0.11} \pm 0.02$

Table 64:  $W \to e\nu$  jet multiplicity cross-section for 0-4 inclusive number of jets. This is the production level cross-section version of table 66 and was shown in figure 258 on page 229.

	Cross-section	Total Systematic
$\geq n$ jets	$\sigma_n \text{ (pb)}$	$\Delta \sigma_n \text{ (pb)}$
0	2715	$^{+86.}_{-86.} \pm 163.$
1	271.	$^{+86.}_{-86.} \pm 163.$ $^{+33.}_{-29.} \pm 16.$ $^{+6.3}_{+6.3} \pm 2.1$
2	35.6	$^{+\overline{6.3}}_{-5.6} \pm 2.1$
3	4.68	$^{+1.16}_{-0.95} \pm 0.28$
4	0.69	$^{+0.23}_{-0.18} \pm 0.04$

Table 65:  $W \to \mu\nu$  jet multiplicity cross-section for 0-4 inclusive number of jets. This is the production level cross-section version of table 67 and was shown in figure 259 on page 229.

	Cross-section	Total Systematic
$\geq n$ jets	$\sigma_n$ (pb)	$\Delta \sigma_n \text{ (pb)}$
0	1575	$^{+82}_{-79} \pm 94$
1	128	$^{+18}_{-15} \pm 7.7$
2	15.1	$^{+82}_{-79} \pm 94$ $^{+18}_{-15} \pm 7.7$ $^{+3.4}_{-2.7} \pm 0.9$
3	1.82	$^{+0.61}_{-0.42} \pm 0.11$
4	0.232	$^{+0.13}_{-0.067} \pm 0.014$

Table 66:  $W \to e\nu$  jet multiplicity cross-section for 0-4 inclusive number of jets. This is a table version of plot 260 on page 230.

	Cross-section	Total Systematic
$\geq n$ jets	$\sigma_n \text{ (pb)}$	$\Delta \sigma_n \text{ (pb)}$
0	1603	$^{+66}_{-66} \pm 96$
1	158	$^{+20}_{-18} \pm 9.5$
2	20.7	$^{+66}_{-66} \pm 96$ $^{+20}_{-18} \pm 9.5$ $^{+3.7}_{-3.3} \pm 1.2$ $^{+0.67}_{-0.67} \pm 0.16$
3	2.69	$^{+0.67}_{-0.56} \pm 0.16$
4	0.394	$\begin{array}{c} -0.56 \pm 0.10 \\ +0.13 \\ -0.11 \pm 0.024 \end{array}$

Table 67:  $W \to \mu\nu$  jet multiplicity cross-section for 0-4 inclusive number of jets. This is a table version of plot 261 on page 230.

	Normalized Cross-section	Total
$\geq n$ jets	$\sigma_n/\sigma_0$	Systematic
0	1	+0 -0
1	0.0811	$ \begin{array}{r} -0 \\ +0.0069 \\ -0.0058 \end{array} $
2	0.00957	$ \begin{array}{r} -0.0058 \\ +0.0016 \\ -0.0013 \end{array} $
3	0.00116	+0.00031 $-0.00022$
4	0.000147	+7.3e - 05 $-3.7e - 05$

Table 68:  $W \to e\nu$  jet multiplicity cross-section normalized to the total inclusive cross-section. This is a table version of plot 262 on page 231.

	Normalized Cross-section	Total
$\geq n$ jets	$\sigma_n/\sigma_0$	Systematic
0	1	+0 -0
1	0.0985	+0.0081 -0.0073
2	0.0129	$ \begin{array}{r} -0.0073 \\ +0.0017 \\ -0.0016 \end{array} $
3	0.00168	$ \begin{array}{r} -0.0016 \\ +0.00034 \\ -0.00029 \end{array} $
4	0.000246	+6.9e - 05 -5.8e - 05

Table 69:  $W \to \mu\nu$  jet multiplicity cross-section normalized to the total inclusive cross-section. This is a table version of plot 263 on page 231.

	Cross-section Ratio	Total
$\geq n$ jets	$rac{\sigma_{n+1}}{\sigma_n}$	Systematic
0	0.0811	$+0.0095 \\ -0.0084$
1	0.118	$+0.0094 \\ -0.0086$
2	0.121	$+0.011 \\ -0.0071$
3	0.127	+0.023 $-0.0089$

Table 70:  $W \to e\nu$  jet multiplicity ratio  $(\sigma_{n+1}/\sigma_n)$  with n the number of inclusive jets. This is a table version of plot 264 on page 232.

	Cross-section Ratio	Total
$\geq n$ jets	$\frac{\sigma_{n+1}}{\sigma_n}$	Systematic
0	0.0985	$+0.011 \\ -0.01$
1	0.131	$+0.0066 \\ -0.0077$
2	0.13	$+0.0081 \\ -0.0073$
3	0.146	+0.013 $-0.013$

Table 71:  $W \to \mu\nu$  jet multiplicity ratio  $(\sigma_{n+1}/\sigma_n)$  with n the number of inclusive jets. This is a table version of plot 265 on page 233.

$p_T$ range (GeV/c)	$\sigma \text{ (pb/(GeV/c))}$	$\Delta \sigma \; (\text{pb/(GeV/c}))$
20-25	7.98	$^{+1}_{-1.1} \pm 0.48$
25-30	5.2	$^{+0.64}_{-0.73} \pm 0.31$
30-35	3.44	$+0.44 \pm 0.21$
35-40	2.39	$\begin{bmatrix} -0.4 & \pm & 0.21 \\ +0.27 & \pm & 0.14 \end{bmatrix}$
40-45	1.69	$^{+0.19}_{-0.2} \pm 0.1$
45-50	1.2	$^{+0.13}_{-0.14} \pm 0.072$
50-55	0.914	$^{+0.097}_{-0.1} \pm 0.055$
55-60	0.679	$^{+0.054}_{-0.067} \pm 0.041$
60-65	0.511	$^{+0.048}_{-0.067} \pm 0.031$
65-70	0.377	$^{+0.033}_{-0.032} \pm 0.023$
70-75	0.316	$^{+0.022}_{-0.038} \pm 0.019$
75-80	0.229	$^{+0.015}_{-0.022} \pm 0.014$
80-85	0.196	$^{+0.014}_{-0.021} \pm 0.012$
85-90	0.147	$^{+0.013}_{-0.0099} \pm 0.0088$
90-95	0.129	$^{+0.015}_{-0.025} \pm 0.0078$
95-105	0.0773	$^{+0.0079}_{-0.012} \pm 0.0046$
105-120	0.0478	$\left(\begin{array}{c} +0.0073 \\ -0.006 \end{array}\right) \pm 0.0029$
120-140	0.0238	$^{+0.0022}_{-0.0048} \pm 0.0014$
140-175	0.00785	$\begin{pmatrix} +0.0017 \\ -0.0014 \end{pmatrix} \pm 0.00047$
175-230	0.00185	$\left  \begin{array}{c} +0.00026 \\ -0.00028 \end{array} \right  \pm 0.00011$
230-430	0.000157	$^{+2.5e-05}_{-3.2e-05} \pm 9.4e-06$

Table 72: The leading jet  $p_T$  cross-section for  $W \to e\nu + \ge 1$  inclusive jet. This is a table version of plot 266 on page 234.

$p_T$ range (GeV/c)	$\sigma \text{ (pb/(GeV/c))}$	$\Delta \sigma \; (\mathrm{pb/(GeV/c)})$
20-25	1.23	$^{+0.31}_{-0.27} \pm 0.074$
25-30	0.704	$^{+0.12}_{-0.14} \pm 0.042$
30-35	0.377	$^{+0.058}_{-0.07} \pm 0.023$
35-40	0.226	$\begin{vmatrix} +0.04 \\ -0.029 \\ \pm 0.014 \end{vmatrix}$
40-45	0.159	$^{+0.018}_{-0.02} \pm 0.0095$
45-50	0.112	$\left  \begin{array}{c} +0.014 \\ -0.025 \end{array} \pm 0.0067 \right $
50-55	0.0671	$^{+0.012}_{-0.01} \pm 0.004$
55-60	0.0518	$\begin{vmatrix} +0.0055 \\ -0.0075 \\ \pm 0.0031 \end{vmatrix}$
60-65	0.0351	$\left  \begin{array}{c} +0.0048 \\ -0.0048 \end{array} \pm 0.0021 \right $
65-75	0.0243	$\begin{vmatrix} +0.0018 \\ -0.0029 \\ \pm 0.0015 \end{vmatrix}$
75-85	0.018	$\begin{vmatrix} +0.0013 \\ -0.0017 \\ \pm 0.0011 \end{vmatrix}$
85-100	0.00858	$\begin{vmatrix} +0.0014 \\ -0.0025 \end{vmatrix} \pm 0.00051 \end{vmatrix}$
100-135	0.00257	$\begin{bmatrix} +0.00021 \\ -0.00023 \\ \pm 0.00015 \end{bmatrix}$
135-260	0.000339	$\frac{+3.3e-05}{-3.3e-05} \pm 2e-05$

Table 73: The second leading jet  $p_T$  cross-section for  $W \to e\nu + \ge 2$  inclusive jets. This is a table version of plot 267 on page 235.

$p_T$ range (GeV/c)	$\sigma  (\text{pb/(GeV/c}))$	$\Delta \sigma \; (\mathrm{pb/(GeV/c)})$
20-25	0.187	$^{+0.064}_{-0.052} \pm 0.011$
25-30	0.0839	$\begin{vmatrix} +0.024 \\ -0.019 \end{vmatrix} \pm 0.005$
30-35	0.0419	$\begin{bmatrix} +0.0091 \\ -0.01 \end{bmatrix} \pm 0.0025$
35-40	0.0249	$\begin{bmatrix} +0.0048 \\ -0.0032 \pm 0.0015 \end{bmatrix}$
40-45	0.018	$\begin{bmatrix} +0.003 \\ -0.0071 \\ \end{bmatrix} \pm 0.0011 $
45-50	0.0094	$\left[ \begin{array}{c} +0.0022 \\ -0.0037 \end{array} \pm 0.00056 \right]$
50-70	0.00298	$\begin{bmatrix} +0.00093 \\ -0.00058 \end{bmatrix} \pm 0.00018$
70-170	0.000199	$\begin{bmatrix} +2.3e-05 \\ -2e-05 \end{bmatrix} \pm 1.2\text{e-}05 \end{bmatrix}$

Table 74: The third leading jet  $p_T$  cross-section for  $W \to e\nu + \ge 3$  inclusive jets. This is a table version of plot 268 on page 235.

$p_T$ range (GeV/c)	$\sigma \; (pb/(GeV/c))$	$\Delta \sigma \; (\mathrm{pb/(GeV/c}))$
20-25	0.0282	$^{+0.013}_{-0.0095} \pm 0.0017$
25-35	0.00709	$\begin{bmatrix} +0.0049 \\ -0.003 \end{bmatrix} \pm 0.00043$
35-50	0.00229	$\begin{bmatrix} +0.00067 \\ -0.00097 \\ \end{bmatrix} \pm 0.00014$
50-90	0.00017	$\begin{array}{c} +7.9e-05 \\ -0.00012 \\ \end{array} \pm 1e-05 \end{array}$

Table 75: The fourth leading jet  $p_T$  cross-section for  $W \to e\nu + \ge 4$  inclusive jets. This is a table version of plot 269 on page 236.

$p_T$ range (GeV/c)	$\sigma \; (\mathrm{pb/(GeV/c}))$	$\Delta \sigma \; (\mathrm{pb/(GeV/c)})$
20-25	9.75	$^{+1.2}_{-1.3} \pm 0.59$
25-30	6.32	$^{+0.69}_{-0.76} \pm 0.38$
30-35	4.18	$^{+0.49}_{-0.56} \pm 0.25$
35-40	2.89	$^{+0.26}_{-0.32} \pm 0.17$
40-45	2.12	$^{+0.19}_{-0.25} \pm 0.13$
45-50	1.49	$^{+0.14}_{-0.17} \pm 0.089$
50-55	1.17	$\frac{+0.093}{-0.14} \pm 0.07$
55-60	0.867	$^{+0.088}_{-0.081} \pm 0.052$
60-65	0.623	$^{+0.064}_{-0.057} \pm 0.037$
65-70	0.529	$^{+0.03}_{-0.04} \pm 0.032$
70-75	0.417	$^{+0.024}_{-0.033} \pm 0.025$
75-80	0.311	$^{+0.025}_{-0.026} \pm 0.019$
80-85	0.25	$^{+0.022}_{-0.019} \pm 0.015$
85-90	0.205	$^{+0.014}_{-0.03} \pm 0.012$
90-95	0.161	$^{+0.012}_{-0.0089} \pm 0.0097$
95-105	0.13	$\left[\begin{array}{c} +0.0099 \\ -0.018 \end{array}\right] \pm 0.0078$
105-120	0.068	$\left  \begin{array}{c} +0.0085 \\ -0.0046 \end{array} \pm 0.0041 \right $
120-140	0.0419	$\frac{+0.0027}{-0.0041} \pm 0.0025$
140-175	0.0159	$^{+0.0018}_{-0.0022} \pm 0.00096$
175-230	0.00367	$\begin{bmatrix} +0.00044 \\ -0.00037 \\ \end{bmatrix} \pm 0.00022$
230-430	0.000355	$+5e-05 \\ -5e-05 \pm 2.1e-05$

Table 76: The leading jet  $p_T$  cross-section for  $W \to \mu\nu + \geq 1$  inclusive jet. This is a table version of plot 270 on page 236.

$p_T$ range (GeV/c)	$\sigma \text{ (pb/(GeV/c))}$	$\Delta \sigma \; (\text{pb/(GeV/c}))$
20-25	1.68	$^{+0.31}_{-0.35} \pm 0.1$
25-30	0.89	$^{+0.14}_{-0.15} \pm 0.053$
30-35	0.525	$^{+0.059}_{-0.078} \pm 0.031$
35-40	0.339	$\begin{array}{c} +0.046 \\ -0.049 \pm 0.02 \end{array}$
40-45	0.21	$^{+0.024}_{-0.025} \pm 0.013$
45-50	0.156	$^{+0.018}_{-0.022} \pm 0.0094$
50-55	0.119	$\begin{vmatrix} +0.0074 \\ -0.0081 \end{vmatrix} \pm 0.0071$
55-60	0.0741	$\begin{vmatrix} +0.0084 \\ -0.0093 \pm 0.0044 \end{vmatrix}$
60-65	0.0552	$\begin{vmatrix} +0.006 \\ -0.0068 \end{vmatrix} \pm 0.0033$
65-75	0.0381	$\begin{vmatrix} +0.0024 \\ -0.0024 \\ \pm 0.0023 \end{vmatrix}$
75-85	0.0226	$\begin{vmatrix} +0.002 \\ -0.0054 \\ \pm 0.0014 \end{vmatrix}$
85-100	0.0141	$\begin{bmatrix} +0.0012 \\ -0.00085 \end{bmatrix} \pm 0.00084 \end{bmatrix}$
100-135	0.00427	$\begin{bmatrix} +0.00033 \\ -0.00041 \end{bmatrix} \pm 0.00026 \end{bmatrix}$
135-260	0.000425	$\begin{bmatrix} +6.6e-05 \\ -6.8e-05 \end{bmatrix} \pm 2.5 \text{e-}05 \end{bmatrix}$

Table 77: The second leading jet  $p_T$  cross-section for  $W \to \mu\nu + \geq 2$  inclusive jets. This is a table version of plot 271 on page 237.

$p_T$ range (GeV/c)	$\sigma  (\text{pb/(GeV/c}))$	$\Delta \sigma \; (\mathrm{pb/(GeV/c}))$
20-25	0.265	$^{+0.061}_{-0.071} \pm 0.016$
25-30	0.132	$^{+0.028}_{-0.025} \pm 0.0079$
30-35	0.0674	$^{+0.013}_{-0.011} \pm 0.004$
35-40	0.0401	$^{+0.0055}_{-0.0089} \pm 0.0024$
40-45	0.0213	$^{+0.0093}_{-0.0057} \pm 0.0013$
45-50	0.0116	$^{+0.0066}_{-0.0035} \pm 0.0007$
50-70	0.00461	$\left  \begin{array}{c} +0.00073 \\ -0.0011 \end{array} \right  \pm 0.00028$
70-170	0.000265	$\begin{vmatrix} +2.5e-05 \\ -2.9e-05 \end{vmatrix} \pm 1.6e-05$

Table 78: The third leading jet  $p_T$  cross-section for  $W \to \mu\nu + \geq 3$  inclusive jets. This is a table version of plot 272 on page 237.

$p_T$ range (GeV/c)	$\sigma \; (\mathrm{pb/(GeV/c}))$	$\Delta \sigma \; (\mathrm{pb/(GeV/c}))$
20-25	0.0451	$^{+0.015}_{-0.017} \pm 0.0027$
25-35	0.0139	$\left  \begin{array}{c} +0.005 \\ -0.0045 \end{array} \pm 0.00083 \right $
35-50	0.00254	$ \begin{array}{c} +0.005 \\ -0.0045 \\ +0.0008 \\ -0.0015 \\ -0.0015 \end{array} \pm 0.00015 $
50-90	0.000242	$\begin{vmatrix} +6.3e-05 \\ -0.00014 \end{vmatrix} \pm 1.5e-05 \begin{vmatrix} +6.3e-05 \\ -0.00014 \end{vmatrix}$

Table 79: The fourth leading jet  $p_T$  cross-section for  $W \to \mu\nu + \ge 4$  inclusive jets. This is a table version of plot 273 on page 238.

$p_T$ range (GeV/c)	$\sigma (1/(\text{GeV/c}))$	$\Delta \sigma \ (1/({\rm GeV/c}))$
20-25	0.0624	$+0.00059 \\ -0.0013$
25-30	0.0407	$+0.00067 \\ -0.001$
30-35	0.027	$+5.7e^{-0.00}$ -0.00034
35-40	0.0187	+0.00037 $-0.0005$
40-45	0.0132	+5.2e - 07 $-0.00036$
45-50	0.00939	+6e-05 $-0.00025$
50-55	0.00716	+3.3e-05 $-0.00022$
55-60	0.00532	$ \begin{array}{r} +0.00012 \\ -0.00029 \end{array} $
60-65	0.004	+5.3e-05 $-0.00017$
65-70	0.00295	+0.00012 $-0.00014$
70-75	0.00248	+3.8e - 06 $-0.00015$
75-80	0.0018	+4.9e-05 $-0.00012$
80-85	0.00153	+1.7e - 05 $-9.2e - 05$
85-90	0.00115	+6.7e - 05 -5.3e - 05
90-95	0.00101	+2.3e-05
95-105	0.000606	$ \begin{array}{r} -8.7e - 05 \\ +2.1e - 05 \\ -2.5e - 05 \end{array} $
105-120	0.000374	+4e-06 -3.1e-06
120-140	0.000186	+8.1e - 06 $-1.8e - 05$
140-175	6.15e-05	+3.7e - 06 -4.1e - 06
175-230	1.45e-05	$\begin{array}{r} -4.1e - 00 \\ +7.3e - 09 \\ -5.2e - 07 \end{array}$
230-430	1.23e-06	$\begin{array}{c} -3.2e - 07 \\ +2.2e - 08 \\ -1.2e - 07 \end{array}$

Table 80: The leading jet  $p_T$  cross-section for  $W \to e\nu + \ge 1$  inclusive jet normalized to the inclusive  $\ge 1$  jet multiplicity cross-section. This is a table version of plot 274 on page 238.

$p_T$ range (GeV/c)	$\sigma (1/(\text{GeV/c}))$	$\Delta \sigma \ (1/(\text{GeV/c}))$
20-25	0.0819	$+0.0014 \\ -0.0036$
25-30	0.0467	$\begin{array}{r} +0.0012 \\ -0.0023 \end{array}$
30-35	0.025	$+0.00015 \\ -0.0015$
35-40	0.015	$+0.00096 \\ -0.00061$
40-45	0.0105	+0.00067 $-0.00099$
45-50	0.0074	$+0.0004 \\ -0.00062$
50-55	0.00445	$+0.00017 \\ -0.00016$
55-60	0.00344	+0.00015 $-0.00034$
60-65	0.00233	+0.00012 $-0.00017$
65-75	0.00162	$+0.00012 \\ -0.0002$
75-85	0.00119	$+0.00012 \\ -0.00015$
85-100	0.00057	+2.8e-05 $-7.8e-05$
100-135	0.000171	+1.9e - 05 -2e - 05
135-260	2.25e-05	+2.3e - 06 $-2.4e - 06$

Table 81: The second leading jet  $p_T$  cross-section for  $W \to e\nu + \ge 2$  inclusive jets normalized to the inclusive  $\ge 2$  jets multiplicity cross-section. This is a table version of plot 275 on page 239.

$p_T$ range (GeV/c)	$\sigma (1/(\text{GeV/c}))$	$\Delta \sigma (1/(\text{GeV/c}))$
20-25	0.103	+0.00029 -0.006
25-30	0.046	$\begin{array}{c} -0.00024 \\ +0.0016 \end{array}$
30-35	0.023	$\begin{array}{c} -0.0010 \\ +0.00025 \\ -0.002 \end{array}$
35-40	0.0137	+0.0018 $-0.0015$
40-45	0.00988	$\begin{array}{c} -0.0013 \\ +0.0012 \\ -0.0021 \end{array}$
45-50	0.00515	$ \begin{array}{r} -0.0021 \\ +0.00039 \\ -0.0011 \end{array} $
50-70	0.00163	-0.0011 +7.7e-05 -3e-05
70-170	0.000109	+1.9e-05 $-1.8e-05$

Table 82: The third leading jet  $p_T$  cross-section for  $W \to e\nu + \ge 3$  inclusive jets normalized to the inclusive  $\ge 3$  jets multiplicity cross-section. This is a table version of plot 276 on page 239.

$p_T$ range (GeV/c)	$\sigma (1/(\text{GeV/c}))$	$\Delta \sigma (1/(\text{GeV/c}))$
20-25	0.122	$+0.0084 \\ -0.0089$
25-35	0.0306	$^{+0.0022}_{-0.0057}$
35-50	0.00988	$+0.0018 \\ -0.0019$
50-90	0.000731	-0.0019 +5e-05 -0.00045

Table 83: The fourth leading jet  $p_T$  cross-section for  $W \to e\nu + \ge 4$  inclusive jets normalized to the inclusive  $\ge 4$  jets multiplicity cross-section. This is a table version of plot 277 on page 240.

$p_T$ range (GeV/c)	$\sigma (1/(\text{GeV/c}))$	$\Delta \sigma \ (1/({\rm GeV/c}))$
20-25	0.0617	$+0.00033 \\ -0.0017$
25-30	0.04	+0.00037 $-0.00062$
30-35	0.0265	$+0.0002\overline{2} \\ -0.00065$
35-40	0.0183	+3.3e - 05 -0.00057
40-45	0.0134	+0.0001 $-0.00044$
45-50	0.00944	+4.3e - 05 -0.00025
50-55	0.00738	+4.6e - 05 $-0.0003$
55-60	0.00549	$+0.00011 \\ -0.00012$
60-65	0.00394	$+8.8e - 05 \\ -8e - 05$
65-70	0.00335	+0.00013 $-0.0002$
70-75	0.00264	+9.5e-05 $-0.00016$
75-80	0.00197	+6e-05 $-8e-05$
80-85	0.00159	+6.7e - 05 $-5.6e - 05$
85-90	0.0013	+5.1e-05 -6.7e-05
90-95	0.00102	+6.5e-05
95-105	0.00082	$ \begin{array}{r} -4.9e - 05 \\ +2.5e - 05 \\ -3.6e - 05 \end{array} $
105-120	0.000431	$\begin{array}{c} -3.0e-05 \\ +2.1e-05 \\ -6.7e-07 \end{array}$
120-140	0.000265	-0.7e-07 +4e-06 -1.5e-05
140-175	0.000101	+1.2e-06
175-230	2.32e-05	$ \begin{array}{r} -3.3e - 06 \\ +3.1e - 07 \\ -1.5e - 07 \end{array} $
230-430	2.25e-06	-1.3e - 07 +2.7e - 08 -7.8e - 08

Table 84: The leading jet  $p_T$  cross-section for  $W \to \mu\nu + \ge 1$  inclusive jet normalized to the inclusive  $\ge 1$  jet multiplicity cross-section. This is a table version of plot 278 on page 240.

$p_T$ range (GeV/c)	$\sigma (1/(\text{GeV/c}))$	$\Delta \sigma \ (1/(\text{GeV/c}))$
20-25	0.0814	$+0.00053 \\ -0.0045$
25-30	0.0431	+0.00039 -0.00076
30-35	0.0254	$+0.00034 \\ -0.0014$
35-40	0.0164	+0.00031 $-0.00059$
40-45	0.0102	$+0.00051 \\ -0.00056$
45-50	0.00754	$\begin{array}{c} -0.00030 \\ +0.00016 \\ -0.00041 \end{array}$
50-55	0.00574	$\begin{array}{r} -0.00041 \\ +0.00063 \\ -0.00057 \end{array}$
55-60	0.00359	$\begin{array}{r} -0.00031 \\ +0.00015 \\ -0.0002 \end{array}$
60-65	0.00267	$\begin{array}{r} -0.0002\\ +0.00012\\ -0.00016 \end{array}$
65-75	0.00185	$\begin{array}{c} -0.00010 \\ +0.00021 \\ -0.00018 \end{array}$
75-85	0.00109	$-0.00013 \\ +8.5e-05 \\ -0.0001$
85-100	0.000681	$-0.0001 \\ +8.1e-05 \\ -5.4e-05$
100-135	0.000207	$-3.4e - 05 \\ +1.6e - 05 \\ -1.8e - 05$
135-260	2.06e-05	$-1.3e - 03 \\ +1.1e - 08 \\ -4.2e - 07$

Table 85: The second leading jet  $p_T$  cross-section for  $W \to \mu\nu + \geq 2$  inclusive jets normalized to the inclusive  $\geq 2$  jets multiplicity cross-section. This is a table version of plot 279 on page 241.

$p_T$ range (GeV/c)	$\sigma (1/({\rm GeV/c}))$	$\Delta \sigma \ (1/({\rm GeV/c}))$
20-25	0.0987	$+0.0017 \\ -0.0077$
25-30	0.049	$+0.001 \\ -0.0016$
30-35	0.025	$^{+0.0012}_{-0.0012}$
35-40	0.0149	$+0.00028 \\ -0.0013$
40-45	0.0079	$+0.0012 \\ -0.00059$
45-50	0.00432	$+0.0011 \\ -0.00049$
50-70	0.00171	+5.6e-05 $-0.00013$
70-170	9.83e-05	-0.00013 +1.2e-05 -1.2e-05

Table 86: The third leading jet  $p_T$  cross-section for  $W \to \mu\nu + \geq 3$  inclusive jets normalized to the inclusive  $\geq 3$  jets multiplicity cross-section. This is a table version of plot 280 on page 241.

$p_T$ range (GeV/c)	$\sigma (1/(\text{GeV/c}))$	$\Delta \sigma (1/(\text{GeV/c}))$
20-25	0.115	+0.00033 $-0.016$
25-35	0.0353	$+0.00059 \\ -0.0026$
35-50	0.00645	+9.9e-05 -0.0028
50-90	0.000615	+3.5e - 0.0000000000000000000000000000000000

Table 87: The fourth leading jet  $p_T$  cross-section for  $W \to \mu\nu + \ge 4$  inclusive jets normalized to the inclusive  $\ge 4$  jets multiplicity cross-section. This is a table version of plot 281 on page 242.

$p_T$ range (GeV/c)	Data/Theory	Total Systematic
20-25	1.02	$^{+0.13}_{-0.14}$
25-30	1.01	$ \begin{array}{r} -0.14 \\ +0.12 \\ -0.14 \end{array} $
30-35	1.01	$+0.13 \\ -0.12$
35-40	0.993	$+0.11 \\ -0.14$
40-45	0.982	$+0.11 \\ -0.12$
45-50	0.946	$+0.11 \\ -0.11$
50-55	0.962	$\begin{array}{c} -0.11 \\ +0.1 \\ -0.11 \end{array}$
55-60	0.979	$ \begin{array}{r} -0.11 \\ +0.077 \\ -0.097 \end{array} $
60-65	1.01	$\begin{array}{r} -0.097 \\ +0.095 \\ -0.13 \end{array}$
65-70	0.935	$\begin{array}{r} -0.13 \\ +0.083 \\ -0.078 \end{array}$
70-75	1.01	$\begin{array}{c} -0.073 \\ +0.071 \\ -0.12 \end{array}$
75-80	0.955	$\begin{array}{c} -0.12 \\ +0.064 \\ -0.091 \end{array}$
80-85	0.996	$\begin{array}{c} -0.091 \\ +0.073 \\ -0.11 \end{array}$
85-90	0.933	$+0.083 \\ -0.063$
90-95	1.05	$-0.003 \\ +0.12 \\ -0.2$
95-105	0.882	$\begin{array}{c} -0.2 \\ +0.091 \\ -0.14 \end{array}$
105-120	0.853	$-0.14 \\ +0.13 \\ -0.11$
120-140	0.949	$\begin{array}{c} -0.11 \\ +0.087 \\ -0.19 \end{array}$
140-175	0.77	$-0.19 \\ +0.16 \\ -0.14$
175-230	0.872	$-0.14 \\ +0.12 \\ -0.13$
230-430	0.856	$-0.13 \\ +0.14 \\ -0.17$

Table 88: The leading jet  $p_T$  cross-section for  $W \to e\nu + \ge 1$  inclusive jets. This is a table version of plot 282 on page 243.

$p_T$ range (GeV/c)	Data/Theory	Total Systematic
20-25	0.985	$^{+0.24}_{-0.21}$
25-30	1.03	$+0.17 \\ -0.21$
30-35	0.928	$+0.\overline{14} \\ -0.17$
35-40	0.968	$+0.17 \\ -0.12$
40-45	1.09	$\begin{array}{c} -0.12 \\ +0.12 \\ -0.14 \end{array}$
45-50	1.11	$\begin{array}{c} -0.14 \\ +0.14 \\ -0.25 \end{array}$
50-55	0.964	$\begin{array}{c} -0.25 \\ +0.18 \\ -0.14 \end{array}$
55-60	1.06	$\begin{array}{c} -0.14 \\ +0.11 \\ -0.15 \end{array}$
60-65	1.02	$\begin{array}{c} -0.13 \\ +0.14 \\ -0.14 \end{array}$
65-75	1.09	$\begin{array}{c} -0.14 \\ +0.081 \\ -0.13 \end{array}$
75-85	1.46	$\begin{array}{c} -0.13 \\ +0.1 \\ -0.14 \end{array}$
85-100	1.32	$\begin{array}{c} -0.14 \\ +0.22 \\ -0.39 \end{array}$
100-135	1	$\begin{array}{c} -0.39 \\ +0.083 \\ -0.09 \end{array}$
135-260	1.39	$\begin{array}{c} -0.09 \\ +0.13 \\ -0.14 \end{array}$

Table 89: The second leading jet  $p_T$  cross-section for  $W \to e\nu + \ge 2$  inclusive jets. This is a table version of plot 283 on page 244.

$p_T$ range (GeV/c)	Data/Theory	Total Systematic
20-25	0.944	$+0.32 \\ -0.26$
25-30	0.982	$+0.\overline{28} \\ -0.22$
30-35	1.02	$+0.\overline{22} \\ -0.24$
35-40	1.12	$+0.\overline{22} \\ -0.15$
40-45	1.49	$+0.25 \\ -0.59$
45-50	1.36	$+0.32 \\ -0.54$
50-70	1.28	$+0.4 \\ -0.25$
70-170	1.7	$\begin{array}{c} -0.23 \\ +0.19 \\ -0.17 \end{array}$

Table 90: The third leading jet  $p_T$  cross-section for  $W \to e\nu + \ge 3$  inclusive jets. This is a table version of plot 284 on page 244.

$p_T$ range (GeV/c)	Data/Theory	Total Systematic
20-25	0.97	+0.44 -0.33
25-35	0.954	$-0.33 \\ +0.65 \\ 0.4$
35-50	1.98	$-0.4 \\ +0.58$
50-90	1.98	$-0.84 \\ +0.92$
50-90	1.90	-1.4

Table 91: The forth leading jet  $p_T$  cross-section for  $W \to e\nu + \ge 4$  inclusive jets. This is a table version of plot 285 on page 245.

$p_T$ range (GeV/c)	Data/Theory	Total Systematic
20-25	1.02	$^{+0.12}_{-0.14}$
25-30	1.02	$+0.11 \\ -0.12$
30-35	0.988	$+0.1\overline{2} \\ -0.13$
35-40	0.987	+0.09 -0.11
40-45	0.995	$+0.088 \\ -0.12$
45-50	0.948	$+0.092 \\ -0.11$
50-55	0.974	$^{-0.11}_{+0.078}_{-0.11}$
55-60	0.971	+0.099 $-0.09$
60-65	0.895	$\begin{array}{c} -0.09 \\ +0.093 \\ -0.082 \end{array}$
65-70	0.973	$\begin{array}{c} -0.032 \\ +0.056 \\ -0.074 \end{array}$
70-75	0.999	$\begin{array}{r} -0.074 \\ +0.058 \\ -0.08 \end{array}$
75-80	0.95	+0.076
80-85	0.946	$ \begin{array}{r} -0.08 \\ +0.082 \\ -0.07 \end{array} $
85-90	1.01	$-0.07 \\ +0.069 \\ -0.15$
90-95	0.997	+0.071
95-105	1.1	$ \begin{array}{c} -0.055 \\ +0.084 \end{array} $
105-120	0.949	$ \begin{array}{c} -0.15 \\ +0.12 \\ 0.067 \end{array} $
120-140	1.21	$ \begin{array}{c} -0.065 \\ +0.077 \end{array} $
140-175	1.09	$ \begin{array}{c} -0.12 \\ +0.12 \end{array} $
175-230	1.04	$ \begin{array}{c} -0.15 \\ +0.12 \end{array} $
230-430	1.35	$ \begin{array}{c} -0.1 \\ +0.19 \\ -0.19 \end{array} $

Table 92: The leading jet  $p_T$  cross-section for  $W \to \mu\nu + \geq 1$  inclusive jets. This is a table version of plot 286 on page 245.

$p_T$ range (GeV/c)	Data/Theory	Total Systematic
20-25	0.982	$^{+0.18}_{-0.2}$
25-30	0.946	$+0.\overline{15} \\ -0.16$
30-35	0.974	$+0.11 \\ -0.15$
35-40	1.04	$+0.14 \\ -0.15$
40-45	1.04	$\begin{array}{c} -0.13 \\ +0.12 \\ -0.12 \end{array}$
45-50	1.13	$\begin{array}{c} -0.12 \\ +0.13 \\ -0.16 \end{array}$
50-55	1.25	+0.078
55-60	1.19	$ \begin{array}{c c} -0.085 \\ +0.14 \\ -0.15 \end{array} $
60-65	1.13	$\begin{array}{c} -0.13 \\ +0.12 \\ -0.14 \end{array}$
65-75	1.21	+0.075
75-85	1.33	$ \begin{array}{c} -0.076 \\ +0.12 \\ 0.22 \end{array} $
85-100	1.46	$ \begin{array}{c} -0.32 \\ +0.13 \\ 0.000 \end{array} $
100-135	1.32	$-0.088 \\ +0.1$
135-260	1.3	$ \begin{array}{c} -0.13 \\ +0.2 \\ -0.21 \end{array} $

Table 93: The second leading jet  $p_T$  cross-section for  $W \to \mu\nu + \geq 2$  inclusive jets. This is a table version of plot 287 on page 246.

$p_T$ range (GeV/c)	Data/Theory	Total Systematic
20-25	0.94	$+0.22 \\ -0.25$
25-30	1.02	$+0.\overline{21} \\ -0.19$
30-35	1.05	$+0.2 \\ -0.18$
35-40	1.19	+0.16
40-45	1.15	$ \begin{array}{r} -0.26 \\ +0.5 \\ -0.31 \end{array} $
45-50	1.1	$+0.62 \\ -0.33$
50-70	1.27	$+0.2 \\ -0.3$
70-170	1.53	$+0.14 \\ -0.17$

Table 94: The third leading jet  $p_T$  cross-section for  $W \to \mu\nu + \geq 3$  inclusive jets. This is a table version of plot 288 on page 246.

$p_T$ range (GeV/c)	Data/Theory	Total Systematic
20-25	0.959	+0.32 -0.36
25-35	1.1	$ \begin{array}{c} -0.36 \\ +0.39 \\ 0.35 \end{array} $
35-50	1.29	$ \begin{array}{c} -0.35 \\ +0.41 \\ 0.75 \end{array} $
50-90	2.12	$ \begin{array}{r} -0.75 \\ +0.55 \\ -1.2 \end{array} $

Table 95: The forth leading jet  $p_T$  cross-section for  $W \to \mu\nu + \ge 4$  inclusive jets. This is a table version of plot 289 on page 247.

$m_{jj}$ range $(\text{GeV/c}^2)$	$\sigma  (\mathrm{pb}/(\mathrm{GeV/c^2}))$	$\Delta \sigma \; (\mathrm{pb/(GeV/c^2)})$
0-30	0.0459	$^{+0.014}_{-0.01} \pm 0.0028$
30-35	0.1	$^{+0.024}_{-0.021} \pm 0.006$
35-40	0.118	$^{+0.027}_{-0.028} \pm 0.0071$
40-45	0.127	$^{+0.039}_{-0.034} \pm 0.0076$
45-50	0.175	$^{+0.038}_{-0.036} \pm 0.011$
50-55	0.175	$^{+0.04}_{-0.036} \pm 0.01$
55-60	0.203	$^{+0.041}_{-0.037} \pm 0.012$
60-65	0.181	$^{+0.029}_{-0.025} \pm 0.011$
65-70	0.177	$^{+0.029}_{-0.034} \pm 0.011$
70-75	0.172	$^{+0.033}_{-0.034} \pm 0.01$
75-80	0.134	$^{+0.022}_{-0.019} \pm 0.008$
80-85	0.144	$^{+0.012}_{-0.021} \pm 0.0086$
85-90	0.138	$^{+0.025}_{-0.032} \pm 0.0083$
90-95	0.1	$^{+0.016}_{-0.0096} \pm 0.006$
95-100	0.114	$^{+0.011}_{-0.022} \pm 0.0068$
100-105	0.109	$^{+0.016}_{-0.019} \pm 0.0065$
105-110	0.0672	$^{+0.016}_{-0.0096} \pm 0.004$
110-120	0.0588	$^{+0.0099}_{-0.0076} \pm 0.0035$
120-130	0.0515	$^{+0.0046}_{-0.0079} \pm 0.0031$
130-140	0.0434	$^{+0.0046}_{-0.005} \pm 0.0026$
140-155	0.0309	$^{+0.0028}_{-0.0053} \pm 0.0019$
155-170	0.0213	$^{+0.0039}_{-0.0044} \pm 0.0013$
170-190	0.0172	$^{+0.002}_{-0.0016} \pm 0.001$
190-215	0.0116	$^{+0.0014}_{-0.0026} \pm 0.0007$
215-250	0.00543	$^{+0.00044}_{-0.00047} \pm 0.00033$
250-295	0.00351	$^{+0.00057}_{-0.00033} \pm 0.00021$
295-425	0.00107	$^{+0.00018}_{-0.00022} \pm 6.4$ e-05

Table 96: Dijet mass  $(m_{jj})$  cross-section for  $W \to e\nu + \geq 2$  jets. This is a table version of plot 290 on page 248.

$m_{jj}$ range (GeV/c <sup>2</sup> )	$\sigma  (\mathrm{pb}/(\mathrm{GeV/c^2}))$	$\Delta \sigma \; (\text{pb/(GeV/c}^2))$
0-30	0.0595	$^{+0.014}_{-0.012} \pm 0.0036$
30-35	0.163	$^{+0.012}_{-0.035} \pm 0.0098$
35-40	0.16	$^{+0.038}_{-0.038} \pm 0.0096$
40-45	0.18	$^{+0.027}_{-0.033} \pm 0.011$
45-50	0.201	$^{+0.042}_{-0.031} \pm 0.012$
50-55	0.288	$^{+0.029}_{-0.065} \pm 0.017$
55-60	0.251	$^{+0.058}_{-0.042}\pm0.015$
60-65	0.268	$^{+0.032}_{-0.048} \pm 0.016$
65-70	0.217	$^{+0.041}_{-0.037}\pm0.013$
70-75	0.219	$^{+0.027}_{-0.029} \pm 0.013$
75-80	0.203	$^{+0.028}_{-0.041} \pm 0.012$
80-85	0.173	$^{+0.027}_{-0.024} \pm 0.01$
85-90	0.169	$^{+0.018}_{-0.025} \pm 0.01$
90-95	0.139	$^{+0.012}_{-0.012} \pm 0.0083$ $^{+0.018}_{+0.018} \pm 0.0075$
95-100	0.124	$-0.018 \pm 0.0075$
100-105	0.123	$^{+0.01}_{-0.017} \pm 0.0074$
105-110	0.104	$^{+0.015}_{-0.02} \pm 0.0062$
110-120	0.0849	$^{+0.014}_{-0.01} \pm 0.0051$
120-130	0.069	$^{+0.0065}_{-0.0068} \pm 0.0041$
130-140	0.0644	$^{+0.0051}_{-0.0098} \pm 0.0039$
140-155	0.0454	$^{+0.0083}_{-0.0061} \pm 0.0027$
155-170	0.0306	$^{+0.0028}_{-0.0035} \pm 0.0018$
170-190	0.0235	$^{+0.0021}_{-0.0031} \pm 0.0014$
190-215	0.0171	$^{+0.00099}_{-0.0017} \pm 0.001$
215-250	0.00871	$^{+0.0019}_{-0.001} \pm 0.00052$
250-295	0.00486	$^{+0.00035}_{-0.00067} \pm 0.00029$
295-425	0.00131	$^{+0.00018}_{-0.00016} \pm 7.8\text{e-}05$

Table 97: Dijet mass  $(m_{jj})$  cross-section for  $W \to \mu\nu + \geq 2$  jets. This is a table version of plot 291 on page 249.

$m_{jj}$ range (GeV/c <sup>2</sup> )	$\sigma (1/(\text{GeV/c}^2))$	$\Delta \sigma \ (1/({\rm GeV/c^2}))$
0-30	0.00305	$+0.0002 \\ -0.00017$
30-35	0.00665	$+6e-05 \\ -0.00025$
35-40	0.00781	+8.2e-06 $-0.00053$
40-45	0.00844	$+0.00056 \\ -0.00087$
45-50	0.0116	$+0.00011 \\ -0.00038$
50-55	0.0116	+2.4e-05
55-60	0.0135	$ \begin{array}{r} -0.00034 \\ +2.6e-05 \\ -0.00027 \end{array} $
60-65	0.012	$+0.00061 \\ -0.00064$
65-70	0.0118	$+0.00018 \\ -0.00061$
70-75	0.0114	$+0.00023 \\ -0.00035$
75-80	0.00886	$+0.00042 \\ -0.00044$
80-85	0.00955	$+0.00042 \\ -0.0011$
85-90	0.00913	$+0.00036 \\ -0.00057$
90-95	0.00666	$+0.00069 \\ -0.00035$
95-100	0.00753	+9.8e-05 $-0.0008$
100-105	0.00721	$+6e-05 \\ -0.00045$
105-110	0.00446	+0.0002 $-1.5e-05$
110-120	0.0039	$^{+0.00024}_{-0.00019}$
120-130	0.00342	+0.00011 $-0.00039$
130-140	0.00288	+0.00023 $-0.00028$
140-155	0.00205	$+2.1e-05 \\ -0.00023$
155-170	0.00142	$+4.3e-05 \\ -5.4e-05$
170-190	0.00114	$+0.00012 \\ -0.00011$
190-215	0.000773	+4.2e-05 $-6.7e-05$
215-250	0.00036	+4.1e-05 $-4.3e-05$
250-295	0.000233	+2.4e-05 $-1.3e-05$
295-425	7.11e-05	$+2.2e-06 \\ -3.6e-06$

Table 98: Dijet mass  $(m_{jj})$  cross-section normalized to the inclusive 2 jets cross-section for  $W \to e\nu + \geq 2$  jets. This is a table version of plot 292 on page 250.

$m_{jj}$ range (GeV/c <sup>2</sup> )	$\sigma (1/(\text{GeV/c}^2))$	$\Delta \sigma \ (1/({\rm GeV/c^2}))$
0-30	0.00288	$+0.00012 \\ -0.00016$
30-35	0.0079	$+0.00028 \\ -0.00053$
35-40	0.00773	$+0.0004 \\ -0.00069$
40-45	0.00872	$+0.00021 \\ -0.00023$
45-50	0.00973	+0.00024 $-9.9e-05$
50-55	0.0139	+0.00091 $-0.0011$
55-60	0.0121	$+0.00055 \\ -9.7e-05$
60-65	0.013	+0.00029
65-70	0.0105	$ \begin{array}{r} -0.00064 \\ +9.9e-05 \\ -0.0001 \end{array} $
70-75	0.0106	+0.00033 $-0.00052$
75-80	0.00983	$+0.0003\overline{3} \\ -0.00048$
80-85	0.0084	$+0.00022 \\ -0.00016$
85-90	0.0082	$+0.00015 \\ -0.0005$
90-95	0.0067	$+0.00061 \\ -0.00054$
95-100	0.00603	$+0.00012 \\ -0.00017$
100-105	0.00596	+0.00014 $-0.00048$
105-110	0.00502	$+0.00015 \\ -0.00018$
110-120	0.00411	+0.00018 $-5e-05$
120-130	0.00334	$+0.00024 \\ -0.00024$
130-140	0.00312	+3.2e - 0.5 $-0.00027$
140-155	0.0022	$+6.7e - 05 \\ -8.1e - 06$
155-170	0.00148	+8.3e-05 -0.00011
170-190	0.00114	+3.7e-05
190-215	0.000829	$-8.4e-05 \\ +5.9e-05 \\ -8.5e-05$
215-250	0.000422	$+2.3e-05 \\ -1.5e-05$
250-295	0.000235	+6.3e-06
295-425	6.32e-05	$ \begin{array}{r} -2.1e - 05 \\ +3.1e - 06 \\ -2.3e - 06 \end{array} $

Table 99: Dijet mass  $(m_{jj})$  cross-section normalized to the inclusive 2 jets cross-section for  $W \to \mu\nu + \geq 2$  jets. This is a table version of plot 293 on page 250.

$R_{jj}$ range (GeV/c <sup>2</sup> )	$\sigma  (\mathrm{pb}/(\mathrm{GeV/c^2}))$	$\Delta \sigma \; (\text{pb/(GeV/c}^2))$
0.35-0.5	0.0943	$+0.02 \pm 0.0057$
0.5-0.65	1.04	$\begin{bmatrix} -0.025 \pm 0.0037 \\ +0.32 \\ -0.3 \pm 0.062 \end{bmatrix}$
0.65-0.8	2.98	$^{+0.84}_{-0.59} \pm 0.18$
0.8-0.95	3.31	$^{+1.1}_{-0.75} \pm 0.2$
0.95-1.1	3.27	$^{+0.91}_{-0.76} \pm 0.2$
1.1-1.25	3.05	$^{+0.68}_{-0.8} \pm 0.18$
1.25-1.4	3.03	$^{+0.8}_{-0.81} \pm 0.18$
1.4-1.55	3.16	$^{+1}_{-0.78}^{+1} \pm 0.19$
1.55-1.7	3.17	$^{+0.71}_{-0.8} \pm 0.19$
1.7-1.85	3.49	$^{+0.9}_{-0.76} \pm 0.21$
1.85-2	3.65	$^{+1}_{-1.1} \pm 0.22$
2-2.15	3.87	$^{+0.98}_{-0.93} \pm 0.23$
2.15-2.3	4.77	$^{+1}_{-1} \pm 0.29$
2.3-2.45	5.67	$^{+1.1}_{-1.1} \pm 0.34$
2.45-2.6	5.68	$^{+1.1}_{-1.1} \pm 0.34$
2.6-2.75	7.1	$^{+0.82}_{-1.3} \pm 0.43$
2.75-2.9	8.31	$\frac{11.2}{-1.3} \pm 0.5$
2.9-3.05	9.56	$^{+1.4}_{-1.5} \pm 0.57$
3.05-3.2	9.27	$-1.7 \pm 0.00$
3.2-3.35	5.88	$_{-1}^{+0.83} \pm 0.35$
3.35-3.5	3.87	$^{+0.62}_{-0.61} \pm 0.23$
3.5-3.65	3.05	$^{+0.67}_{-0.52} \pm 0.18$
3.65-3.8	2.01	$^{+0.36}_{-0.37} \pm 0.12$
3.8-3.95	1.36	$^{+0.28}_{-0.25} \pm 0.082$
3.95-4.1	0.887	$^{+0.15}_{-0.1} \pm 0.053$
4.1-4.25	0.755	$^{+0.13}_{-0.18} \pm 0.045$
4.25-4.4	0.435	$\frac{+0.087}{-0.091} \pm 0.026$
4.4-4.55	0.19	$\begin{array}{c} +0.058 \\ -0.057 \\ -0.054 \end{array} \pm 0.011$
4.55-4.7	0.155	$\left[\begin{array}{c} +0.054 \\ -0.049 \\ -0.049 \end{array} \pm 0.0093 \right]$
4.7-4.85	0.0438	$^{+0.019}_{-0.007} \pm 0.0026$

Table 100: Dijet separation  $(R_{jj})$  cross-section for  $W \to e\nu + \ge 2$  jets. This is a table version of plot 294 on page 251.

$R_{jj}$ range (GeV/c <sup>2</sup> )	$\sigma  (\mathrm{pb/(GeV/c^2)})$	$\Delta \sigma \; (\mathrm{pb/(GeV/c^2)})$
0.35-0.5	0.118	+0.006 + 0.0071
0.5-0.65	1.83	$^{-0.0003}_{+0.38}$ $+$ 0.11
0.65-0.8	4.53	+0.73 + 0.27
0.8-0.95	5.26	$^{-0.95}_{+1.2} \pm 0.27$
0.95-1.1	4.79	$^{-0.99}_{+0.79}_{0.08} \pm 0.29$
1.1-1.25	4.16	$^{-0.93}_{\stackrel{+0.92}{-0.75}} \pm 0.25$
1.25-1.4	4.45	$^{+0.61}_{-0.8} \pm 0.27$
1.4-1.55	4.49	$^{+0.86}_{-1} \pm 0.27$
1.55-1.7	4.73	$^{+0.82}_{-1.1} \pm 0.28$
1.7-1.85	4.93	$_{-1.1}^{+1} \pm 0.3$
1.85-2	5.53	$^{+0.9}_{-1.2} \pm 0.33$
2-2.15	5.89	$^{+0.9}_{-1.1} \pm 0.35$
2.15-2.3	6.74	$^{+1.1}_{-1.3} \pm 0.4$
2.3-2.45	7.37	$^{+1.2}_{-1.2} \pm 0.44$ $^{+1.3}_{+1.3} \pm 0.48$
2.45-2.6	8.03	$^{+\bar{1}.\bar{3}}_{-1.3} \pm 0.48$
2.6-2.75	10.1	$^{+1.3}_{-1.7} \pm 0.61$
2.75-2.9	10.8	$^{+1.3}_{-1.6} \pm 0.65$
2.9-3.05	12	$^{+1.9}_{-1.7} \pm 0.72$
3.05-3.2	11.8	$^{+1.5}_{-1.9} \pm 0.71$
3.2-3.35	7.16	$^{+0.86}_{-1.2} \pm 0.43$
3.35-3.5	5.05	$^{+0.77}_{-0.74} \pm 0.3$
3.5-3.65	3.82	$^{+0.52}_{-0.66} \pm 0.23$
3.65-3.8	2.38	$^{+0.45}_{-0.38} \pm 0.14$
3.8-3.95	1.74	$^{+0.32}_{-0.35} \pm 0.1$
3.95-4.1	1.04	$^{+0.19}_{-0.23} \pm 0.063$
4.1-4.25	0.942	$^{+0.14}_{-0.23} \pm 0.056$
4.25-4.4	0.422	$^{+0.15}_{-0.07} \pm 0.025$
4.4-4.55	0.294	$^{+0.068}_{-0.046} \pm 0.018$
4.55-4.7	0.158	$^{+0.03}_{-0.068} \pm 0.0095$
4.7-4.85	0.0868	$^{+0.013}_{-0.013} \pm 0.0052$

Table 101: Dijet separation  $(R_{jj})$  cross-section for  $W \to \mu\nu + \geq 2$  jets. This is a table version of plot 295 on page 251.

$R_{jj}$ range (GeV/c <sup>2</sup> )	$\sigma  (\mathrm{pb/(GeV/c^2)})$	$\Delta \sigma \; (\mathrm{pb/(GeV/c^2)})$
0.35-0.5	0.00626	$+9.2e-05 \\ -0.00065$
0.5-0.65	0.0687	$+0.0048 \\ -0.0089$
0.65-0.8	0.197	$\begin{array}{c} -0.0039 \\ +0.009 \\ -0.0042 \end{array}$
0.8-0.95	0.219	+0.016
0.95-1.1	0.217	$ \begin{array}{c} -0.012 \\ +0.0088 \end{array} $
1.1-1.25	0.203	$ \begin{array}{c} -0.014 \\ +0.0011 \end{array} $
1.25-1.4	0.201	$ \begin{array}{r} -0.021 \\ +0.0058 \end{array} $
1.4-1.55	0.21	$ \begin{array}{r} -0.021 \\ +0.018 \end{array} $
1.55-1.7	0.21	$ \begin{array}{r} -0.017 \\ +0.00052 \end{array} $
1.7-1.85	0.232	$ \begin{array}{r} -0.019 \\ +0.0059 \end{array} $
1.85-2	0.242	$ \begin{array}{r} -0.011 \\ +0.012 \end{array} $
2-2.15	0.242	$-0.033 \\ +0.0055$
2.15-2.3	0.317	$ \begin{array}{r} -0.019 \\ +0.0049 \end{array} $
2.3-2.45	0.376	$ \begin{array}{r} -0.014 \\ +0.0092 \end{array} $
2.45-2.6	0.377	$ \begin{array}{c} -0.012 \\ +0.0027 \end{array} $
2.6-2.75	0.471	$ \begin{array}{r} -0.013 \\ +0.0015 \end{array} $
2.75-2.9	0.551	$ \begin{array}{r} -0.043 \\ +0.016 \end{array} $
2.9-3.05	0.634	$ \begin{array}{r} -0.038 \\ +0.017 \end{array} $
3.05-3.2	0.615	$ \begin{array}{r} -0.041 \\ +0.0026 \end{array} $
3.2-3.35	0.39	$ \begin{array}{r} -0.035 \\ +0.0045 \end{array} $
3.35-3.5	0.39 $0.257$	$ \begin{array}{r} -0.028 \\ +0.007 \end{array} $
3.5-3.65	0.202	$ \begin{array}{r} -0.014 \\ +0.0027 \end{array} $
3.65-3.8	0.202	$ \begin{array}{r} -0.0014 \\ +0.00075 \end{array} $
		$-0.005 \\ +1.4e-05$
3.8-3.95	0.0905	$ \begin{array}{r} -0.0019 \\ +0.0046 \end{array} $
3.95-4.1	0.0589	$ \begin{array}{r} -0.0026 \\ +0.0023 \end{array} $
4.1-4.25	0.0501	$-0.0035 \\ +0.00063$
4.25-4.4	0.0288	$ \begin{array}{r}                                     $
4.4-4.55	0.0126	$ \begin{array}{r} +0.00032 \\ -0.0019 \\ +0.001 \end{array} $
4.55-4.7	0.0103	$ \begin{array}{r} +0.001 \\ -0.0017 \\ +0.00049 \end{array} $
4.7-4.85	0.00291	-7.4e-05

Table 102: Dijet separation  $(R_{jj})$  cross-section normalized to the inclusive 2 jets cross-section for  $W \to e\nu + \geq 2$  jets. This is a table version of plot 296 on page 252.

$R_{jj}$ range (GeV/c <sup>2</sup> )	$\sigma \; (\mathrm{pb}/(\mathrm{GeV/c^2}))$	$\Delta \sigma \; (\text{pb/(GeV/c}^2))$
0.35-0.5	0.00573	$+0.00072 \\ -0.00062$
0.5-0.65	0.0888	+0.0021
0.65-0.8	0.219	$ \begin{array}{r} -0.0093 \\ +0.0032 \end{array} $
0.8-0.95	0.255	$ \begin{array}{c} -0.013 \\ +0.012 \end{array} $
0.95-1.1	0.232	$ \begin{array}{r} -0.0084 \\ +0.0027 \end{array} $
1.1-1.25	0.201	$ \begin{array}{r} -0.012 \\ +0.0074 \end{array} $
1.25-1.4	0.215	$ \begin{array}{r} -0.0047 \\ +0.005 \end{array} $
1.4-1.55	0.215 $0.217$	$ \begin{array}{r} -0.0075 \\ +0.0022 \end{array} $
1.55-1.7	0.229	$ \begin{array}{r} -0.016 \\ +0.00094 \end{array} $
1.7-1.85	0.238	$ \begin{array}{r} -0.017 \\ +0.0058 \end{array} $
1.85-2	0.268	$ \begin{array}{r} -0.017 \\ +0.0039 \end{array} $
2-2.15	0.285	$ \begin{array}{r} -0.017 \\ +0.0066 \end{array} $
2.15-2.3	0.326	$ \begin{array}{r} -0.0066 \\ +0.0057 \end{array} $
2.3-2.45	0.357	$ \begin{array}{r} -0.014 \\ +0.0012 \end{array} $
2.45-2.6	0.389	$ \begin{array}{r} -0.0041 \\ +0.00078 \end{array} $
2.45-2.0	0.369	$ \begin{array}{r} -0.0063 \\ +0.0027 \end{array} $
2.75-2.9	0.49 $0.521$	$ \begin{array}{r} -0.02 \\ +0.007 \end{array} $
2.75-2.9 2.9-3.05	0.521 $0.582$	$ \begin{array}{r} -0.026 \\ +0.015 \end{array} $
		$ \begin{array}{c} -0.01 \\ +0.0021 \end{array} $
3.05-3.2	0.569	$ \begin{array}{r} -0.026 \\ +0.0055 \end{array} $
3.2-3.35	0.347	$ \begin{array}{c}     -0.017 \\     +0.004 \end{array} $
3.35-3.5	0.245	$ \begin{array}{r}     -0.0054 \\     +0.0027 \end{array} $
3.5-3.65	0.185	$ \begin{array}{r}     -0.0068 \\     +0.00095 \end{array} $
3.65-3.8	0.115	$-0.00039 \\ +0.00014$
3.8-3.95	0.0844	$ \begin{array}{r} +0.00014 \\ -0.0042 \\ +0.00011 \end{array} $
3.95-4.1	0.0504	-0.0035
4.1-4.25	0.0456	$\begin{array}{c} +0.00099 \\ -0.0046 \end{array}$
4.25-4.4	0.0204	$\begin{array}{c} +0.003 \\ -0.00013 \end{array}$
4.4-4.55	0.0142	+0.00063 $-4.4e-05$
4.55-4.7	0.00764	$+6.8e-05 \\ -0.0025$
4.7-4.85	0.0042	$+2.6e-05 \\ -8.7e-05$

Table 103: Dijet separation  $(R_{jj})$  cross-section normalized to the inclusive 2 jets cross-section for  $W \to \mu\nu + \geq 2$  jets. This is a table version of plot 297 on page 252.

$\Delta \eta$ range	$\sigma$ (pb)	$\Delta \sigma \text{ (pb)}$
0-0.4	7.41	$^{+1.3}_{-1.4} \pm 0.44$
0.4-0.8	8.14	$\begin{vmatrix} +1.4 \\ -1.3 \pm 0.49 \end{vmatrix}$
0.8-1.2	6.85	$\begin{vmatrix} +1.1 \\ -1.3 \pm 0.41 \end{vmatrix}$
1.2-1.6	5.4	$^{+0.99}_{-1} \pm 0.32$
1.6-2	4.77	$^{+0.87}_{-0.94} \pm 0.29$
2-2.4	2.75	$^{+0.57}_{-0.44} \pm 0.16$
2.4-2.8	1.93	$^{+0.38}_{-0.39} \pm 0.12$
2.8-3.2	1.03	$^{+0.22}_{-0.19} \pm 0.062$
3.2-3.6	0.326	$\left  \begin{array}{c} +0.094 \\ -0.074 \end{array} \pm 0.02 \right $
3.6-4	0.0483	$\left[ \begin{array}{c} +0.016 \\ -0.014 \end{array} \pm 0.0029 \right]$

Table 104: Closest  $\Delta \eta$  cross-section for  $W \to e\nu + \geq 2$  jets. This is a table version of plot 298 on page 253.

$\Delta \eta$ range	$\sigma$ (pb)	$\Delta \sigma \text{ (pb)}$
0-0.4	0.177	$^{+0.045}_{-0.059} \pm 0.011$
0.4-0.8	0.628	$^{+0.11}_{-0.17} \pm 0.038$
0.8-1.2	0.786	$^{+0.2}_{-0.18} \pm 0.047$
1.2-1.6	0.854	$^{+0.19}_{-0.17} \pm 0.051$
1.6-2	0.907	$^{+0.24}_{-0.23} \pm 0.054$
2-2.4	0.544	$^{+0.2}_{-0.11} \pm 0.033$
2.4-2.8	0.459	$^{+0.12}_{-0.12} \pm 0.028$
2.8-3.2	0.283	$^{+0.1}_{-0.067} \pm 0.017$
3.2-3.6	0.136	$^{+0.034}_{-0.03} \pm 0.0082$
3.6-4	0.00994	$^{+0.0043}_{-0.0044} \pm 0.0006$

Table 105: Closest  $\Delta \eta$  cross-section for  $W \to e\nu + \geq 3$  jets. This is a table version of plot 302 on page 255.

$\Delta \eta$ range	$\sigma$ (pb)	$\Delta \sigma$ (pb)
0-0.4	0.492	+0.0019 $-0.023$
0.4-0.8	0.54	+0.011
0.8-1.2	0.455	$ \begin{array}{c c} -0.023 \\ +0.0027 \end{array} $
1.2-1.6	0.358	$ \begin{array}{c c} -0.026 \\ +0.0043 \end{array} $
1.6-2	0.316	$ \begin{array}{r} -0.013 \\ +0.0069 \end{array} $
2-2.4	0.182	$ \begin{array}{c c} -0.012 \\ +0.0042 \end{array} $
2.4-2.8	0.102	$ \begin{array}{r r} -0.0029 \\ +0.0031 \end{array} $
2.8-3.2	0.0682	$\begin{vmatrix} -0.0032 \\ +0.00074 \end{vmatrix}$
3.2-3.6	0.0032 $0.0216$	$ \begin{array}{r r} -0.001 \\ +0.0011 \end{array} $
3.6-4		$ \begin{array}{r} -0.0012 \\ +0.00027 \end{array} $
3.0-4	0.00321	-0.00046

Table 106: Closest  $\Delta \eta$  cross-section normalized to the inclusive 2 jet cross-section for  $W \to e\nu + \geq 2$  jets. This is a table version of plot 300 on page 254.

$\Delta \eta$ range	$\sigma$ (pb)	$\Delta \sigma \text{ (pb)}$
0-0.4	0.0969	+0.006 $-0.013$
0.4-0.8	0.344	$\begin{array}{c c} +0.016 \\ -0.043 \end{array}$
0.8-1.2	0.431	+0.0019 $-0.025$
1.2-1.6	0.468	+0.018 -0.041
1.6-2	0.498	+0.012 $-0.025$
2-2.4	0.298	+0.0078 $-0.0072$
2.4-2.8	0.251	$\begin{array}{c c} -0.0072 \\ +0.0096 \\ -0.015 \end{array}$
2.8-3.2	0.155	$\begin{array}{c c} -0.013 \\ +0.0032 \\ -0.0012 \end{array}$
3.2-3.6	0.0747	+0.00087
3.6-4	0.00545	$ \begin{vmatrix} -0.005 \\ +0.00039 \\ -0.0015 \end{vmatrix} $

Table 107: Closest  $\Delta \eta$  cross-section normalized to the inclusive 3 jet cross-section for  $W \to e\nu + \geq 3$  jets. This is a table version of plot 304 on page 256.

$\Delta \eta$ range	$\sigma$ (1)	$\Delta\sigma$ (1)
0-0.4	10.9	$^{+1.5}_{-1.7} \pm 0.65$
0.4-0.8	11.4	$^{+1.6}_{-1.9} \pm 0.68$
0.8-1.2	9.33	$^{+1.3}_{-1.5} \pm 0.56$
1.2-1.6	7.86	$^{+0.95}_{-1.2} \pm 0.47$
1.6-2	5.58	$^{+0.85}_{-0.96} \pm 0.34$
2-2.4	3.55	$^{+0.6}_{-0.67} \pm 0.21$
2.4-2.8	2.34	$^{+0.37}_{-0.39} \pm 0.14$
2.8-3.2	1.32	$^{+0.29}_{-0.25} \pm 0.079$
3.2-3.6	0.386	$^{+0.086}_{-0.091} \pm 0.023$
3.6-4	0.121	$\left  \begin{array}{c} +0.04 \\ -0.032 \end{array} \pm 0.0073 \right $

Table 108: Closest  $\Delta \eta$  cross-section for  $W \to \mu \nu + \geq 2$  jets. This is a table version of plot 299 on page 253.

$\Delta \eta$ range	$\sigma$ (pb)	$\Delta \sigma \text{ (pb)}$
0-0.4	0.228	$^{+0.039}_{-0.063} \pm 0.014$
0.4-0.8	0.947	$\left[ \begin{array}{c} +0.19 \\ -0.18 \end{array} \pm 0.057 \right]$
0.8-1.2	1.24	$\begin{bmatrix} +0.21 \\ -0.22 \\ \end{bmatrix} \pm 0.074$
1.2-1.6	1.33	$^{+0.24}_{-0.28} \pm 0.08$
1.6-2	1.06	$^{+0.2}_{-0.27} \pm 0.063$
2-2.4	0.868	$\left[\begin{array}{c} +0.22 \\ -0.23 \end{array} \pm 0.052 \right]$
2.4-2.8	0.666	$\begin{array}{c} +0.16 \\ -0.14 \pm 0.04 \end{array}$
2.8-3.2	0.407	$\begin{bmatrix} +0.1 \\ -0.081 \\ \end{bmatrix} \pm 0.024$
3.2-3.6	0.158	$\begin{bmatrix} +0.037 \\ -0.044 \end{bmatrix} \pm 0.0095 \ \end{bmatrix}$
3.6-4	0.0398	$\begin{bmatrix} +0.023 \\ -0.013 \end{bmatrix} \pm 0.0024 \end{bmatrix}$

Table 109: Closest  $\Delta \eta$  cross-section for  $W \to \mu \nu + \geq 3$  jets. This is a table version of plot 303 on page 255.

$\Delta \eta$ range	$\sigma$ (pb)	$\Delta \sigma \text{ (pb)}$
0-0.4	0.526	$+0.0032 \\ -0.017$
0.4-0.8	0.55	$\begin{array}{r} +0.0025 \\ -0.019 \end{array}$
0.8-1.2	0.452	$+0.0017 \\ -0.017$
1.2-1.6	0.381	$+0.0019 \\ -0.019$
1.6-2	0.27	+0.0037 $-0.0061$
2-2.4	0.172	+0.0015 $-0.0056$
2.4-2.8	0.113	+0.00099 $-0.0022$
2.8-3.2	0.0639	+0.0022 $-0.0025$
3.2-3.6	0.0187	+0.0007 -0.0017
3.6-4	0.00587	$+0.00077 \\ -0.00074$

Table 110: Closest  $\Delta \eta$  cross-section normalized to the inclusive 2 jets cross-section for  $W \to \mu\nu + \geq 2$  jets. This is a table version of plot 301 on page 254.

$\Delta \eta$ range	$\sigma$ (pb)	$\Delta \sigma \text{ (pb)}$
0-0.4	0.0848	$+0.0055 \\ -0.0076$
0.4-0.8	0.352	$\begin{array}{c c} +0.0072 \\ -0.013 \end{array}$
0.8-1.2	0.46	$+0.019 \\ -0.028$
1.2-1.6	0.494	+0.0039 $-0.026$
1.6-2	0.393	+0.02 $-0.025$
2-2.4	0.323	+0.00069 $-0.024$
2.4-2.8	0.248	+0.00035 $-0.0026$
2.8-3.2	0.151	$+0.0016 \\ -0.00045$
3.2-3.6	0.0588	$+0.00068 \\ -0.0055$
3.6-4	0.0148	+0.0038 $-0.0023$

Table 111: Closest  $\Delta \eta$  cross-section normalized to the inclusive 3 jets cross-section for  $W \to \mu\nu + \geq 3$  jets. This is a table version of plot 305 on page 256.

$\Delta \eta$ range	$\sigma$ (1)	$\Delta\sigma$ (1)
0-0.4	0.0239	$+0.0023 \\ -0.0046$
0.4-0.8	0.0771	+0.0054 -0.01
0.8-1.2	0.115	$+0.012 \\ -0.0089$
1.2-1.6	0.158	+0.01 $-0.01$
1.6-2	0.19	$+0.016 \\ -0.013$
2-2.4	0.198	+0.027 $-0.012$
2.4-2.8	0.237	$+0.014 \\ -0.019$
2.8-3.2	0.275	+0.034 -0.014
3.2-3.6	0.418	$+0.039 \\ -0.046$
3.6-4	0.206	+0.023 $-0.066$

Table 112: Ratio of closest  $\Delta \eta$  cross-section  $(r_{\Delta \eta})$  for  $W \to e\nu \geq 3$  and 2 jets as described in equation 86 on page 248. This is a table version of plot 306 on page 257.

$\Delta \eta$ range	$\sigma$ (pb)	$\Delta \sigma \text{ (pb)}$
0-0.4	0.021	+0.0021 $-0.0034$
0.4-0.8	0.0833	$+0.0062 \\ -0.005$
0.8-1.2	0.133	$+0.0083 \\ -0.0082$
1.2-1.6	0.169	$+0.012 \\ -0.013$
1.6-2	0.189	$+0.012 \\ -0.022$
2-2.4	0.244	$+0.019 \\ -0.024$
2.4-2.8	0.284	+0.022 $-0.014$
2.8-3.2	0.308	+0.0092 $-0.0078$
3.2-3.6	0.41	+0.015 $-0.031$
3.6-4	0.328	$+0.063 \\ -0.022$

Table 113: Ratio of closest  $\Delta \eta$  cross-section  $(r_{\Delta \eta})$  for  $W \to \mu \nu \geq 3$  and 2 jets as described in equation 86 on page 248. This is a table version of plot 307 on page 257.

$\Delta \eta$ range	$\sigma$ (pb)	$\Delta \sigma \text{ (pb)}$
0-0.6	0.173	$^{+0.12}_{-0.046} \pm 0.01$
0.6-1.2	0.161	$^{+0.022}_{-0.032} \pm 0.0097$
1.2-1.8	0.0979	$^{+0.031}_{-0.038} \pm 0.0059$
1.8-2.4	0.0516	$^{+0.0094}_{-0.015} \pm 0.0031$
2.4-3	0.0048	$^{+0.0019}_{-0.0018} \pm 0.00029$

Table 114:  $|\eta^*|$  cross-section for  $W \to e\nu + \ge 3$  jets with  $|\Delta \eta_{jj}| > 2.0$ . This is a table version of plot 308 on page 258.

$\Delta \eta$ rang	ge $\sigma$ (pb)	$\Delta \sigma \text{ (pb)}$
0-0.6	0.244	$^{+0.067}_{-0.059} \pm 0.015$
0.6-1.2	0.202	$^{+0.057}_{-0.058} \pm 0.012$
1.2-1.8	0.154	$\left  \begin{array}{c} +0.039 \\ -0.043 \end{array} \pm 0.0092 \right $
1.8-2.4	0.0713	$\left  \begin{array}{c} +0.029 \\ -0.024 \end{array} \right. \pm 0.0043$
2.4-3	0.017	$\left( \begin{array}{c} +0.0044 \\ -0.0061 \end{array} \pm 0.001 \right)$

Table 115:  $|\eta^*|$  cross-section for  $W \to \mu\nu + \geq 3$  jets with  $|\Delta \eta_{jj}| > 2.0$ . This is a table version of plot 309 on page 259.

$\Delta \eta$ range	$\sigma$ (pb)	$\Delta \sigma$ (pb)
0-0.6	0.0948	+0.025 $-0.0046$
0.6-1.2	0.0885	+0.0036 -0.013
1.2-1.8	0.0537	+0.00089 $-0.011$
1.8-2.4	0.0283	+0.0024 $-0.0033$
2.4-3	0.00263	$+0.00012 \\ -0.00049$

Table 116:  $|\eta^*|$  cross-section normalized to the inclusive 3 jets cross-section for  $W \to e\nu + \ge 3$  jets with  $|\Delta \eta_{jj}| > 2.0$ . This is a table version of plot 310 on page 259.

$\Delta \eta$ range	$\sigma$ (pb)	$\Delta \sigma \text{ (pb)}$
0-0.6	0.0908	$+0.0017 \\ -0.004$
0.6-1.2	0.0752	$+0.0018 \\ -0.0076$
1.2-1.8	0.0571	+0.00025 $-0.005$
1.8-2.4	0.0265	+0.0033 $-0.0043$
2.4-3	0.00632	+4.9e - 05 -0.0012

Table 117:  $|\eta^*|$  cross-section normalized to the inclusive 3 jets cross-section for  $W \to \mu\nu + \geq 3$  jets with  $|\Delta \eta_{jj}| > 2.0$ . This is a table version of plot 311 on page 260.